Numéro d'ordre : 106542

LILLE UNIVERSITY
DALIAN UNIVERSITY OF TECHNOLOGY

LABORATOIRE DE GENIE CIVIL ET GEO-ENVIRONNEMENT
ÉCOLE DOCTORALE SCIENCES POUR L'INGÉNIEUR (SPI)

THESE

Pour obtenir le grade de

Docteur de l'Université de Lille

Discipline : Mécanique, Energétique, Matériaux
Présentée et soutenue publiquement

par

Qiang GUO

18 January 2019

Réponse thermo-mécanique des élastomères sous chargement cyclique: Modélisation constitutive et expérience

Thermo-mechanical response of rubbers under cyclic loading: Constitutive modeling and experiments

Jury

Issam DOGHRI	Professor	Louvain University	President
Mikhail ITSKOV	Professor	RWTH Aachen University	Reviewer
Jean-Benoît LE CAM	Professor	Rennes University	Reviewer
Valérie GAUCHER	Professor	Lille University	Member
Fahmi ZAIRI	Professor	Lille University	Thesis supervisor
Xinglin GUO	Professor	Dalian University of Technology	Thesis Co-supervisor

Boulevard Paul Langevin, Cité Scientifique, 59655 VILLENEUVE D'ASCQ CEDEX

CONTENTS

ACKNOWLEDGMENTS

The work presented in this thesis has been an exciting, as well as a challenging one. Its conclusion is much more than the summary of research in the last more than three years, rather a new beginning for further research. All the achievements of this period are due to our joint efforts with the people who provided helpful assistance and suggestion.

First of all, I would like to express my sincere gratitude to my supervisor, Prof. Fahmi Zaïri. It is his precious guidance, unlimited patience, selfless help and constant encouragement that continuously supported me to finish this work. I have benefited a lot from his extensive knowledge, enthusiasm and enlightening ideas. I could not have imagined having a better supervisor for my PhD study. The same gratitude should be attributed to Prof. Xinglin Guo, the other advisor of my PhD thesis. I appreciate all his concern and guidance in my research work. He helped me to obtain the opportunity to stay in France and apply for a doctoral degree.

Next, I would like to thank to the professors, colleagues and friends who have supported me during my PhD study. They are: Prof. Moussa Naït-Abdelaziz, Prof. Ali Zaoui, Prof. Jean-Michel Gloaguen, Dr. Zhengwei Qu, Dr. Jewan Ismail, Dr. Cristian Ovalle-Rodas, Dr. Amil Derrouiche, Dr. Hamza Lamnii, Dr. Christian Kamdem, Dr. Karim Kandil, Dr. Wanqing Shen, Dr. Zhu Yan, Hiba Baraket, Yao She, Li Peng, Junxiong Wang and Siyang Lu.

Last but not least, I am deeply grateful to my family. To my mother, thanks for her warmness, kindness and unconditional tolerance to me. To my father, thanks for his grit, supporting me behind my back. To my brother, thanks for your care and support, motivating me to live up to my aspirations. To my wife, thanks for her accompany, encouraging me to grasp every opportunity for promising future. To my daughter, thanks for being such an angel in my life.

Sincere acknowledgement to all the people. “Tous pour un, un pour tous”

INTRODUCTION

The present PhD dissertation deals with the coupled thermo-mechanical behavior of rubbers in relation with microstructure. In many common industrial applications, rubbers are cyclically loaded and exhibit a complex history-dependent thermo-mechanical response characterized by fatigue-induced stress-softening and hysteresis along with dissipative heating. Establishing the coupling between the different inelastic phenomena, usually appearing together during the cyclic loading history, is an open issue to be addressed.

This work is dedicated to the formulation and experimental verification of thermo-mechanical constitutive models for rubbers. It is divided into three main Chapters. *Chapter 1* brings a brief review about the necessary contents to understand the following chapters. *Chapter 2* is focused on the thermo-mechanical response of cyclically loaded filled rubbers. *Chapter 3* is focused on the thermo-mechanical response of stretch-induced crystallizable rubbers.

Chapter 1 is a succinct summary of classic knowledge which can be found in specialized works and that have been selected for their relevancy in the present study for the reader convenience. The industrial applications and the research history are briefly reported. Moreover, in order to understand the rubber behavior at the macro-scale from their microscopic architecture, the chemical characterization is presented. Then, the thermo-mechanical response of filled rubbers will be drawn. In the last section, the well known continuum mechanics theory as well as the laws of the thermodynamics are recalled. Finally, some notions about models to describe the large strain elastic behavior of rubber-type materials are provided.

Chapter 2 is focused on filled rubbers. In a first Part, the effects of pre-stretch and filler content on the history-dependent cyclic response of a representative carbon-filled synthetic rubber (styrene-butadiene rubber) are qualitatively and quantitatively analyzed by using the internal state variable theory. An interpretation of the

underlying physical mechanisms is proposed in which two types of dissipative network rearrangements are considered, i.e. recoverable rearrangements inducing viscoelasticity and unrecoverable rearrangements inducing damage. In order to predict the main set of inelastic fatigue effects (fatigue-induced stress-softening and hysteresis along with dissipative heating), in a second Part, we formulate a new thermo-viscoelastic-damage constitutive model based on the internal state variable theory. The proposed constitutive model is implemented into a finite element program and numerical applications on rubber structures are performed. The predictive capabilities of the model are verified by comparisons with our experimental observations in a third Part.

Chapter 3 is focused on stretch-induced crystallizable rubbers. In a first Part, we develop a new micro-mechanism inspired molecular chain model to describe the progressive evolution of the crystallinity degree in rubbers and the history-dependent thermo-mechanical response within the context of the thermodynamic framework. In this model, the molecular configuration of the partially crystallized single chain is analyzed and calculated by means of some statistical mechanical methods. The micro-macro transition is achieved by means of the microsphere-based strategy. The proposed constitutive model is then used to discuss some important aspects of the micro-mechanism and the macro-response under the equilibrium state and the non-equilibrium state involved during stretching/recovery and continuous relaxation. In a second Part, the model simulations are compared to experimental data at different stretch levels and temperatures. Local fields in terms of crystallization-induced anisotropy are presented on illustrative numerical examples. The results show that the proposed model offers a satisfactory way to predict the thermo-mechanical response of stretch-induced crystallizable rubbers.

General conclusions and *Research perspectives* are presented at the end of the document.

CHAPTER 1. ELEMENTS OF STRUCTURE, MECHANICS AND THERMODYNAMICS OF ELASTOMERS

The *Chapter 1* is intended to offer a conceptual frame of reference that allows the reader to deep into the posterior contents with a major sensation of comfort. In the *generalities* section the application and the polymers research history, giving relative emphasis to the rubber materials, is briefly reported. Later, the definitions of concepts related with the chemistry that characterize the different polymers and that allow to understand their behavior in the macroscopic scale from their microscopic architecture are presented. From this characterization, it is possible to go more deeply into the particular characteristics of the elastomers and, especially, into the studied material: styrene-butadiene rubber filled with carbon-black particles. The thermo-mechanical behavior of the elastomers as a result of different test conditions will be drawn in the section dedicated to the *filled elastomers thermo-mechanical behavior*. At the same time, the effects in the thermo-mechanical behavior of elastomers by the incorporation of carbon-black fillers are described in this section. In the last section, *elements of continuum mechanics and thermodynamics*, the classic knowledge of finite strain mechanics of continuum medium as well as the thermodynamics laws that describe the material behavior in a coherent way regarding the physical laws is exposed. Finally, some notions concerning statistical and phenomenological models to describe the large strain elastic behavior of rubber-type materials are presented.

1.1. Generalities

1.1.1. Historical background[1]

In 1496, after his second voyage to America, Christopher Columbus brought back to Europe crude rubber balls after having seen the Haitian natives playing with rubber balls. The natives in Haiti made these by cutting into bark of the rubber tree, smearing the latex which exuded onto the pointed end of a wooden stick and then drying it near a fire. In fact, it is well established that ancient American cultures as the Olmec, the Aztecs, the Mayas and the Incas already used the latex to manufacture common objects like boots, containers, covered tiles and, especially, balls, as they used to play with them an ancient game representing an important aspect of their cosmogony (Ximenez, 1715). Although there was much interest in Europe in this material little progress was made concerning its use: the latex would coagulate on its long voyage from the New to the Old World and coagulated latex was hard to work with.

The South America exploration by the Frenchman Charles-Marie de La Condamine, in 1736, brought again the potential of rubber to the attention of the Europeans. He gallicizes the word "cao tchu", meaning *tree that cries* in the native language, to *caoutchouc* and bring back some samples to the French Guyana. The first scientific studies are attributed to the French engineer François Fresneau who has impregnated his boots of latex to waterproof them. Unfortunately, the rubber is sensitive to the temperature (i.e. it rigidifies at low temperatures and becomes viscous at high temperatures) so its application remained very limited. In 1791, the British manufacturer Samuel Peal got a patent of the first industrial application of rubber related with the fabric waterproofing by means of a rubber - oil of turpentine solution. Around 1818, Charles Macintosh discovered another way to waterproof fabrics: he adhered two fabric sheets together using a rubber - coal-tar naphtha solution. The waterproof property is obtained when the solvent is evaporated. In 1835, the chloride of vinyl polymerization was accidentally discovered by Henri Victor Regnault. A great advance in rubber application was the discovery by Charles Goodyear in 1838 that natural rubber containing sulfur turned elastic after heat treatment (i.e. vulcanization). In 1862, Alexander Parks made a material named Parkesine modifying cellulose with nitric acid to form cellulose nitrate and mixing this polymer with a plasticizer. This discovery is the base of the modern plastic industry. The growth of rubber

[1] The text is based on the natural rubber history section from Baranwal and Stephens (2001); however, additional references have been added.

products was increasing and, in 1888, John Dunlop developed a pneumatic rubber tire for bicycles hereby initiating the *tire age*.

The 20th century marks the beginning of significant studies related with the behavior and properties of polymers and, specially, the development of synthetic polymers. In 1905, Leo Baekeland made the Bakelite, the first wholly synthetic polymer from phenol and formaldehyde. It can be said that the polymer science began in the 20s with the formulation of the macromolecular concept by Hermann Staudinger. In the 1930s, Werner Kuhn, Eugene Guth and Herman Mark proposed the statistical mechanical theory for rubber elasticity; besides, they found evidence that polymer chains in solution were flexible and that the viscosity in a solution was related to the molar mass of the polymer. Around 1933, the styrene-butadiene rubber was made in Germany; meantime, Wallace Carothers synthesize the first aliphatic polyester, and later and more importantly, the polychloroprene and the polyamide 6.6 (Nylon). The epoxy resins, the silicone rubbers and the polytetrafluoroethylene (Teflon®) were made, respectively, by Pierre Castan, Eugene Rochow and Roy Plunkett in the second half of the 30s. The thermodynamics theory for polymer solutions was presented, independently, in 1942 by Paul Flory and Maurice Huggins. The low-density polyethylene and the glass-fiber reinforced polyester were made during this decade. It is possible to say that since 1920 to 1950 a first generation of polymers was developed. Between 1950 and 1965 polymers of second generation were proposed. Karl Ziegler and Guilio Natta work led to the development of linear polyethylene and isotactic polypropylene. Theories for liquid crystals of rod-like polymers were proposed by Lars Onsager in 1949 and by Paul Flory in 1956. In this same year Michael Szwarc discovered living anionic polymerization - Kraton® is prepared by this method. The polyoxymethyle (Delrin®) and the aromatic polyamide (Nomex®) were made by DuPont in the first half of the 60s. Finally, a third generation of polymers, introduced since 1965, consisting mainly of polymers with a more complex chemical structure was developed. These polymers were characterized by high thermal and chemical stability and high strength. Meanwhile, existing polymers such as polyethylene have undergone significant improvement. In 1971, Pierre-Gilles de Gennes presented the reptation model to describe the diffusion of chain molecules in a matrix of similar chain molecules. The first melt-processable polymer (Xydar®) was reported by Steven Cottis in 1972. Theories for the crystallization of polymers were introduced by John Hoffman and coworkers in the mid-70s. Paul Morgan and Stefanie Kwolek reported, in 1977, that solutions of poly(phenylene terephthalamide) could be spun to super-strong and stiff fibers (Kevlar®). In 1977, the first electrically conductive polymer was prepared by Alan MacDiarmid, Alan Heeger and Hideka

Shirikawa. Nowadays, considering the nearby end of petroleum the industry of polymers contemplates, again, the use of natural rubber and searches substitutes to petroleum products by means of the synthesis of vegetal-based polymers.

1.1.2. Polymers

A polymer is a substance composed of molecules of high relative molecular mass, in which the structure essentially consists in the multiple repetition of units derived from molecules of low relative molecular mass connected between them in sufficient quantity to provide a set of properties that not varies significantly with the addition of one or few repetition units (Jones, 2008).

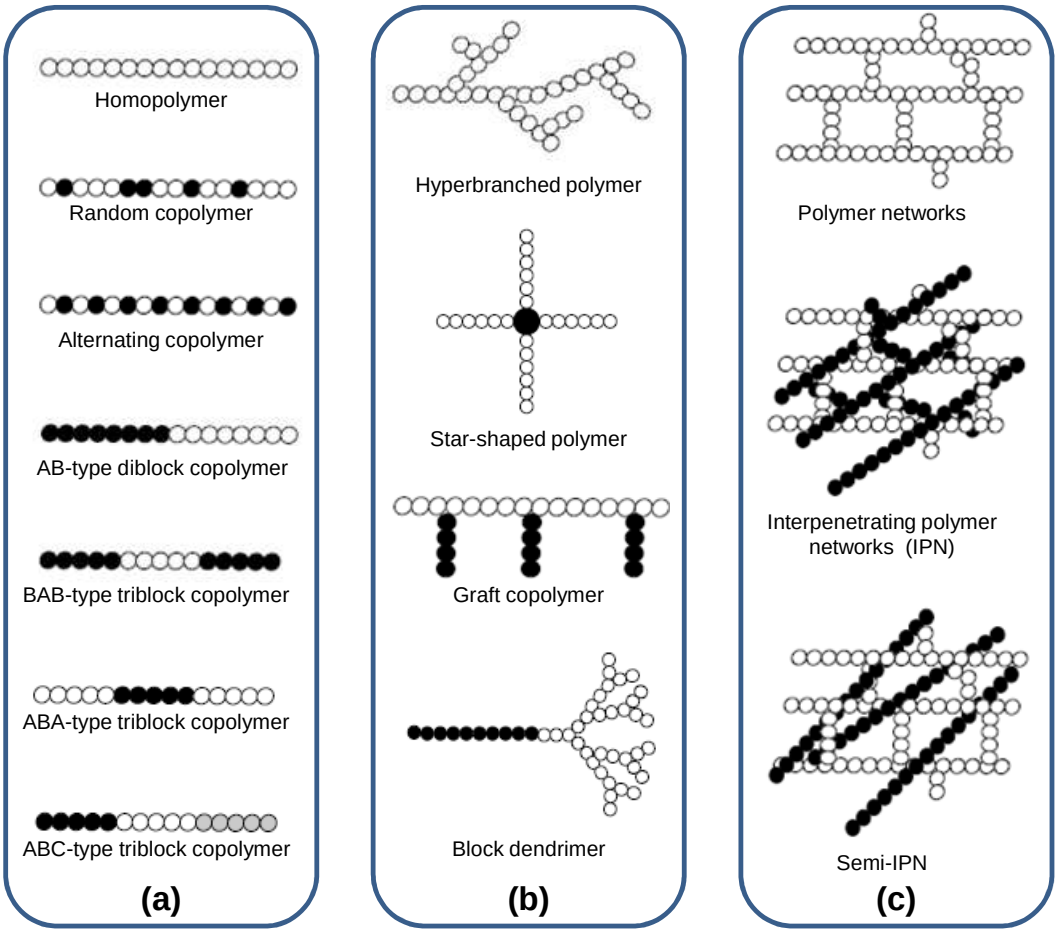

Figure 1.1. Polymer architectures: (a) linear polymers, (b) branched polymers, and (c) cross-linked polymers (Qiu and Bae, 2006).

The polymer architecture, the shape of a single polymer molecule, is constituted by the chemical composition of the monomer (repetition unit), the atoms disposition and links, the sequence order and the topologic aspects. Common polymer architectures are presented in Figure 1.1. The molecular architecture is important to describe many properties:

- Short-chain branching tends to reduce crystallinity,
- Long-chain branching tends to have a profound effects on rheological properties,
- Hyperbranched polymers consist of molecules with an approximately spherical shape, and
- Cross-linked polymers do not melt.

Considering the number of repeating units, a homopolymer consists of only one type of repeating unit whereas, on the other hand, a copolymer consists of two or more repeating units.

In general, the polymers are constituted by nine chemical elements: the carbon, the hydrogen, the sulfur, the oxygen, the fluorine, the silicon, the phosphor, the nitrogen and the chlorine (Kausch et al., 2001). The chain framework is constituted principally of carbon atoms linked by covalent bonds where the dissociation energy is in the order of E_C = 300 kJ/mol. Other types of atoms or molecules can be linked to the framework by polar or by van der Waals bonds where the dissociation energy is in the order of E_P = 10 kJ/mol, see Figure 1.2. The large difference in dissociation energy between different molecules is of great importance for polymer properties. A polymer preserves its configuration, 'permanent' stereostructure of a polymer, until it reacts chemically. The configuration is defined by the polymerization method - chemical reaction that converts monomers to a polymer.

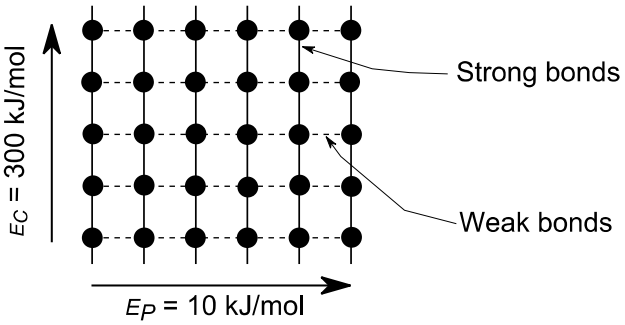

Figure 1.2. Schematic representation of a polymer crystal illustrating the bonds type.

The polymerization method can be divided into step-growth and chain-growth polymerization. In the step-growth process the kinetics of polymerization is not affected by the size of the reacting parts. The number of reacting groups decreases with increasing length of the molecules. At any given moment, the system will consist of a mixture of growing chains and water. Chain-growth polymerization involves several consecutives stages: initiation, propagation and termination. Each chain is individually initiated and grows very rapidly to a high molar mass, until its growth is terminated. At a given time, there are

essentially only two types of molecules present: monomer and polymer. The number of growing chains is always very low.

1.1.2.1. Amorphous and semi-crystalline polymers

The flexibility of the molecules allows different kinds of organization that presents an order less regular than within the metallic crystals. In fully amorphous polymers the chains are randomly arranged in the scale of a set of molecules but with certain order at a smaller scale (Figure 1.3). In spite of the random arrangement, the amorphous polymers are isotropic and frequently transparent in the macroscopic scale.

Figure 1.3. Structural representation of an amorphous polymer: (a) (Flory, 1953), (b) (Privalko and Lipatov, 1974), and (c) (Yeh, 1980).

A polymer is called semi-crystalline when the molecules of long chains tend to be arranged in packages to form crystallites separated by amorphous regions (Figure 1.4). In order that a polymer crystallizes it is necessary that its macromolecular chain has a strong regularity and also that its crystallization kinetics is not relatively slow. The crystallizable polymers will have a regular configuration and a regular global conformation, planar or helical zigzag in the thermoplastic polymers (Haudin, 1995). However, the macromolecular chains are not rigorously regular and the minimal irregularity, the enchainment of composing monomers or the presence of a ramification into the chain, will modify, limit, or avoid the crystallization. From the crystallization, the regular macromolecular chains, that can measure some micrometers of length, are organized and fold to form lamellae. The lamella crystallites form a superstructure with an average mesh size of 1 μm. They represent zones more resistant than the amorphous zones even that they contain an imperfect organization. The thickness and the regularity of the lamellae depend on the crystallization conditions and on the chains rigidity, ramifications, and the entanglements faults. These imperfections favor the connection

between lamellae, where they are linked by means of chunks of macromolecular chains (link chains) that belongs to other lamellae. The partially crystalline polymers are translucent and opaque, although the individual crystallites are far too small to scatter visible light individually.

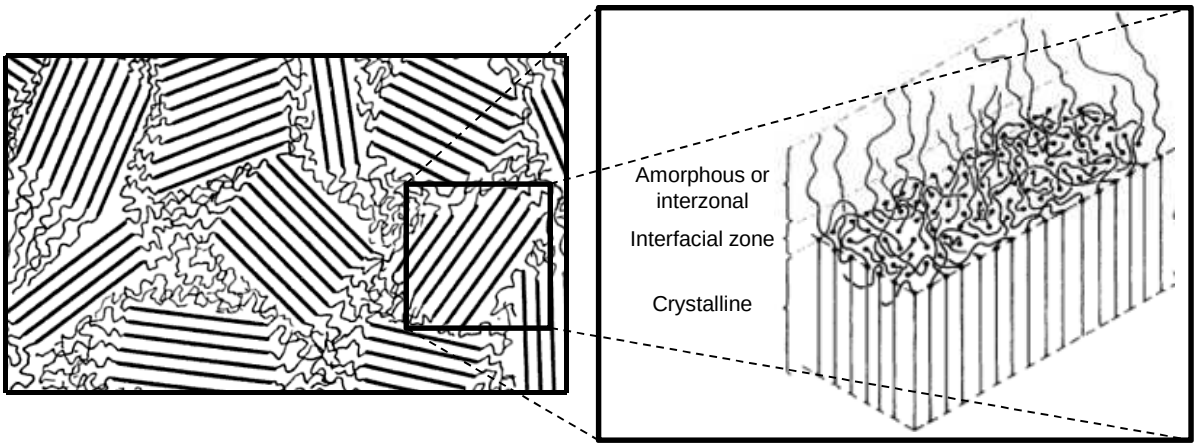

Figure 1.4. Structural representation of a semi-crystalline polymer.

A third recently developed group of polymers is the liquid-crystalline polymers, showing orientational order but not positional order. They are thus intermediates between the amorphous and the crystalline polymers. The nematic is the most probable liquid-crystalline phase to be formed directly from an isotropic melt, see Figure 1.5.

Figure 1.5. Structural representation of a liquid-crystalline polymer.

The differences in crystallinity can lead to differences in physical properties. A polymer can appear in four different states, as a function of the temperature, which corresponds to a temperature-function growth of the intermolecular free volume and a decrease of the link

forces, e.g. analyzing the curve of the density or of the elasticity modulus as a function of temperature, different polymer states can be observed (Figure 1.6).

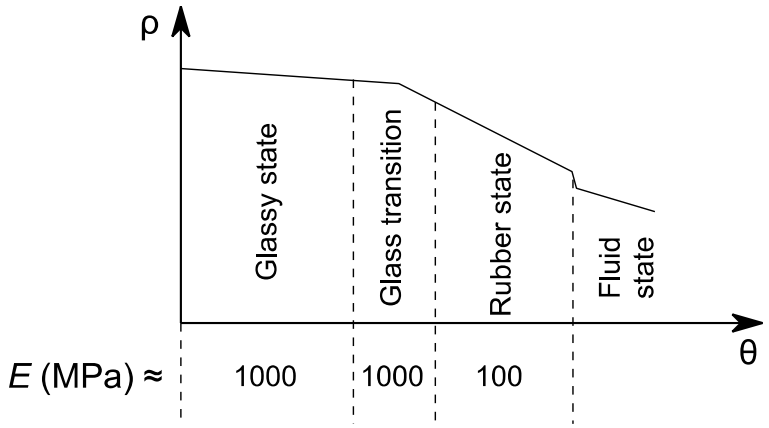

Figure 1.6. Polymer states.

According to the polymer, the environment temperature can be found into one of the four zones. At the glass transition region a fully amorphous polymer shows an important drop in modulus. The material state is glassy at temperatures below the glass transition temperature, θ_g. Under these conditions the organic glasses admits uniquely weak deformations predominantly due to stretching of secondary bonds and bond angle deformation. The glass transition region shows many kinetic peculiarities (e.g., damping behavior) and it is not a true thermodynamic phase transition like crystal melting. In this region, the linear thermoplastic and cross-linked polymers where the chemical decomposition occurs before fusion are found. At temperatures above θ_g, the materials are rubber-like with a weak modulus. In the rubber state region, large groups of atoms can change their conformation, e.g. cross-linked polymers show elastic properties due to the high rate at which the conformational changes occurs that the strain response to a step stress is instantaneous. On the other hand, the pronounced drop in modulus occurring at higher temperatures in uncross-linked polymers is due to the melting of the crystalline component.

1.1.2.2. Polymer categories

One suitable way to categorize the polymers is in terms of their mechanical and thermal behavior as:

- Thermoplastics are composed of long chains produced by a chain-growth polymerization; they typically behave in a plastic-ductile manner. The chains may or may not have branches. Individual chains are intertwined. There are relatively weak van der Waals bonds between atoms of different chains. This is somewhat similar to a few

trees that are tangled up together. The trees may or may not have branches, each tree is on its own and not connected to another. The chains in the thermoplastics can be untangled by application of a tensile stress. Thermoplastics can be amorphous or crystalline. Upon heating, thermoplastics soften and melt. They are processed into shapes by heating to elevated temperatures. Thermoplastics are easily recycled.

- Thermosetting polymers are composed of long chains (linear or branched) of molecules that are strongly cross-linked to one another to form three-dimensional network structures. Network of thermosetting polymers are like a bunch of strings that are knotted to one another in several places and not just tangled up. Each string may have other side strings attached to it. Thermosets are generally stronger, but more brittle, than thermoplastics. Thermosets do not melt upon heating but begin to decompose. They cannot easily be reprocessed after cross-linking reaction has occurred and hence recycling is difficult.
- Elastomers may be thermoplastics or lightly cross-linked thermosets. The polymer chains consist of coil-like molecules that can reversible stretch by applying a force. They can be stretched easily to high extensions and rapidly recover their original dimensions. They are commonly known as rubbers.

1.1.3. Elastomers

1.1.3.1. Processes to obtain synthetic elastomers

The synthetic elastomers are obtained by means of polymerization, polycondensation or copolymerization reactions that consist on the creation of chemical bonds between molecules to develop other molecules of higher dimensions.

The polymerization confronts the monomer with activation elements into a reactor[2]. The polymerization takes place in several stages:

- Activation: this reaction aims to create active centers, A* and B* (Figure 1.7), if R is the monomer.
- Propagation: the active center (ion or radical) is placed at an extremity of the chain and reacts little by little with the monomer.

[2] The chemical reactors offer the ideal conditions in terms of temperature, pH, solvents, pressure, etc. to obtain a certain type of elastomer.

- Chain transfer and ending: the active center can be preserved or destroyed during the ending stage.

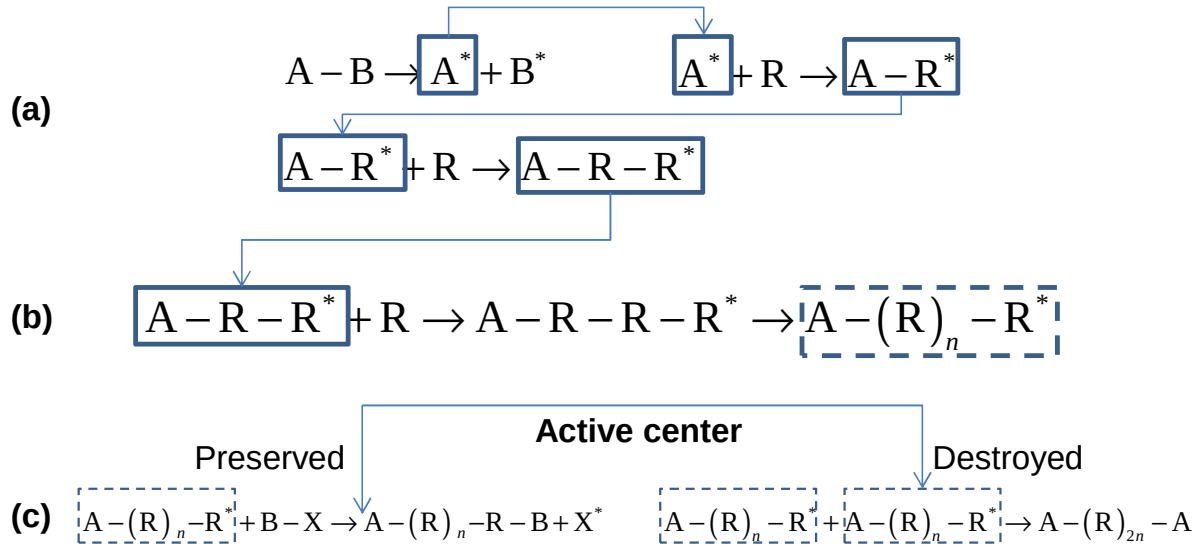

Figure 1.7. Polymerization reaction: (a) activation, (b) propagation, and (c) chain transfer and ending.

On the other hand, during the polycondensation the macromolecule is produced by the reaction of molecules having different chemical nature. Finally, the copolymerization consists of associate different types of monomers in order to improve the properties of the final material. There are three types of copolymers: alternating copolymer, statistical copolymer and block copolymer (Figure 1.1).

1.1.3.2. Formulation of elastomers

Seven categories of ingredients in the composition of an elastomer are distinguished:

A. Elastomeric matrix: The most important ingredient in rubber formulation. The elastomers can have natural or synthetic origin. Diverse elastomer grades exist differentiating, for example, the molecular distribution, the chain-length, the link rate, the monomer rate – copolymers and terpolymers[3] – and the oil or carbon-black presence. Specific elastomers are selected for desired compound properties. An elastomeric matrix can be used alone or associated with one or several elastomeric matrices.

B. Fillers: They are particles used to reinforce or enhance properties of elastomers while reducing cost of the compound. Their ability to interact with the elastomeric matrix

[3] Polymer consisting of three distinct monomers.

confers a, more or less, reinforcing character to the final mixture. Evidently, the reinforcing character depends on the filler-matrix chemical compatibility. Usually, the used mixtures have a load-rate that place them near the percolation limit, e.g., for a mixture containing 100 g of elastomer (ρ_e = 1000 kg /m^3) and 50 g of filler (ρ_f = 2000 kg /m^3), the volumetric fraction, φ_{filler}, is 0.2, whereas the limit is 0.3. The average particle size of the filler is the most important parameter concerning the capability to impart reinforcement to elastomers – reinforcement is obtained with sizes smaller than 100 nm.

There are two types of fillers commonly used by the rubber industry: Carbon-black and white fillers. High-resolution electron microscopy has shown (Leblanc, 2002) that carbon-black is built up of complex arrangements of spherical entities (colloidal black) whose diameter ranges from 10 to 90 nm (Figure 1.8). In general, the smaller the particle size, the more reinforcing the carbon-black, i.e. improvement in tensile, modulus, hardness and abrasion strength. The colloidal blacks are spheres made-up of broken quasi-graphitic layers whose stacking gives edges with a steps-like structure; depending on the manufacturing process, they exist in various forms of aggregation. The aggregates – smallest dispersible entity – form complex tri-dimensional objects (structure) which are associated into agglomerates. In a rubber compound, the void spaces within the aggregates are filled with rubber. This rubber – occluded rubber – is partly shielded from deformation and thus acts as part of the filler rather than as part of the rubber matrix (Medalia, 1970).

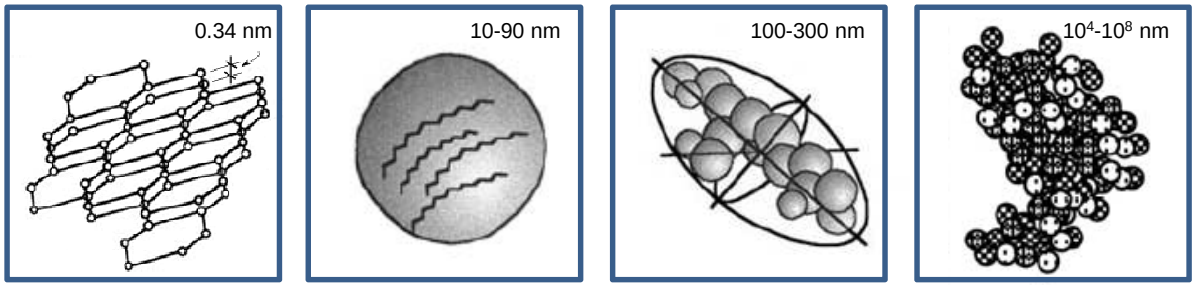

Figure 1.8. Relevant dimensions concerning the filler structure.

On the other hand, the non-black fillers contribution to the compound properties depends exclusively on the surface area. The first fillers used in rubber products were minerals that were naturally available: zinc oxide, clay, mica and asbestos. As in the carbon-black fillers, they were added to reduce tack, increase hardness and reduce the cost of the

compound. It must be taken into account that the fillers increase up to 10° the glass transition temperature.

C. Processing aids: They aim to improve the mixing operation of the different constituents of the material and to facilitate the calendering, extrusion and molding of the final product having increased the mobility of the polymer chains diminishing, therefore, the viscosity of the mixture. They act – without a chemical reaction – upon the mechanical properties of the final mixture and especially upon the viscoelastic properties – inverse relation between the chains mobility and the glass transition temperature. Additionally, they are used as dilution component of the elastomeric matrix in order to obtain a more economic mixture and to preserve satisfactory mechanical properties with higher filler molecules.

   Hydrocarbon oils are the most commonly used processing aids. Other processing aids used in rubber compounds are fatty acids, waxes, organic esters and low molecular weight polymers.

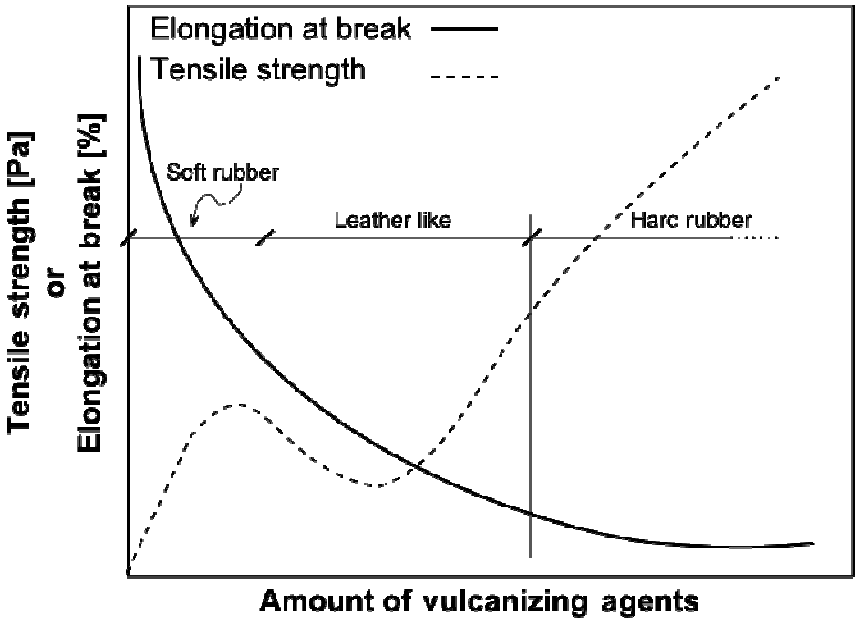

Figure 1.9. Influence of the amount of vulcanizing agents on common mechanical properties of natural rubber.

D. Deterioration inhibitors: The deterioration inhibitors or antidegradants are chemical products used to protect rubber both in uncured and cured states. The time, the temperature, the ozone and the light evolve the material structure (i.e. aging). These environment phenomena break in depth the double links within the material; as a consequence, a mechanical properties evolution can be seen. Evidently, good aging

properties of rubber compounds are essential for providing acceptable service life. In general, the more saturated the main chain of the elastomer matrix, the better are the aging properties.

E. Vulcanizing agents: They are chemical products that, upon heating, crosslink elastomer molecules to provide harder, more thermally stable elastic products. The most common vulcanizing agent is sulfur. During curing (vulcanization) a three-dimensional crosslinked network which imparts properties to compounds is formed. In fact, upon the vulcanization the rubber is changed from essentially a plastic material to either elastic or hard material (Figure 1.9).

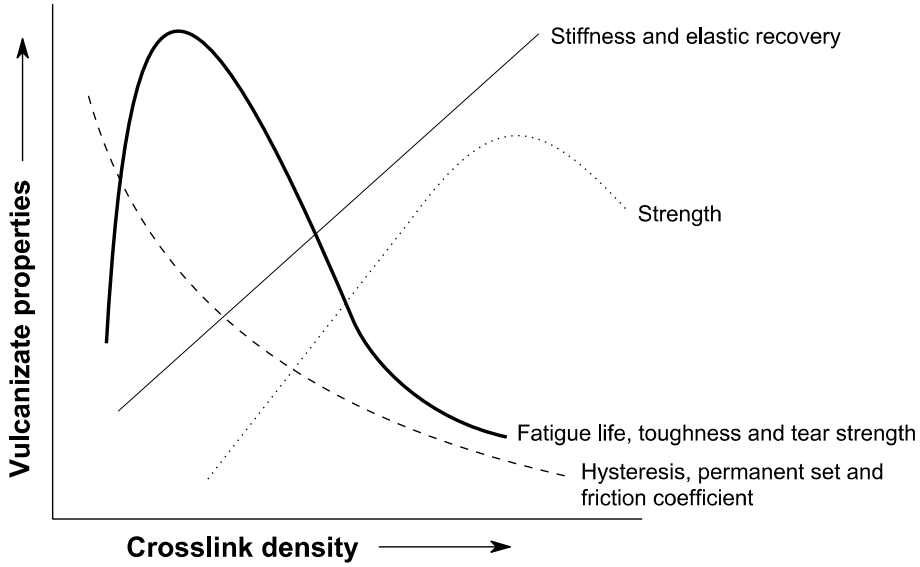

Figure 1.10. Effect of cross-link density on common properties of natural rubber.

In general, crosslink density, which is a measure of the extent of vulcanization, increases with cure time. Crosslink density and type of crosslinks (polysulfidic or monosulfidic) both affect compound properties. In Figure 1.10 it can be seen the cross-link density effect on properties. In relation to the type of crosslinks, the polysulfidic crosslink gives poor aging properties and poorer long-term flex life. On the other hand, mono- or di-sulfidic crosslinks provide poor fatigue life.

F. Accelerators: The chemical accelerators help raise the vulcanization speed by increasing the rate of crosslinking reactions. As sulfur alone takes a commercially prohibitive length of time to cure a rubber compound then chemical accelerators to speed up the curing rate are used.

G. Activators: Chemical products used to form complexes with accelerators and further activate the curing process. Most commonly used activators are zinc oxide and stearic acid.

1.1.3.3. Carbon-black in rubber

Carbon-black has been known and produced since antiquity but its discovery is attributed to S.C. Mote who came upon this in 1904. When it was discovered that carbon-black improves the mechanical properties of rubber compounds, it was extensively manufactured and used.

The *carbon-black* term refers to a group of industrial products consisting of:

- Furnace black: Furnace-made by the partial combustion of hydrocarbons.
- Thermal black: Produced by the thermal decomposition of natural gas.
- Channel black: Produced by the impingement of natural gas flames on channel irons.
- Lampblack: Made by burning hydrocarbons in open, shallow pans.

The most important characteristic of carbon-black, as rubber filler, is its specific surface area (total exposed surface per unit mass); it directly impacts the amount of interfacial contact area with the rubber. As its measurement involves molecular adsorption – phenomenon influenced by the carbon-black surface energy and activity (inhomogeneous across the surface) – the measurements of the specific surface area become a physicochemical characteristic as well as a geometrical characteristic. The second characteristic is the volume of the carbon-black aggregate. Carbon-black is commonly incorporated into rubber by shear forces practiced in an open mill. The carbon-black agglomerates become encapsulated by polymer during the first stage of incorporation, but the interstices between agglomerates and aggregates are still filled with air. Then, the rubber is forced through the channels between agglomerates and aggregates to form a reinforced rubber compound. The properties of uncured rubber are greatly influenced by the incorporation of carbon-black fillers: they change significantly the flow and viscosity. Contrary to unfilled compounds, carbon-black filled compounds have highly non-Newtonian flow and high viscosity – when the compound is forced to flow the hydrodynamic effect from the filler reduces the volume fraction of the flow medium causing shear strain amplification.

1.1.3.4. Styrene-butadiene rubber

Styrene and butadiene are co-monomers used in the manufacture of ESBR (emulsion) and SSBR (solution) by a chemical reaction (Figure 1.11).

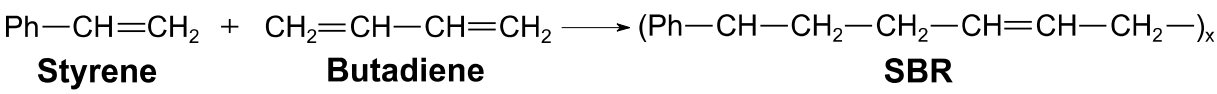

Figure 1.11. Styrene-butadiene rubber chemical reaction.

SBR compounding is similar to that of natural rubber (NR). It requires reinforcing fillers, as natural rubber, to acquire the necessary modulus and strength. The SBR does not change viscosity as much as natural rubber during mixing, extrusion and remilling. As in NR compounds, other ingredients such as plasticizers, activators and accelerators are used in SBR compounds as well. Compared to NR, SBR requires additional acceleration and less sulfur during vulcanization. Additionally, as it takes longer to cure, increasing the primary accelerator or adding a second one the required cure rate for the compound is accomplished. Whereas sulfur and accelerators are optimized for rapid cure rate, fillers and processing aids need to be balanced to attain a smooth extrusion.

Product categories	**Usage, % of total**
Tires and related products	65
Belt and Hose	10
Footwear	5
Foamed products	5
Mechanical goods	5
High Impact Polystyrene	–

Table 1.1. Major applications and uses of SBR by category.

SBR has a higher heat build-up behavior than a comparable NR compound. This is not a significant factor in many applications so, additional to their intrinsic advantages, the SBR is the preferably selected material. SBR is commonly blended with NR or low-cis polybutadiene to get optimum balance of properties for some applications. The major applications and uses of SBR are listed in Table 1.1.

1.2. Filled elastomers thermo-mechanical behavior

1.2.1. Thermo-mechanical behavior of elastomers

1.2.1.1. Finite deformation rubber elasticity

An unvulcanized elastomer flows easily under applied loads since the interactions between the chains are weak – these having great movement freedom under the influence of thermal agitation. On the other hand, the vulcanization turns solid the links among macromolecules – by means of sulfur and oxygen bridges – then the movements between chains are limited but the structure preserves, generally, an enormous flexibility. As a consequence, the elastomers behavior is directly related to the possibility of movement between the polymeric chains. Besides, this architecture is responsible of the different macroscopic behaviors under variable deformation.

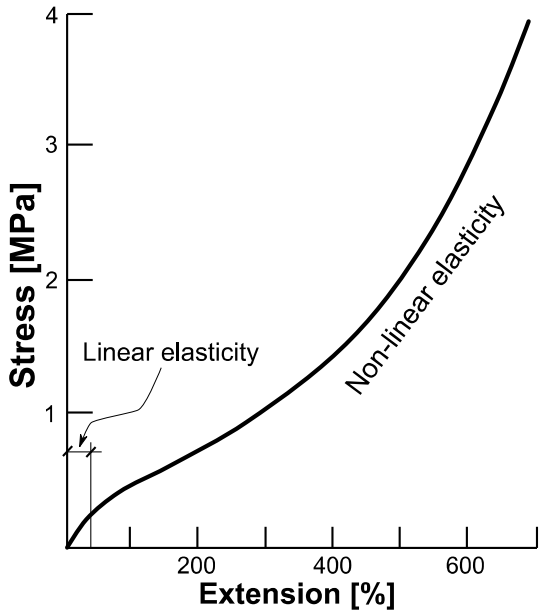

Figure 1.12. Common stress-extension curve of a vulcanized rubber.

The stress-strain curve obtained from a uniaxial traction test can be divided into two domains: linear and, predominantly, non-linear elasticity (Figure 1.12). Under small deformations, the stress-strain relation is linear, exhibiting a Young's modulus in the order of 1 MPa. This behavior is strongly related with the filler network created into the elastomeric matrix: the occluded rubber inside the carbon-black network or carbon-black agglomerates does not take part in the deformation – the volumetric fraction of the active elastomeric matrix is smaller than expected. If the deformation is superior to 1 or 10% then the filler network is fractured

and the initially occluded rubber is activated. Above this limit, the resistance of the mixture increases slowly under higher deformations. Besides, the secondary structures of the volume fraction of non-occluded rubber, entanglements between macromolecules, are loaded. At high deformation the high increase in stress is due largely, if not entirely, to strain-induced crystallization (Mark, 1982). Finally, the deformation strength grows highly up to break: the chains have attained their extensibility limit – the maximum extensibility for NR usually falls within the range 500-1000%.

1.2.1.2. Thermoelastic effects and temperature-dependent mechanical behavior

In 1805, James Gough published his results concerning the thermal behavior of natural rubber (Gough, 1805) evidencing the following observations:

- Rubber self-heats under stretching loads.
- Rubber held in a stretched state, under a constant load, contracts on heating.

These conclusions were confirmed for vulcanized rubber by Joule (1859). Since then both effects are known as the Gough-Joule effects. The rubber heat build-up effect depends on two different phenomena. First, the extension work is transformed into heat and, inversely, heat is absorbed pending relaxation. Second, if the elongation is considerable, the stretching induces the formation of a crystalline phase in the rubber matrix accompanied by the evolution of the latent heat of crystallization (Ehrbar and Boissonas, 1955). Concerning the second observation, the consequences are given in more detail.

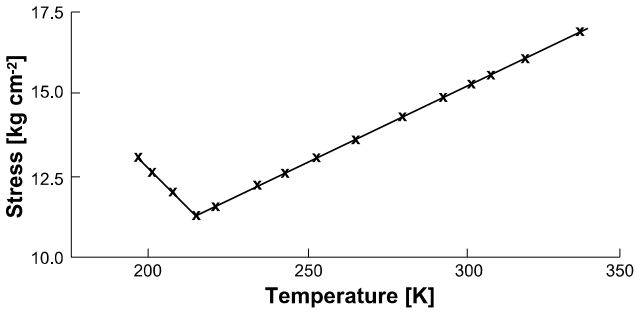

Figure 1.13. Stress at constant length, extension 350%, as function of the absolute temperature of a vulcanized rubber-sulfur compound (Meyer and Ferri, 1935).

The experiments of Meyer and Ferri (1935) demonstrate that the stretching force, for a given state of strain, is proportional to the absolute temperature (Figure 1.13). Such proportionality is related with the modification of the conformations of a system of long-chain molecules – associated uniquely with changes in the configurational entropy of the system – in passing from the unstrained to the strained state. However, under lower strains, the thermo-

mechanical behavior is inversed, i.e. the force decreases as the temperature raises (Figure 1.14). It can be seen that the inversion point occurs at an extension of about 10% – the thermoelastic inversion point. The negatives slopes at small extensions and the existence of an inversion point are due to the volume thermal expansion which is present in both the stretched and the unstretched states of rubber, i.e. even that the rubber samples were held at constant length it does not mean that they were held at constant elongation – at each temperature the unstressed length will have a different value.

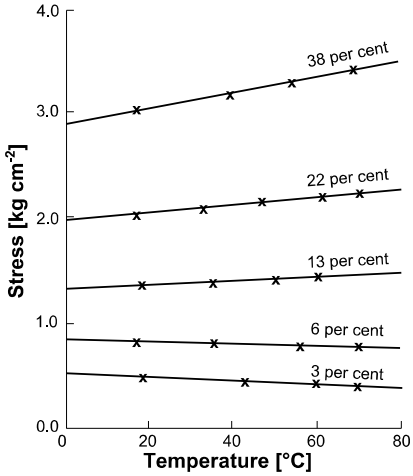

Figure 1.14. Stress-temperature curves obtained for elongations ranging from 3% to 38% from a vulcanized rubber (Anthony et al., 1943).

Therefore, even though the force at a given strain increases with the temperature, this increase is counterbalanced by the associated reduction in strain. Then, if the strain is calculated on the basis of the unstrained length at a given temperature, all stress curves pass through a single origin and the stress value is proportional to the absolute temperature, Figure 1.15.

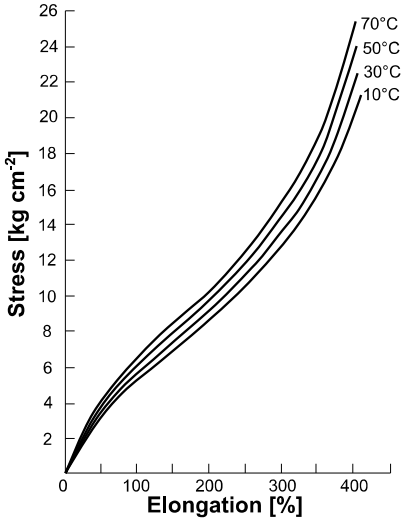

Figure 1.15. Stress-elongation curves obtained at various temperatures from a vulcanized rubber (Anthony et al., 1943).

1.2.1.3. Time effects

The elastomers exhibit a strong time-dependent mechanical behavior: response of the material under creep and stress-relaxation tests. A creep test consists on following the time evolution of the deformation of a test sample under a constant stress σ_0 during a sufficiently long time interval t before suppressing it. An elastic deformation (segment *AB*) appears instantaneously after the application of the stress (Figure 1.16). The viscoelastic behavior is seen under the form of a delayed deformation (segment *BC*) and a continuous evolution of the deformation (segment CD). Posterior to unloading the test sample there is an instantaneous recovery of the elastic deformation (segment *DE*) and, later, a total recovery of the delayed deformation (segment *EF*). From point *F* the test sample presents a residual deformation that is recovered after long periods of time.

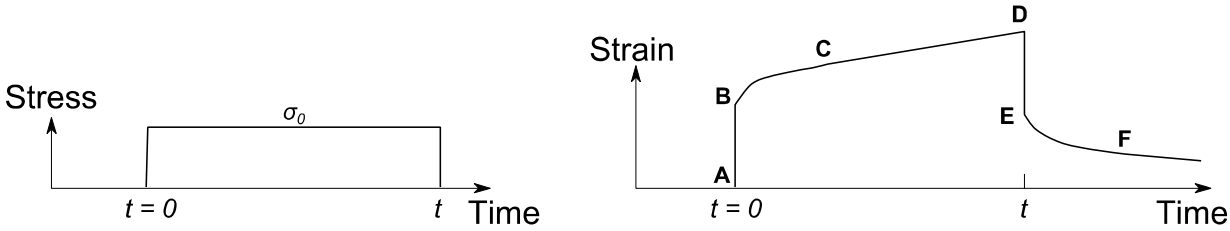

Figure 1.16. Creep behavior.

A stress-relaxation test consists on following the time evolution of the stress of a test sample under a constant deformation ε_0. An elastic stress (segment *AB*) appears instantaneously after the application of the deformation (Figure 1.17). The viscoelastic behavior is seen under the form of a progressive decrease of the stress (segment *BC*) up to a constant not-null value (from point *C*).

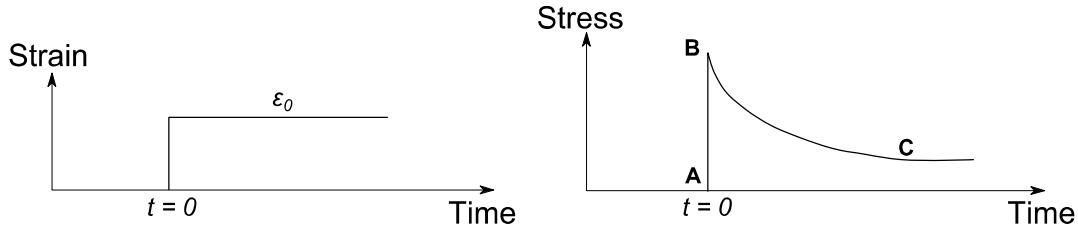

Figure 1.17. Stress-relaxation behavior.

The results of these tests demonstrate that to establish a relationship between the stress σ and the strain ε it is necessary to account for this time-dependence.

1.2.1.4. Dynamic properties and hysteretic behavior

Elastomers exhibit a complex mechanical behavior including both the behavior of a solid characterized by an instantaneous response and the viscous behavior of a liquid characterized

by a delayed response and a loss of energy at each cycle. The response of an elastomer under dynamic loads is better visualized in terms of a specimen undergoing uniform sinusoidal deformation as shown in Figure 1.18. The stress response is nearly sinusoidal but out of phase with the strain. The total stress response can be resolved into two components: one in-phase response (elastic stress) and one out-of-phase response (viscous stress), so at any time the measured stress is the algebraic sum of its two components. The phase is expressed by defining a cycle as a circle. Dividing the stress amplitudes by the strain amplitude gives the modulus components: storage modulus G' (related with elastic response) and the loss modulus G'' (related with viscous response)[4]. The storage modulus is related with the stored energy that will be recovered during the deformation process compensating partially or completely the, previously obtained, deformation of the structure. The loss modulus is related with the dissipated energy responsible of the heating-up of the test material – another part may be lost in the form of heat to the surrounding environment.

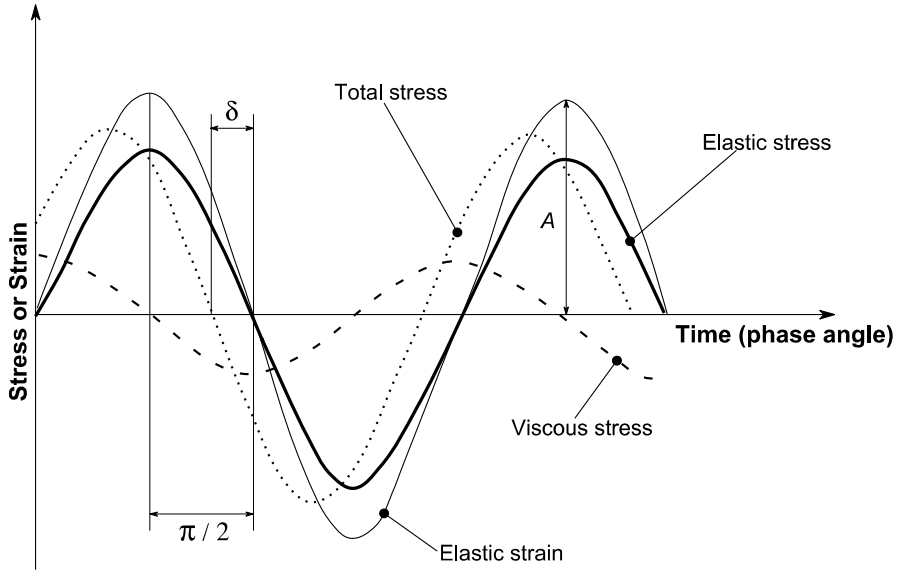

Figure 1.18. Stress components of an elastomer under dynamic loads.

The complex modulus G^* can be calculated as:

$$G^* = G' + iG'' \tag{1.1}$$

and the absolute value of the complex modulus can be calculated by:

$$\left|G^*\right| = \sqrt{G'^2 + G''^2} \tag{1.2}$$

where $\left|G^*\right|$ is simply called the dynamic modulus. Finally, the loss factor (or damping factor)

[4] *G* or *E* letters denote the shear and longitudinal modulus, respectively.

$$\tan\delta = \frac{G''}{G'} \tag{1.3}$$

is a measure of the loss energy from internal friction of the material.

If the stress is plotted against strain, for a single cycle, a hysteresis loop is seen (Figure 1.19). The area inside the hysteresis loop represents the mechanical energy which is not recovered during a cycle but instead is converted into heat. The isolating nature of rubbers can retain this heat and generate a thermal gradient (heat build-up). The mechanical energy loss or heat generated per cycle in compression-extension tests is the hysteresis (Medalia, 1991):

$$H = \frac{\pi}{4}\frac{2A}{100}E'\tan\delta \tag{1.4}$$

where A is the strain amplitude (see Figure 1.18).

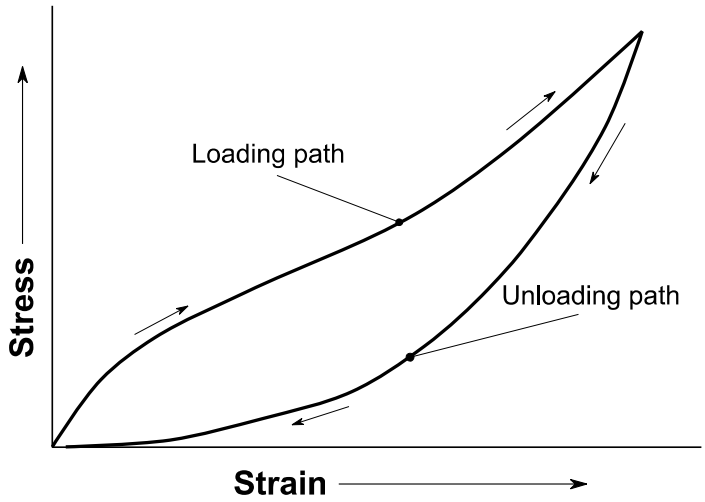

Figure 1.19. Hysteresis loop.

1.2.1.5. Mullins effect

The Mullins effect consists in an appreciable change of the mechanical properties of filled and non-filled rubber-type materials resulting from the first extension. This change is made evident as a stress-softening – lower resulting stress for the same applied strain – after the first load which increases progressively with the increasing maximum stretch (Figure 1.20). After a few cycles the material responses coincide during the following ones. This property was firstly observed by Bouasse and Carrière (1903) and intensively investigated by Mullins and his co-workers (Mullins, 1948, 1969; Mullins and Tobin, 1957, 1965). The principal phenomenological observations described by Mullins and co-workers can be summarized as follows:

- The softening is uniquely observed under higher elongations than the preceding ones in the loading history.
- An induced anisotropy as a consequence of the softening.

- The softening increases with an increasing volume of the initial fraction of filler.
- The complete recovery of the initial stiffness is never reached.
- The softening behavior is seen also from non-dilating load conditions, i.e. compression and shearing tests.

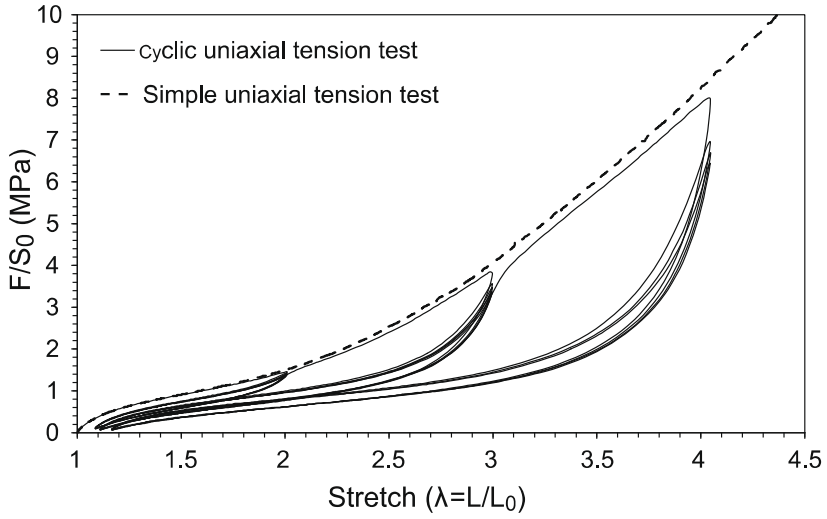

Figure 1.20. Stress-strain response of a filled SBR submitted to a simple uniaxial tension test and to a cyclic uniaxial tension test with increasing maximum stretch every 5 cycles (Diani et al., 2009).

Several physical interpretations have been proposed in order to explain the Mullins effect (Figure 1.21). The numerous interpretations proposed for the Mullins effect evidence that there is still no general agreement on the microscopic or mesoscopic origin of this effect. Blanchard and Parkinson (1952) related the first pre-strain softening with the rupture of the weaker bonds (physical bonds) at the rubber-particle interface while a further pre-strain would break the stronger bonds (chemical bonds). Bueche (1960) interpreted the Mullins effect in a similar way as Blanchard and Parkinson (1952); however, he has added to his interpretation an explanation of the softening in unfilled rubbers considering that the junctions arrange so as not to over-stretch the shorter chains. Simo (1987) and Govindjee and Simo (1991), pursuing the model proposed by Bueche (1960), estimated that the deformation induced by the relative movement between the fillers and the elastomeric matrix was the origin of the stress-softening. Houwink (1956) argued that the Mullins effect was related with the molecules slip over the surface of the fillers, considering the slow recovery of the stress-softening which could not be explained by the bond rupture source because, otherwise, this behavior would be permanent. During the first extension new bonds are instantaneously created, at different places of the original ones, along the rubber molecules. After measuring no significant change

in the crosslink density of stretched networks – no reversible part of the Mullins effect results in bond breakage – Dannenberg and Brennan (1965) adhered to Houwink model (Houwink, 1956). Admitting that bond ruptures happen and vacuoles form in the material during the first strain, Kraus et al. (1966) have proposed to attribute the main source of the Mullins effect to the rupture of the carbon-black structure.

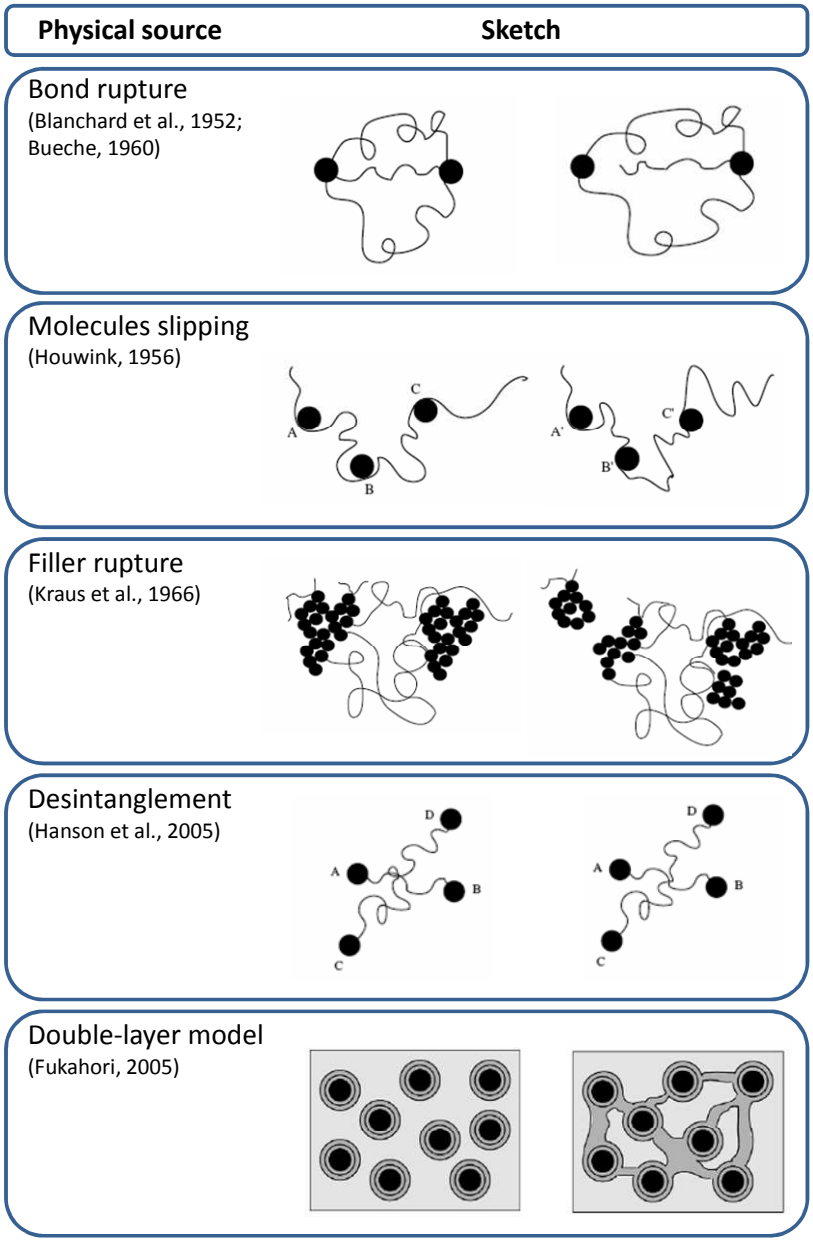

Figure 1.21. Physical interpretations of the Mullins effect (Diani et al., 2009).

Pursuing the interpretation proposed by Kraus et al. (1966), Kluppel and Schramm (2000) developed a macromolecular model which uses a strain amplification factor – the filler seen as a local strain amplifier – that decreases with an increasing maximum strain. Hanson et al. (2005), adopting Hamed and Hatfield (1989) configuration of chain entanglements between

particles, proposed a new interpretation of the Mullins effect which takes into account the induced anisotropy. Finally, Fukahori (2005) proposed an interface model – the material is represented by particle aggregates surrounded by a double-layer structure of bound rubber embedded in a crosslinked rubbery matrix – to explain the mechanics and mechanisms of reinforcement and softening.

1.2.1.6. Cyclic stress-softening

Additional to the first pre-strain softening (Mullins effect), the effect of repeated deformation leads the rubber to approach asymptotically a steady state with a constant – equilibrium – stress response (Figure 1.22). Softening occurs in both filled and non-filled rubber-type materials.

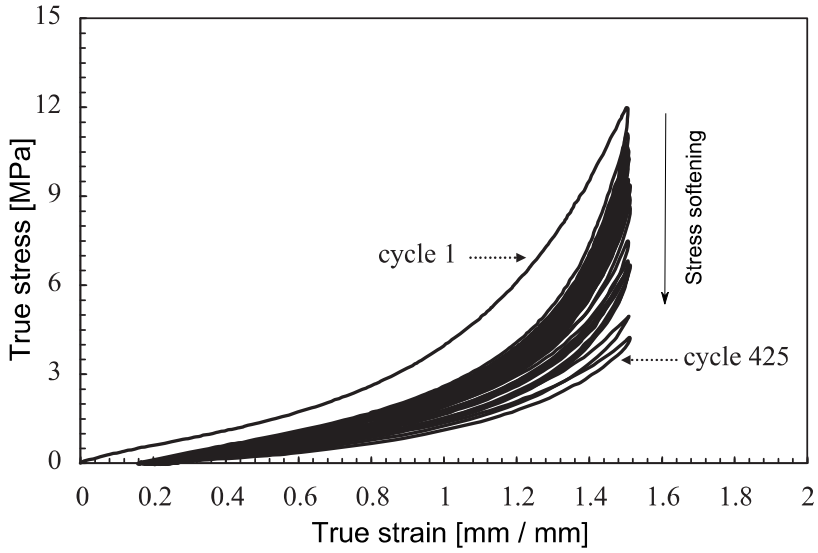

Figure 1.22. Stress-strain curves of SBR submitted to a cyclic tension test: from the first cycle up to 425 cycles (Ayoub et al., 2011a).

Numerous authors (Bouasse and Carrière, 1903; Shedd and Ingersol, 1904; Schwartz, 1907) published data demonstrating that stretching resulted in a softening of rubber; however, Holt (1931) was the first to describe the effects of repeated stretching and stretching-speed on the stress-strain properties of rubber compounds. Together with the progressive softening during repeated deformation, Holt also showed that stretching to a series of increasing strains resulted in a progressive increase in the observed softening at low strains, as can be deducted from Figure 1.20. In both unfilled and filled rubbers, most of the softening appears to be due to configurational changes of the rubber molecular network due to displacement of network junctions and entanglements during deformation and incomplete recovery to their original positions. The remaining and minor part of the softening in filled rubbers can be related to

break-down or slippage of filler-filler and filler-rubber linkages – any linkage broken and reformed while the rubber is deformed also contribute to softening and incomplete recovery after deformation.

1.2.1.7. Fatigue lifetime of rubber materials

The rubber lifetime can be seen as the result of three successive phenomena (Legorjujago and Bathias, 2002; Mars and Fatemi, 2003; Aït Hocine et al., 2011):

1. Crack nucleation
2. Crack propagation, and
3. Total failure.

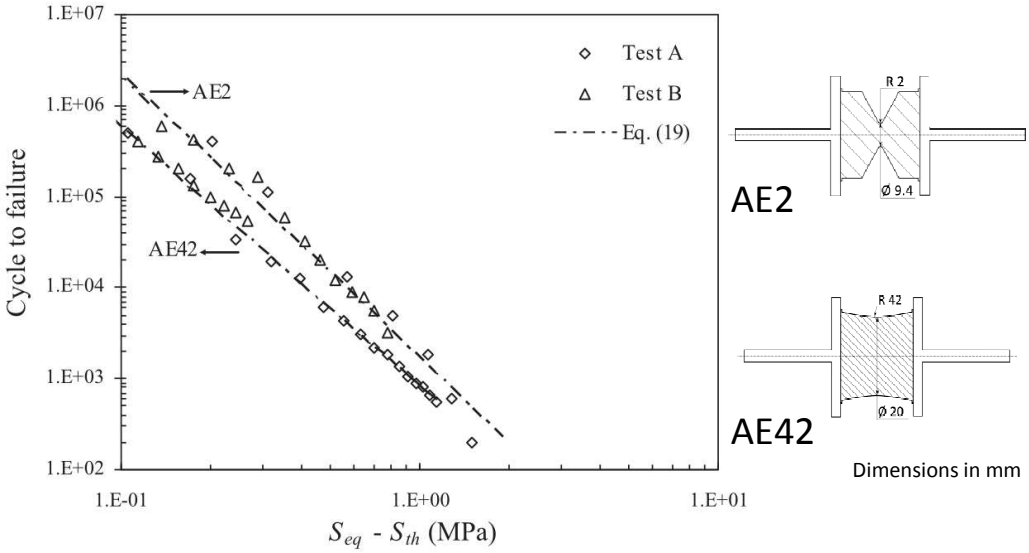

Figure 1.23. Fatigue lifetime of a SBR as a function of a multiaxial fatigue predictor S_{eq} and a threshold damage stress S_{th} (Ayoub et al., 2012).

In general, it is considered that the crack precursors are flaws that originally exist in the virgin material (Mars and Fatemi, 2006; Naït-Abdelaziz et al., 2012). Besides, the lifetime under fatigue depends on many parameters such as the microstructure, the fatigue-induced crystallinity, the specimen geometry, the loading conditions, etc.

In order to account for the lifetime of rubber components under multi-axial loading conditions, Ayoub et al. (2012) have proposed a model based on the continuum damage mechanics approach, see Figure 1.23. The proposed model was able to unify the multi-axial experimental data (tension-torsion) for two specimen geometries (AE2 and AE42), but it fails to unify the data regarding the specimen geometry. The divergence was attributed to the

material heat build-up, as during a fatigue test, the two specimens do not reach the same surface stabilized temperature[5].

1.2.2. Carbon-black effects on the rubber properties

1.2.2.1. Carbon-black effect on rubber elastic behavior

It is well known that adding small amounts of filler particles to a rubber can significantly improve both the stiffness and the strength of the rubber compound. Numerous authors (Smallwood, 1944; Guth, 1945; Vand, 1948; Mooney, 1951) have investigated the influence of filler particles on the stiffness of rubbers compounds. The filler volume has an increasing effect on the stress-strain behavior of NR vulcanizates (Figure 1.24). Independently of the filler concentration, all curves have a linear behavior from the origin up to strains of about 0.02. At higher strains all curves showed the characteristic sigmoid shape of rubber-type materials with an upward sweep of the curve at strains greater than 1.

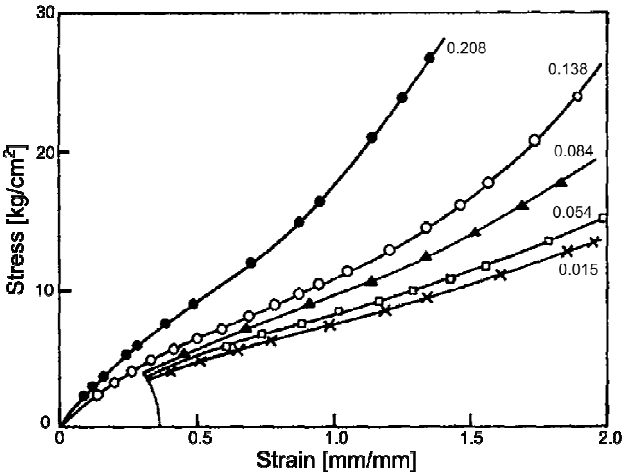

Figure 1.24. Stress-strain curves of NR containing different volumes of carbon-black (Mullins and Tobin, 1965).

The mechanism by which the stiffness increase occurs is still a subject of debate; it has been considered to result from two contributions:

- Continuum level: the stiffness of a rubber compound will be the weighted combination of the stiffnesses of the individual constituent materials, depending on the exact microstructure (Bueche, 1960).

[5] The divergence in both temperatures is related with the difference in the volume of material implied in the fatigue process.

- Molecular level: the filler acts both to effectively increase the crosslink density of the material – providing additional crosslinking sites at the particle-matrix interface – and to reduce the segmental mobility close to the filler particles (Kraus, 1978).

In addition to the volume fraction of filler particles, a number of state variable were supposed to influence the stiffness increase magnitude: the size, type and shape of the fillers (Mullins, 1950), the filler aggregate structure (Smallwood, 1944) and the rubber-filler interface area (Medalia and Kraus, 2013). In spite of the diverse number of contributions, Smallwood (1944) demonstrated that the main influence is found by changing the aggregate structure. The filler effect on the elastic behavior of filled rubbers has been extensively modeled (see Figure 1.25). One approach consists on taking into account the increase in viscosity of a viscous fluid – rubber matrix – caused by a suspension of colloidal particles – carbon-black. Using this concept Smallwood (1944) predicted the small-strain Young's modulus of particle-filled solids:

$$E = E_m \left(1 + 2.5 v_f\right) \tag{1.5}$$

where E_m is the Young's modulus of the rubber matrix and v_f is the filler volume fraction; however, this estimate is valid uniquely for very low filler concentrations. Attempting to incorporate interactions between neighboring particles – allowing predictions for higher volume fractions – Guth and Gold (1938) have added one more term to the polynomial series expansion of the amplification factor:

$$E = E_m \left(1 + 2.5 v_f + 14.1 v_f^2\right) \tag{1.6}$$

Using an experimental crowding factor k to incorporate particle-particle interactions, Mooney (1951) proposed a different method:

$$E = E_m \exp\left(\frac{2.5 v_f}{1 - k v_f}\right) \tag{1.7}$$

Guth (1945) have developed a model that accounts for rod-like shapes other than spherical-shape particles (as the aforementioned models). The shape is characterized by the ratio of the length to the width of the particles or the filler aggregate structures, g_f:

$$E = E_m \left(1 + 0.67 g_f v_f + 1.62 g_f^2 v_f^2\right) \tag{1.8}$$

This model attempts to account for the rapid increase with concentration in the viscosity of suspensions of rod-like particles, in contrast to the slower increase for spherical particles. Govindjee and Simo (1991) have developed another approach based on the concept of

amplified strain which, for the case of rigid particles in a neo-Hookean matrix, can be written as:

$$E = E_m \frac{1-\frac{v_f}{2}}{1-v_f} \tag{1.9}$$

In addition to these models specifically developed for filled rubbers, a number of general composite theory model have been developed (Hashin and Shtrikman, 1963; Budiansky, 1965; Ponte Castañeda, 1989; Bergstrom and Boyce, 1999).

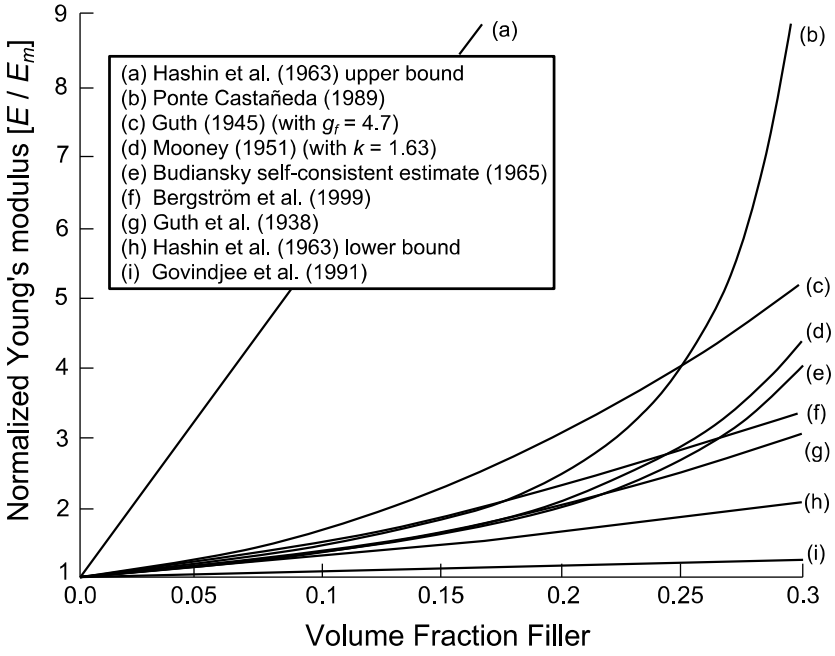

Figure 1.25. Theoretical predictions of the normalized Young's modulus, $E_{filler} = 100E_m$.

1.2.2.2. Carbon-black effect on dynamic[6] elastic modulus

Dynamic measurements demonstrate the significant difference between dynamic and static properties, e.g. the dynamic elastic modulus E' is greater than the static modulus E. This effect is considerably greater with black-filled than with gum compounds (Dillon et al., 1944). Under a shear dynamic test, pure rubber shows a linear behavior of the storage modulus G' in the domain of deformations below 100 %. The adding of fillers drives the compound to a non-linear behavior. Figure 1.26 shows the diminution of the storage modulus as a function of impose deformation amplitude. The values of G' remained constant up to about 0.1 to 0.5% double strain amplitude (DSA) and thereafter decreased tending to an apparent constant

[6] The term dynamic, as applied to rubber-type materials, refers to the response – after reaching a pseudo-equilibrium state – to periodic or transient forces which do not cause failure.

minimal value G'_{∞} – this value is superior to the unfilled rubber modulus. This phenomenon is known as the Payne effect (Payne, 1960).

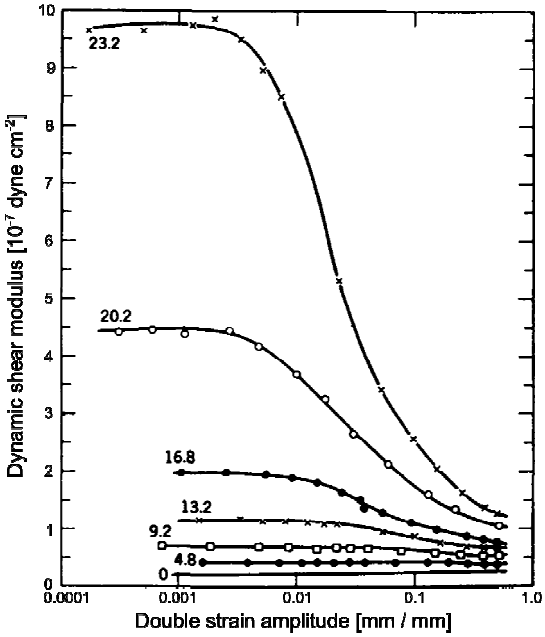

Figure 1.26. Storage modulus-strain amplitude relation for a rubber compound with different volumes of carbon-black (Payne, 1963a).

In Payne's experiments the value of G' at low amplitudes was constant, called G'_0, over a range of more than a decade (e.g., 0.05 to 0.5% DSA); however, Voet and Cook (1967) and Sircar and Lamond (1975a; 1975b) have shown, using an apparatus slightly modified from that of Payne, G' increasing from a low value at 0.01% DSA to a maximum at about 0.1% DSA. At high amplitudes the carbon network structure is broken down – regardless of the loading or interaggregate bond strength – and the storage modulus is governed by the individual carbon-black aggregates. Similarly, in a well-dispersed compound at low loadings, where the individual aggregates are well separated, the amplitude effect is very small and the storage modulus is governed uniquely by the individual aggregates. Under these conditions the effect of carbon-black is essentially equivalent to the hydrodynamic effect of isolated spheres on the modulus of rubber, corresponding to the effect of perturbation of flow behavior on the viscosity of liquids. The contribution of carbon-black to the storage modulus under these conditions depends on structure or bulkiness and is independent of surface area (Medalia, 1973; Ulmer et al., 1973; Kraus, 1978). At amplitudes between G'_0 and G'_{∞}, the storage modulus is the sum of G'_{∞} and the contribution $\Delta G'$ related with the augmentation made by still unbroken agglomerates of varying dimensions, e.g. a relatively small amount of

strain-work would be required to reduce the agglomerate size by a factor of 2 and more work is then required to reduce each of the residues by another factor of 2, and so on. The increase of G' is greatly affected by loading characteristics, i.e. at high loadings the low-amplitude modulus is dominated by the surface area of the carbon-black (Payne, 1963b) while at low loadings it is dominated by the carbon-black structure (Medalia, 1973; Ulmer et al., 1973). From a practical point of view, the dependence of G' on both structure and surface area can cause that the modulus-amplitude curve of a high structure-low area black intersects the one of a low structure-high area black.

1.2.2.3. Carbon-black effect on loss parameters and hysteresis

Along with the amplitude dependence of the storage modulus there is a significant amplitude dependence of the loss factor and the loss modulus which is more pronounced as the loading is increased (Figures 1.27 and 1.28). The loss factor at low amplitudes rises to a maximum at around 5 to 15% DSA in shear, and then decreases at still higher amplitudes; however, it generally remains higher than its value at very low amplitudes. The loss modulus passes through a maximum, as an amplitude function, which is reached at the amplitude at which the storage modulus changes most rapidly – the inflection point. As for the storage modulus, the amplitude dependence of the viscous parameters has been interpreted on the basis of the interaggregate interaction (Ulmer et al., 1998). It is assumed that hysteresis H results from breakdown and reformation of interaggregate bonds: at low amplitude there is little breakdown of bonds, therefore little hysteresis; at intermediate amplitudes considerable breakdown and reformation of bonds take place, thus hysteresis is high; and at high amplitudes both G' and $\tan\delta$ continue to decrease, thus their product, the loss modulus G'', can become quite low.

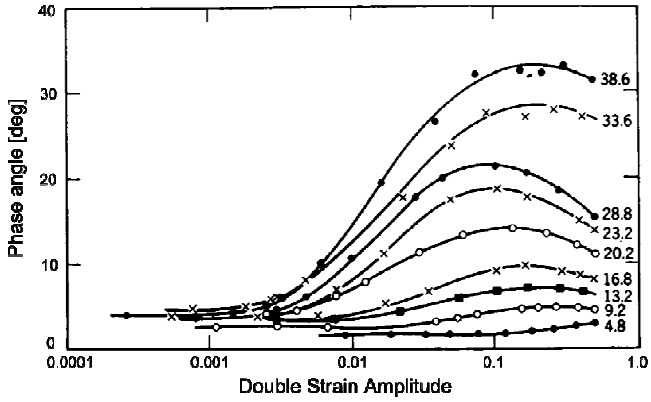

Figure 1.27. Phase angle-strain amplitude relation for a rubber compound with different volumes of carbon-black (Payne, 1963a).

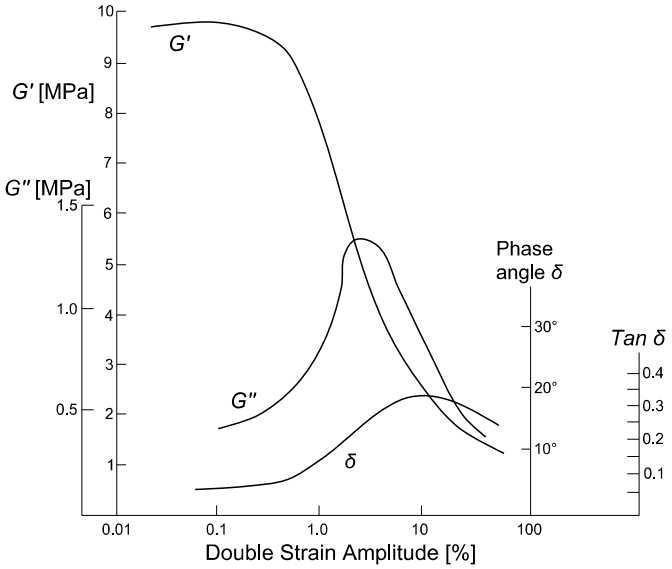

Figure 1.28. Dynamic parameters-strain amplitude relation for a rubber compound with 23.2 volume % of carbon-black (Figures 1.26 and 1.27).

Low values of G'' at high amplitudes have been interpreted on the basis that at high amplitude the structure destruction is complete and little energy needs to be expanded (Voet and Cook, 1967) – the decrease in loss factor at high amplitudes indicates that less reformation of interaggregate bonds takes place than at intermediate amplitudes. Note that in comparing different compounds, H is proportional to $\tan\delta$ when the compounds are cycled at the same energy input, H is proportional to G'' under equal strain conditions, while under equal stress conditions, H is approximately proportional to $\tan\delta/G'$ (Medalia, 2001).

1.2.2.4. Temperature effect in carbon-black rubber compounds

Dynamic properties of rubber compounds are important over a wide range of temperatures, especially in the so-called rubbery region of polymer behavior (Figure 1.6). In this region, the storage modulus of carbon-black filled rubbers increases with lower temperature – entanglements and other physical crosslinks become more effective. The loss factor increases with lower temperature in the rubber region and passes through a maximum in the region where G' is changing most rapidly (transition to glassy state), while G'' reaches a maximum at somewhat lower temperature.

Fletcher and Gent (1957) showed, using carbon-black filled NR flat samples, that the values of G' were relatively high at high temperatures and the increase in G' on going to low temperature was less steep than for the gum. Over the temperature range examined (-62 to 81.5°C), $\tan\delta$ passed through a maximum which was much lower and less sharp for the filled vulcanizates that for the gum. Similar results were reported by Payne (1958). Using

different carbon-blacks at 50 phr (parts per hundred of rubber) loading vulcanizates, Medalia (1973) evidenced the decreasing of the elastic modulus with an increasing temperature. Payne (1963b) experiments over carbon-black filled NR vulcanizates reported similar results (Figure 1.29). Concerning pure gum thermo-mechanical behavior, Medalia (1978) shown the increasing of the elastic modulus with an increasing temperature, as later reported by Treloar (2005). The temperature dependence of the dynamic parameters has been interpreted on the basis of the loading characteristics, e.g., at low temperatures the low-amplitude modulus is dominated by the surface area of the black, while at high temperature it is dominated by carbon-black structure.

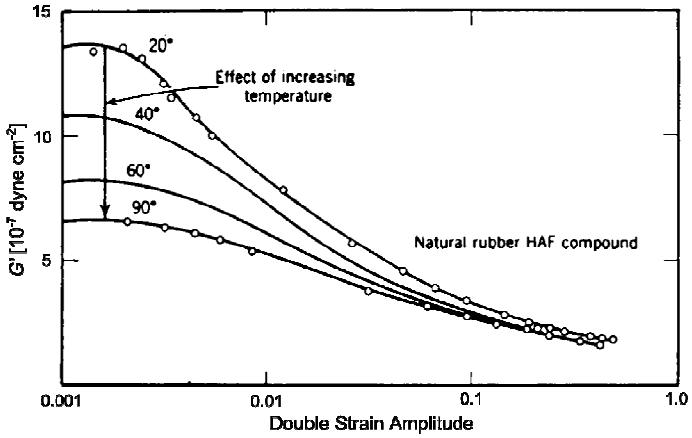

Figure 1.29. Effect of temperature on strain amplitude dependence of G' (Payne, 1963a).

1.2.2.5. Carbon-black rubber interactions effect

The carbon-black effect on the dynamic properties of rubbers differs quantitatively from one rubber to another and also depends upon various procedures which are known to alter interaction of the polymer with the carbon-black. The carbon-black dispersion affected by both the size and number of agglomerates and the distance of interaggregate separation is the most sensible interaction, e.g. reduction in hysteresis after increasing time of mixing or heat treatment, attributed to reduction in carbon-carbon frictional losses as the dispersion was improved (Dannenberg, 1952). Boonstra and Medalia (1963) found that large agglomerates are responsible for the poor ultimate properties of short-time mixes, interaggregate occlusion of a large amount of rubber, high Mooney viscosity and high vulcanizates modulus at low strain. As mixing proceeds the large agglomerates virtually disappear and the now existing small agglomerates are gradually dispersed. During the later stages of mixing there was a significant decrease in torsional hysteresis and heat buildup. These changes were related to the disappearance of the small agglomerates and the separation of the aggregates from each

other. Numerous authors (Payne, 1965; Medalia, 1973; Sommer and Meyer, 1974) have confirmed the positive effect of improved dispersion on dynamic properties of rubber compounds. It is well known that an undercured rubber is related with high hysteresis (Baranwal and Stephens, 2001). In pure rubber vulcanizates this has been generally attributed to the slow response of untrapped entanglements and dangling chain ends (Ferry, 1980); however, recent studies have related hysteresis to trapped entanglements (Cohen et al., 1977) and questioned the importance of dangling chain ends (Sullivan et al., 1978).

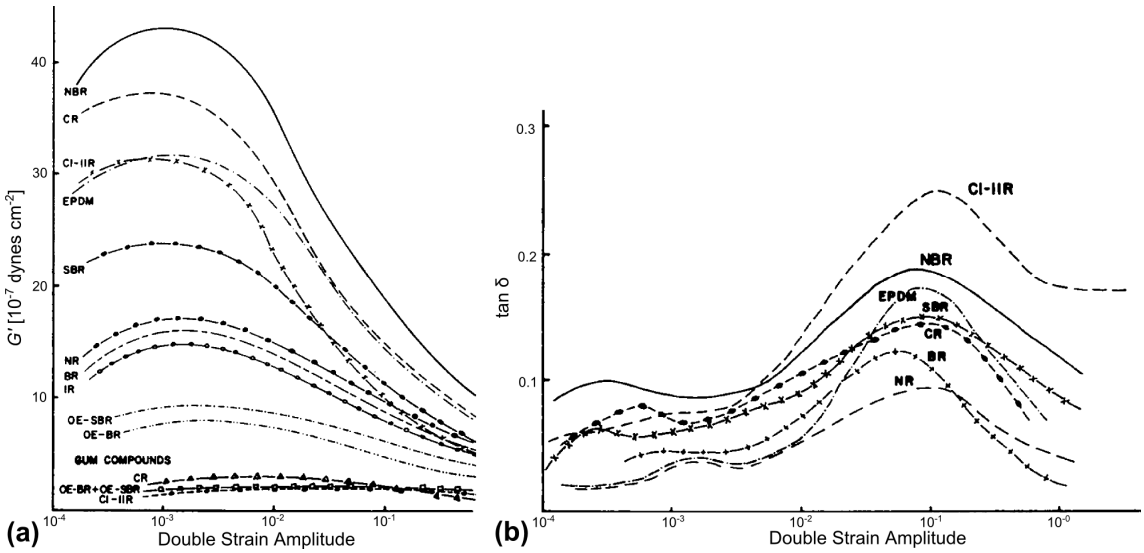

Figure 1.30. Effect of the elastomer type: (a) on the storage modulus G', and (b) on the loss factor $\tan\delta$ (Sircar and Lamond, 1975a).

Payne et al. (1972) shown that the loss factor of pure rubber vulcanizates decreased progressively with increasing cure, and this was reflected in the filled compounds. On the other hand, comparing NR compounds at three curative levels, Sommer and Meyer (1974) reported increasing values of G' and G'' with increasing cure time – increasing level of crosslinking. Similar results were found by Medalia (1978) – the author suggests that "the viscoelastic behavior of the rubber immobilized by the carbon-black could somehow be responsible for this effect". In an interesting study by Sircar and Lamond (1975a; 1975b) dynamic parameters of ten elastomers were evaluated (Figure 1.30); however, microscopic measurement of dispersion did not help to give a simple explanation of the order. There are wide differences in G', having the nitrile-butadiene rubber (NBR) the highest value. The maximum values of $\tan\delta$, for only seven of these compounds, were found at close to 10% DSA (in shear). The $\tan\delta$ values were in somewhat the same order of G'. Payne (1964)

reported the same rubber-type dependence; however, the values were not in the same order – different compounding and curing systems were used for each polymer.

1.3. Elements of continuum mechanics and thermodynamics

The continuum medium is an infinite set of particles (region or part of a solid, fluid or gas) that can be studied macroscopically without considering the possible existing discontinuities in the microscopic level – atomic or molecular level. In consequence, the mathematical description of this medium and of his properties can be developed by means of continuous functions.

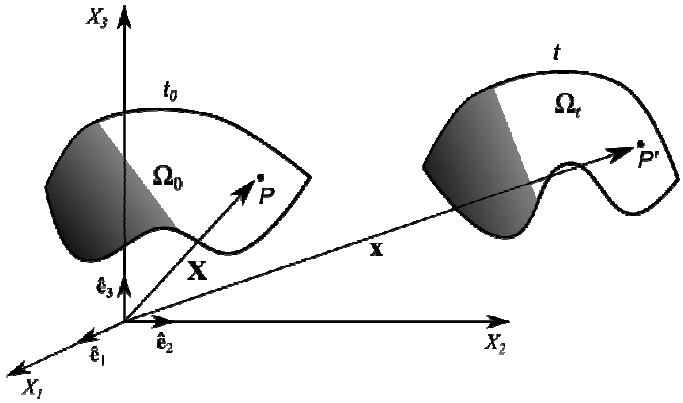

Figure 1.31. Configuration of the continuum medium.

The continuum medium configuration Ω_t is the geometric place of the positions that the material points – particles – of the continuum medium occupy in the space at a certain time *t*. The configuration at a given time $t = t_0$ of the time interval of analysis is named initial, material or reference configuration Ω_0 (Figure 1.31). In the reference configuration, the position vector **X** of a particle that occupies a point *P* in the space is given by:

$$\mathbf{X} = X_i \hat{\mathbf{e}}_i \tag{1.10}$$

where X_i are the material coordinates of the particle and $\hat{\mathbf{e}}_i$ is a unit vector of orthonormal basis. In the current configuration Ω_t, the particle, originally situated in the material point *P*, occupies the spatial point *P'* and his position vector x is given by:

$$\mathbf{x} = x_i \hat{\mathbf{e}}_i \tag{1.11}$$

where x_i are the spatial coordinates of the particle in the time instant *t*.

Finally, the mathematical description of the properties of the particles can be done by means of two alternative ways according to the configuration: the Lagrangian description (reference configuration) and the Eulerian description (current configuration)

1.3.1. Finite deformation and stress

1.3.1.1. Description of the deformation

A key quantity to describe finite deformation in the continuum mechanics framework is the deformation gradient tensor **F** defined as:

$$\mathbf{F} = \frac{\partial \mathbf{x}}{\partial \mathbf{X}} \tag{1.12}$$

The deformation gradient tensor contains the information relative to the movement, throughout time, of all the material particles in the differential neighborhood of a given one. The determinant of **F**, denoted *J* (for Jacobian), represents the local variation of volume and it is always positive because of the principle of non-interpenetration of the material: $J = \det \mathbf{F} > 0$. On the other hand, the displacement of a particle *P* at a given time is defined by the vector u which joins the position *P* of the particle in the reference configuration and its actual position *P'* (Figure 1.32). The displacement of all the particles of the medium defines the displacement field vector:

$$\mathbf{u}(\mathbf{x}, t) = \mathbf{x} - \mathbf{X}(x, t) \tag{1.13}$$

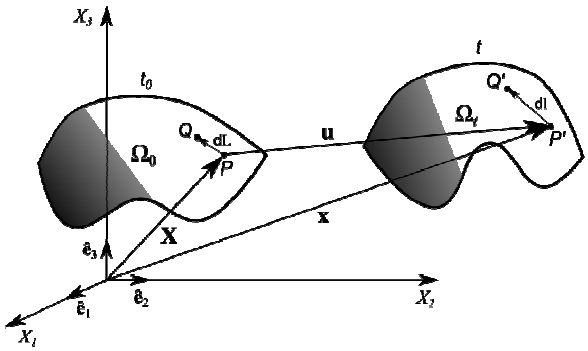

Figure 1.32. Displacement vector.

The relative movement in the neighborhood of a particle through the deformation process (characterized by **F**) can be understood as the composition (Figure 1.33) of a rotation and a deformation – polar decomposition theorem – as:

$$d\mathbf{x} = \mathbf{F}d\mathbf{X} = \mathbf{V}\mathbf{R}d\mathbf{X} = \mathbf{V}(\mathbf{R}d\mathbf{X}) \tag{1.14}$$

in which $\mathbf{F} = \mathbf{V}\mathbf{R}$ is the right polar decomposition, **V** is the right stretch tensor and **R** is the orthogonal rotation tensor, and

$$d\mathbf{x} = \mathbf{F}d\mathbf{X} = \mathbf{R}\mathbf{U}d\mathbf{X} = \mathbf{R}\left(\mathbf{U}d\mathbf{X}\right) \tag{1.15}$$

and $\mathbf{F} = \mathbf{R}\mathbf{U}$ is the left polar decomposition and **U** is the left stretch tensor.

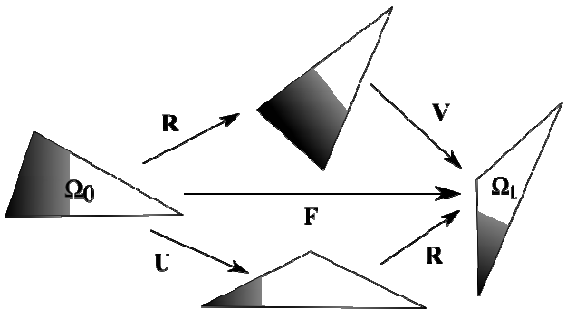

Figure 1.33. Polar decomposition.

The time-dependent deformation is described by means of the velocity gradient tensor:

$$\mathbf{L} = \dot{\mathbf{F}}\mathbf{F}^{-1} = \mathbf{D} + \mathbf{W} \tag{1.16}$$

where **D** is the stretching rate (symmetric tensor) and **W** is the spin rate (non-symmetric tensor). The stretching rate tensor gives the rate of stretching of line elements while the spin rate tensor indicates the rate of rotation or vorticity of the motion.

Let us consider now a particle situated in *P* in the reference configuration, and a second one situated in his differential neighboring *Q* separated from the previous one by the segment d**X** (length $dL = \sqrt{d\mathbf{X}d\mathbf{X}}$). The segment d**x** (length $dl = \sqrt{d\mathbf{x}d\mathbf{x}}$) is its counterpart in the current configuration (Figure 1.31), from which some quantities can be defined:

$$\begin{aligned} \left(dl\right)^2 &= d\mathbf{x}d\mathbf{x} = \left[\mathbf{F}d\mathbf{X}\right]\left[\mathbf{F}d\mathbf{X}\right] = d\mathbf{X}\mathbf{F}^T\mathbf{F}d\mathbf{X} = d\mathbf{X}\mathbf{C}d\mathbf{X} \\ \left(dL\right)^2 &= d\mathbf{X}d\mathbf{X} = \left[\mathbf{F}^{-1}d\mathbf{x}\right]\left[\mathbf{F}^{-1}d\mathbf{x}\right] = d\mathbf{x}\mathbf{F}^{-1}\mathbf{F}^{-T}d\mathbf{x} = d\mathbf{x}\mathbf{B}^{-1}d\mathbf{x} \end{aligned} \tag{1.17}$$

where $\mathbf{C} = \mathbf{F}^T\mathbf{F}$ and $\mathbf{B} = \mathbf{F}\mathbf{F}^T$ are the right and left Cauchy-Green strain tensors, respectively. Subtracting both expressions of Eq. (1.14) between them we have:

$$\begin{aligned} \left(dl\right)^2 - \left(dL\right)^2 &= d\mathbf{X}\mathbf{C}d\mathbf{X} - d\mathbf{X}d\mathbf{X} = 2d\mathbf{X}\mathbf{E}d\mathbf{X} \\ \left(dl\right)^2 - \left(dL\right)^2 &= d\mathbf{x}d\mathbf{x} - d\mathbf{x}\mathbf{B}^{-1}d\mathbf{x} = 2d\mathbf{x}\mathbf{e}d\mathbf{x} \end{aligned} \tag{1.18}$$

where

$$\mathbf{E} = \frac{1}{2}\left(\mathbf{C} - \mathbf{I}\right) \tag{1.19}$$

is the Green-Lagrange finite strain tensor,

$$\mathbf{e} = \frac{1}{2}\left(\mathbf{I} - \mathbf{B}^{-1}\right) \tag{1.20}$$

is the Euler-Almasi finite strain tensor and **I** is the unit vector.

Finally, since each previously defined strain tensor is symmetrical and positive then six independent components must be defined to characterize the current configuration of a body; however, another way consists on defining the corresponding principal strain invariants I_1, I_2 and I_3. Invariants of **C** and **B** are often used in the expressions for strain energy density functions. The principal strain invariants, considering **B**, are defined as:

$$I_1 = \mathrm{tr}\mathbf{B} = B_1 + B_2 + B_3 = \lambda_1^2 + \lambda_2^2 + \lambda_3^2 \tag{1.21}$$

$$I_2 = \frac{1}{2}\left[\left(\mathrm{tr}\mathbf{B}\right)^2 - \mathrm{tr}\mathbf{B}^2\right] = B_1B_2 + B_2B_3 + B_1B_3 = \lambda_1^2\lambda_2^2 + \lambda_2^2\lambda_3^2 + \lambda_1^2\lambda_3^2 \tag{1.22}$$

$$I_3 = \det\mathbf{B} = B_1B_2B_3 = \lambda_1^2\lambda_2^2\lambda_3^2 = J^2 \tag{1.23}$$

where λ_i are stretch ratios of the unit fibers that are initially oriented along the directions of the orthonormal axis in the coordinate system.

1.3.1.2. Description of the stress

The stress at a given point is defined as the resultant of the internal forces through a surface element, relative to a certain configuration (Figure 1.34). As for the deformations, it is possible to use a eulerian or lagrangian description, or even a mixed formulation.

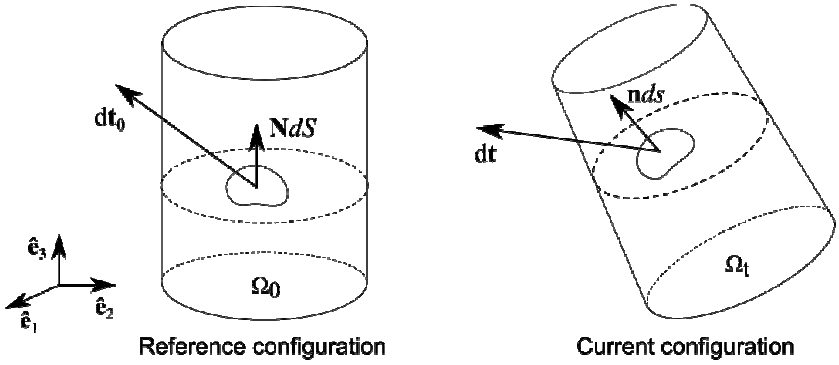

Figure 1.34. Stress vectors in the reference and current configuration.

In the eulerian description, the inner forces d**t** in the current configuration applied by a solid region over another one through a deformed surface element **n***ds* are considered. This definition drives us to the Cauchy stress tensor expression:

$$d\mathbf{t} = \mathbf{T}\mathbf{n}ds \tag{1.24}$$

where **T** is the Cauchy stress tensor. However, it can be useful to describe the stress field in the reference configuration, e.g., the application of the boundary conditions. The transport of the deformed surface element **n**ds to the reference configuration returns:

$$d\mathbf{t} = \boldsymbol{\pi}\mathbf{N}dS \tag{1.25}$$

where $\boldsymbol{\pi} = J\mathbf{T}\mathbf{F}^{-T}$ is the first Piola-Kirchhoff stress tensor (non-symmetric). This stress describes the real cohesion forces applied through a deformed surface element per unit of non-deformed surface. The description of the stress field under a total lagrangian formulation needs the transport of the real force d**t** to the reference configuration:

$$d\mathbf{t}_0 = \mathbf{S}\mathbf{N}dS \tag{1.26}$$

where $\mathbf{S} = J\mathbf{F}^{-1}\mathbf{T}\mathbf{F}^{-T} = \mathbf{F}^{-1}\boldsymbol{\pi}$ is the second Piola-Kirchhoff stress tensor (symmetric).

1.3.1.3. Equilibrium equations

The continuum mechanics is based upon a series of general postulates or principles that are supposed valid, independently of the type of material and of the range of displacements or of deformations. Among them we can find the so-called Conservation-Balance postulates: Conservation of momentum, Conservation of mass and Energy Balance postulates.

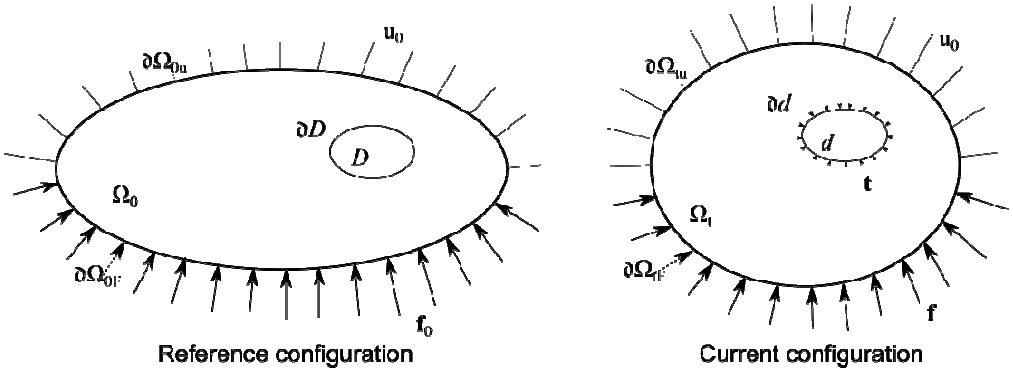

Figure 1.35. Boundary conditions in the reference and current configuration.

The application of the momentum conservation postulate – in a closed system the total momentum is constant – in the current configuration (Figure 1.35) of a solid sub-domain *d* gives:

$$\int_{\partial\delta} \mathbf{t}ds + \int_{\delta} \rho\mathbf{b}dv = 0 \tag{1.27}$$

where **t** is the cohesion forces tensor acting over the surface $\partial\delta$, ρ is the mass density per unit volume in the current configuration and **b** is the force density tensor acting over the volume δ.

From the divergence theorem[7], Eq. (1.24) and considering the boundary conditions, it is possible to establish the equilibrium equations for the current configuration:

[7] The outward flux of a vector field through a closed surface is equal to the volume integral of the divergence over the region inside the surface.

$$\begin{aligned} &\nabla_x \mathbf{T} + \rho \mathbf{b} = 0 && \text{over } \Omega_t \\ &\mathbf{T}\mathbf{n} = \mathbf{f} && \text{over } \Omega_{tF} \\ &\mathbf{u} = \mathbf{u_0} && \text{over } \Omega_{tu} \end{aligned} \tag{1.28}$$

On the other hand, if Eq. (1.27) is modified to take into account the sub-domain *D* then it is possible to establish the equilibrium equations for the reference configuration:

$$\begin{aligned} &\nabla_X \boldsymbol{\pi} + \rho_0 \mathbf{b} = 0 && \text{over } \Omega_0 \\ &\boldsymbol{\pi}\mathbf{N} = \mathbf{f}_0 && \text{over } \Omega_{0F} \\ &\mathbf{u} = \mathbf{u_0} && \text{over } \Omega_{0u} \end{aligned} \tag{1.29}$$

where

$$\rho_0 = J\rho \tag{1.30}$$

is the mass density per unit volume in the reference configuration, as the mass conservation postulate – the mass of a closed system must remain constant over time – must be considered.

1.3.2. Elements of thermodynamics

1.3.2.1. Fundamental principles of the thermodynamics

If we consider a solid in a certain configuration Ω_t (respectively Ω_0) then there is a state function E, internal energy of the system, such that its variation per unit time is equal to the sum of the inner mechanical power P and the amount of heat supplied to the system Q:

$$\dot{E} = P + Q \tag{1.31}$$

It is possible to express each term of Eq. (1.31) in the current or reference configuration, e.g. the internal energy of the system is given by:

$$E = \int_{\Omega_t} \rho e dv = \int_{\Omega_0} \rho_0 e dV \tag{1.32}$$

where *e* is the specific internal energy. The inner mechanical power is deducted from the principle of virtual powers – the virtual power of an acceleration quantity is equal to the sum of the virtual power of the internal and external forces – and it is equal to the product of a kinematic variable with its corresponding stress:

$$-P = \int_{\Omega_t} \mathbf{T} : \mathbf{D} dv = \int_{\Omega_0} \mathbf{S} : \dot{\mathbf{E}} dV = \int_{\Omega_0} \boldsymbol{\pi} : \dot{\mathbf{F}} dV \tag{1.33}$$

Finally, the amount of heat supplied to the system can be decomposed into an energy source per unit mass *r* and a heat flux loss $\mathbf{q}$ (respectively $\mathbf{q}_0$) in the surface border $\partial\Omega_t$ (respectively $\partial\Omega_0$):

$$Q = \int_{\Omega_t} r dv - \int_{\partial\Omega_t} \mathbf{q}\mathbf{n} ds = \int_{\Omega_0} r dV - \int_{\partial\Omega_0} \mathbf{q}_0 \mathbf{N} dS \tag{1.34}$$

where $\mathbf{q}\mathbf{n}ds = \mathbf{q}_0\mathbf{N}dS$ is the heat flux lagrangian expression. Then, the energy conservation expression – first law of thermodynamics – can be defined, in a Eulerian formulation, as:

$$\rho \dot{e} = \mathbf{T} : \mathbf{D} + r - \nabla_x \mathbf{q} \tag{1.35}$$

in Lagrangian formulation as:

$$\rho_0 \dot{e} = \mathbf{S} : \dot{\mathbf{E}} + r - \nabla_X \mathbf{q}_0 \tag{1.36}$$

and, in a mixed formulation as:

$$\rho_0 \dot{e} = \boldsymbol{\pi} : \dot{\mathbf{F}} + r - \nabla_X \mathbf{q}_0 \tag{1.37}$$

It is necessary to add a restriction to the energy balance equation introduced by the second principle of the thermodynamics. The second law establishes the following postulates:

There is a state function called absolute temperature $\theta(\mathbf{x}, t)$ which is strictly positive, i.e. $\theta > 0$.

There is a state function called entropy *S* with the following characteristics:

It is an extensive variable, i.e. there is a specific entropy η such that:

$$S = \int_{\Omega_t} \rho \eta dv = \int_{\Omega_0} \rho_0 \eta dV \tag{1.38}$$

The following inequality is fulfilled:

$$\frac{dS}{dt} \geq Q_{ext} \tag{1.39}$$

where $Q_{ext} = Q/\theta$ is the heat rate supplied to the system divided by the absolute temperature.

If $\frac{dS}{dt} = Q_{ext}$ the process is called reversible – it is possible to return from the final thermodynamic state *B* to the initial thermodynamic state *A* by the same way – and if $\frac{dS}{dt} > Q_{ext}$ the process is called irreversible – it is not possible to return from the final thermodynamic state *B* to the initial thermodynamic state *A* by the same way, even if it is possible to return by a different way. Introducing the corresponding expression of Eqs. (1.34) and (1.38) into Eq. (1.39), the abovementioned inequality can be formulated, in the current configuration, as:

$$\rho \dot{\eta} - \frac{r}{\theta} + \mathbf{q} \nabla_x \frac{1}{\theta} \geq 0 \tag{1.40}$$

or in the reference configuration:

$$\rho_0 \dot{\eta} - \frac{r}{\theta} + \mathbf{q}_0 \nabla_X \frac{1}{\theta} \geq 0 \tag{1.41}$$

Furthermore, substituting *r* from Eq. (1.35) into Eq. (1.40) or *r* from Eqs. (1.36) and (1.37) into Eq. (1.41), three new expressions for the second law of thermodynamics are defined:

$$-\rho\left(\dot{e} - \theta\dot{\eta}\right) + \mathbf{T} : \mathbf{D} - \frac{1}{\theta}\mathbf{q}\nabla_x \theta \geq 0 \tag{1.42}$$

in the Eulerian formulation,

$$-\rho_0\left(\dot{e} - \theta\dot{\eta}\right) + \mathbf{S} : \dot{\mathbf{E}} - \frac{1}{\theta}\mathbf{q}_0\nabla_X \theta \geq 0 \tag{1.43}$$

in the Lagrangian formulation, and:

$$-\rho_0\left(\dot{e} - \theta\dot{\eta}\right) + \boldsymbol{\pi} : \dot{\mathbf{F}} - \frac{1}{\theta}\mathbf{q}_0\nabla_X \theta \geq 0 \tag{1.44}$$

in the mixed formulation.

Introducing a new variable, the specific free energy:

$$\psi = e - \theta\eta \tag{1.45}$$

it is possible to define the Clausius-Duhem inequality – common way to express the second law of thermodynamics – in the mixed formulation, as:

$$-\rho_0\left(\dot{\psi} + \eta\dot{\theta}\right) + \boldsymbol{\pi} : \dot{\mathbf{F}} - \frac{1}{\theta}\mathbf{q}_0\nabla_X \theta \geq 0 \tag{1.46}$$

1.3.2.2. Thermodynamics of local state

The local state method postulates that the thermodynamic state of a point in a continuum medium at a given time is completely defined by the values of a certain number of variables that depend uniquely on the given material point. The time derivatives of these variables are not required to define the thermodynamic state, i.e. any time evolution could be considered as a succession of equilibrium states. It is by the choice of the nature and the number of state variables that a physical phenomenon can be described. Two types of state variables can be distinguished:

- The observable variables are related with directly measurable properties of the continuum. The mechanics and thermodynamics formalism impose the deformation-temperature variables $(\mathbf{F}, \theta)$.
- The internal variables are introduced to describe the dissipative phenomena, e.g. the viscosity or the plasticity, or to describe the inner state of the material, e.g. dislocation density, microcracks configuration or cavities, without the possibility to measure the aforementioned properties in a direct way. There is not an objective method to choose the

nature of the internal variables. Depending on the complexity of the phenomenon, the internal variables could be scalar $(V_1, V_2, \ldots V_k)$ or tensorial $(\mathbf{V}_1, \mathbf{V}_2, \ldots \mathbf{V}_k)$.

Once that the state variables are defined, the existence of a thermodynamic potential – specific free energy potential – from which the state laws are derived can now be postulated. This function allows checking the conditions of thermodynamic stability imposed by the inequalities that can be deduced from the second thermodynamic principle. Then, the specific free energy potential, for *k* tensorial internal variables, can be defined as:

$$\psi = \psi\left(\mathbf{F}, \theta, \mathbf{V}_k\right) \tag{1.47}$$

and the specific free energy potential rate as:

$$\dot{\psi} = \frac{\partial \psi}{\partial \mathbf{F}} : \dot{\mathbf{F}} + \frac{\partial \psi}{\partial \theta}\dot{\theta} + \frac{\partial \psi}{\partial \mathbf{V}_k} : \dot{\mathbf{V}}_k \tag{1.48}$$

From Eq. (1.48) the thermodynamic force associated with the internal variable $\mathbf{V}_k$ is defined as follows:

$$\mathbf{A}_k = \rho \frac{\partial \psi}{\partial \mathbf{V}_k} \tag{1.49}$$

The thermodynamic potential allows writing the state relations between the observable variables and its associate variables; however, for the internal variables, it only allows the definition of its associate variables. The description of the evolution of the internal variables is carried out by means of a complementary formalism: the dissipation potential. The dissipation potential (or dissipation pseudo-potential) is expressed as a continuous function in which the state variables are introduced as parameters:

$$\varphi = \varphi\left(\dot{\mathbf{F}}, \dot{\mathbf{V}}_k, \mathbf{q}/\theta\right) \tag{1.50}$$

Then, considering that the thermodynamic forces are the components of the $\nabla\varphi$ vector, the complementary law can be expressed as:

$$\boldsymbol{\pi} = \frac{\partial \varphi}{\partial \dot{\mathbf{F}}} \quad \mathbf{A}_k = -\frac{\partial \varphi}{\partial \dot{\mathbf{V}}_k} \quad \nabla\theta = -\frac{\partial \varphi}{\partial\left(\mathbf{q}/\theta\right)} \tag{1.51}$$

Finally, the Clausius-Duhem inequality can be reduced to a dissipation expression as:

$$\gamma = \Phi_m + \Phi_T \geq 0 \tag{1.52}$$

where γ is the dissipation,

$$\Phi_m = \boldsymbol{\pi} : \dot{\mathbf{F}} - \mathbf{A}_k : \mathbf{V}_k \tag{1.53}$$

is the intrinsic dissipation (or mechanical dissipation), and

$$\Phi_T = -\frac{1}{\theta}\mathbf{q}_0 \nabla_X \theta \tag{1.54}$$

is the thermal dissipation by conduction.

1.3.2.3. Heat transfer

The heat transfer by conduction is a way of inner heat propagation, independent of the movement, associated with the thermal gradient inside the continuum medium which is characterized by Fourier's Law:

$$\mathbf{q}_0 = -\mathbf{K}_X \nabla \theta_X \tag{1.55}$$

where

$$\mathbf{K}_X = \mathbf{F}^{-1}\mathbf{K}\mathbf{F}^{-T} \tag{1.56}$$

is the conductivity tensor in the initial configuration, and $\mathbf{K}$ is the Euler conductivity tensor. In the isotropic case, this one reduces to $\mathbf{K} = \kappa\mathbf{I}$, where κ is the material conductivity factor. Inserting the specific internal energy rate expressed in mixed formulation, after a series of straightforward derivations using Eqs. (1.45) and (1.47), as:

$$\dot{e} = \frac{1}{\rho_0}\boldsymbol{\pi} : \dot{\mathbf{F}} + \frac{1}{\rho_0}\mathbf{A}_k : \mathbf{V}_k - \theta\left(\frac{\partial \boldsymbol{\pi}}{\partial \theta} : \dot{\mathbf{F}} + \frac{\partial \mathbf{A}_k}{\partial \theta} : \dot{\mathbf{V}}_k\right) - \theta\frac{\partial^2 \psi}{\partial \theta^2}\dot{\theta} \tag{1.57}$$

into the standard formulation of the first thermodynamics law, Eq. (1.37), leads to the heat equation:

$$\rho_0 C\dot{\theta} = -\mathbf{A}_k : \dot{\mathbf{V}}_k + \rho_0\theta\left[\frac{\partial \boldsymbol{\pi}}{\partial \theta} : \dot{\mathbf{F}} + \frac{\partial \mathbf{A}_k}{\partial \theta} : \dot{\mathbf{V}}_k\right] + r + \mathbf{K}_X \nabla \theta_X \tag{1.58}$$

where C is the specific heat per unit mass:

$$C\left(\mathbf{F}, \theta, \mathbf{V}_k\right) = -\theta\frac{\partial^2 \psi}{\partial \theta^2} \tag{1.59}$$

1.3.3. Hyperelastic models

The hyperelasticity is the capability of a material to experience large elastic strains due to small forces – nonlinear behavior – without losing its original properties. An elastic material is hyperelastic if there is a scalar function – denoted by W and called strain energy function – such that:

$$\mathbf{T} = 2\frac{\partial W}{\partial \mathbf{B}} \tag{1.60}$$

in the current configuration,

$$\mathbf{S} = 2\frac{\partial W}{\partial \mathbf{C}} \tag{1.61}$$

in the reference configuration, and

$$\boldsymbol{\pi} = \frac{\partial W}{\partial \mathbf{F}} \tag{1.62}$$

in the mixed configuration.

1.3.3.1. Statistical mechanics treatments

The statistical mechanics approach begins by assuming a structure of randomly-oriented long molecular chains. In the Gaussian treatment, when deformation is applied, the chain structure stretches and its configurational entropy decreases. If one considers the deformation of an assembly of *n* chains by a principal stretch state $(\lambda_1, \lambda_2, \lambda_3)$ and the deformation is such that the chain length *r* does not approach its fully extended length *Nl*, *N* being the number of connected rigid-links in a chain and *l* the length of each link, then the elastic strain energy function can be derived from the change in configurational entropy:

$$W = \frac{1}{2}nk\theta\left(\lambda_1^2 + \lambda_2^2 + \lambda_3^2 - 3\right) \tag{1.63}$$

where *k* is Boltzmann's constant. At large deformations where *r* begins to approach *Nl*, the non-Gaussian nature of the chain stretch must be taken into account. Kuhn and Grun (1942) accounted for the finite extensibility of chain stretch using Langevin chain statistics which account for the effect of the relative chain length on the configuration available to the chain. The resulting non-Gaussian force-extension relationship for a chain is given by:

$$f = \frac{k\theta}{l}\mathcal{L}^{-1}\left(\frac{r}{Nl}\right) = \frac{k\theta}{l}\mathcal{L}^{-1}\left(\frac{\lambda}{\sqrt{N}}\right) \tag{1.64}$$

where $\mathcal{L}^{-1}$ is the inverse of the Langevin function given by:

$$\mathcal{L}^{-1}(\beta) = \coth(\beta) - 1/\beta \tag{1.65}$$

Assuming a representative network structure (Figure 1.36), to link the chain stretch of individual chains to the applied deformation, it is possible to incorporate the non-Gaussian relationship into a constitutive framework. The models differ in how the chains deformation is related to the deformation of the unit cell.

In the 3-chain model (James and Guth, 1943), the chains deform with the cell and the stretch on each chain will then correspond to a principal stretch value. The resulting strain energy function is given by:

$$W = \frac{nk\theta}{3}\sqrt{N}\sum_{i=1}^{3}\left(\lambda_i\beta_i + \sqrt{N}\ln\left(\frac{\beta_i}{\sinh\beta_i}\right)\right) \tag{1.66}$$

where $\beta_i = \mathcal{L}^{-1}\left(\lambda_i/\sqrt{N}\right)$. In the 4-chain model (Flory and Rehner, 1943), the tetrahedron deforms according to the imposed deformation and the chains deform accordingly with the interior junction point displacing in a non-affine manner such that the equilibrium is satisfaid.

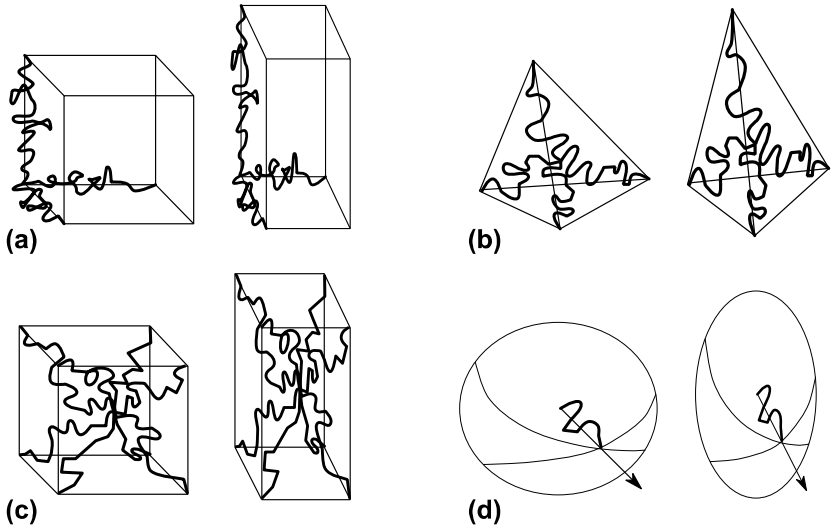

Figure 1.36. Non-Gaussian networks: (a) 3-chain model, (b) 4-chain model, (c) 8-chain model, and (d) full network model. Each model is depicted in its undeformed and deformed state.

This model provides a more cooperative network deformation than the 3-chain model as the chains stretch and rotate with deformation; however, the individual chain stretch-applied stretch relationship is obtained by iterative methods. In the 8-chain model (Arruda and Boyce, 1993), the chains undergo tensile stretching for all imposed deformations and also rotate towards the principal axis of stretch mimicking, in an average sense, what would be expected in the cooperative deformation of a real network. Due to the symmetry of the chain structure the interior junction point remains centrally located throughout the deformation and the resulting strain energy function is given by:

$$W = nk\theta\sqrt{N}\left[\beta_{ch}\lambda_{ch} + \sqrt{N}\ln\left(\frac{\beta_{ch}}{\sinh\beta_{ch}}\right)\right] \tag{1.67}$$

where $\beta_{ch} = \mathcal{L}^{-1}\left(\lambda_{ch}/\sqrt{N}\right)$ and

$$\lambda_{ch} = \left[\frac{1}{3}\left(\lambda_1^2 + \lambda_2^2 + \lambda_3^2\right)\right]^{1/2} \tag{1.68}$$

is the stretch on each chain in the structure. In the full-network model (Wu and van der Giessen, 1993), the chains are assumed to be randomly distributed in space and to deform in an affine manner. The strain energy function is found by integrating over the stress-stretch response of all chains.

1.3.3.2. Invariant-based and stretch-based continuum mechanics treatments

The continuum mechanics treatment of rubber elasticity is based upon dependence between the strain energy density and stretch via one or more of the three invariants of the stretch tensor, Eqs. (1.21), (1.22) and (1.23). The elastomer is often approximated to be incompressible, thus $I_3 = 1$ and does not contribute to the strain energy. Considering out this dependence relation, Rivlin (1948) proposed one general representation of W given by

$$W = \sum_{i,j=0}^{\infty} C_{ij} \left(I_1 - 3\right)^i \left(I_2 - 3\right)^j \tag{1.69}$$

where C_{ij} are material parameters. By keeping only the first term of the Rivlin expression, it returns,

$$W = C_{10} \left(I_1 - 3\right) \tag{1.70}$$

which is often called the Neo-Hookean model – note that Eq. (1.70) is the continuum mechanics equivalent to the Gaussian model, Eq. (1.63), where $C_{10} = nk\theta/2$. The often referred to as Mooney-Rivlin model is obtained by keeping the second term of the Rivlin expression:

$$W = C_{10} \left(I_1 - 3\right) + C_{01} \left(I_2 - 3\right) \tag{1.71}$$

This equation was first derived by Mooney (1940) by determining an expression for the strain energy that would provide a constant modulus in shear, i.e. a modulus that did not depend on the shear strain. The apparent success in capturing deviations from the Gaussian/Neo-Hookean model in uniaxial tension is, perhaps, the responsible of the popularity of the Mooney-Rivlin model. Several researchers have used higher order terms in I_1 and, in some cases, I_2, to account for the departure from neo-Hookean/Gaussian behavior at large stretches – as for the Gaussian model, at large deformation, the real stress-stretch behavior departs significantly from that predicted by the neo-Hookean model. Using higher order I_1 terms, Yeoh (1993) proposed a strain energy function,

$$W = C_{10} \left(I_1 - 3\right) + C_{20} \left(I_1 - 3\right)^2 + C_{30} \left(I_1 - 3\right)^3 \tag{1.72}$$

that has been shown to work well in capturing different deformation state from moderate to large deformations. An alternate high order I_1 model has been proposed by Gent (1996):

$$W = -\frac{E}{6}\ln\left(1-\frac{J_1}{J_\infty}\right) \tag{1.73}$$

where E is the small-strain tensile modulus, $J_1 = (I_1 - 3)$ and J_∞ denotes a maximum value for J_1 accounting for the limiting extensibility. The natural logarithm term can be expanded to yield to the following formulation:

$$W = \frac{E}{6}\left[\sum_{n=0}^{\infty}\frac{1}{(n+1)J_\infty^n}(I_1-3)^{n+1}\right] \tag{1.74}$$

which is a form of the Rivlin expression, with all coefficients, C_{i0}, now related to the two material parameters E and J_∞. Considering that the aforementioned 8-chain model (Arruda and Boyce, 1993), is I_1-based since it is a function of chain stretch λ_{ch}, which is equivalent to $\sqrt{I_1/3}$, then a invariant-based form can be formulated:

$$W = \sum_{i=1}^{n} C_i\left(I_1^i - 3_i\right) \tag{1.75}$$

where the C_i are all determined a priori as functions of the material properties n and N. The success of the higher order I_1 continuum mechanics models is due to their mimicking the physics of successful non-Gaussian statistics models thus providing the connection between the higher order continuum models and the statistical mechanics models – similar to the neo-Hooken model being equivalent to the Gaussian model. One caution regarding the use of phenomenological higher order I_1 continuum mechanics models is that the constants chosen must result in physically realistic and stable constitutive responses in all deformation states – one judicious choice would be to choose all coefficients to be positive-valued.

Strain energy density functions based on the principal stretches, as opposed to the stretch invariants, have also been proposed by several investigators. Valanis and Landel (1967) proposed a strain energy function related with the principal stretches:

$$W = \sum_{i=1}^{3} w(\lambda_i) \tag{1.76}$$

The functions $w(\lambda_i)$ are experimentally obtained. Following a similar approach, Ogden (1972) proposed a strain energy function in terms of principal stretches:

$$W = \sum_n \frac{\mu_n}{\alpha_n}\left(\lambda_1^{\alpha_n} + \lambda_2^{\alpha_n} + \lambda_3^{\alpha_n} - 3\right) \tag{1.77}$$

where μ_n and α_n are data-fit constants.

Statistical mechanics models which account for the non-Gaussian nature of the molecular chain stretch together with and effective or representative network structure provide the most predictive model of the larger strain behavior under different states of deformations. Furthermore, the physically based foundation of the non-Gaussian statistical mechanics network models provides a constitutive law that requires only two material properties – the network chain density *n*, which is determined from the small strain behavior, and the limiting chain extensibility $\sqrt{N}$, which is determined from the behavior at large strain. Besides, the continuum mechanics invariant-based constitutive models are equivalent phenomenological representations of the microstructurally based statistical mechanics models – the first invariant I_1 is correlated with the average chain stretch in the network model. Strain energy expressions which contain a polynomial series in I_1 including higher order I_1 terms capture the non-Gaussian nature of the network stretch behavior while, on the other hand, strain energy expressions which contain the second invariant of stretch I_2 should be used with caution – results are stiffer in certain types of deformation.

1.4. References

Aït Hocine, N., Hamdi, A., Naït-Abdelaziz, M., Heuillet, P., Zaïri, F., 2011. Experimental and finite element investigation of void nucleation in rubber-like materials. International Journal of Solids and Structures 48, 1248-1254.

Anthony, R., Caston, R., Guth, E., 1943. Equations of state for natural and synthetic rubber-like materials. I Unaccelerated natural soft rubber. Rubber Chemistry and Technology 16, 297-309.

Arruda, E., Boyce, M., 1993. A three-dimensional constitutive model for the large stretch behavior of rubber elastic materials. Journal of the Mechanics and Physics of Solids 41, 389-412.

Ayoub, G., Zaïri, F., Naït-Abdelaziz, M., J.M., Gloaguen, J.M., 2011a. Modeling the low-cycle fatigue behavior of visco-hyperelastic elastomeric materials using a new network alteration theory: Application to styrene-butadiene rubber. Journal of the Mechanics and Physics of Solids 59, 473-495.

Ayoub, G., Zaïri, F., Naït-Abdelaziz, M.,J.M., Gloaguen, J.M., Charrier, P., 2012. Fatigue life prediction of rubber-like materials under multiaxial loading using a continuum damage mechanics approach: Effects of two-blocks loading and R ratio. Mechanics of Materials 52, 87-102.

Baranwal, K., Stephens, H., 2001. Basic Elastomer Technology. Rubber Division.

Bergström, J., Boyce, M., 1999. Mechanical behavior of particle filled elastomers. Rubber Chemistry and Technology 72, 633-656.

Blanchard, A., Parkinson, D., 1952. Breakage of carbon-rubber networks by applied stress. Industrial Engineering Chemistry 44, 799-812.

Boonstra, B., Medalia, A., 1963. Effect of carbon black dispersion on the mechanical properties of rubber vulcanizates. Rubber Chemistry and Technology 36, 115-142.

Bouasse, H., Carrière, Z., 1903. Sur les courbes de traction du caoutchouc vulcanisé. Annales de la faculté des sciences de Toulouse5, 257-283.

Budiansky, B., 1965. On the elastic moduli of some heterogeneous materials. Journal of the Mechanics and Physics of Solids13, 223-227.

Bueche, F., 1960. Molecular basis for the Mullins effect. Journal of Applied Polymer Science4, 107-114.

Cohen, R., Severson, S., Yu, C., Mark, J., 1977. Viscoelastic properties of polydimethylsiloxane networks prepared by cross-linking the chains in solution. Macromolecules 10, 663-667.

Dannenberg, E., 1952. Carbon black dispersion and reinforcement. Industrial, Engineering Chemistry 44, 813-818.

Dannenberg, E., Brennan, J., 1965. Strain-energy as a criterion for stress softening in carbon-black-filled vulcanizates. Rubber Chemistry and Technology 39, 597-608.

Diani, J., Fayolle, B., Gilormini, P., 2009. A review on the Mullins effect. European Polymer Journal 45, 601-612.

Dillon, J., Prettyman, J., Hall, G., 1944. Hysteretic and elastic properties of rubberlike materials under dynamic shear stresses. Journal of Applied Physics 15, 309-323.

Ehrbar, J., Boissonas, C., 1955. The termal effect in the elongation and relaxation of rubber. Rubber Chemistry and Technology 28, 675-683.

Ferry, J., 1980. Viscoelastic Properties of Polymers.Wiley.

Fletcher, W., Gent, A., 1957. Dynamic shear properties of some rubber-like materials. British Journal of Applied Physics 8, 194-201.

Flory, P., 1953. Principles of polymer chemistry. United States of America: Cornell University Press.

Flory, P., Rehner, J., 1943. Statistical mechanics of cross-linked polymer networks. Journal of Chemistry and Physics 11, 512-520.

Fukahori, Y., 2005. New progress in the theory and model of carbon black reinforcement of elastomers. Journal of Applied Polymer Science95, 60-67.

Gent, A., 1996. A new constitutive relation for rubber. Rubber Chemistry and Technology 69, 59-61.

Gough, J., 1805. A description of a property of Caoutchouc, or Indian rubber; with some reflections on the cause of the elasticity of this substance. In a letter to Dr. Holmf.. Memoirs of the Literary and Philosophical Society of Manchester 1, 288.

Govindjee, S., Simo, J., 1991. A micro-mechanically based continuum damage model for carbon black-filled rubbers incorporating Mullins' effect. Journal of the Mechanics and Physics of Solids 39, 87-112.

Guth, E., 1945. Theory of filler reinforcement. Journal of Applied Physics16, 20-25.

Guth, E., Gold, O., 1938. On the hydrodynamical theory of the viscosity of suspensions. Physical review53, 322.

Hamed, G., Hatfield, S., 1989. On the role of bound rubber in carbon-black reinforcement. Rubber Chemistry and Technology62, 143-156.

Hanson, D., Hawley, M., Houlton, R., Chitanvis, K., Rae, P., Orler, E.B., Wrobleski, D.A., 2005. Stress softening experiments in silica-filled polydimethysiloxane provide insight into a mechanism for the Mullins effect. Polymer 46, 10989-10995.

Hashin, Z., Shtrikman, S., 1963. A variational approach to the theory of the elastic behaviour of multiphase materials. Journal of the Mechanics and Physics of Solids11, 127-140.

Haudin, J., 1995. Introduction à la mécanique des polymères. France: Institut National Polytechnique de Lorraine.

Holt, W., 1931. Behaviour of Rubber under Repeated Stresses. Industrial and Engineering Chemistry23, 1471–1475.

Houwink, R., 1956. Slipping of molecules during the deformation of reinforced rubber. Rubber Chemistry and Technology 29, 888-893.

James, H., Guth, E., 1943. Theory of the elastic properties of rubber. Journal of Chemistry and Physics 10, 455-481.

Jones, R., 2008. Compendium of polymer terminology and nomenclature. United Kingdom: Royal Society of Chemistry.

Joule, J., 1859. On some thermo-dynamic properties of solids. Philosophical Transactions of the Royal Society of London 149, 91-131.

Kausch, H., Heymans, N., Plummer, C., Decroly, P., 2001. Matériaux polymères : propiétés mécaniques et physiques. France: Presses polytechniques et universitaires romandes.

Klüppel, M., Schramm, M., 2000. A generalized tube model of rubber elasticity and stress softening of filler reinforced elastomer systems. Macromolecular Theory and Simulations 9, 742-754.

Kraus, G., 1978. Reinforcement of elastomers by carbon black. Rubber Chemistry and Technology 51, 297-321.

Kraus, G., Childers, C., Rollman, K., 1966. Stress softening in carbon black reinforced vulcanizates. Strain rate and temperature effects. Journal of Applied Polymer Science 10, 229-240.

Kuhn, W., Grun, F., 1942. Beziehungen zwischen elastischen Konstanten und Dehnungsdoppelbrechung hochelastischer Stoffe. Kolloid-Zeitschrift 101, 248-271.

Leblanc, J., 2002. Rubber-filler interactions and rheological properties in filled compounds. Progress in Polymer Science 27, 627-687.

Legorjujago, K., Bathias, C., 2002. Fatigue initiation and propagation in natural and synthetic rubbers. International Journal of Fatigue 24, 85-92.

Mark, J., 1982. Rubber Elasticity. Rubber Chemistry and Technology 55, 1123-1136.

Mars, W.,V., Fatemi, A., 2003. Fatigue crack nucleation and growth in filled natural rubber. Fatigue and Fracture of Engineering Materials and Structures 26, 779-789.

Mars, W.,V., Fatemi, A., 2006. Multiaxial stress effects on fatigue behavior of filled natural rubber. International Journal of Fatigue 28, 521-529.

Medalia, A., 1970. Morphology of aggregates: VI. Effective volume of aggregates of carbon black from electron microscopy; Application to vehicle absorption and to die swell of filled rubber. Journal of Colloid and Interface Science 32, 115-131.

Medalia, A., 1973. Selecting carbon blacks for Dynamic properties. Rubber World 168, 49.

Medalia, A., 1978. Effect of carbon black on dynamic properties of rubber vulcanizates. Rubber Chemistry and Technology 51, 437-523.

Medalia, A., 1991. Heat generation in elastomer compounds: causes and effects. Rubber Chemistry and Technology 64, 481-492.

Medalia, A., 2001. Elastomers, Reinforcement of. Dans: Encyclopedia of Materials: Science and Technology. Pergamon, 2475-2480.

Medalia, A., Kraus, G., 2013. Science and Technology of Rubber. 4e ed. Academic Press Inc.

Meyer, K., Ferri, C., 1935. Sur l'élasticité du caoutchouc. Helvetica Chimica Acta 18, 570-589.

Mooney, M., 1940. A theory of large elastic deformation. Journal of Applied Physics 11, 582-591.

Mooney, M., 1951. The viscosity of a concentrated suspension of spherical particles. Journal of Colloid Science 6, 162-170.

Mullins, L., 1948. Effect of stretching on the properties of rubber. Rubber Chemistry and Technology 21, 281-300.

Mullins, L., 1950. Thixotropic behavior of carbon black in rubber. Rubber Chemistry and Technology 23, 733-743.

Mullins, L., 1969. Softening of rubber by deformation. Rubber Chemistry and Technology 42, 339-362.

Mullins, L., Tobin, N., 1957. Theoretical model for the elastic behavior of filler-reinforced vulcanized rubbers. Rubber Chemistry and Technology 30, 551-571.

Mullins, L., Tobin, N., 1965. Stress softening in rubber vulcanizates. Part I. Use of a strain amplification factor to describe the elastic behavior of filler-reinforced vulcanized rubber. Journal of Applied Polymer Science 9, 2993-3009.

Naït-Abdelaziz, M., Zaïri, F., Qu, Z., Hamdi, A., Aït Hocine, N., 2012. J integral as a fracture criterion of rubber-like materials using the intrinsic defect concept. Mechanics of Materials 53, 80-90.

Ogden, R., 1972. Large deformation isotropic elasticity - On the correlation of theory and experiment for incompressible rubberlike solids. Proceedings of the Royal Society of London A 326, 565-584.

Payne, A., 1958. The Rheology of Elastomers. Pergamon Press, 86.

Payne, A., 1960. A note on the existence of a yield point in the dynamic modulus of loaded vulcanizates. Journal of Applied Polymer Science 3, 127.

Payne, A., 1963a. Dynamic properties of heat-treated Butyl vulcanisates. Journal of Applied Polymer Science 7, 873-885.

Payne, A., 1963b. The Dynamic properties of carbon black-loaded natural rubber vulcanizates. Part I. Rubber Chemistry and Technology 36, 432-443.

Payne, A., 1964. Strainwork dependence of filler-loaded vulcanizates. Journal of Applied Polymer Science8, 2661–2686.

Payne, A., 1965. Effect of dispersion on the dynamic properties of filler-loaded rubbers. Journal of Applied Polymer Science9, 2273-2284.

Payne, A., Whittaker, R., Smith, J., 1972. Effect of vulcanization on the low-strain dynamic properties of filled rubbers. Journal of Applied Polymer Science16, 1191-1212.

Ponte Castañeda, P., 1989. The overall constitutive behaviour of nonlinearly elastic composites. Proceedings of the Royal Society A 422, 147-171.

Privalko, V., Lipatov, Y., 1974. On the folding of the macromolecules in bulk polymers. The structure of interchain "entaglements" in amorphous polymers. Polymer Science U.S.S.R. 16, 1809-1816.

Qiu, L., Bae, Y., 2006. Polymer architecture and drug delivery. Pharmaceutical Research23, 1-30.

Rivlin, R., 1948. Large Elastic Deformations of isotropic materials. IV. Further developments of the general theory. Philosophical Transactions of the Royal Society of London A 241, 379-397.

Schwartz, A., 1907. "Flexibles", with notes on the testing of rubber. Journal of the Institution of Electrical Engineers 39, 31-100.

Shedd, J., Ingersol, R., 1904. The elastic modulus and elastic limit of rubber and their relation to change of temperature. Physical Review 19, 107-116.

Simo, J., 1987. On a fully three-dimensional finite-strain viscoelastic damage model: formulation and computational aspects. Computer Methods in Applied Mechanics and Engineering 60, 153-173.

Sircar, A., Lamond, T., 1975a. Strain-dependent dynamic properties of carbon-black reinforced vulcanizates. I. Individual elastomers. Rubber Chemistry and Technology 48, 79-88.

Sircar, A., Lamond, T., 1975b. Strain-dependent dynamic properties of carbon-black reinforced vulcanizates. II. Elastomer blends. Rubber Chemistry and Technology 48, 89-96.

Smallwood, H., 1944. Limiting law of the reinforcement of rubber. Journal of Applied Physics 15, 758-766.

Sommer, J., Meyer, D., 1974. Factors controlling the dynamic properties of elastomeric products. Journal of Elastomers and Plastics 6, 49-68.

Sullivan, J., Mark, J., Hampton, P., Cohen, R., 1978. Model networks of end-linked polydimethylsiloxane chains. II. Viscoelastic losses. The Journal of Chemical Physics 68, 2010-2012.

Treloar, L., 2005. The Physics of Rubber Elasticity. 3rd ed. Great Britain: Clarendon Press - Oxford.

Ulmer, J., Chirico, V., Scott, C., 1973. The Effect of Carbon Black Type on the Dynamic Properties of Natural Rubber. Rubber Chemistry and Technology 46, 897-926.

Ulmer, J., Hergenrother, W., Lawson, D., 1998. Hysteresis Contributions in Carbon Black-Filled Rubbers Containing Conventional and Tin End-Modified Polymers. Rubber Chemistry and Technology 71, 637-667.

Valanis, K., Landel, R., 1967. The Strain Energy Function of a Hyperelastic Material in Terms of the Extension Ratios. Journal of Applied Physics 38, 2997-3002.

Vand, V., 1948. Viscosity of solutions and suspensions. 1. theory. Journal of Physical and Colloid Chemistry, 277-299.

Voet, A., Cook, F., 1967. Mild Stress Softening and Dynamic Properties of Rubber Vulcanizates. Rubber Chemistry and Technology 40, 1364-1372.

Wu, P., van der Giessen, E., 1993. On improved network models for rubber elasticity and their application to orientation hardening in glassy polymers. Journal of the Mechanics and Physics of Solids 41, 427-456.

Ximenez, F., 1715. Empiezan las historias del origen de los indios de esta provincia de Guatemala. Guatemala.

Yeh, G., 1980. Current concepts of morphology of amorphous polymers - II. Degree of local order an overall chain conformation. Polymer Science U.S.S.R. 21, 2686-2703.

Yeoh, O., 1993. Some Forms of the Strain Energy Function for Rubber. Rubber Chemistry and Technology 66, 754-771.

CHAPTER 2. FATIGUE RESPONSE OF FILLED RUBBERS

2.1. PRE-STRETCH DEPENDENCY OF THE CYCLIC DISSIPATION IN CARBON-FILLED SBR[8]

This Part of the *Chapter 2* explores the inelastic fatigue process in filled rubbers using the internal state variable theory. The theory is used to qualitatively and quantitatively analyze the complex history-dependent cyclic response of filled rubbers, but also to reveal the underlying physical mechanisms. Experimental observations are reported on a styrene-butadiene rubber (SBR) containing different amounts of carbon-black and cyclically loaded under a wide range of pre-stretch levels. The effects of pre-stretch and filler content on the carbon-filled SBR history-dependent cyclic response, characterized by stress-softening and hysteresis along with dissipative heating, are examined. The intrinsic dissipation, regarded as a consequence of two types of rearrangements in the rubber-filler material system, i.e. viscoelastic and damage mechanisms, is quantified and used to propose a plausible explanation of the underlying inelastic fatigue mechanisms consistent with our experimental observations.

Keywords: Filled rubbers; cyclic dissipation; pre-stretch.

[8] This Part of this Chapter is based on the following paper: Qiang Guo, Fahmi Zaïri, H. Baraket, M. Chaabane, Xinglin Guo, 2017. Pre-stretch dependency of the cyclic dissipation in carbon-filled SBR. *European Polymer Journal* 96, 145-158.

2.1.1. Partial introduction

Rubbers have a wide range of engineering applications, such as tires, dampers and hoses, and may be cyclically loaded under typical operating conditions (Ward, 1985). While many fatigue life predictors were proposed in the literature for rubbers (Mars, 2002; Wang et al., 2002; Saintier et al., 2006; Verron and Andriyana, 2008; Brunac et al., 2009; Ayoub et al., 2011a, 2012, 2014a; Zarrin-Ghalami et al., 2013; Grandcoin et al., 2014), the study of the coupling between the different underlying inelastic fatigue phenomena is less common. The physical essence of the fatigue process is attributed to the damage accumulation within the materials, interpreted as the irreversible changes of the microstructure towards degradation and failure. In rubbers, the viscoelastic effects may play an important role in the fatigue process and both irreversible and reversible network rearrangements are involved (Derham and Thomas, 1977; McKenna and Zapas, 1981). Rubbers used in engineering applications tend to contain a large concentration of fillers dispersed in the rubber matrix in order to improve the mechanical properties and reduce the cost. While unfilled rubbers exhibit quasi purely elastic response, filled rubbers exhibit a complex history-dependent cyclic response characterized by stress-softening, residual strain and hysteresis (Mullins, 1948; Houwink, 1956; Bueche, 1960; Kraus et al., 1966; Kraus, 1984; Lion, 1996; Marckmann et al., 2002; Laiarinandrasana et al., 2003; Hanson et al., 2005; Chagnon et al., 2006; Ayoub et al., 2011b, 2014b; Diaz et al., 2014) along with dissipative heating (Gough, 1805; Medalia, 1991; Meinecke, 1991; Samaca Martinez et al., 2013; Ovalle-Rodas et al., 2015a, 2016). The fatigue analysis of filled rubbers necessitates to consider the evolution of this set of inelastic phenomena with the cyclic loading history since the fatigue process is inevitably related to cyclic loading histories. Moreover, these inelastic effects usually appearing together should not be examined separately of each other but in the sense of a coupling. Establishing this coupling is an open issue to be addressed.

In cyclically loaded filled rubbers a heat quantity may be generated and lead, depending on the heat removal rate, to a temperature increment. The heat energy dissipated during a cycle originates from the conversion of a large part of the mechanical energy dissipated because of a stress difference between unloading and reloading paths. The latter, referred to as hysteresis, is due to the presence of a viscous stress component in the rubber-filler medium which deviates from the purely elastic stress. Since the hysteretic response and the purely elastic response are temperature-dependent, the heat build-up generated in the viscoelastic medium

may evidently influence in turn the viscoelastic response. In light of the significance of the thermo-mechanical coupling to rubber mechanical response, it is surprising to find only a few thermo-mechanical constitutive models presented in the literature (Ovalle-Rodas et al., 2013, 2014, 2015a, 2016; Meo et al., 2002; Reese, 2003; Behnke et al., 2016; Johlitz et al., 2016; Li et al., 2016).

Nevertheless, from the basic viewpoint of the continuum thermodynamics, all the irreversible microstructure motions occurring inside the rubber-filler material system during the fatigue loading process can induce energy dissipation. The underlying physical mechanisms include the fatigue damage mechanisms with unrecoverable network rearrangement towards degradation and failure, but also other physical mechanisms related to the hysteretic response due to recoverable network rearrangement. Since it is infeasible by means of the existing experimental methods to identify and directly measure these network rearrangements which may take place at any location in the rubber-filler material system and at any time of the fatigue process, some macroscopic quantities associated with microstructure evolution may be employed as indicators of the viscoelastic and damage effects, respectively. In this contribution, the internal state variable (ISV) theory, serving as a profound basis for the development of thermo-mechanical constitutive models (Ovalle-Rodas et al., 2013, 2014, 2015a, 2016; Meo et al., 2002; Reese, 2003; Behnke et al., 2016; Johlitz et al., 2016; Li et al., 2016), is adopted to investigate the inelastic fatigue process in filled rubbers. The basic idea behind the ISV theory is that the thermodynamics state of the material is defined by expanding the dimensions of the state space of deformation and temperature, referred to as external state variables due to their measurability and controllability, by the addition of state variables, ISVs, describing the microstructure changes and associated with the dissipative effects (Coleman and Noll, 1963; Rice, 1971; Horstemeyer and Bammann, 2010). A similar approach was adopted very recently by Loukil et al. (2018). The ISV theory provides a feasible way to qualitatively and quantitatively analyze the complex history-dependent cyclic response of filled rubbers, but also to reveal the underlying inelastic fatigue mechanisms. The application is performed on a styrene-butadiene rubber (SBR) containing different amounts of carbon-black and cyclically loaded under a wide range of pre-stretch levels.

This Part is organized as follows. Section 2.1.2 introduces the thermodynamic framework including the dissipation concept and the ISV theory. Section 2.1.3 presents the materials and the experimental methods. Section 2.1.4 presents and discusses the experimental results,

especially related to the dissipative effects and guiding a plausible explanation of the underlying physical mechanisms. Concluding remarks are finally given in Section 2.1.5.

2.1.2. Theory

2.1.2.1. Thermodynamic framework

According to the basic viewpoint of continuum thermodynamics, the fatigue process can be explored as an irreversible thermodynamic process, which is accompanied with the internal microstructure evolution, and has to satisfy the first and second laws of thermodynamics[9].

The first law of thermodynamics requires the following energy balance equation to be satisfied[10]:

$$\rho \dot{e} = \mathbf{S} : \dot{\mathbf{E}} - \nabla \cdot \boldsymbol{q} \tag{2.1.1}$$

where ρ is the mass density, e is the specific internal energy, $\mathbf{S}$ is the second Piola-Kirchhoff stress tensor, $\mathbf{E}$ is the Green-Lagrange strain tensor and $\nabla \cdot \boldsymbol{q}$ is the divergence of the Piola-Kirchhoff heat flux $\boldsymbol{q}$.

The second law requires that the Clausius-Duhem inequality is satisfied:

$$\eta = \rho \dot{s} - \nabla \cdot \left(-\boldsymbol{q}/T \right) \geq 0 \tag{2.1.2}$$

where s is the specific entropy, T is the absolute temperature and η represents the entropy generation rate being equal to the difference between the change rate of the entropy $\rho \dot{s}$ and the divergence of the entropy flow $\nabla \cdot \left(-\boldsymbol{q}/T \right)$. Thus, to assure that the process is thermodynamically admissible, the entropy generation rate η should be non-negative at every instant, and it may be in turn additively split into two parts:

$$\eta = \underbrace{\rho \dot{s} + \frac{\nabla \cdot \boldsymbol{q}}{T}}_{\eta_1} + \underbrace{\boldsymbol{q} \cdot \nabla \left(\frac{1}{T} \right)}_{\eta_2} \geq 0 \tag{2.1.3}$$

in which the first part η_1 is due to the irreversible energy conversion, such as from the mechanical energy to the thermal energy, and the second part η_2 is due to the heat flowing in non-uniform temperature fields.

[9] In all that follows, scalars are denoted by normal italicized letters; vectors are denoted by italicized boldfaced letters; tensors are denoted by normal boldfaced letters; and the dot on the letters denotes the time derivative.
[10] The volumetric heat supply is neglected in the first and second laws of thermodynamics.

Combining Eqs. (2.1.1) and (2.1.3), we obtain the following hybrid inequality for the total energy dissipation d which may be correspondingly split into two parts:

$$d = \underbrace{\mathbf{S} : \dot{\mathbf{E}} - \rho\dot{e} + \rho T\dot{s}}_{d_1} + \underbrace{\nabla T \cdot \left(-\boldsymbol{q}/T\right)}_{d_2} \geq 0 \tag{2.1.4}$$

in which the first part d_1 represents the intrinsic dissipation induced by the irreversible energy conversion and the second part d_2 represents the thermal dissipation induced by the irreversible energy flow.

A stronger constraint can be then imposed by assuming that the two parts d_1 and d_2 satisfy the dissipation inequality separately. Therefore, we can write the hybrid inequality (2.1.4) in the following form:

$$d_1 = \mathbf{S} : \dot{\mathbf{E}} - \rho\dot{e} + \rho T\dot{s} \geq 0 \text{ and } d_2 = \nabla T \cdot \left(-\boldsymbol{q}/T\right) \geq 0 \tag{2.1.5}$$

which requires that the dissipations d_1 and d_2 are non-negative at any particle of a deformable body and at all times during the fatigue loading history.

The existence of a free energy function ψ, a special form of the Helmholtz free energy potential, is postulated via the Legendre transformation:

$$\psi = e - Ts \tag{2.1.6}$$

Subsequently, the intrinsic dissipation d_1 in the inequality (2.1.5) can be re-written as:

$$d_1 = \mathbf{S} : \dot{\mathbf{E}} - \rho\dot{\psi} - \rho s\dot{T} \geq 0 \tag{2.1.7}$$

2.1.2.2. Recoverable and unrecoverable network rearrangements

The history-dependent effects in filled rubbers involves two types of network rearrangements, i.e. the recoverable rearrangement inducing viscoelasticity and the unrecoverable rearrangement inducing damage. The precise types of network rearrangements remain imprecisely understood as multiple plausible explanations have been proposed to explain the origin of the different history-dependent effects. The most popular, namely the Mullins effect (Mullins, 1948), is trivially attributed to chain scission mechanism (Marckmann et al., 2002; Chagnon et al., 2006; Ayoub et al., 2011b, 2014b) within the rubber matrix. The scission of short chains is believed to be activated at stretch values greater than a maximum obtained in the previous deformation history. During the first extension due to the Mullins effect, short chains reaching the limit of their extensibility breakdown along with some weak molecular interactions between chains. The degradation in stress resulting from the fatigue loading history has the same origin than that resulting from the first extension due

to the Mullins effect, but with a lower intensity as it is extended over time. Short chains being stuck between entangled chains progressively breakdown resulting in the progressive stress-softening. At each cycle, some entanglements between chains split open and some short chains being stuck between them breakdown, until the degradation is totally consumed leading to the stabilization of the stress (Ayoub et al., 2011b). Although this set of plausible fatigue damage mechanisms (i.e. disentanglement of chains, fatigue of weak bonds and chain scission but also break of chemical cross-links) may explain the progressive stress degradation in pure rubbers, it does not consider the interaction with the fillers. Especially considering the fact that inelastic effects are much more present in filled rubbers than in pure rubbers. Over the time, various competing views were proposed to explain the origin of the Mullins effect by involving the filler: breakage of short chains between two filler aggregates (Bueche, 1960), chain "slipping" over the filler surface (Houwink, 1956), rupture of filler aggregates (Kraus et al., 1966) and chain disentanglement between two filler aggregates (Hanson et al., 2005). In carbon-filled rubbers, the size of the carbon-black filler is generally very small (less than 100 nm) but aggregates whose size can reach a few microns can form during the production process and influence their strength (Ovalle-Rodas et al., 2015b) or fatigue (Ovalle-Rodas et al., 2015a, 2016). Experimental evidence via electrical resistivity measurements (Kraus et al., 1966; Pramanik et al., 1992; Diaz et al., 2014) showed that the increase in the filler concentration in carbon-filled rubbers leads to the development of a filler network across the rubber matrix and a higher number of inter-aggregates links. The higher electrical resistivity observed in pre-stretched carbon-filled rubbers in comparison to virgin ones may be explained by the rupture of inter-aggregates links during the cyclic loading, beginning with the weakest links and progressing into the strongest ones. As the carbon-filled rubber is in a deformed state, the filler aggregates form new links in new positions, which are again broken and then reformed in other positions. In conclusion, all these network rearrangements may contribute to the hysteretic process, which is associated with energy dissipation at the macroscopic scale. Further, a large part of the dissipated mechanical energy due to the hysteretic effect is converted into dissipative heating which manifests itself in the form of a change in temperature.

The dissipation of energy, and especially the intrinsic dissipation, are closely associated with these irreversible thermodynamic processes involving recoverable and unrecoverable rearrangements in the rubber-filler material system. The ISV theory is used to accurately describe the thermodynamic response of filled rubbers under fatigue loading. The free energy

function ψ is regarded as a thermodynamics function depending on a number of independent state variables:

$$\psi = \psi\left(T, \mathbf{E}, \boldsymbol{\alpha}, \boldsymbol{\beta}\right) \tag{2.1.8}$$

It includes not only two external state variables, the absolute temperature T and the Green-Lagrange strain tensor $\mathbf{E}$, but also ISVs represented by the two vectors $\boldsymbol{\alpha}$ and $\boldsymbol{\beta}$. Although introduced in the free energy function as macroscopic quantities, the two ISVs are actually related to the irreversible movement of the internal microstructures and describe the deviations from thermodynamic equilibrium. More specifically, $\boldsymbol{\alpha}$ is related to the recoverable network rearrangement inducing viscoelasticity, such as the move of free chains included in the relaxed network[11], the viscous friction between fillers and matrix / fillers, and the breakdown and rebound of inter-aggregates links, while $\boldsymbol{\beta}$ is related to the unrecoverable network rearrangement inducing damage, such as the chain scission and the permanent filler aggregate rupture. Nevertheless, it should be noted that the recoverable and unrecoverable network rearrangements are two relative concepts dependent on the loading condition, especially on the load time-scale. By inserting the time derivative of the free energy function $\dot{\psi}$ by means of the chain rule of differentiation:

$$\dot{\psi} = \frac{\partial \psi}{\partial T}\dot{T} + \frac{\partial \psi}{\partial \mathbf{E}} : \dot{\mathbf{E}} + \frac{\partial \psi}{\partial \boldsymbol{\alpha}} \cdot \dot{\boldsymbol{\alpha}} + \frac{\partial \psi}{\partial \boldsymbol{\beta}} \cdot \dot{\boldsymbol{\beta}} \tag{2.1.9}$$

into the inequality (2.1.7), the intrinsic dissipation d_1 can be re-written as:

$$d_1 = \left(\mathbf{S} - \rho \frac{\partial \psi}{\partial \mathbf{E}}\right) : \dot{\mathbf{E}} - \rho\left(s + \frac{\partial \psi}{\partial T}\right)\dot{T} - \rho \frac{\partial \psi}{\partial \boldsymbol{\alpha}} \cdot \dot{\boldsymbol{\alpha}} - \rho \frac{\partial \psi}{\partial \boldsymbol{\beta}} \cdot \dot{\boldsymbol{\beta}} \geq 0 \tag{2.1.10}$$

Applying the Coleman-Noll procedure (Coleman and Noll, 1963) to the inequality (2.1.10), we can obtain the constitutive relationships:

$$\mathbf{S} = \rho \frac{\partial \psi}{\partial \mathbf{E}}, \; s = -\frac{\partial \psi}{\partial T} \tag{2.1.11}$$

and a residual inequality indicating that the intrinsic dissipation d_1 can originate from two types of network rearrangements, i.e. viscoelastic mechanisms and damage mechanisms:

$$d_1 = \boldsymbol{A} \cdot \dot{\boldsymbol{\alpha}} + \boldsymbol{B} \cdot \dot{\boldsymbol{\beta}} \geq 0, \; \boldsymbol{A} = -\rho \frac{\partial \psi}{\partial \boldsymbol{\alpha}}, \; \boldsymbol{B} = -\rho \frac{\partial \psi}{\partial \boldsymbol{\beta}} \tag{2.1.12}$$

[11] A physical interpretation of the viscosity in a pure rubber is due to the chain reptation concept finding its origin from the relaxation of a single entangled chain in a polymer gel (de Gennes et al., 1971). This concept attributes the origin of the viscosity in a pure rubber to the slow return of free chains to a more relaxed configuration when the rubber network is in a deformed and relaxed state.

where $\boldsymbol{A}$ and $\boldsymbol{B}$ are the thermodynamic conjugate vectors for $\boldsymbol{\alpha}$ and $\boldsymbol{\beta}$, respectively, and they can be interpreted as the internal non-equilibrium forces that drive the material towards a thermodynamic equilibrium state, thus being referred to as generalized thermodynamic forces. Correspondingly, the change rates of the internal variables, $\dot{\boldsymbol{\alpha}}$ and $\dot{\boldsymbol{\beta}}$, can be taken as the generalized thermodynamic fluxes. Therefore, the intrinsic dissipation d_1 is actually equal to the total amount of the two types of internal thermodynamic works, namely, $\boldsymbol{A}\cdot\dot{\boldsymbol{\alpha}}$ and $\boldsymbol{B}\cdot\dot{\boldsymbol{\beta}}$, related with the recoverable and unrecoverable network rearrangements, respectively. Due to the fact that the irreversible thermodynamic processes in the rubber-filler material system are coupled with each other, we cannot conclude that the $\boldsymbol{A}\cdot\dot{\boldsymbol{\alpha}}$ and $\boldsymbol{B}\cdot\dot{\boldsymbol{\beta}}$ are simultaneously positive. As a matter of fact, a negative internal thermodynamic work is probable during the fatigue process, which means that this internal work is stored as thermodynamic potential energy by means of the corresponding network rearrangements.

Based on these constitutive relations and applying the chain rule of differentiation, a coupled energy balance equation is deduced from Eqs. (2.1.1) and (2.1.7) in two alternative forms:

$$\rho C\dot{T} = d_1 - \nabla\cdot\boldsymbol{q} + \hbar_{\mathrm{te}} + \hbar_{\mathrm{ti}} \tag{2.1.13}$$

$$\mathbf{S}:\dot{\mathbf{E}} - d_1 = \rho\dot{e} - \rho C\dot{T} + \hbar_{\mathrm{te}} + \hbar_{\mathrm{ti}} \tag{2.1.14}$$

where C is the specific heat capacity at deformation and internal variables fixed, $\hbar_{\mathrm{te}}$ is the structural thermoelastic heating (cooling), $\hbar_{\mathrm{ti}}$ is the heating (cooling) induced by the coupling effect between the temperature and the internal variables:

$$C = T\frac{\partial s}{\partial T},\ \hbar_{\mathrm{te}} = T\frac{\partial \mathbf{S}}{\partial T}:\dot{\mathbf{E}},\ \hbar_{\mathrm{ti}} = T\frac{\partial \boldsymbol{A}}{\partial T}\cdot\dot{\boldsymbol{\alpha}} + T\frac{\partial \boldsymbol{B}}{\partial T}\cdot\dot{\boldsymbol{\beta}} \tag{2.1.15}$$

2.1.2.3. Dissipations

Let us consider a flat and thin specimen with a constant cross-section subjected to a constant-amplitude cyclic loading. In this case, the temperature variations are relatively low (Ovalle-Rodas et al., 2013, 2014, 2015a, 2016). We will therefore assume that the fatigue-induced temperature variations have no influence on the network rearrangements. Naturally, this assumption is quite reasonable as long as the dissipative heating does not reach a very high level. Hence, the non-equilibrium thermodynamic forces can be considered to be temperature-independent:

$$\frac{\partial \boldsymbol{A}}{\partial T} = 0,\ \frac{\partial \boldsymbol{B}}{\partial T} = 0 \tag{2.1.16}$$

Also, the specific heat capacity is considered as a constant independent on the state variables, i.e. $C = C_0$. Based on these assumptions, Eqs. (2.1.13) and (2.1.14) become:

$$\rho C_0 \dot{T} = d_1 - \nabla \cdot \boldsymbol{q} + \hbar_{\mathrm{te}} \tag{2.1.17}$$

$$\mathbf{S} : \dot{\mathbf{E}} - d_1 = \rho \dot{e} - \rho C_0 \dot{T} + \hbar_{\mathrm{te}} \tag{2.1.18}$$

The integration of Eq. (2.1.18) over n_c complete cycles with the loading frequency f_L gives:

$$\bar{D} - \bar{d}_1 = \int_0^{\frac{n_c}{f_L}} \left(\rho \dot{e} - \rho C_0 \dot{T} + \hbar_{\mathrm{te}} \right) dt \tag{2.1.19}$$

in which $\bar{D}$ is the average mechanical dissipation and $\bar{d}_1$ is the average intrinsic dissipation given, respectively, by:

$$\bar{D} = \frac{1}{n_c} \int_0^{\frac{n_c}{f_L}} \left(\mathbf{S} : \dot{\mathbf{E}} \right) dt \text{ and } \bar{d}_1 = \frac{1}{n_c} \int_0^{\frac{n_c}{f_L}} d_1 dt \tag{2.1.20}$$

Considering the fact that the accumulation of the thermoelastic heating $\hbar_{\mathrm{te}}$ over one complete cycle is imperceptible, the right term of Eq. (2.1.19) may be simplified:

$$\frac{1}{n_c} \int_0^{\frac{n_c}{f_L}} \left(\rho \dot{e} - \rho C_0 \dot{T} \right) dt = \frac{\rho}{n_c} \left(e - e_0 - C_0 \theta \right) \tag{2.1.21}$$

in which e_0 is the initial internal energy and $\theta = T - T_0$ is the average temperature variation of the specimen gauge zone, T_0 being the initial temperature.

Applying the first order Taylor series approximation on the specific internal energy $e = e\left(T, \mathbf{E}, \boldsymbol{\alpha}, \boldsymbol{\beta}\right)$ leads to:

$$e - e_0 = \frac{\partial e}{\partial T}\left(T - T_0\right) + \frac{\partial e}{\partial \mathbf{E}} : \left(\mathbf{E} - \mathbf{E}_0\right) + \frac{\partial e}{\partial \boldsymbol{\alpha}} \cdot \left(\boldsymbol{\alpha} - \boldsymbol{\alpha}_0\right) + \frac{\partial e}{\partial \boldsymbol{\beta}} \cdot \left(\boldsymbol{\beta} - \boldsymbol{\beta}_0\right) \tag{2.1.22}$$

Recall that only the constant-amplitude cyclic loading is treated here, and the internal state variable $\boldsymbol{\alpha}$ characterizes the recoverable network rearrangement induced by the cyclic loading and thus changing with it. Consequently, after one complete cycle, the state variables $\mathbf{E}$ and $\boldsymbol{\alpha}$ will return to their original values, i.e. $\mathbf{E} = \mathbf{E}_0$ and $\boldsymbol{\alpha} = \boldsymbol{\alpha}_0$. Considering $\partial e / \partial T = T\left(\partial s / \partial T\right) = C_0$ and $\partial e / \partial \boldsymbol{\beta} = \partial \psi / \partial \boldsymbol{\beta} = -\left(\boldsymbol{B} / \rho\right)$, Eq. (2.1.19) may be further simplified as:

$$\bar{D} - \bar{d}_1 = \frac{-\boldsymbol{B}}{n_c}\left(\boldsymbol{\beta} - \boldsymbol{\beta}_0\right) \tag{2.1.23}$$

Since the internal state variable $\boldsymbol{\beta}$ is related to the unrecoverable network rearrangement, it can be concluded from Eq. (2.1.23) that the difference between the average mechanical

dissipation $\bar{D}$ and the average intrinsic dissipation $\bar{d}_1$ characterizes the process of the fatigue damage evolution.

Moreover, on basis of Eq. (2.1.17), a local zero-dimensional thermal equilibrium equation was proposed by Boulanger et al. (2004):

$$\rho C_0\left(\dot{\theta}+\frac{\theta}{\tau}\right)=\hbar_{\mathrm{te}}+d_1 \tag{2.1.24}$$

where τ is a time constant characterizing the heat exchanges of the zone with the surroundings.

Considering that the time integral of the temperature change rate is equal to the final temperature increment and again that the accumulation of the thermoelastic heating $\hbar_{\mathrm{e}}$ over one complete cycle is imperceptible, the average intrinsic dissipation $\bar{d}_1$ over the cyclic loading process can be calculated by processing the temperature data:

$$\bar{d}_1=\frac{\rho C_0}{n_c}\left(\theta_{n_c}+\frac{1}{\tau}\int_0^{\frac{n}{f_L}}\theta(t)\,dt\right) \tag{2.1.25}$$

where θ_{n_c} is the temperature increment at the end of the cyclic loading history n_c.

2.1.3. Experiments

A series of fatigue tests were achieved on carbon-filled SBR containing different amounts of carbon-black in order to gain insight into pre-stretch and filler content effects on the different cyclic history-dependent effects.

	SBR15	SBR25	SBR43
SBR	100	100	100
Carbon-black	15	25	43
Processing oil	37.5	37.5	37.5
Antioxidant	5.5	5.5	5.5
Zinc oxide	5	5	5
Accelerators	4	4	4
Stearic acid	3	3	3

Table 2.1.1. Compound formulation (value in phr, in weight).

2.1.3.1. Materials and specimen

Rubber sheets, produced by compression moulding, were supplied by the Trelleborg Group. The investigated rubber is a sulfur-vulcanized SBR filled with three different amounts

of carbon-black: 15, 25 and 43 phr (part per hundred of rubber in weight), denoted by SBR15, SBR25 and SBR43, respectively. The details about the compound formulation, provided by the manufacturer, are given in Table 2.1.1.

Dog-bone shaped specimens were cut from the rubber sheets with a thickness of 2 mm. Although material isotropy is expected, the specimens were cut along the same direction. The specimen dimensions are given in Figure 2.1.1. The specimen gauge zone allows locating the highest strain in this region and, as a consequence, the highest temperature increase. Furthermore, its small thickness allows avoiding a high temperature gradient in the transverse direction.

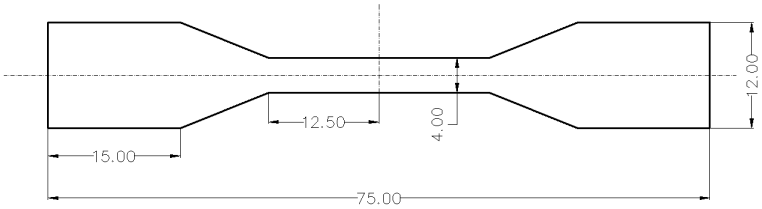

Figure 2.1.1. Specimen geometry (dimensions in mm).

2.1.3.2. Methods

2.1.3.2.1. Mechanical measurements

The fatigue tests were performed with the help of an electro-pulse testing machine Instron-5500 and consist in three loading steps as illustrated in Figure 2.1.2.

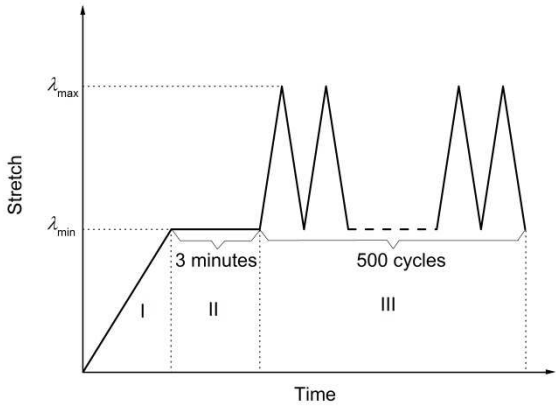

Figure 2.1.2. Stretch vs. time, stage I: ramp to λ_{min}, stage II: relaxation period with hold time of 3 minutes, stage III: cyclic loading.

The stretch was first ramped to the prescribed minimum value λ_{min}. After a hold time of 3 minutes guarantying thermo-mechanical equilibrium, the stretch was ramped, repetitively, to a maximum value λ_{max} and then ramped down to the minimum value λ_{min}, load and displacement versus time being recorded during the cyclic tests. The same absolute axial strain rate was imposed to the loading and unloading paths. The pre-stretch dependency was quantified using the ratio between the minimum applied stretch λ_{min} and the maximum applied stretch λ_{max} defined as:

$$R = \frac{\lambda_{min} - 1}{\lambda_{max} - 1} \tag{2.1.26}$$

Five stretch ratios were considered: R = [0.286, 0.444, 0.545, 0.615, 0.667], in which the stretch amplitude $\lambda_{amp} = \lambda_{max} - \lambda_{min}$ is set to be the same. All tests were performed at ambient conditions. Unless explicitly otherwise stated, the amplitude and the axial strain rate are λ_{amp} = 1.25 and $\dot{\varepsilon}$ = 1 s^{-1}, respectively.

2.1.3.2.2. Temperature-field measurements

Full-field surface temperature of the specimen gauge zone was monitored by means of an infrared camera Flir SC300 with the following main characteristics: Spectrum response ranged from 7.5 to 13 μm, resolution of 320 × 240 pixel, sensitivity / NETD less than 25 mK and image update rate of 9 Hz. The camera was located at a distance of about 0.5 m from the specimen surface in order to reduce the reflected radiation due to surrounding humidity. To improve accuracy a dummy specimen made of the same material was positioned close to the tested one to monitor the environmental changes and further to eliminate their effects on the temperature data. In addition, the set-up was packed in a relatively closed space using a special thermal insulation material to reduce the external radiation sources. The stored images were post-processed to determine the temperature evolution in the region of interest of the gauge zone. Thermal equilibrium is ensured by a hold time of 10 minutes before testing.

Pre-conditioning tests were initially run, with R = 0, in which an overstretch of 1.0 at a frequency of 1 Hz was applied for 15 cycles. The pre-conditioning was applied, previous to measurements, in order to eliminate the surface flake that appears in the specimen during cyclic loading, which can alter the temperature-field measurements because of the surface emissivity variation.

2.1.4. Results and discussion

2.1.4.1. Large-strain viscoelastic relaxations

The large-strain viscoelastic behavior is examined in Figure 2.1.3 in which multi-step stress relaxations under a loading-unloading cycle were performed for the three carbon-filled SBR materials. At each relaxation period, the stretch is maintained constant during only 10 seconds. The figure provides a quantitative judgment of the nonlinear response and the material viscosity related to both the relaxation response and the hysteresis loop, i.e. the stress difference between loading and unloading paths. Due to the strain-amplifying effect of the fillers, the material becomes stiffer, the hysteresis loop area gets larger and the strain-hardening increases with increasing filler content. The stress during the relaxation periods seems to evolve towards an end, if the hold time is sufficiently long, corresponding to a stabilized relaxed-stress, which is a function of the stretch level (Laiarinandrasana et al., 2012). The stress evolution during the relaxation periods is much less marked in the unloading path than in the loading one since the required time to reach the equilibrium exceeds the magnitude of the applied hold time.

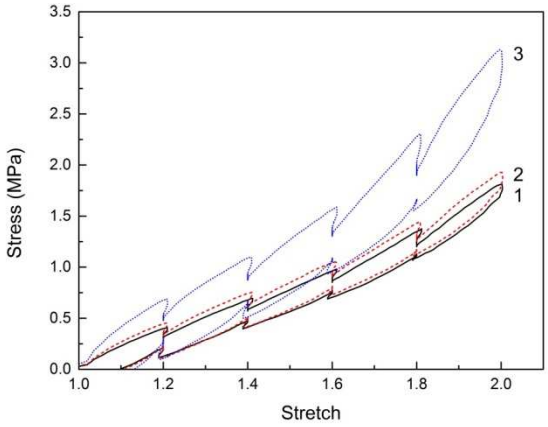

Figure 2.1.3. Multi-step stress relaxations under a loading-unloading cycle (1: SBR15, 2: SBR25, 3: SBR43).

The carbon-filled SBR history-dependence can be also examined with the relaxation periods of the stage II of Figure 2.1.2. As an example, the stress evolution, normalized by the maximum value, is presented for the SBR43 material in Figure 2.1.4. It can be observed that the normalized maximum stress depends on the pre-stretch level. The higher the minimum

stretch, the smaller the decrease in stress. This pre-stretch dependency of the plots points out the nonlinearity of the material viscosity.

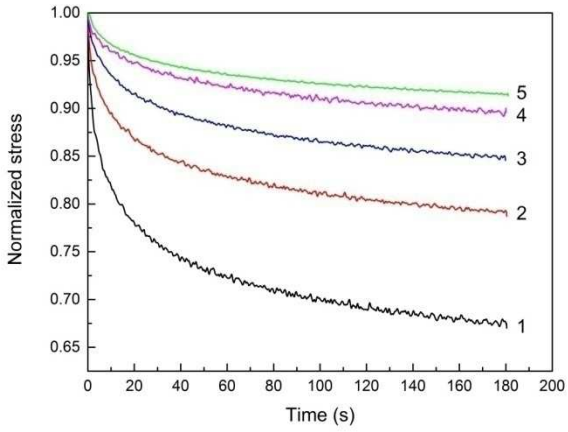

Figure 2.1.4. Normalized stress under relaxation for SBR43 corresponding to stage II of Figure 2.1.2 (1: λ_{min} = 1.1, 2: λ_{min} = 1.2, 3: λ_{min} = 1.3, 4: λ_{min} = 1.4, 5: λ_{min} = 1.5).

2.1.4.2. Fatigue-induced stress-softening

The fatigue-induced stress-softening is shown in Figure 2.1.5 for the SBR43 at different stretch ratios material subjected to multi-step cyclic tests in which the stages II and III of Figure 2.1.2 were repeated 5 times.

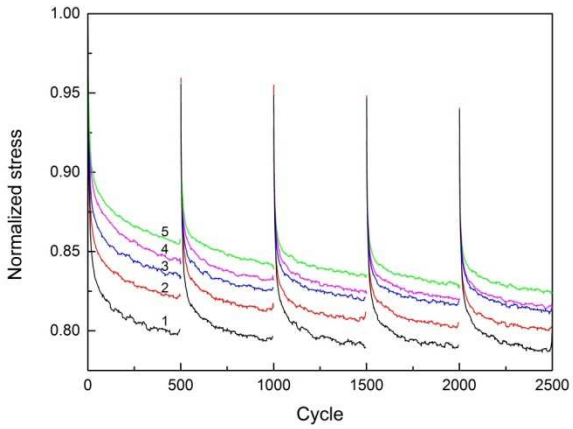

Figure 2.1.5. Normalized stress under cyclic loading for SBR43 corresponding to stage III of Figure 2.1.2 (1: R = 0.286, 2: R = 0.444, 3: R = 0.545, 4: R = 0.615, 5: R = 0.667).

The figure provides the stress evolution during the stage III normalized by the maximum value. We firstly focus on the first block in which a substantial decrease in stress is observed during the first few cycles. Following this rapid decrease in stress, the rubber undergoes a

more gradual softening and tends towards a stabilized state for which there is no significant change in stress. The degree to which the material is softened depends strongly on the stretch ratio. The smaller the stretch ratio experienced during the cyclic loading history, the softer the stabilized response. The rapid initial decrease in stress, as well as the associated development of a slight residual strain, is generally regarded as a damage effect related to the irreversible breakage of various types of bonds in the rubber network (Mullins, 1948; Houwink, 1956; Bueche, 1960; Kraus et al., 1966; Kraus, 1984; Lion, 1996; Marckmann et al., 2002; Laiarinandrasana et al., 2003; Hanson et al., 2005; Chagnon et al., 2006; Ayoub et al., 2011b, 2014b; Diaz et al., 2014). Due to their time-dependent memory effects, the inelastic phenomena in polymers can be recovered as long as ageing (Belbachir et al., 2010; Ben Hassine et al., 2014) or inelastic volumetric effects (Aït Hocine et al., 2011; Zaïri et al., 2008, 2011) are avoided. An illustrative example concerns the plastic deformation in thermoplastic polymers which can be recovered with heating. In the same way, it was reported in the review of Mullins (1969) that the original stiffness of filled rubbers is partially or totally recovered, very slowly at ambient temperature and very rapidly with heating. At each block of Figure 2.1.5 the first few cycles invariably induce a considerable decrease in stress which cannot be attributed solely to the effect of the damage. Indeed, a large portion of the initial transient softening is recovered when one passes from one block to another. The recovery in fatigue-induced stress-softening, which could increase with the magnitude of the applied hold time of the stage II of Figure 2.1.2, can be only associated with viscoelastic relaxations, i.e. recoverable mechanisms. Therefore, the observable decrease in stress is believed to be associated in part with unrecoverable breakage of bonds and in another part with recoverable viscoelastic mechanisms. It can be also observed that the portion of the recoverable stress-softening diminishes with the block number. In addition, after the initial transient softening, the stress tends further to recapture the same path as that corresponding to the interrupted cyclic test. This observation poses a challenge for the development of predictive constitutive models. Although current theoretical works on the stress-softening may contain the underlying physical structure and damage mechanisms, they typically ignore the stress-softening recovery which would require to consider the material viscosity, significant in filled rubbers as shown in the previous sub-section. In addition to the move of free chains included in the relaxed network and the viscous friction between fillers and matrix / fillers, during the network rearrangement some broken chains may be transformed into dangling chains which contributes to increase the material viscosity.

The strain-amplifying effect of the fillers acts both on damage intensity and on viscoelastic relaxations. The dependence of both stretch ratio and filler effects on the degree to which the material is softened may be quantified by the softening rate expressed by the following parameter:

$$\delta = \frac{1\text{-}\delta_{n_c}}{n_c} \tag{2.1.27}$$

in which δ_{n_c} is the normalized stress at the end of the cyclic loading history n_c.

This parameter is plotted as a function of the stretch ratio in Figure 2.1.6 such that a straight-line fit adequately describes the results. Although its value is significantly amplified by the filler content, the rate of the decrease in the δ parameter with the stretch ratio is observed to slightly vary with the filler content.

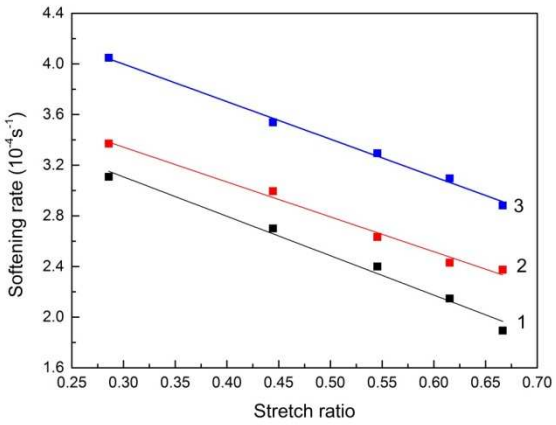

Figure 2.1.6. Softening rate as a function of stretch ratio (1: SBR15, 2: SBR25, 3: SBR43).

2.1.4.3. Dissipations

As introduced in the theory section, the mechanical dissipation due to the hysteretic process in the carbon-filled SBR cyclic response is a consequence of the internal network rearrangements during the cyclic loading. Although being an irreversible process in thermodynamics, the rearrangement of the network in the rubber-filler material system leads to both recoverable and unrecoverable mechanisms. As an illustrative example, Figure 2.1.7 presents the hysteretic response for the SBR43 material at a given cycle of the stage III of Figure 2.1.2. The pre-stretch dependency of the hysteresis loop area is evidenced in the figure. The smaller the stretch ratio, the higher the loop area. The decrease of the loop area with the

stretch ratio is mainly due to the nonlinear material response which also induce a slight effect on the shape of the hysteresis loop.

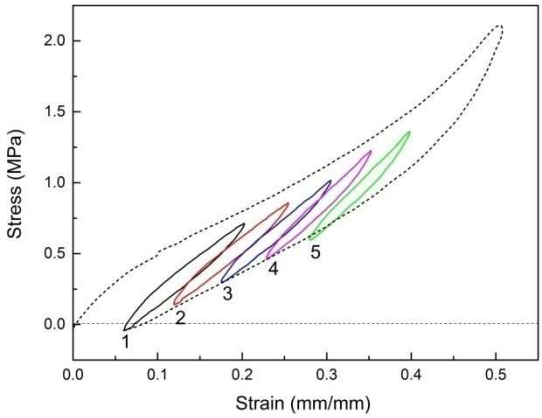

Figure 2.1.7. Hysteretic response at 250th cycle for SBR43 (1: R = 0.286, 2: R = 0.444, 3: R = 0.545, 4: R = 0.615, 5: R = 0.667).

The mechanical energy dissipated during one hysteresis loop is quantified by its area. Figure 2.1.8 shows the evolution of the mechanical dissipation with the cycle number after reaching different assigned pre-stretches.

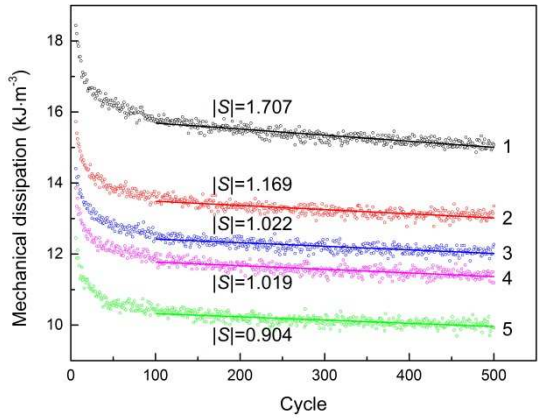

Figure 2.1.8. Mechanical dissipation under cyclic loading for SBR43 (1: R = 0.286, 2: R = 0.444, 3: R = 0.545, 4: R = 0.615, 5: R = 0.667).

By virtue of the fatigue-induced stress-softening, the hysteresis during the first few cycles is much greater than that under subsequent steady-state cyclic loading. Indeed, as shown in the figure the strongest decrease in mechanical dissipation occurs during the first few cycles. Following this rapid decrease, the mechanical dissipation tends towards a stabilized state for which the rate of the decrease with the cycles is observed to decrease with the pre-stretch. In

order to give an indication of the average mechanical energy dissipated during the cyclic loading history, the mechanical dissipation is averaged over all cycles via Eq. (2.1.20). The average mechanical dissipation $\bar{D}$ is plotted as a function of stretch ratio in Figure 2.1.9 such that a straight-line fit adequately describes the results. It can be observed in the figure that the slope, characterizing the stretch ratio dependency of the mechanical dissipation, increases with the filler content.

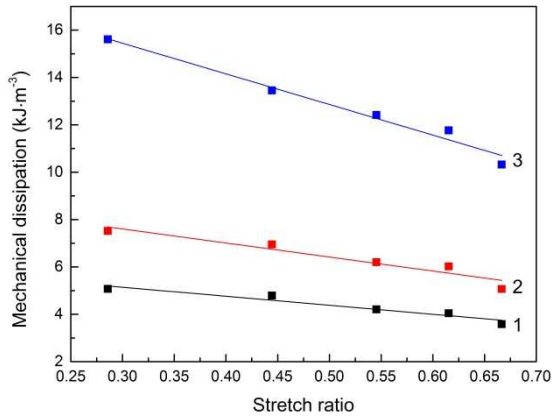

Figure 2.1.9. Mechanical dissipation as a function of stretch ratio (1: SBR15, 2: SBR25, 3: SBR43).

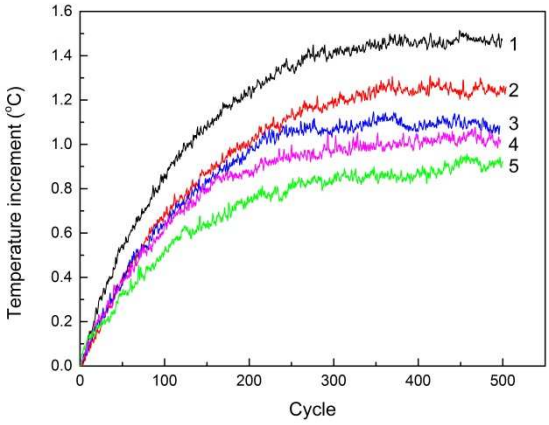

Figure 2.1.10. Temperature increment under cyclic loading for SBR43 (1: R = 0.286, 2: R = 0.444, 3: R = 0.545, 4: R = 0.615, 5: R = 0.667).

When the carbon-filled rubber is cyclically loaded, parts of the applied mechanical energy are converted into thermal energy which drives to a temperature evolution within the material. As illustrative examples, Figures 2.1.10 and 2.1.11 report the surface temperature evolution extracted in the specimen gauge zone with the pre-stretch and filler content effects, respectively.

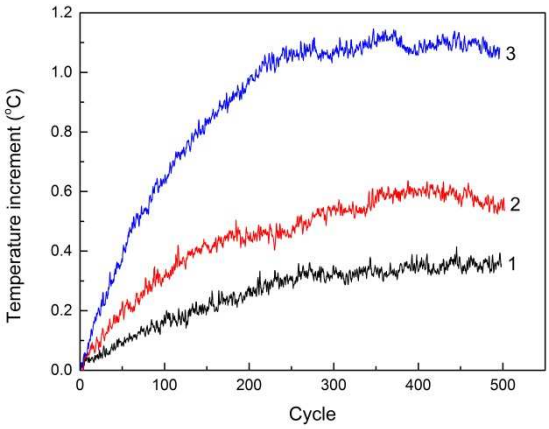

Figure 2.1.11. Temperature increment under cyclic loading for R = 0.545 (1: SBR15, 2: SBR25, 3: SBR43).

It can be clearly observed that an abrupt temperature increase occurs in the beginning of the cyclic loading and then the temperature tends to stabilize because of the equality of the generated heat and the heat lost into the environment. A global view at these results indicates that there is a quite significant effect of the two above factors on the stabilized temperature which increases with the stretch ratio decrease and with the filler content increase. The average intrinsic dissipation $\overline{d_1}$ was evaluated by processing the temperature data via Eq. (2.1.25) and plotted as a function of the stretch ratio in Figure 2.1.12 such that a straight-line fit adequately describes the results. Indeed, the intrinsic dissipation decreases with the stretch ratio following a linear relationship for which the slope increases with the filler content.

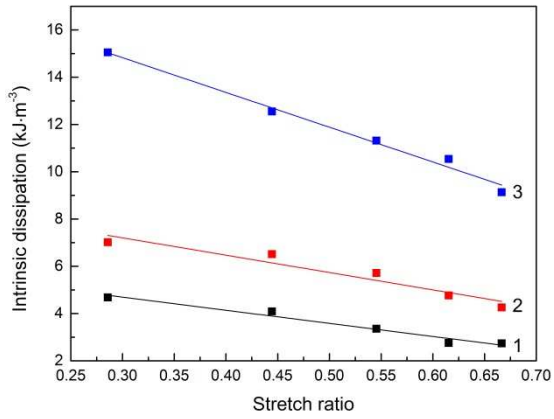

Figure 2.1.12. Intrinsic dissipation as a function of stretch ratio (1: SBR15, 2: SBR25, 3: SBR43).

The inherent inelastic fatigue mechanisms may be studied under the guidance of the intrinsic dissipation estimation with the pre-stretch dependency. The carbon-filled SBR has different intrinsic dissipation mechanisms which, as introduced in the theory section, may be classified into two types, namely, viscoelastic mechanisms corresponding to recoverable network rearrangement and damage mechanisms corresponding to unrecoverable network rearrangement.

The level of interactions between the chains and the fillers, the chains and the fillers themselves plays an important role in the viscoelastic mechanisms. Its degree depends, respectively, on the rubber-filler interface, the chain entanglement density (viscous friction between chains), and the contact surface area between fillers inside the aggregates (viscous friction between carbon-black fillers). Also, as explained in the theory section, the breakdown-rebound of inter-aggregates links completes this set of recoverable network rearrangements. The latter mechanism is a progressive process, beginning with the weakest links and progressing into the strongest ones. Indeed, the breakdown of inter-aggregates links and the formation of new links in new positions are two irreversible processes in thermodynamics viewpoint, but the whole breakdown-rebound process may be considered in a large part as a recoverable mechanism highly dependent on the load time-scale. The increase in filler content is related to a higher number of inter-aggregates interactions which leads thus to a higher additional energy dissipated within the breakdown and rebound of inter-aggregates links, and, a higher viscous friction between carbon-black fillers inside the aggregates.

We can illustrate these inelastic fatigue mechanisms by the scenario presented in Figure 2.1.13. In the initial state (Figure 2.1.13a), the filled rubber is represented by entangled chains between two filler aggregates. It is believed that the application of a pre-stretch (Figure 2.1.13b) has for main consequences to decrease the rubber-filler interaction (chain "slipping" over the filler surface, desorption at the filler surface, bond breakage at the filler surface[12]), the chain entanglement density and the contact surface area between fillers inside the aggregates. Therefore, the viscous friction degree decreases with the applied pre-stretch level and, consequently, a higher pre-stretch implies a lower intrinsic dissipation. During the cyclic loading (Figure 2.1.13c), some damage happens. It is believed that the chains between two

[12] High resolution solid-state NMR experiments provide insights into the existence of mobility gradients in filled rubbers, through variations in the glass transition temperature as a function of the distance to the filler surface (Berriot et al., 2002, 2003; Boutaleb et al., 2009). The degradation of this perturbed region of chains around the fillers due the application of the pre-stretch is potentially an additional cause of the weaker matrix-filler interactions (Diaz et al., 2014; Boutaleb et al., 2009; Zaïri et al., 2011).

filler aggregates progressively breakdown, and in the meantime, a part of the breakdown of the inter-aggregates links cannot be reformed on the time scale of measurements.

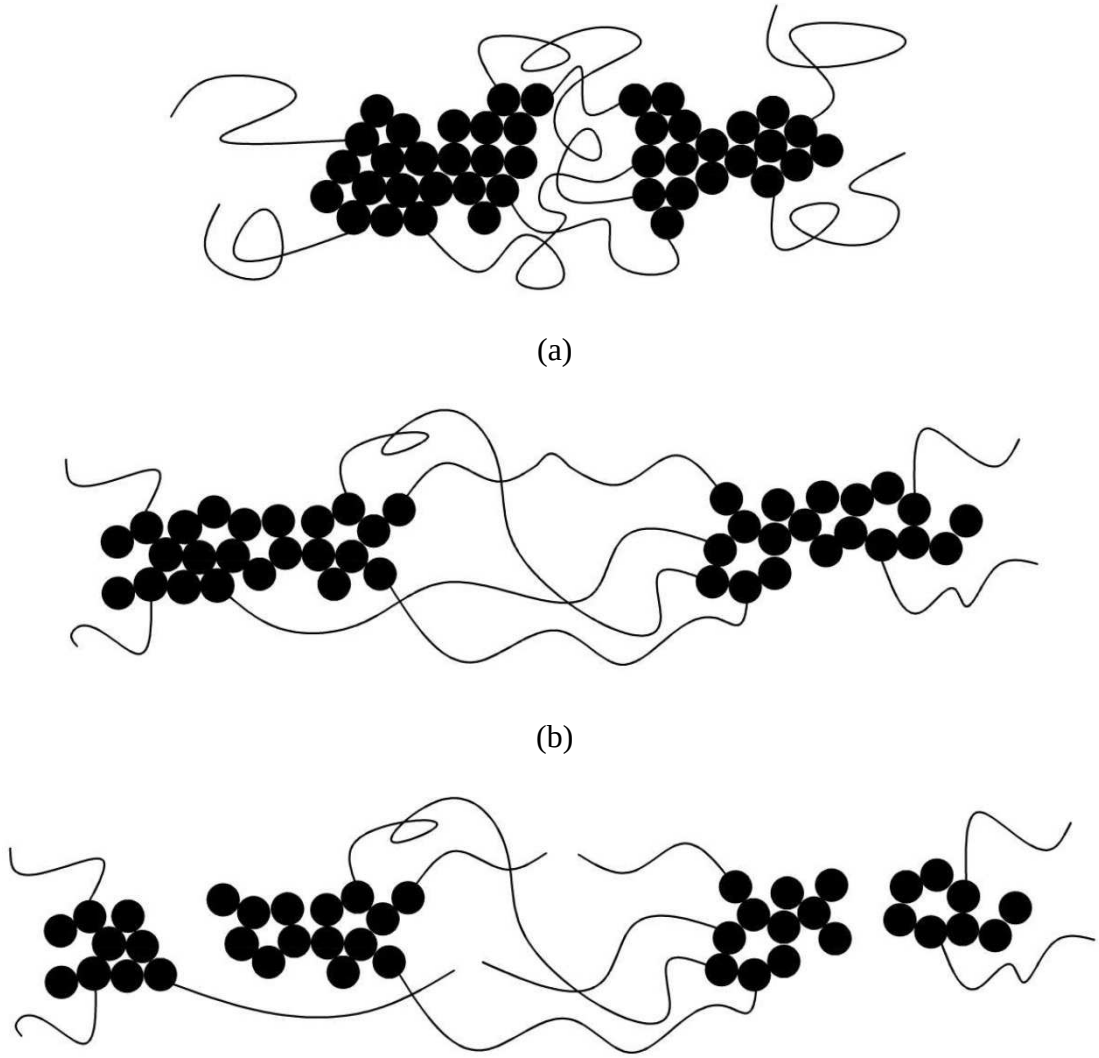

(a)

(b)

(c)

Figure 2.1.13. Physical mechanisms in pre-stretched cyclically loaded filled rubbers: (a) initial network, (b) pre-stretched network and (c) network rearrangement after pre-stretched cyclic loading.

These two unrecoverable network rearrangements contribute to the intrinsic dissipation, but in a lower extent than the recoverable ones in consistence with our experimental observations. Some of broken chains may be transformed into dangling chains and potentially contribute to increase the viscous friction and, therefore, to increase the dissipation. The permanent filler aggregate rupture acts as an antagonist mechanism since it leads to a lower contact surface area and then to a lower energy dissipated. The decrease in dissipation with the cyclic loading

as shown in Figure 2.1.8 is a sign that the permanent filler aggregate rupture dominates among the two possible damage effects.

As a final point, the effects of stretch amplitudes and strain rates on the dissipations are presented in Figures 2.1.14 to 2.1.16 for the three carbon-filled SBR.

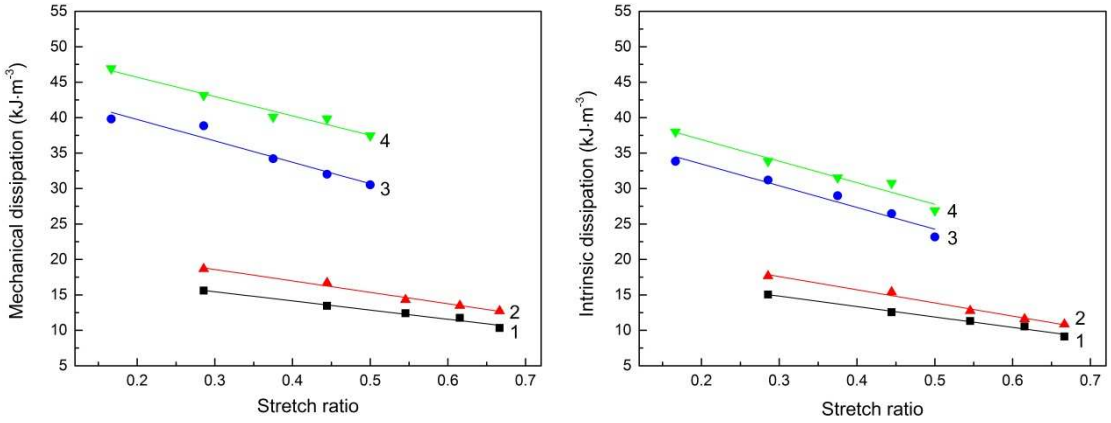

(a) (b)

Figure 2.1.14. Amplitude and strain rate effect on stretch ratio dependency of SBR43 dissipations: (a) mechanical dissipation and (b) intrinsic dissipation (1: $\lambda_{amp} = 1.25$, $\dot{\varepsilon} = 1\ s^{-1}$; 2: $\lambda_{amp} = 1.25$, $\dot{\varepsilon} = 2\ s^{-1}$; 3: $\lambda_{amp} = 2.5$, $\dot{\varepsilon} = 1\ s^{-1}$; 4: $\lambda_{amp} = 2.5$, $\dot{\varepsilon} = 2\ s^{-1}$).

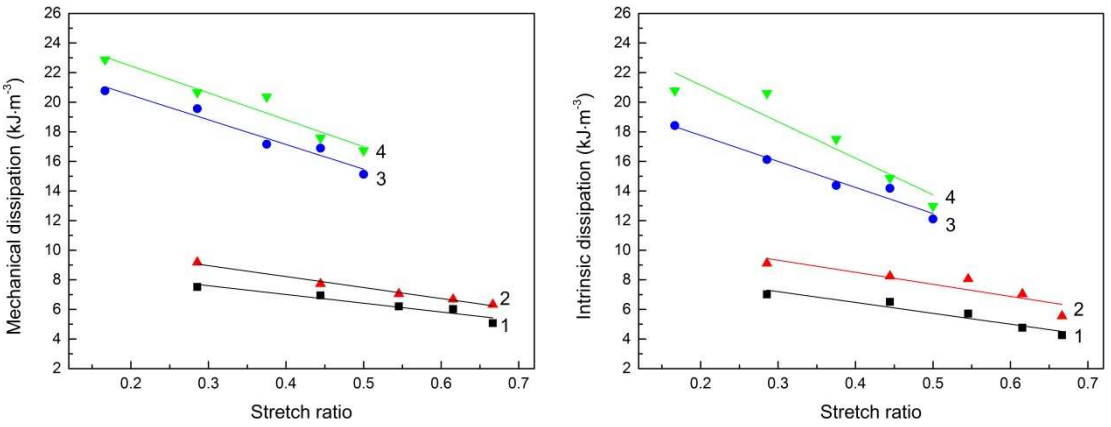

(a) (b)

Figure 2.1.15. Amplitude and strain rate effect on stretch ratio dependency of SBR25 dissipations: (a) mechanical dissipation and (b) intrinsic dissipation (1: $\lambda_{amp} = 1.25$, $\dot{\varepsilon} = 1\ s^{-1}$; 2: $\lambda_{amp} = 1.25$, $\dot{\varepsilon} = 2\ s^{-1}$; 3: $\lambda_{amp} = 2.5$, $\dot{\varepsilon} = 1\ s^{-1}$; 4: $\lambda_{amp} = 2.5$, $\dot{\varepsilon} = 2\ s^{-1}$).

Both mechanical and intrinsic dissipations manifest a good linear correlation with the pre-stretch whatever the strain amplitude experienced during the loading history and the strain rate. Higher strain amplitude or strain rate results in amplified effects at the scale of the above physical mechanisms and then in more dissipations. From these figures, it can be also

observed that the mechanical dissipation is higher than the intrinsic dissipation. In the theory section, the difference between the two dissipations was considered as a fatigue damage indicator, but our experimental observations point out a weak difference. That means that the viscoelastic recoverable rearrangement is the dominate mechanism of the carbon-filled SBR fatigue.

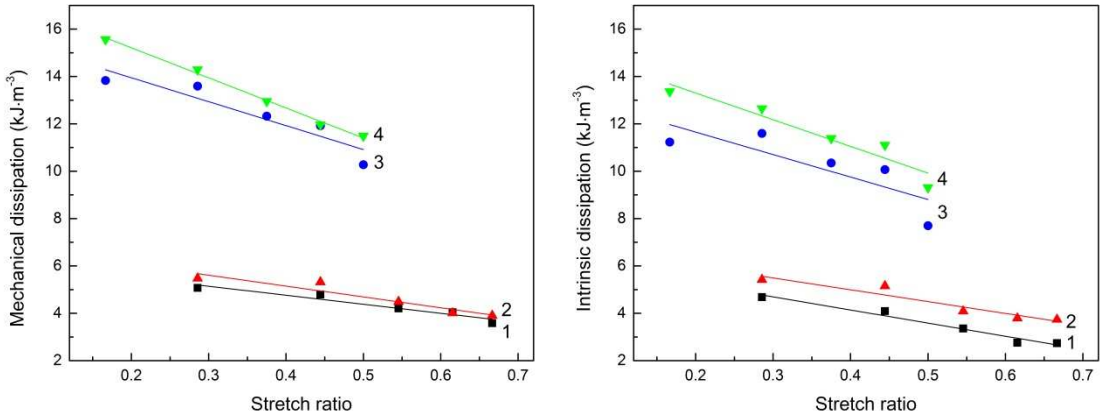

(a) (b)

Figure 2.1.16. Amplitude and strain rate effect on stretch ratio dependency of SBR15 dissipations: (a) mechanical dissipation and (b) intrinsic dissipation (1: $\lambda_{amp} = 1.25$, $\dot{\varepsilon} = 1\ s^{-1}$; 2: $\lambda_{amp} = 1.25$, $\dot{\varepsilon} = 2\ s^{-1}$; 3: $\lambda_{amp} = 2.5$, $\dot{\varepsilon} = 1\ s^{-1}$; 4: $\lambda_{amp} = 2.5$, $\dot{\varepsilon} = 2\ s^{-1}$).

2.1.5. Partial conclusions

The internal state variable theory was adopted for the first time to investigate the inelastic fatigue process in carbon-black filled SBR. The theory accounts for the two types of rearrangements in the rubber-filler material by introducing the internal state variables related to the recoverable rearrangement inducing viscoelasticity and the unrecoverable rearrangement inducing damage. The intrinsic dissipation was quantified by considering the respective influence of filler content and pre-stretch level. The underlying physical mechanisms, consistent with our experimental observations, are proposed by involving plausible recoverable and unrecoverable rearrangements in the rubber-filler material system.

2.1.6. References

Aït Hocine, N., Hamdi, A., Naït-Abdelaziz, M., Heuillet, P., Zaïri, F., 2011. Experimental and finite element investigation of void nucleation in rubber-like materials. International Journal of Solids and Structures 48, 1248-1254.

Ayoub, G., Naït-Abdelaziz, M., Zaïri, F., Gloaguen, J.M., Charrier, P., 2011a. A continuum damage model for the high-cycle fatigue life prediction of styrene-butadiene rubber under multiaxial loading. International Journal of Solids and Structures 48, 2458-2466.

Ayoub, G., Zaïri, F., Naït-Abdelaziz, M., Gloaguen, 2011b. Modeling the low-cycle fatigue behavior of visco-hyperelastic elastomeric materials using a new network alteration theory: Application to styrene-butadiene rubber. Journal of the Mechanics and Physics of Solids 59, 473-795.

Ayoub, G., Naït-Abdelaziz, M., Zaïri, F., Gloaguen, J.M., Charrier, P., 2012. Fatigue life prediction of rubber-like materials under multiaxial loading using a continuum damage mechanics approach: Effects of two-blocks loading and R ratio. Mechanics of Materials 52, 87-102.

Ayoub, G., Naït-Abdelaziz, M., Zaïri, F., 2014a. Multiaxial fatigue life predictors for rubbers: application of recent developments to a carbon-filled SBR. International Journal of Fatigue 66, 168-176.

Ayoub, G., Zaïri, F., Naït-Abdelaziz, M., Gloaguen, J.M., Kridli, G., 2014b. A visco-hyperelastic damage model for cyclic stress-softening, hysteresis and permanent set in rubber using the network alteration theory. International Journal of Plasticity 54, 19-33.

Behnke, R., Kaliske, M., Kluppel, M., 2016. Thermo-mechanical analysis of cyclically loaded particle-reinforced elastomer components: experiment and finite element simulation. Rubber Chemistry and Technology 89, 154-176.

Belbachir, S., Zaïri, F., Ayoub, G., Maschke, U., Naït-Abdelaziz, M., Gloaguen, J.M., Benguediab, M., Lefebvre, J.M., 2010. Modelling of photodegradation effect on elastic-viscoplastic behaviour of amorphous polylactic acid films. Journal of the Mechanics and Physics of Solids 58, 241-255.

Ben Hassine, M., Naït-Abdelaziz, M., Zaïri, F., Colin, X., Tourcher, C., Marque, G., 2014. Time to failure prediction in rubber components subjected to thermal ageing: a combined approach based upon the intrinsic defect concept and the fracture mechanics. Mechanics of Materials 79, 15-24.

Berriot, J., Lequeux F., Monnerie, L., Montes, H., Long, D., Sotta, P., 2002. Filler-elastomer interaction in model filled rubbers, a ^{1}H NMR study. Journal of Non-Crystalline Solids 307-310, 719-724.

Berriot, J., Martin, F., Montes, H., Monnerie, L., Sotta, P., 2003. Reinforcement of model filled elastomers: characterization of the cross-linking density at the filler-elastomer interface by ^{1}H NMR measurements. Polymer 44, 1437-1447.

Boulanger, T., Chrysochoos A., Mabru, C., Galtier, A., 2004. Calorimetric analysis of dissipative and thermoelastic effects associated with the fatigue behavior of steels. International Journal of Fatigue 26, 221-229.

Boutaleb, S., Zaïri, F., Mesbah, A., Naït-Abdelaziz, M., Gloaguen, J.M., Boukharouba, T., Lefebvre, J.M., 2009. Micromechanics-based modelling of stiffness and yield stress for silica/polymer nanocomposites. International Journal of Solids and Structures 46, 1716-1726.

Brunac, J.B., Gerardin, O., Leblond, J.B., 2009. On the heuristic extension of Haigh's diagram for the fatigue of elastomers to arbitrary loadings. International Journal of Fatigue 31, 859-867.

Bueche, F., 1960. Molecular basis for the Mullins effect. Journal of Applied Polymer Science 4, 107-114.

Chagnon, G., Verron, E., Marckmann, G., Gornet, L., 2006. Development of new constitutive equations for the Mullins effect in rubber using the network alteration theory. International Journal of Solids and Structures 43, 6817-6831.

Coleman, B.D., Noll, W., 1963. The thermodynamics of elastic materials with heat conduction and viscosity. Archive for Rational Mechanics and Analysis 13, 167-178.

Diaz, R., Diani, J., Gilormini, P., 2014. Physical interpretation of the Mullins softening in a carbon-black filled SBR. Polymer 55, 4942-4947.

Rice, J.R., 1971. Inelastic constitutive relations for solids: an internal-variable theory and its application to metal plasticity. Journal of the Mechanics and Physics of Solids 19, 433-455.

de Gennes, P.G., 1971. Reptation of a polymer chain in the presence of fixed obstacles. Journal of Chemical Physics 55, 572-579.

Derham, C.J., Thomas, A.G., 1977. Creep of rubber under repeated stressing. Rubber Chemistry and Technology 50, 397-402.

Gough, J., 1805. A description of a property of Caoutchouc, or Indian rubber; with some reflections on the cause of the elasticity of this substance. Memoirs of the Literary and Philosophical Society of Manchester 1, 288-295.

Grandcoin, J., Boukamel, A., Lejeunes, S., 2014. A micro-mechanically based continuum damage model for fatigue life prediction of filled rubbers. International Journal of Solids and Structures 51, 1274-1286.

Hanson, D.E., Hawley, M., Houlton, R., Chitanvis, K., Rae, P., Orler, E.B., Wrobleski, D.A., 2005. Stress softening experiments in silica-filled polydimethylsiloxane provide insight into a mechanism for the Mullins effect. Polymer 46, 10989-10995.

Houwink, R., 1956. Slipping of molecules during the deformation of reinforced rubber. Rubber Chemistry and Technology 29, 888-893.

Johlitz, M., Dippel, B., Lion, A., 2016. Dissipative heating of elastomers: a new modelling approach based on finite and coupled thermomechanics. Continuum Mechanics and Thermodynamics 28, 1111-1125.

Kraus, G., Childers, C.W., Rollmann, K.W., 1966. Stress softening in carbon black-reinforced vulcanizates: strain rate and temperature effects. Journal of Applied Polymer Science 10, 229-244.

Kraus, G., 1984. Mechanical losses in carbon black filled rubbers. Journal of Applied Polymer Science 39, 75-92.

Li, F., Liu, J., Yang, H., Lu, Y., Zhang, L., 2016. Numerical simulation and experimental verification of heat build-up for rubber compounds. Polymer 101, 199-207.

Laiarinandrasana, L., Piques, R., Robisson, A., 2003. Visco-hyperelastic model with internal state variable coupled with discontinuous damage concept under total Lagrangian formulation. International Journal of Plasticity 19, 977-1000.

Laiarinandrasana, L., Jean, A., Jeulin, D., Forest, S., 2012. Modelling the effects of various contents of fillers on the relaxation rate of elastomers. Materials and Design 33, 75-82.

Lion, A., 1996. A constitutive model for carbon black filled rubber: experimental investigations and mathematical representation. Continuum Mechanics and Thermodynamics 8, 153-169.

Loukil, M.T., Corvec, G., Robin, E., Miroir, M., Le Cam, J.B., Garnier P., 2018. Stored energy accompanying cyclic deformation of filled rubber. European Polymer Journal 98, 448-455.

Marckmann, G., Verron, E., Gornet, L. Chagnon, G., Charrier, P., Fort, P., 2002. A theory of network alteration for the Mullins effect. Journal of the Mechanics and Physics of Solids 50, 2011-2028.

Mars, W.V., 2002. Cracking energy density as a predictor of fatigue life under multiaxial conditions. Rubber Chemistry and Technology 75, 1-17.

McKenna, G.B., Zapas, L.J., 1981. Response of carbon black filled butyl rubber to cyclic loading. Rubber Chemistry and Technology 54, 718-733.

Medalia, A., 1991. Heat generation in elastomer compounds: Causes and effects. Rubber Chemistry and Technology 64, 481-492.

Meinecke, E., 1991. Effect of carbon-black loading and crosslink density on the heat build-up in elastomers. Rubber Chemistry and Technology 64, 269-284.

Meo, S., Boukamel, A., Debordes, O., 2002. Analysis of a thermoviscoelastic model in large strain. Computers and Structures 80, 2085-2098.

Mullins, L., 1948. Effect of stretching on the properties of rubber. Rubber Chemistry and Technology 21, 281-300.

Mullins, L., 1969. Softening of rubber by deformation. Rubber Chemistry Technology 42, 339-362.

Ovalle-Rodas, C., Zaïri, F., Naït-Abdelaziz, M., 2013. Thermo-visco-hyperelastic modeling of the rubber self-heating under fatigue. Constitutive Models for Rubber VIII - Proceedings of the 8th European Conference on Constitutive Models for Rubbers, ECCMR 2013, 131-136.

Ovalle-Rodas, C., Zaïri, F., Naït-Abdelaziz, M., 2014. A finite strain thermo-viscoelastic constitutive model to describe the self-heating in elastomeric materials during low-cycle fatigue. Journal of the Mechanics and Physics of Solids 64, 396-410.

Ovalle-Rodas, C., Zaïri, F., Naït-Abdelaziz, M., Charrier, P., 2015a. Filler effects on the heat build-up of filled rubbers during fatigue: experimental observations and constitutive modelling. Constitutive Models for Rubber IX - Proceedings of the 9th European Conference on Constitutive Models for Rubbers, ECCMR 2015, 173-180.

Ovalle-Rodas, C., Zaïri, F., Naït-Abdelaziz, M., Charrier, P., 2015b. Temperature and filler effects on the relaxed response of filled rubbers: Experimental observations on a carbon-filled SBR and constitutive modeling. International Journal of Solids and Structures 58, 309-321.

Ovalle-Rodas, C., Zaïri, F., Naït-Abdelaziz, M., Charrier, P., 2016. A thermo-visco-hyperelastic model for the heat build-up during low-cycle fatigue of filled rubbers: formulation, implementation and experimental verification. International Journal of Plasticity 79, 217-236.

Pramanik, P., Khastgir, D., Saha, T., 1992. Conductive nitrile rubber composite containing carbon fillers: Studies on mechanical properties and electrical conductivity. Composites Part A: Applied Science and Manufacturing 23, 183-191.

Reese, S., 2003. A micromechanically motivated material model for the thermo-viscoelastic material behaviour of rubber-like polymers. International Journal of Plasticity 19, 909-940.

Saintier, N., Cailletaud, G., Piques, R., 2006. Crack initiation and propagation under multiaxial fatigue in a natural rubber. International Journal of Fatigue 28, 61-72.

Samaca Martinez, J.R., Le Cam, J.-B., Balandraud, X., Toussaint, E., Caillard, J., 2013. Filler effects on the thermomechanical response of stretched rubbers. Polymer Testing 32, 835-841.

Verron, E., Andriyana, A., 2008. Definition of a new predictor for multiaxial fatigue crack nucleation in rubber. Journal of the Mechanics and Physics of Solids 56, 417-443.

Wang, B., Lu, H., Kim, G.H., 2002. A damage model for the fatigue life of elastomeric materials. Mechanics of Materials 34, 475-483.

Ward, I.M., 1985. Mechanical Properties of Solid Polymers. Wiley, New York.

Zaïri, F., Naït-Abdelaziz, M., Gloaguen, J.M., Lefebvre, J.M., 2008. Modelling of the elasto-viscoplastic damage behaviour of glassy polymers. International Journal of Plasticity 24, 945-965.

Zaïri, F., Naït-Abdelaziz, M., Gloaguen, J.M., Lefebvre, J.M., 2011a. A physically-based constitutive model for anisotropic damage in rubber-toughened glassy polymers during finite deformation. International Journal of Plasticity 27, 25-51.

Zaïri, F., Gloaguen, J.M., Naït-Abdelaziz, M., Mesbah, A., Lefebvre, J.M., 2011b. Study of the effect of size and clay structural parameters on the yield and post-yield response of polymer/clay nanocomposites via a multiscale micromechanical modelling. Acta Materialia 59, 3851-3863.

Zarrin-Ghalami, T., Fatemi, A., 2013. Multiaxial fatigue and life prediction of elastomeric components. International Journal of Fatigue 55, 92-101.

CHAPTER 2. FATIGUE RESPONSE OF FILLED RUBBERS

2.2. A THERMO-VISCOELASTIC-DAMAGE CONSTITUTIVE MODEL. FORMULATION AND NUMERICAL EXAMPLES[13]

Cyclically loaded rubbers exhibit a complex history-dependent response characterized by fatigue-induced stress-softening and hysteresis along with dissipative heating. The coupling between these different inelastic effects usually appearing together is far from being fully established. In this Part of the *Chapter 2*, we present a new thermo-viscoelastic-damage approach, in accordance with the thermodynamic principles, for the prediction of this set of inelastic fatigue phenomena. An interpretation of the underlying physical mechanisms is proposed in which two types of dissipative network rearrangements are considered, i.e. recoverable rearrangements inducing viscoelasticity and unrecoverable rearrangements inducing damage. The recoverable viscoelastic rearrangements are assumed to be induced by the move of entangled and non-entangled free chains superimposed on a purely elastic perfect rubber network. Each population of free chains is considered to be the main source of one aspect of the history-dependent mechanical cyclic features, i.e. stress-softening and hysteresis, respectively. The thermo-mechanical coupling is defined by postulating the existence of a free energy in which two internal state variables are introduced to account for the two types of dissipative network rearrangements. Network thermal kinetics, induced by the dissipative heating, as well as network damage kinetics, induced by the fatigue damage, are defined and used to alter the cyclically loaded perfect rubber network. The proposed constitutive model is implemented into a finite element program and a parametric study is presented via numerical applications on rubber structures in order to analyze the effects of key model parameters on the rubber inelastic fatigue response. A focus is especially made on the respective influence of temperature, viscoelasticity and damage on the rubber softening.

Keywords: Thermo-viscoelastic-damage coupling; fatigue; dissipative heating; rubbers.

[13] This Part of this Chapter is based on the following paper: Qiang Guo, Fahmi Zaïri, Xinglin Guo, 2018. A thermo-viscoelastic-damage constitutive model for cyclically loaded rubbers. Part I: Model formulation and numerical examples. *International Journal of Plasticity* 101, 106-124.

2.2.1. Partial introduction

Rubbers used in engineering applications are often cyclically loaded and exhibit a complex history-dependent fatigue response characterized by fatigue-induced stress-softening and hysteresis along with dissipative heating. Establishing the coupling between these different inelastic fatigue phenomena, usually appearing together during the cyclic loading history, is an open issue to be addressed.

The physical essence of the fatigue-induced stress-softening is generally attributed to the network degradation, interpreted as an accumulation of the damage effects within the rubber medium (Bouasse and Carrière, 1903; Mullins, 1948; Houwink, 1956; Bueche, 1960; Kraus et al., 1966; Simo, 1987; Govindjee and Simo, 1991; Wineman and Huntley, 1994; Miehe, 1995a; Ogden and Roxburgh, 1999; Drozdov and Dorfmann, 2001; Marckmann et al., 2002; Laiarinandrasana et al., 2003; Chagnon et al., 2004, 2006; Goktepe and Miehe, 2005; Hanson et al., 2005; Dargazany and Itskov, 2009; Ayoub et al., 2011a, 2014; Freund et al., 2011; Lorenz and Kluppel, 2012; Dargazany et al., 2014; Osterlof et al., 2016; Raghunath et al., 2016; Khiem and Itskov, 2017; Makki et al., 2017; Plagge and Kluppel, 2017). Paradoxically, the partial or total recovery in stress-softening gives significance of the viscoelastic effects (Mullins, 1969; Derham and Thomas, 1977; McKenna and Zapas, 1981; Guo et al., 2017). It should be then recognized that the underlying physical process in the fatigue of rubbers is attributed to both unrecoverable damage mechanisms and recoverable viscoelastic mechanisms. In the meantime, cyclically loaded rubbers exhibit an hysteretic response, manifested by a stress difference between loading and unloading paths, and induced by the presence of the viscous stress in the rubber medium which deviates from the purely elastic response. During the fatigue process, a large part of the dissipated mechanical energy due to the hysteretic effect may be converted into heat energy which manifests itself in the form of a change in temperature (Gough, 1805; Medalia, 1991; Meinecke, 1991). The temperature increment generated in the viscoelastic medium may evidently influence in turn the rubber mechanical response due to its thermo-dependence.

A literature survey shows that there exists very few contributions dealing with the thermo-mechanical constitutive modeling of polymers in spite of the significance of the thermo-mechanical coupling (Miehe, 1995b; Holzapfel and Simo, 1996a; Lion, 1997, 2000; Khan et al., 2006; Anand et al., 2009; Ames et al., 2009; Drozdov and Christiansen, 2009; Laiarinandrasana et al., 2009; Kim et al., 2010; Srivastava et al., 2010; Zaïri et al., 2010; Bouvard et al., 2013; Krairi and Doghri, 2014; Lion et al., 2014; Maurel-Pantel et al., 2015;

Ovalle-Rodas et al., 2015a; Garcia-Gonzalez et al., 2017; Yu et al., 2017a, 2017b; Gudimetla and Doghri, 2017). Most of these contributions do not consider the change in temperature due to dissipative heating. The situation is more critical for cyclically loaded rubbers for which the modeling of the thermo-mechanical response has been little investigated to date (Reese and Govindjee, 1998; Boukamel et al., 2001; Meo et al., 2002; Reese, 2003; Ovalle-Rodas et al., 2013, 2014, 2015b, 2016; Dippel et al., 2014; Behnke et al., 2016; Johlitz et al., 2016; Li et al., 2016). In this Part I of the present two-part paper, we propose a thermo-viscoelastic-damage approach, in accordance with the thermodynamic principles, for the prediction of the inelastic fatigue effects in rubbers. The inelastic fatigue phenomena at the macroscopic scale are assumed to be the consequence of two types of network rearrangements, i.e. recoverable viscoelastic mechanisms and unrecoverable damage mechanisms. The move of entangled and non-entangled free chains superimposed on the relaxed network is considered to be the main source of the history-dependent mechanical cyclic features, i.e. stress-softening and hysteresis, respectively. The thermo-mechanical coupling is defined by postulating the existence of a free energy in which two internal state variables are introduced to account for the two types of dissipative network rearrangements. In the thermo-viscoelastic-damage coupling, network thermal kinetics and network damage kinetics are defined and used to alter the relaxed network during the fatigue loading process. In the network alteration, both the average chain length and the average chain density are taken as functions of the temperature and the fatigue damage. The proposed constitutive model is implemented into a finite element code and a parametric study is presented via numerical applications on rubber structures in order to put in light the respective effects of key model parameters on the rubber inelastic fatigue response.

This part is organized as follows. Section 2.2.2 presents the main elements of the constitutive theory. Section 2.2.3 is devoted to numerical examples and the parametric study. Concluding remarks are finally given in Section 2.2.4.

2.2.2. Model formulation

The rubber is constituted by a perfect network and superimposed free chains as illustrated in Figure 2.2.1. The perfect network consists of randomly distributed chains interlinked with cross-links and is responsible to the entropic resistance to deformation. It is recognized that the rubber viscosity is attributed to the slow return of the free chains to a more relaxed configuration when the rubber network is deformed at a high enough rate and then held

constant in the deformed state (de Gennes, 1971; Doi and Edwards, 1986; Bergstrom and Boyce, 1998; Li et al., 2016).

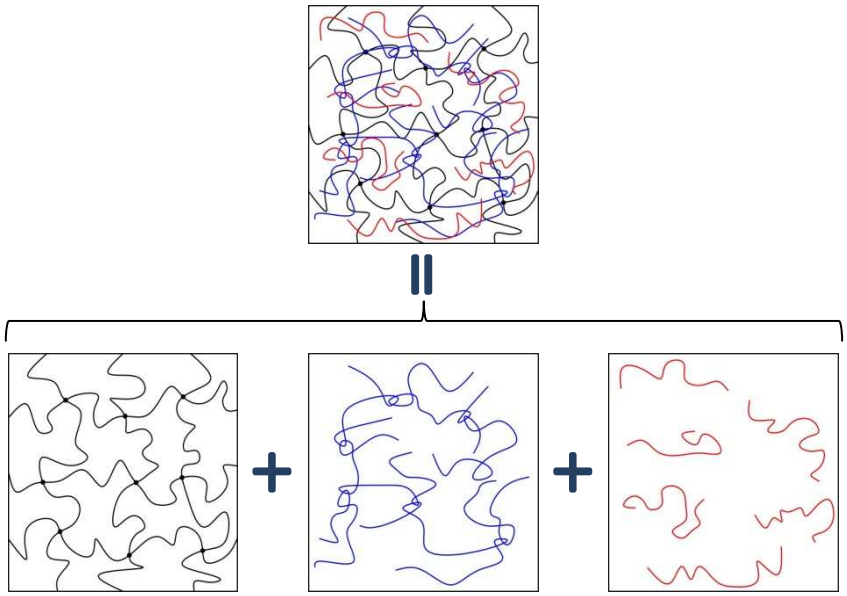

Figure 2.2.1. Decomposition of the rubber network into three superimposed chain populations.

In the present model, the physical origin of the history-dependent cyclic features in rubbers is attributed to the move of both entangled and non-entangled free chains. The distinct mobility degree of these two populations of free chains leads to distinct rates of relaxation, and affects differently the different inelastic fatigue phenomena at the macroscopic scale. The three chain populations are supposed to participate to deformation via the Taylor assumption, i.e. the perfect network alignment is in parallel with the free chains moving.

The following notation is used throughout the text. Tensors and vectors are denoted by normal boldfaced letters and italicized boldfaced letters, respectively, while scalars and individual components of vectors and tensors are denoted by normal italicized letters. The superposed dot designates the time derivative.

2.2.2.1. Kinematics

Before the formulation of the fully three-dimensional constitutive theory, the kinematics is briefly addressed in this subsection. Let us first consider the rubber medium as a homogeneous continuum body with the reference configuration Ω_0 and a current configuration Ω. The mapping of the initial position vector $\boldsymbol{X}$ of a given material point in

the configuration Ω_0 to the current position vector $\boldsymbol{x}=\boldsymbol{\varphi}(\boldsymbol{X},t)$ in the configuration Ω is given by the deformation gradient tensor $\mathbf{F}$:

$$\mathbf{F}=\nabla_X\boldsymbol{\varphi} \tag{2.2.1}$$

The time derivative of the deformation gradient tensor $\mathbf{F}$ is given by:

$$\dot{\mathbf{F}}=\mathbf{L}\mathbf{F} \tag{2.2.2}$$

where $\mathbf{L}$ is the gradient tensor of the spatial velocity $\boldsymbol{v}=\partial\boldsymbol{\varphi}/\partial t$:

$$\mathbf{L}=\nabla_x\boldsymbol{v} \tag{2.2.3}$$

The multiplicative decomposition considers a conceptual sequence of configurations as proposed by several authors (Lee, 1969; Sidoroff, 1974; Lu and Pister, 1975; Miehe, 1995b; Holzapfel and Simo, 1996b; Lion, 1997). The multiplicative decomposition of the deformation gradient $\mathbf{F}$ is schematically illustrated in Figure 2.2.2.

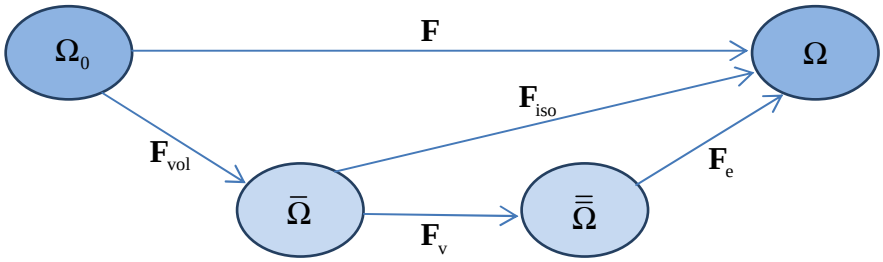

Figure 2.2.2. Multiplicative decomposition of the volumetric-isochoric and elastic-inelastic deformations.

The volumetric-isochoric configuration $\bar{\Omega}$ is related to both the thermal-induced dilatation and the mechanical-induced dilatation of the continuum body. The volumetric-isochoric response is described as the multiplicative decomposition of the deformation gradient tensor into an isochoric part $\mathbf{F}_{\text{iso}}$ and a volumetric part $\mathbf{F}_{\text{vol}}$ as:

$$\mathbf{F}=\mathbf{F}_{\text{iso}}\mathbf{F}_{\text{vol}} \tag{2.2.4}$$

in which the isochoric part $\mathbf{F}_{\text{iso}}$ is given by:

$$\mathbf{F}_{\text{iso}}=J^{-1/3}\mathbf{F} \tag{2.2.5}$$

and the volumetric part $\mathbf{F}_{\text{vol}}$ is expressed, in the isotropic case, by:

$$\mathbf{F}_{\text{vol}}=J^{1/3}\mathbf{I} \tag{2.2.6}$$

in which $\mathbf{I}$ is the unit tensor and $J=\det(\mathbf{F})>0$ denotes the determinant of the deformation gradient tensor $\mathbf{F}$.

The isochoric part $\mathbf{F}_{\text{iso}}$ can be in turn decomposed into stretching and rotation components:

$$\mathbf{F}_{\text{iso}} = \mathbf{V}_{\text{iso}}\mathbf{R}_{\text{iso}} \tag{2.2.7}$$

The corresponding kinematic rate can be additively decomposed as:

$$\mathbf{L} = \mathbf{L}_{\text{iso}} + \mathbf{L}_{\text{vol}} \tag{2.2.8}$$

in which $\mathbf{L}_{\text{iso}}$ is the isochoric part of the spatial velocity gradient tensor $\mathbf{L}$:

$$\mathbf{L}_{\text{iso}} = \dot{\mathbf{F}}_{\text{iso}}\mathbf{F}_{\text{iso}}^{-1} \tag{2.2.9}$$

and $\mathbf{L}_{\text{vol}}$ is the volumetric part of the spatial velocity gradient tensor $\mathbf{L}$:

$$\mathbf{L}_{\text{vol}} = \mathbf{F}_{\text{iso}}\dot{\mathbf{F}}_{\text{vol}}\mathbf{F}_{\text{vol}}^{-1}\mathbf{F}_{\text{iso}}^{-1} = \frac{\dot{J}}{3J}\mathbf{I} \tag{2.2.10}$$

The elastic-inelastic configuration $\bar{\bar{\Omega}}$ is related to the obtained configuration during a spontaneous virtual elastic unloading of the isochoric part which can be written using a multiplicative form and decomposed into an elastic part $\mathbf{F}_{\text{e}}$ and a viscous part $\mathbf{F}_{\text{v}}$:

$$\mathbf{F}_{\text{iso}} = \mathbf{F}_{\text{e}}\mathbf{F}_{\text{v}} \tag{2.2.11}$$

This multiplicative decomposition of the isochoric deformation gradient tensor $\mathbf{F}_{\text{iso}}$ accounts for the viscoelastic damping mechanisms due to the presence of the superimposed entangled and non-entangled free chains. The elastic part $\mathbf{F}_{\text{e}}$ and the viscous part $\mathbf{F}_{\text{v}}$ can be in turn decomposed into stretching and rotation components:

$$\mathbf{F}_{\text{e}} = \mathbf{V}_{\text{e}}\mathbf{R}_{\text{e}} \tag{2.2.12}$$

$$\mathbf{F}_{\text{v}} = \mathbf{V}_{\text{v}}\mathbf{R}_{\text{v}} \tag{2.2.13}$$

The viscous flow is assumed incompressible, i.e. the corresponding determinant J_{v} of the viscous deformation gradient $\mathbf{F}_{\text{v}}$ is:

$$J_{\text{v}} = \det\left(\mathbf{F}_{\text{v}}\right) = 1 \tag{2.2.14}$$

Hence, using Eqs. (2.2.5), (2.2.11) and (2.2.14), the determinant J_{e} of the elastic deformation gradient $\mathbf{F}_{\text{e}}$ is:

$$J_{\text{e}} = \det\left(\mathbf{F}_{\text{e}}\right) = 1 \tag{2.2.15}$$

Introducing the elastic and viscous parts of the corresponding kinematic rates leads to:

$$\mathbf{L}_{\text{iso}} = \mathbf{L}_{\text{e}} + \mathbf{L}_{\text{v}} \tag{2.2.16}$$

in which $\mathbf{L}_{\text{e}}$ is the elastic velocity gradient tensor:

$$\mathbf{L}_{\text{e}} = \dot{\mathbf{F}}_{\text{e}}\mathbf{F}_{\text{e}}^{-1} \tag{2.2.17}$$

and $\mathbf{L}_{\mathrm{v}}$ is the viscous velocity gradient tensor:

$$\mathbf{L}_{\mathrm{v}} = \mathbf{F}_{\mathrm{e}}\dot{\mathbf{F}}_{\mathrm{v}}\mathbf{F}_{\mathrm{v}}^{-1}\mathbf{F}_{\mathrm{e}}^{-1} \tag{2.2.18}$$

The viscous velocity gradient tensor $\mathbf{L}_{\mathrm{v}}$, characterizing constitutively the history-dependent effects induced by the free chains, can be further decomposed into a viscous stretching rate $\mathbf{D}_{\mathrm{v}}$ and a viscous spin rate $\mathbf{W}_{\mathrm{v}}$:

$$\mathbf{L}_{\mathrm{v}} = \mathbf{D}_{\mathrm{v}} + \mathbf{W}_{\mathrm{v}} \tag{2.2.19}$$

where:

$$\mathbf{D}_{\mathrm{v}} = \frac{1}{2}\left(\mathbf{L}_{\mathrm{v}} + \mathbf{L}_{\mathrm{v}}^{\mathrm{T}}\right) \tag{2.2.20}$$

$$\mathbf{W}_{\mathrm{v}} = \frac{1}{2}\left(\mathbf{L}_{\mathrm{v}} - \mathbf{L}_{\mathrm{v}}^{\mathrm{T}}\right) \tag{2.2.21}$$

in which the superscript T indicates the transpose quantity.

During the unloading step, the viscous flow does not change and remains frozen. With no loss in generality, the viscous flow is assumed irrotational and, consequently the viscous spin rate $\mathbf{W}_{\mathrm{v}}$ drops out (Gurtin and Anand, 2005):

$$\mathbf{W}_{\mathrm{v}} = \mathbf{0} \tag{2.2.22}$$

and Eq. (2.2.19) becomes:

$$\mathbf{L}_{\mathrm{v}} = \mathbf{D}_{\mathrm{v}} \tag{2.2.23}$$

In addition, the different contributions of the right and left Cauchy-Green deformation tensors, $\mathbf{C} = \mathbf{F}^{\mathrm{T}}\mathbf{F}$ and $\mathbf{B} = \mathbf{F}\mathbf{F}^{\mathrm{T}}$, are defined in the corresponding configurations:

$$\bar{\mathbf{C}}_{\mathrm{iso}} = \mathbf{F}_{\mathrm{iso}}^{\mathrm{T}}\mathbf{F}_{\mathrm{iso}},\ \mathbf{B}_{\mathrm{iso}} = \mathbf{F}_{\mathrm{iso}}\mathbf{F}_{\mathrm{iso}}^{\mathrm{T}} \tag{2.2.24}$$

$$\mathbf{C}_{\mathrm{vol}} = J^{2/3}\mathbf{I},\ \bar{\mathbf{B}}_{\mathrm{vol}} = J^{2/3}\mathbf{I} \tag{2.2.25}$$

$$\bar{\bar{\mathbf{C}}}_{\mathrm{e}} = \mathbf{F}_{\mathrm{e}}^{\mathrm{T}}\mathbf{F}_{\mathrm{e}},\ \mathbf{B}_{\mathrm{e}} = \mathbf{F}_{\mathrm{e}}\mathbf{F}_{\mathrm{e}}^{\mathrm{T}} \tag{2.2.26}$$

$$\bar{\mathbf{C}}_{\mathrm{v}} = \mathbf{F}_{\mathrm{v}}^{\mathrm{T}}\mathbf{F}_{\mathrm{v}},\ \bar{\bar{\mathbf{B}}}_{\mathrm{v}} = \mathbf{F}_{\mathrm{v}}\mathbf{F}_{\mathrm{v}}^{\mathrm{T}} \tag{2.2.27}$$

2.2.2.2. Stress decomposition

The Cauchy stress $\boldsymbol{\sigma}$ in the rubber medium is additively split into a volumetric part $\boldsymbol{\sigma}_{\mathrm{vol}}$ and an isochoric part $\boldsymbol{\sigma}_{\mathrm{iso}}$ as:

$$\boldsymbol{\sigma} = \boldsymbol{\sigma}_{\mathrm{vol}} + \boldsymbol{\sigma}_{\mathrm{iso}} \tag{2.2.28}$$

The volumetric Cauchy stress $\boldsymbol{\sigma}_{\mathrm{vol}}$ is given by:

$$\boldsymbol{\sigma}_{\text{vol}} = p\mathbf{I} \tag{2.2.29}$$

in which p is the hydrostatic pressure:

$$p = \frac{1}{3}\text{trace}(\boldsymbol{\sigma}) \tag{2.2.30}$$

Hence, the isochoric Cauchy stress $\boldsymbol{\sigma}_{\text{iso}}$ is expressed as:

$$\boldsymbol{\sigma}_{\text{iso}} = \boldsymbol{\sigma} - p\mathbf{I} \tag{2.2.31}$$

In line with our decomposition of the rubber network, the isochoric Cauchy stress $\boldsymbol{\sigma}_{\text{iso}}$ may be additively split into a relaxed part $\boldsymbol{\sigma}_{\text{R}}$ and a viscous part $\boldsymbol{\sigma}_{\text{v}}$:

$$\boldsymbol{\sigma}_{\text{iso}} = \boldsymbol{\sigma}_{\text{R}} + \boldsymbol{\sigma}_{\text{v}} \tag{2.2.32}$$

The relaxed part $\boldsymbol{\sigma}_{\text{R}}$ originates from the entropic resistance to the perfect network alignment, and results in the purely elastic response, whereas the viscous part $\boldsymbol{\sigma}_{\text{v}}$ originates from the history-dependent movements of the free chains and results in the time-dependent deviation from the relaxed state. Because they are related to the isochoric deformation gradient $\mathbf{F}_{\text{iso}}$ and its elastic part $\mathbf{F}_{\text{e}}$ (also being isochoric), the two parts of the isochoric Cauchy stress $\boldsymbol{\sigma}_{\text{iso}}$ can be considered as two traceless tensors:

$$\text{trace}(\boldsymbol{\sigma}_{\text{R}}) = \text{trace}(\boldsymbol{\sigma}_{\text{v}}) = 0 \tag{2.2.33}$$

2.2.2.3. Thermodynamics

According to the basic viewpoint of the continuum thermodynamics, the fatigue process in the rubber medium is an irreversible thermodynamic process accompanied with the internal network rearrangements, and has to satisfy the first and second thermodynamic principles. The second thermodynamic principle restricts the constitutive model via the so-called Clausius-Duhem inequality, written in the reference configuration, as:

$$P - \dot{e} + T\dot{\eta} - \frac{\boldsymbol{q}}{T} \cdot \nabla_X T \geq 0 \tag{2.2.34}$$

in which P is the stress power, e is the specific internal energy per unit volume, η is the specific entropy per unit volume, $\boldsymbol{q}$ is the Piola-Kirchhoff heat flux, T is the absolute temperature and $\nabla_X T$ is the temperature gradient.

The stress power is expressed as:

$$P = \frac{1}{2}\mathbf{S} : \dot{\mathbf{C}} = \boldsymbol{\tau} : \mathbf{L} \tag{2.2.35}$$

in which $\mathbf{S}$ is the second Piola-Kirchhoff stress tensor:

$$\mathbf{S} = \mathbf{F}^{-1}\boldsymbol{\tau}\mathbf{F}^{-\mathrm{T}} \tag{2.2.36}$$

and $\boldsymbol{\tau}$ is the Kirchhoff stress tensor:

$$\boldsymbol{\tau} = J\boldsymbol{\sigma} \tag{2.2.37}$$

The stress power P is additively split into a volumetric part P_{vol} and an isochoric part P_{iso} as:

$$P = P_{\mathrm{vol}} + P_{\mathrm{iso}} \tag{2.2.38}$$

in which the isochoric part P_{iso} is given by:

$$P_{\mathrm{iso}} = \boldsymbol{\tau}_{\mathrm{iso}} : \mathbf{L}_{\mathrm{iso}} \tag{2.2.39}$$

and the volumetric part P_{vol} is given by:

$$P_{\mathrm{vol}} = \boldsymbol{\tau}_{\mathrm{vol}} : \mathbf{L}_{\mathrm{vol}} \tag{2.2.40}$$

The terms $\boldsymbol{\tau}_{\mathrm{vol}}$ and $\boldsymbol{\tau}_{\mathrm{iso}}$ denote the volumetric and isochoric Kirchhoff stresses, respectively:

$$\boldsymbol{\tau}_{\mathrm{vol}} = J\boldsymbol{\sigma}_{\mathrm{vol}} \tag{2.2.41}$$

$$\boldsymbol{\tau}_{\mathrm{iso}} = J\boldsymbol{\sigma}_{\mathrm{iso}} \tag{2.2.42}$$

Using Eqs. (2.2.10), (2.2.29), (2.2.40) and (2.2.41), the volumetric stress power P_{vol} reads:

$$P_{\mathrm{vol}} = p\dot{J} \tag{2.2.43}$$

Considering Eqs. (2.2.16), (2.2.23), (2.2.32) and (2.2.39), it is also possible to obtain, after a series of lengthy but straightforward derivations, the following expression of the isochoric stress power P_{iso}:

$$P_{\mathrm{iso}} = \frac{1}{2}\bar{\mathbf{S}}_{\mathrm{R}} : \dot{\bar{\mathbf{C}}}_{\mathrm{iso}} + \frac{1}{2}\bar{\bar{\mathbf{S}}}_{\mathrm{v}} : \dot{\bar{\bar{\mathbf{C}}}}_{\mathrm{e}} + \boldsymbol{\tau}_{\mathrm{v}} : \mathbf{D}_{\mathrm{v}} \tag{2.2.44}$$

in which the three terms are defined in the volumetric-isochoric configuration $\bar{\Omega}$, the elastic-inelastic configuration $\bar{\bar{\Omega}}$ and the current configuration Ω, respectively.

In the first term of Eq. (2.2.44), $\bar{\mathbf{S}}_{\mathrm{R}}$ is the relaxed second Piola-Kirchhoff stress tensor defined by:

$$\bar{\mathbf{S}}_{\mathrm{R}} = \mathbf{F}_{\mathrm{iso}}^{-1}\boldsymbol{\tau}_{\mathrm{R}}\mathbf{F}_{\mathrm{iso}}^{-\mathrm{T}} \tag{2.2.45}$$

$\boldsymbol{\tau}_{\mathrm{R}}$ being the relaxed Kirchhoff stress tensor:

$$\boldsymbol{\tau}_{\mathrm{R}} = J\boldsymbol{\sigma}_{\mathrm{R}} \tag{2.2.46}$$

In the second term of Eq. (2.2.44), $\bar{\bar{\mathbf{S}}}_{\mathrm{v}}$ is the viscous second Piola-Kirchhoff stress tensor defined by:

$$\bar{\bar{\mathbf{S}}}_{\mathrm{v}} = \mathbf{F}_{\mathrm{e}}^{-1}\boldsymbol{\tau}_{\mathrm{v}}\mathbf{F}_{\mathrm{e}}^{-\mathrm{T}} \tag{2.2.47}$$

$\boldsymbol{\tau}_{\mathrm{v}}$ being the viscous Kirchhoff stress tensor:

$$\boldsymbol{\tau}_{\mathrm{v}} = J\boldsymbol{\sigma}_{\mathrm{v}} \tag{2.2.48}$$

The existence of a free energy potential function is postulated. More specifically, the specific Helmholtz free energy per unit volume is defined by the Legendre transformation $\psi = e - T\eta$. The presented constitutive theory is based on an additive split of the Helmholtz free energy function ψ into two contributions:

$$\psi = \psi_{\mathrm{vol}} + \psi_{\mathrm{iso}} \tag{2.2.49}$$

The volumetric contribution ψ_{vol} is associated with the temperature T and the volumetric effects characterized by the determinant J which considers both the thermal-induced dilatation and the mechanical-induced dilatation[14]:

$$\psi_{\mathrm{vol}} = \hat{\psi}_{\mathrm{vol}}\left(T, J\right) \tag{2.2.50}$$

The isochoric contribution ψ_{iso} is additively split into a relaxed part ψ_{R} and a viscous part ψ_{v}:

$$\psi_{\mathrm{iso}} = \psi_{\mathrm{R}} + \psi_{\mathrm{v}} \tag{2.2.51}$$

in which the two parts ψ_{R} and ψ_{v} are related to the energy storages in the perfect network and the free chains due to the corresponding configuration transformation, respectively.

As an irreversible thermodynamic process that involves dissipation, it is well known that the thermodynamic state during the fatigue process cannot be adequately described by only the current deformation and temperature, since the current thermodynamic state heavily depends on the thermo-mechanical history that the rubber experienced. In order to solve this problem, the internal state variable theory is further developed and applied to the inelastic process modeling of cyclically loaded rubbers. The basic idea behind this theory is that the thermodynamics state of the material is defined by expanding the dimensions of the state space of deformation and temperature, referred to as external state variables due to their measurability and controllability, by adding state variables describing the microstructure changes and associated with the dissipative effects, referred to as internal state variables (Horstemeyer and Bammann, 2010). Thus, the relaxed free energy ψ_{R} and the viscous free energy ψ_{v} are assumed to depend on a number of independent state variables:

[14] The mechanical-induced dilatation considers only the bulk modulus effect and the cavitational-induced volumetric effects (Aït Hocine et al., 2011; Zaïri et al., 2008, 2011), which can interact with the other inelastic fatigue effects, are not considered.

$$\psi_{\mathrm{R}} = \hat{\psi}_{\mathrm{R}}\left(T, \overline{\mathbf{C}}_{\mathrm{iso}}, \chi\right) \tag{2.2.52}$$

$$\psi_{\mathrm{v}} = \hat{\psi}_{\mathrm{v}}\left(T, \overline{\overline{\mathbf{C}}}_{\mathrm{e}}\right) \tag{2.2.53}$$

where χ is an internal state variable introduced to account for the unrecoverable network rearrangements occurring in the perfect network and inducing the fatigue damage, and $\overline{\overline{\mathbf{C}}}_{\mathrm{e}}$ may be considered as another internal state variable introduced to account for the viscoelastic damping mechanisms due to the presence of the superimposed (entangled and non-entangled) free chains.

By inserting the time derivative of the internal energy:

$$\dot{e} = \dot{\psi} + \dot{T}\eta + T\dot{\eta} \tag{2.2.54}$$

with:

$$\dot{\psi} = \frac{\partial \hat{\psi}_{\mathrm{vol}}}{\partial T}\dot{T} + \frac{\partial \hat{\psi}_{\mathrm{vol}}}{\partial J}\dot{J} + \frac{\partial \hat{\psi}_{\mathrm{R}}}{\partial T}\dot{T} + \frac{\partial \hat{\psi}_{\mathrm{R}}}{\partial \overline{\mathbf{C}}_{\mathrm{iso}}} : \dot{\overline{\mathbf{C}}}_{\mathrm{iso}} + \frac{\partial \hat{\psi}_{\mathrm{v}}}{\partial T}\dot{T} + \frac{\hat{\psi}_{\mathrm{v}}}{\partial \overline{\overline{\mathbf{C}}}_{\mathrm{e}}} : \dot{\overline{\overline{\mathbf{C}}}}_{\mathrm{e}} + \frac{\partial \hat{\psi}_{\mathrm{R}}}{\partial \chi}\dot{\chi} \tag{2.2.55}$$

into Eq. (2.2.34), it leads to:

$$\begin{aligned} &\left(p - \frac{\partial \hat{\psi}_{\mathrm{vol}}}{\partial J}\right)\dot{J} + \left(\frac{1}{2}\overline{\mathbf{S}}_{\mathrm{R}} - \frac{\partial \hat{\psi}_{\mathrm{R}}}{\partial \overline{\mathbf{C}}_{\mathrm{iso}}}\right) : \dot{\overline{\mathbf{C}}}_{\mathrm{iso}} + \left(\frac{1}{2}\overline{\overline{\mathbf{S}}}_{\mathrm{v}} - \frac{\hat{\psi}_{\mathrm{v}}}{\partial \overline{\overline{\mathbf{C}}}_{\mathrm{e}}}\right) : \dot{\overline{\overline{\mathbf{C}}}}_{\mathrm{e}} \\ &-\left(\frac{\partial \hat{\psi}_{\mathrm{vol}}}{\partial T} + \frac{\partial \hat{\psi}_{\mathrm{R}}}{\partial T} + \frac{\partial \hat{\psi}_{\mathrm{v}}}{\partial T} + \eta\right)\dot{T} + \boldsymbol{\tau}_{\mathrm{v}} : \mathbf{D}_{\mathrm{v}} - \frac{\partial \hat{\psi}_{\mathrm{R}}}{\partial \chi}\dot{\chi} - \frac{\boldsymbol{q}}{T}\cdot\nabla_X T \geq 0 \end{aligned} \tag{2.2.56}$$

In order to satisfy the inequality (2.2.56) for arbitrary variations of temperature and deformation, the usual Coleman-Noll procedure (Coleman and Noll, 1963) is used. From the first three terms of the inequality (2.2.56), the following potential relations, depending on the earlier defined independent state variables, are derived:

$$p = \hat{p}\left(T, J\right) = \frac{\partial \hat{\psi}_{\mathrm{vol}}\left(T, J\right)}{\partial J} \tag{2.2.57}$$

$$\overline{\mathbf{S}}_{\mathrm{R}} = \hat{\overline{\mathbf{S}}}_{\mathrm{R}}\left(T, \overline{\mathbf{C}}_{\mathrm{iso}}, \chi\right) = 2\frac{\partial \hat{\psi}_{\mathrm{R}}\left(T, \overline{\mathbf{C}}_{\mathrm{iso}}, \chi\right)}{\partial \overline{\mathbf{C}}_{\mathrm{iso}}} \tag{2.2.58}$$

$$\overline{\overline{\mathbf{S}}}_{\mathrm{v}} = \hat{\overline{\overline{\mathbf{S}}}}_{\mathrm{v}}\left(T, \overline{\overline{\mathbf{C}}}_{\mathrm{e}}\right) = 2\frac{\hat{\psi}_{\mathrm{v}}\left(T, \overline{\overline{\mathbf{C}}}_{\mathrm{e}}\right)}{\partial \overline{\overline{\mathbf{C}}}_{\mathrm{e}}} \tag{2.2.59}$$

The fourth term of the inequality (2.2.56) leads to:

$$\eta = \eta_{\mathrm{vol}} + \eta_{\mathrm{R}} + \eta_{\mathrm{v}} \tag{2.2.60}$$

in which η_{vol}, η_{R} and η_{v} are the volumetric, relaxed and viscous parts of the entropy η, respectively, which depend on the earlier defined independent state variables:

$$\eta_{\mathrm{vol}} = \hat{\eta}_{\mathrm{vol}}\left(T, J\right) = -\frac{\partial \hat{\psi}_{\mathrm{vol}}\left(T, J\right)}{\partial T} \tag{2.2.61}$$

$$\eta_{\mathrm{R}} = \hat{\eta}_{\mathrm{R}}\left(T, \bar{\mathbf{C}}_{\mathrm{iso}}, \chi\right) = -\frac{\partial \hat{\psi}_{\mathrm{R}}\left(T, \bar{\mathbf{C}}_{\mathrm{iso}}, \chi\right)}{\partial T} \tag{2.2.62}$$

$$\eta_{\mathrm{v}} = \hat{\eta}_{\mathrm{v}}\left(T, \bar{\bar{\mathbf{C}}}_{\mathrm{e}}\right) = -\frac{\partial \hat{\psi}_{\mathrm{v}}\left(T, \bar{\bar{\mathbf{C}}}_{\mathrm{e}}\right)}{\partial T} \tag{2.2.63}$$

The remainder of the inequality (2.2.56) leads the following inequality for the dissipation Φ:

$$\Phi = \boldsymbol{\tau}_{\mathrm{v}} : \mathbf{D}_{\mathrm{v}} + \kappa\dot{\chi} - \frac{1}{T}\mathbf{q}\cdot\nabla_X T \geq 0 \tag{2.2.64}$$

in which κ denotes the thermodynamic conjugate quantity for χ:

$$\kappa = \hat{\kappa}\left(T, \bar{\mathbf{C}}_{\mathrm{iso}}, \chi\right) = -\frac{\partial \hat{\psi}_{\mathrm{R}}\left(T, \bar{\mathbf{C}}_{\mathrm{iso}}, \chi\right)}{\partial \chi} \tag{2.2.65}$$

In Eq. (2.2.64), the quantity:

$$\Phi_1 = \boldsymbol{\tau}_{\mathrm{v}} : \mathbf{D}_{\mathrm{v}} + \kappa\dot{\chi} \tag{2.2.66}$$

corresponds to the intrinsic dissipation, induced by the irreversible energy conversion, in which the term $\boldsymbol{\tau}_{\mathrm{v}} : \mathbf{D}_{\mathrm{v}}$ is the dissipation related to the viscoelastic material response, while the term $\kappa\dot{\chi}$ is the internal work related to the damage-induced unrecoverable network rearrangement.

In Eq. (2.2.64), the quantity:

$$\Phi_2 = -\frac{\boldsymbol{q}}{T}\cdot\nabla_X T \tag{2.2.67}$$

corresponds to the thermal dissipation, induced by the irreversible energy flow, in which the Piola-Kirchhoff heat flux $\boldsymbol{q}$ is given by the Fourier law:

$$\boldsymbol{q} = -\mathbf{K}_X \cdot \nabla_X T \tag{2.2.68}$$

where:

$$\mathbf{K}_X = \mathbf{F}^{-1}\mathbf{K}\mathbf{F}^{-\mathrm{T}} \tag{2.2.69}$$

is the conductivity tensor in the reference configuration, $\mathbf{K}$ being the Eulerian conductivity tensor. In the isotropic case, the tensor $\mathbf{K}$ reduces to:

$$\mathbf{K} = k_{\mathrm{T}}\mathbf{I} \tag{2.2.70}$$

where k_{T} is the coefficient of thermal conductivity.

The intrinsic dissipation Φ_1 and the thermal dissipation Φ_2 are assumed to satisfy the inequality condition separately, i.e. $\Phi_1 \geq 0$ and $\Phi_2 \geq 0$. Furthermore, the first law of thermodynamics requires the following energy balance equation to be satisfied:

$$\dot{e} = P - \mathrm{Div}\boldsymbol{q} \tag{2.2.71}$$

Introducing Eqs. (2.2.35) and (2.2.54) into Eq. (2.2.71) and taking into account the constitutive relationships (2.2.57) to (2.2.63) with the chain rules of differentiation, we get:

$$C_\mathrm{T}\dot{T} = \Phi_1 - \mathrm{Div}\boldsymbol{q} + \hbar \tag{2.2.72}$$

where C_T is a heat capacity-related coefficient[15]:

$$C_\mathrm{T} = T\left(\frac{\partial \hat{\eta}_\mathrm{vol}}{\partial T} + \frac{\partial \hat{\eta}_\mathrm{R}}{\partial T} + \frac{\partial \hat{\eta}_\mathrm{v}}{\partial T}\right) \tag{2.2.73}$$

and $\hbar$ is a thermo-visoelastic-damage coupling coefficient:

$$\hbar = T\left(\frac{\partial \hat{p}}{\partial T}\dot{J} + \frac{1}{2}\frac{\partial \hat{\bar{\mathbf{S}}}_\mathrm{R}}{\partial T} : \dot{\bar{\mathbf{C}}}_\mathrm{iso} + \frac{1}{2}\frac{\partial \hat{\bar{\bar{\mathbf{S}}}}_\mathrm{v}}{\partial T} : \bar{\bar{\mathbf{C}}}_\mathrm{e} - \frac{\partial \hat{\kappa}}{\partial T}\dot{\kappa}\right) \tag{2.2.74}$$

2.2.2.4. Constitutive equations

2.2.2.4.1. Free energy functions

In order to take into consideration the rubber network properties, the relaxed free energy function is given by the Arruda and Boyce (1993) formulation based on the eight-chain network of non-Gaussian chains:

$$\psi_\mathrm{R} = \hat{\psi}_\mathrm{R}\left(T, \bar{\mathbf{C}}_\mathrm{iso}, \chi\right) = n_\mathrm{R} k_\mathrm{B} T N_\mathrm{R}\left(\zeta_\mathrm{iso}\frac{\lambda_\mathrm{iso}}{\sqrt{N_\mathrm{R}}} + \ln\frac{\zeta_\mathrm{iso}}{\sinh\zeta_\mathrm{iso}}\right) \tag{2.2.75}$$

In Eq. (2.2.75), n_R and N_R are the average number of chains in the perfect network per unit volume (i.e. average chain density) and the average number of segments in the chain (i.e. average chain length), which are consider to dependent on the temperature T and the fatigue damage χ (as described in the subsection 2.2.2.4.3), k_B is the Boltzmann's constant, λ_iso is

[15] Note that by considering Eqs. (2.2.91), (2.2.92), (2.2.93), and the selected parameters (see Section 2.2.3), $\partial\hat{\eta}_\mathrm{R}/\partial T << C_{\mathrm{T}0}/T$ and $\partial\hat{\eta}_\mathrm{v}/\partial T = 0$, such that $C_\mathrm{T} \approx T\,\partial\hat{\eta}_\mathrm{vol}/\partial T = C_{\mathrm{T}0}$, the constant $C_{\mathrm{T}0}$ being the specific heat capacity at constant deformation.

the average stretch on each chain in the network:

$$\lambda_{\text{iso}} = \sqrt{\frac{1}{3}\text{tr}\left(\bar{\mathbf{C}}_{\text{iso}}\right)} \tag{2.2.76}$$

and ζ_{iso} is the inverse of the Langevin function:

$$\mathcal{L}\left(\zeta_{\text{iso}}\right) = \coth\left(\zeta_{\text{iso}}\right) - \frac{1}{\zeta_{\text{iso}}} = \frac{\lambda_{\text{iso}}}{\sqrt{N_{\text{R}}}} \tag{2.2.77}$$

which is approximated by its Padé approximation (Cohen, 1991):

$$\zeta_{\text{iso}} = \mathcal{L}^{-1}\left(\frac{\lambda_{\text{iso}}}{\sqrt{N_{\text{R}}}}\right) \approx \frac{\lambda_{\text{iso}}}{\sqrt{N_{\text{R}}}}\frac{3N_{\text{R}} - \lambda_{\text{iso}}^2}{N_{\text{R}} - \lambda_{\text{iso}}^2} \tag{2.2.78}$$

The viscous free energy function is also expressed using the Arruda and Boyce (1993) formulation:

$$\psi_{\text{v}} = \hat{\psi}_{\text{v}}\left(T, \bar{\bar{\mathbf{C}}}_{\text{e}}\right) = n_{\text{v}} k_{\text{B}} T N_{\text{v}}\left(\zeta_{\text{v}}\frac{\lambda_{\text{e}}}{\sqrt{N_{\text{v}}}} + \ln\frac{\zeta_{\text{v}}}{\sinh\zeta_{\text{v}}}\right) \tag{2.2.79}$$

The terms n_{v} and N_{v} are the viscous material constants, corresponding to the average number of free chains superimposed on the perfect network per unit volume and the average number of segments in the free chain, respectively, the term λ_{e} is the elastic stretch expressed as:

$$\lambda_{\text{e}} = \sqrt{\frac{1}{3}\text{tr}\left(\bar{\bar{\mathbf{C}}}_{\text{e}}\right)} \tag{2.2.80}$$

and ζ_{v} is given by the inverse Langevin function:

$$\zeta_{\text{v}} = \mathcal{L}^{-1}\left(\frac{\lambda_{\text{e}}}{\sqrt{N_{\text{v}}}}\right) = \frac{\lambda_{\text{e}}}{\sqrt{N_{\text{v}}}}\frac{3N_{\text{v}} - \lambda_{\text{e}}^2}{N_{\text{v}} - \lambda_{\text{e}}^2} \tag{2.2.81}$$

The volumetric free energy function is the sum of three contributions (Miehe, 1995b; Holzapfel and Simo, 1996b):

$$\begin{aligned}\psi_{\text{vol}} = \hat{\psi}_{\text{vol}}\left(T, J\right) = {} & \frac{1}{4}k\left(J^2 - 1 - 2\ln J\right) + C_{\text{T0}}\left[\left(T - T_0\right) - T\ln\left(\frac{T}{T_0}\right)\right] \\ & - 3\alpha k\left(J - 1\right)\left(T - T_0\right)\end{aligned} \tag{2.2.82}$$

in which the first term corresponds to the purely volumetric contribution, the second term is the purely thermal contribution and the third term is an energetic contribution due to the thermal-volumetric coupling. The constants k, α and C_{T0} are the bulk modulus, the thermal

dilatation coefficient and the specific heat capacity at constant deformation, respectively, and T_0 is the reference temperature.

2.2.2.4.2. Temperature and damage-induced network rearrangements

The thermo-mechanical response in cyclically loaded rubbers results from network rearrangements modifying the original network to another one at each new cycle. The damage-induced network rearrangements, accompanied by diverse breakdown of bonds, may be introduced into the model formulation by considering both the average chain length and the average chain density as functions of the internal state variable χ. In the same manner, due to its thermo-dependence, the rubber network may be also modified if the dissipative heating reaches a high level. The temperature and damage effects are introduced into the chain-scale material constants of the perfect network through the following general kinetics:

$$N_{\mathrm{R}}\left(T,\chi\right)=N_{\mathrm{R0}}+N_{\mathrm{R}T}\left(T\right)+N_{\mathrm{R}\chi}\left(\chi\right) \tag{2.2.83}$$

which is restricted by the mass conservation law, such that the total number of segments per unit volume remains constant:

$$n_{\mathrm{R}}\left(T,\chi\right)=\frac{n_{\mathrm{R0}}N_{\mathrm{R0}}}{N_{\mathrm{R}}\left(T,\chi\right)} \tag{2.2.84}$$

where n_{R0} and N_{R0} are the reference values, $N_{\mathrm{R}T}\left(T\right)$ is the network thermal kinetics and $N_{\mathrm{R}\chi}\left(\chi\right)$ is the network damage kinetics.

In our previous work (Ovalle-Rodas et al., 2015a), the temperature dependence of the relaxed stress-strain relation of filled rubbers was emphasized and an experimentally-based linear evolution of the network thermal kinetics $N_{\mathrm{R}T}\left(T\right)$ was designed[16]:

$$N_{\mathrm{R}T}\left(T\right)=N_{,T}\left(T-T_0\right) \tag{2.2.85}$$

where $N_{,T}$ is a temperature-rate sensitivity coefficient.

The internal state variable χ is incorporated in a phenomenological way, in order to represent the damage-induced stress-softening macroscopically observed in rubbers, by using the following network damage kinetics $N_{\mathrm{R}\chi}\left(\chi\right)$:

$$N_{\mathrm{R}\chi}\left(\chi\right)=N_{\mathrm{R0}}\chi \tag{2.2.86}$$

[16] The mobility enhancement of the free chains at higher temperatures merited to be considered in future works.

with $\chi_0 = \chi\big|_{t=t_0} = 0$.

2.2.2.4.3. Constitutive relationships

The volumetric, relaxed and viscous Cauchy stresses are obtained from the differentiation of the free energy functions with respect to the corresponding deformations. The details of the derivation are provided in Appendix A. The Cauchy stresses are given by the following set of constitutive equations:

$$\boldsymbol{\sigma}_{\mathrm{vol}} = \left[\frac{1}{2J}k\left(J^2-1\right)-3\alpha k\left(T-T_0\right)\right]\mathbf{I} \tag{2.2.87}$$

$$\boldsymbol{\sigma}_{\mathrm{R}} = \frac{n_{\mathrm{R}}k_{\mathrm{B}}T}{3J}\frac{\sqrt{N_{\mathrm{R}}}}{\lambda_{\mathrm{iso}}}\zeta_{\mathrm{iso}}\left(\mathbf{B}_{\mathrm{iso}}-\left(\lambda_{\mathrm{iso}}\right)^2\mathbf{I}\right) \tag{2.2.88}$$

$$\boldsymbol{\sigma}_{\mathrm{v}} = \frac{n_{\mathrm{v}}k_{\mathrm{B}}T}{3J}\frac{\sqrt{N_{\mathrm{v}}}}{\lambda_{\mathrm{e}}}\zeta_{\mathrm{v}}\left(\mathbf{B}_{\mathrm{e}}-\left(\lambda_{\mathrm{e}}\right)^2\mathbf{I}\right) \tag{2.2.89}$$

According to Eq. (2.2.65), the thermodynamic conjugate quantity κ for the internal state variable χ takes the following specific expression:

$$\kappa = \frac{1}{2}n_{\mathrm{R}}k_{\mathrm{B}}TN_{\mathrm{R0}}\zeta_{\mathrm{iso}}\frac{\lambda_{\mathrm{iso}}}{\sqrt{N_{\mathrm{R}}}} \tag{2.2.90}$$

Using Eqs. (2.2.61), (2.2.62) and (2.2.63), the volumetric, relaxed and viscous parts of the entropy η are, respectively, expressed as follows:

$$\eta_{\mathrm{vol}} = C_{\mathrm{T0}}\ln\left(\frac{T}{T_0}\right)+3\alpha k\left(J-1\right) \tag{2.2.91}$$

$$\eta_{\mathrm{R}} = -n_{\mathrm{R}}k_{\mathrm{B}}N_{\mathrm{R}}\left(\zeta_{\mathrm{iso}}\frac{\lambda_{\mathrm{iso}}}{\sqrt{N_{\mathrm{R}}}}\left(1-\frac{TN_{,T}}{2N_{\mathrm{R}}}\right)+\ln\frac{\zeta_{\mathrm{iso}}}{\sinh\zeta_{\mathrm{iso}}}\right) \tag{2.2.92}$$

$$\eta_{\mathrm{v}} = -n_{\mathrm{v}}k_{\mathrm{B}}N_{\mathrm{v}}\left(\zeta_{\mathrm{v}}\frac{\lambda_{\mathrm{e}}}{\sqrt{N_{\mathrm{v}}}}+\ln\frac{\zeta_{\mathrm{v}}}{\sinh\zeta_{\mathrm{v}}}\right) \tag{2.2.93}$$

2.2.2.4.4. Flow rules

The internal state variables $\bar{\bar{\mathbf{C}}}_{\mathrm{e}}$ and χ are introduced to characterize the history-dependent effects of the cyclically loaded rubbers. To complete the constitutive description, the evolutions of these internal state variables during the fatigue process must be constitutively specified.

The viscous stretching rate $\mathbf{D}_{\mathrm{v}}$, related to the recoverable viscoelastic rearrangements of the superimposed entangled and non-entangled free chains, are defined by the following general flow rule:

$$\mathbf{D}_{\mathrm{v}} = \dot{\gamma}_{\mathrm{v}} \mathbf{N}_{\mathrm{v}} \tag{2.2.94}$$

in which $\dot{\gamma}_{\mathrm{v}}$ is the accumulated viscous strain rate and $\mathbf{N}_{\mathrm{v}}$ is the direction tensor of viscous flow. Noting that $\mathbf{D}_{\mathrm{v}}$ is defined in the current configuration Ω, the viscous flow direction tensor $\mathbf{N}_{\mathrm{v}}$ is aligned with the viscous Kirchhoff stress tensor $\boldsymbol{\tau}_{\mathrm{v}}$:

$$\mathbf{N}_{\mathrm{v}} = \frac{\boldsymbol{\tau}_{\mathrm{v}}}{\left\|\boldsymbol{\tau}_{\mathrm{v}}\right\|} \tag{2.2.95}$$

where $\left\|\boldsymbol{\tau}_{\mathrm{v}}\right\| = \sqrt{\mathrm{tr}\left(\boldsymbol{\tau}_{\mathrm{v}} \boldsymbol{\tau}_{\mathrm{v}}^{\mathrm{T}}\right)}$ is the effective viscous Kirchhoff stress by the Frobenius norm.

By analogy between viscoplasticity and viscoelasticity, the accumulated viscous strain rate $\dot{\gamma}_{\mathrm{v}}$ may be expressed as a function of the effective viscous Kirchhoff stress $\left\|\boldsymbol{\tau}_{\mathrm{v}}\right\|$ using the viscoplasticity theory but without yield surface such that the elastic and inelastic strain rates are non-zero at all stages of loading (Zaïri et al., 2005, 2007):

$$\dot{\gamma}_{\mathrm{v}} = \hat{\dot{\gamma}}_{\mathrm{v}}\left(\left\|\boldsymbol{\tau}_{\mathrm{v}}\right\|\right) \tag{2.2.96}$$

The mechanism responsible for the recoverable viscoelastic rearrangements is the move of free chains that have lower resistance to deformation than the relaxed (perfect) network and have the capability to significantly change conformation by Brownian motion in a combination of reptation motion, as described by Doi and Edwards (1986). More precisely, if the rubber network is stretched at a high enough rate, both free chains and perfect network move affinely. Then, the free chains tend to slowly return to a more relaxed configuration, if the stretch is held constant. The Doi-Edwards tube concept (Doi and Edwards, 1986), considered to be the most successful theory in polymer physics from the past thirty years, assumes that the lateral motion of individual free chains is restricted within a tube-like region due to chains from its neighborhood. Thus, instead of moving randomly in space, an individual free chain can only move back and forth, or reptate, along the centerline of its tube by reptational Brownian motion.

The accumulated viscous strain rate $\dot{\gamma}_{\mathrm{v}}$ takes the form of the Bergstrom-Boyce power law (Bergstrom and Boyce, 1998):

$$\dot{\gamma}_{\mathrm{v}} = r\left|\lambda_{\mathrm{v}} - 1\right|^{d} \left\|\boldsymbol{\tau}_{\mathrm{v}}\right\|^{m} \tag{2.2.97}$$

where r is a positive viscous multiplier parameter, d and m are viscous power parameters, and λ_{v} is the viscous stretch:

$$\lambda_{\mathrm{v}}=\sqrt{\frac{1}{3}\mathrm{tr}\left(\bar{\bar{\mathbf{B}}}_{\mathrm{v}}\right)} \tag{2.2.98}$$

The term $\left|\lambda_{\mathrm{v}}-1\right|^{d}$ is motivated by reptational dynamics to capture the stretch-dependency of the effective viscosity, and the term $\left\|\boldsymbol{\tau}_{\mathrm{v}}\right\|^{m}$ is another key component to capture the nonlinear history-dependent effect which is introduced by considering the reptational Brownian motion of free chains as energy activated.

In our network decomposition, the free chains are superimposed on the perfect network, i.e. the three networks act in parallel and without interaction. The constitutive relationship for each network is then deduced independently - see Eqs. (2.2.84) and (2.2.85) - and the intrinsic dissipation Φ_1 is the sum of the viscoelastic dissipation $\boldsymbol{\tau}_{\mathrm{v}}:\mathbf{D}_{\mathrm{v}}$ induced by the move of the free chains and the damage-related internal work $\kappa\dot{\chi}$ occurring in the perfect network - see Eq. (2.2.66). However, the objectively existing interaction between the networks should not be ignored in the formulation of the thermo-viscoelastic-damage constitutive model. To this end, it is assumed that the internal work $\kappa\dot{\chi}$ is proportional to the viscoelastic dissipation $\boldsymbol{\tau}_{\mathrm{v}}:\mathbf{D}_{\mathrm{v}}$ according to the following relationship:

$$\kappa\dot{\chi}=\left(\beta-1\right)\boldsymbol{\tau}_{\mathrm{v}}:\mathbf{D}_{\mathrm{v}} \tag{2.2.99}$$

where β is a non-negative proportionality coefficient and the viscoelastic dissipation term $\boldsymbol{\tau}_{\mathrm{v}}:\mathbf{D}_{\mathrm{v}}$ becomes using the flow rule (2.2.94):

$$\boldsymbol{\tau}_{\mathrm{v}}:\mathbf{D}_{\mathrm{v}}=r\left|\lambda_{\mathrm{v}}-1\right|^{d}\left\|\boldsymbol{\tau}_{\mathrm{v}}\right\|^{m+1} \tag{2.2.100}$$

Then, the intrinsic dissipation Φ_1 can be rewritten as:

$$\Phi_1=\beta r\left|\lambda_{\mathrm{v}}-1\right|^{d}\left\|\boldsymbol{\tau}_{\mathrm{v}}\right\|^{m+1}\geq 0 \tag{2.2.101}$$

which satisfies the thermodynamics consistency.

Combining Eqs. (2.2.93), (2.2.99) and (2.2.100), the following equation is obtained for the evolution of the internal state variable χ:

$$\dot{\chi}=\frac{2\left(\beta-1\right)r\left|\lambda_{\mathrm{v}}-1\right|^{d}\left\|\boldsymbol{\tau}_{\mathrm{v}}\right\|^{m+1}\sqrt{N_{\mathrm{R}}}}{n_{\mathrm{R}}k_{\mathrm{B}}TN_{\mathrm{R0}}\zeta_{\mathrm{iso}}\lambda_{\mathrm{iso}}} \tag{2.2.102}$$

Note that if the proportionality coefficient β is superior to unity ($\beta>1$), the internal work $\kappa\dot{\chi}$ is positive ($\kappa\dot{\chi}>0$) and the internal variable rate $\dot{\chi}$ is then also positive ($\dot{\chi}>0$). In this

condition, the free energy is dissipated resulting to a softening. If the proportionality coefficient β is lesser than unity ($0 \le \beta < 1$), these quantities $\kappa\dot{\chi}$ and $\dot{\chi}$ become negative ($\kappa\dot{\chi} < 0$ and $\dot{\chi} < 0$) which means that the internal work is stored resulting to a stiffening[17]. In the specific case where the proportionality coefficient β is null ($\beta = 0$), the cyclic loading process metamorphoses into a reversible thermodynamic process without any energy dissipation. Otherwise, if the proportionality coefficient β is equal to unity ($\beta = 1$), the viscoelastic dissipation is fully transformed into heat energy without internal work and network damage kinetics. Furthermore, from the viewpoint of thermodynamics, the cyclically loaded rubber actually carries out two synchronous irreversible thermodynamic processes, that are, the recoverable viscoelastic rearrangements of the free chains and the unrecoverable rearrangements of the perfect network inducing damage. Accordingly, the two generalized thermodynamic fluxes, $\mathbf{D}_v$ and $\dot{\chi}$, are driven jointly by the two generalized thermodynamic forces $\boldsymbol{\tau}_v$ and κ, reflecting the complex coupling between the two physical mechanisms. The proportionality coefficient β may be regarded as a parameter quantifying the coupling effect.

2.2.2.4.5. Three-network decomposition

As described earlier in Figure 2.2.1, the rubber network is decomposed into three parallel networks: a perfect (relaxed) network constituted by cross-linked chains on which entangled and non- entangled free chains are superimposed. The perfect network is the source of the purely elastic response, governed by the relaxed Cauchy stress $\boldsymbol{\sigma}_R$, and the free chains are the source of the history-dependent effects, governed by the viscous Cauchy stress $\boldsymbol{\sigma}_v$ which is in turn additively decomposed into two distinct contributions dedicated to the two populations of free chains:

$$\boldsymbol{\sigma}_v = \boldsymbol{\sigma}_{v\_1} + \boldsymbol{\sigma}_{v\_2} \tag{2.2.103}$$

where $\boldsymbol{\sigma}_{v\_1}$ is the viscous Cauchy stress of the entangled free chains to which we confer the subscript 1 and $\boldsymbol{\sigma}_{v\_2}$ is the viscous Cauchy stress of the non-entangled free chains to which we confer the subscript 2. This notation will be used in the whole paper. The viscous Cauchy stresses of the entangled and non-entangled free chains are given, respectively, by:

[17] The softening may be associated to damage effects whereas the stiffening may be associated to the formation of ordered crystalline regions whose the stiffening effects are amplified if they initiate and develop in a rubbery medium (Ayoub et al., 2010, 2011b; Hachour et al., 2014).

$$\boldsymbol{\sigma}_{\mathrm{v\_1}}=\frac{n_{\mathrm{v\_1}}k_{\mathrm{B}}T}{3J}\frac{\sqrt{N_{\mathrm{v\_1}}}}{\lambda_{\mathrm{e\_1}}}\zeta_{\mathrm{v\_1}}\left(\mathbf{B}_{\mathrm{e\_1}}-\left(\lambda_{\mathrm{e\_1}}\right)^2\mathbf{I}\right) \tag{2.2.104}$$

$$\boldsymbol{\sigma}_{\mathrm{v\_2}}=\frac{n_{\mathrm{v\_2}}k_{\mathrm{B}}T}{3J}\frac{\sqrt{N_{\mathrm{v\_2}}}}{\lambda_{\mathrm{e\_2}}}\zeta_{\mathrm{v\_2}}\left(\mathbf{B}_{\mathrm{e\_2}}-\left(\lambda_{\mathrm{e\_2}}\right)^2\mathbf{I}\right) \tag{2.2.105}$$

where $n_{\mathrm{v\_1}}$, $N_{\mathrm{v\_1}}$, $n_{\mathrm{v\_2}}$ and $N_{\mathrm{v\_2}}$ are the corresponding viscous parameters of the free chains.

The non-entangled free chains have higher capability to change conformation by reptational Brownian motion than the entangled free chains. According to the Doi-Edwards tube concept (Doi and Edwards, 1986), the entanglements can effectively restrict the lateral motion of an individual free chain into the tube (Li et al., 2016). In other words, the higher the chain entanglement degree, the smaller the tube diameter and the lower the mobility of free chains. Thus, compared to the non-entangled free chains, the entangled free chains have a lower viscous strain rate and take a longer time to return to a more relaxed configuration. That may be taken into account by considering distinct rates of relaxation between the two populations of free chains:

$$\dot{\gamma}_{\mathrm{v\_1}}=r_1\left|\lambda_{\mathrm{v\_1}}-1\right|^d\left\|\boldsymbol{\tau}_{\mathrm{v\_1}}\right\|^m \tag{2.2.106}$$

$$\dot{\gamma}_{\mathrm{v\_2}}=r_2\left|\lambda_{\mathrm{v\_2}}-1\right|^d\left\|\boldsymbol{\tau}_{\mathrm{v\_2}}\right\|^m \tag{2.2.107}$$

in which the chain dynamics imposes that the viscous multiplier parameter of the entangled free chains r_1 is significantly lower than that of the non-entangled free chains r_2.

For the sake of completeness, Eqs. (2.2.99), (2.2.101) and (2.2.102) may be also particularized, respectively, as follows:

$$\kappa\dot{\chi}=\left(\beta-1\right)\left(\boldsymbol{\tau}_{\mathrm{v\_1}}:\mathbf{D}_{\mathrm{v\_1}}+\boldsymbol{\tau}_{\mathrm{v\_2}}:\mathbf{D}_{\mathrm{v\_2}}\right) \tag{2.2.108}$$

$$\Phi_1=\beta\left(r_1\left|\lambda_{\mathrm{v\_1}}-1\right|^d\left\|\boldsymbol{\tau}_{\mathrm{v\_1}}\right\|^{m+1}+r_2\left|\lambda_{\mathrm{v\_2}}-1\right|^d\left\|\boldsymbol{\tau}_{\mathrm{v\_2}}\right\|^{m+1}\right)\geq 0 \tag{2.2.109}$$

$$\dot{\chi}=\frac{2\left(\beta-1\right)\sqrt{N_{\mathrm{R}}}\left(r_1\left|\lambda_{\mathrm{v\_1}}-1\right|^d\left\|\boldsymbol{\tau}_{\mathrm{v\_1}}\right\|^{m+1}+r_2\left|\lambda_{\mathrm{v\_2}}-1\right|^d\left\|\boldsymbol{\tau}_{\mathrm{v\_2}}\right\|^{m+1}\right)}{n_{\mathrm{R}}k_{\mathrm{B}}TN_{\mathrm{R0}}\zeta_{\mathrm{iso}}\lambda_{\mathrm{iso}}} \tag{2.2.110}$$

Due to their distinct viscous properties, the two populations of chains have different elastic and viscous stretches and thus contribute differently to the total viscous stress (2.2.103), the internal work (2.2.108), the intrinsic dissipation (2.2.109) and the damage kinetics (2.2.110).

2.2.3. Numerical examples

For a rubber structure, the finite element computation is essential to appreciate the local fields of the different inelastic effects and the associated network rearrangements during the cyclic loading history. The general thermo-viscoelastic-damage constitutive model, described in the previous section, was implemented into the finite element code MSC.Marc to simulate the fatigue response in rubber structures. The main calculation steps are summarized in the flowchart of Figure 2.2.3a.

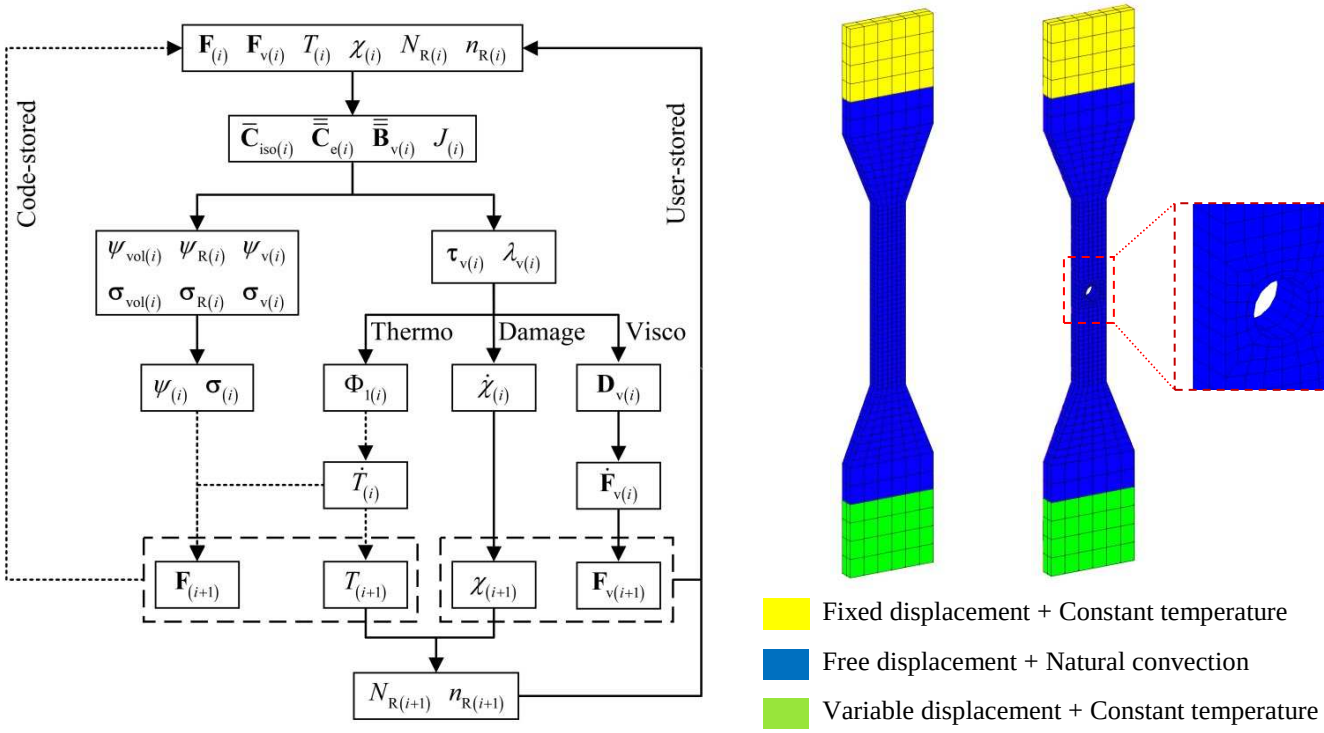

(a) (b)

Figure 2.2.3. Flowchart of the thermo-mechanical algorithm (a) and simulation models with boundary conditions (b).

Numerical examples on rubber structures, a dog-bone shaped specimen without and with a central hole, are presented to illustrate the capability of the approach. The gauge dimensions are 25 mm (length) × 4 mm (width) × 2 mm (thickness) and the hole diameter is 2 mm. Figure 2.2.3b shows the three-dimensional finite element mesh of the specimens using 8-node meshing elements, isoparametric and arbitrarily hexahedrics. The mechanical boundary conditions consist of fixing one specimen end, and imposing to the other a displacement-controlled cyclic loading. The thermal boundary conditions consist of a constant temperature T_0 = 296 K applied at both specimen ends, the remaining frontiers being subjected to a

convection heat transfer. The naturally induced-convention $\boldsymbol{q}_s$ is related to the coefficient of thermal convection *h* by:

$$\boldsymbol{q}_s = -h\left(T - T_\infty\right)\boldsymbol{n} \tag{2.2.111}$$

in which T_∞ = 296 K is the environment temperature and $\boldsymbol{n}$ is the normal vector to the surface of the element.

In what follows, a numerical parametric study is presented to examine the influence of selected material constants on the fatigue response of a fictive rubber medium. Unless explicitly otherwise stated, the values of the different input constants required by the modeling are:

- The network parameters of the cross-linked chains:

  $n_{\mathrm{R0}}k_{\mathrm{B}}T_0$ = 0.6 MPa

  N_{R0} = 5.0

- The viscous parameters of the free chains:

  $n_{\mathrm{v\_1}}k_{\mathrm{B}}T_0$ = 0.2 MPa

  $n_{\mathrm{v\_2}}k_{\mathrm{B}}T_0$ = 0.4 MPa

  $N_{\mathrm{v\_1}}$ = $N_{\mathrm{v\_2}}$ = 5.0

  r_1 = 2.5 $\mathrm{MPa}^{-2}\ \mathrm{s}^{-1}$

  r_2 = 250 $\mathrm{MPa}^{-2}\ \mathrm{s}^{-1}$

  d = -0.01

  m = 2.0

- The coupling parameter:

  β = 1.003

- The volumetric parameters:

  α = $3.6\times10^{-4}\ \mathrm{K}^{-1}$

  k = 200 MPa

- The thermal parameters:

  $N_{,T}$ = 0.02

  k_{T} = 0.2 $\mathrm{W\ m}^{-1}\ \mathrm{K}^{-1}$

  C_{T0} = $1.5\times10^{6}\ \mathrm{J\ m}^{-3}\ \mathrm{K}^{-1}$

  h = 10 $\mathrm{W\ m}^{-2}\ \mathrm{K}^{-1}$

2.2.3.1. Rubber fatigue response: stress-softening, hysteresis and heat build-up

The contribution of the two free chain populations on the inelastic effects is investigated while disregarding in this subsection the temperature and damage effects, i.e. $N_{,T}$ = 0.0 and β = 1.0. By decoupling them from the temperature and damage effects, the focus is made only on the viscoelasticity effects. Figures 2.2.4 and 2.2.5 present the effect of key parameters, related to the entangled and non-entangled free chains, on the viscoelasticity-induced rubber fatigue response. Each material parameter is varied independently while keeping the others constant. A global view at these results confirms that the stress-softening is mainly due to the move of the entangled free chains, whereas the hysteresis originates from the move of the non-entangled free chains. The two inelastic effects have different time-scales reproduced by the distinct relaxation rates of the two populations of free chains.

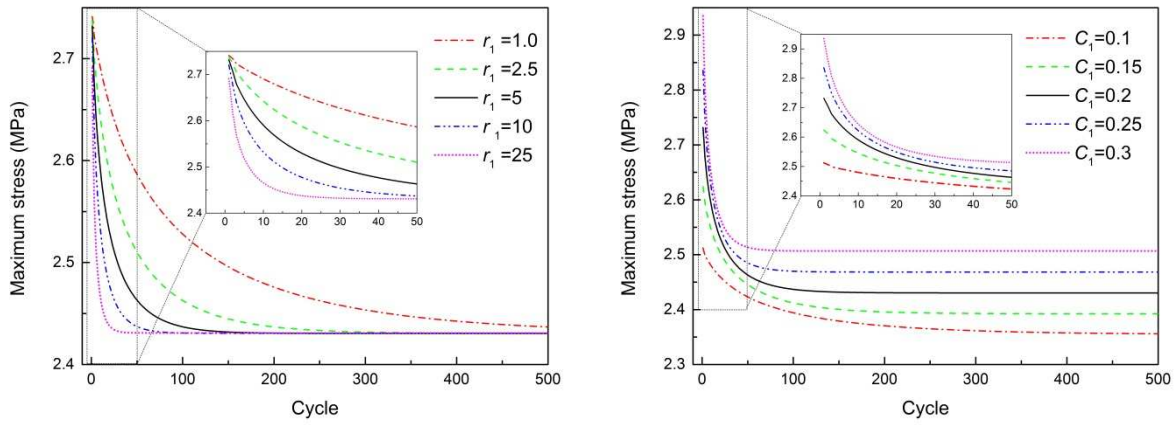

(a) (b)

Figure 2.2.4. Maximum stress evolution during cyclic loading with the effect of (a) r_1 and (b) $C_1 = n_{v\_1} k_B T_0$.

Figure 2.2.4 shows the evolution of the maximum stress for various values of the two main parameters controlling the stress-softening, i.e. r_1 and $C_1 = n_{v\_1} k_B T_0$. A substantial decrease in stress is observed during the first few cycles. Following this rapid decrease in stress, the rubber undergoes a more gradual softening and tends towards a stabilized state for which there is no significant change in stress. The higher the values of r_1 and $C_1 = n_{v\_1} k_B T_0$, the stronger the impact on the degree to which the rubber is softened. The parameter r_1 has nearly no effect on the initial stiffness and the stabilized state, whereas the parameter $C_1 = n_{v\_1} k_B T_0$ can control them due to its role on the overstress.

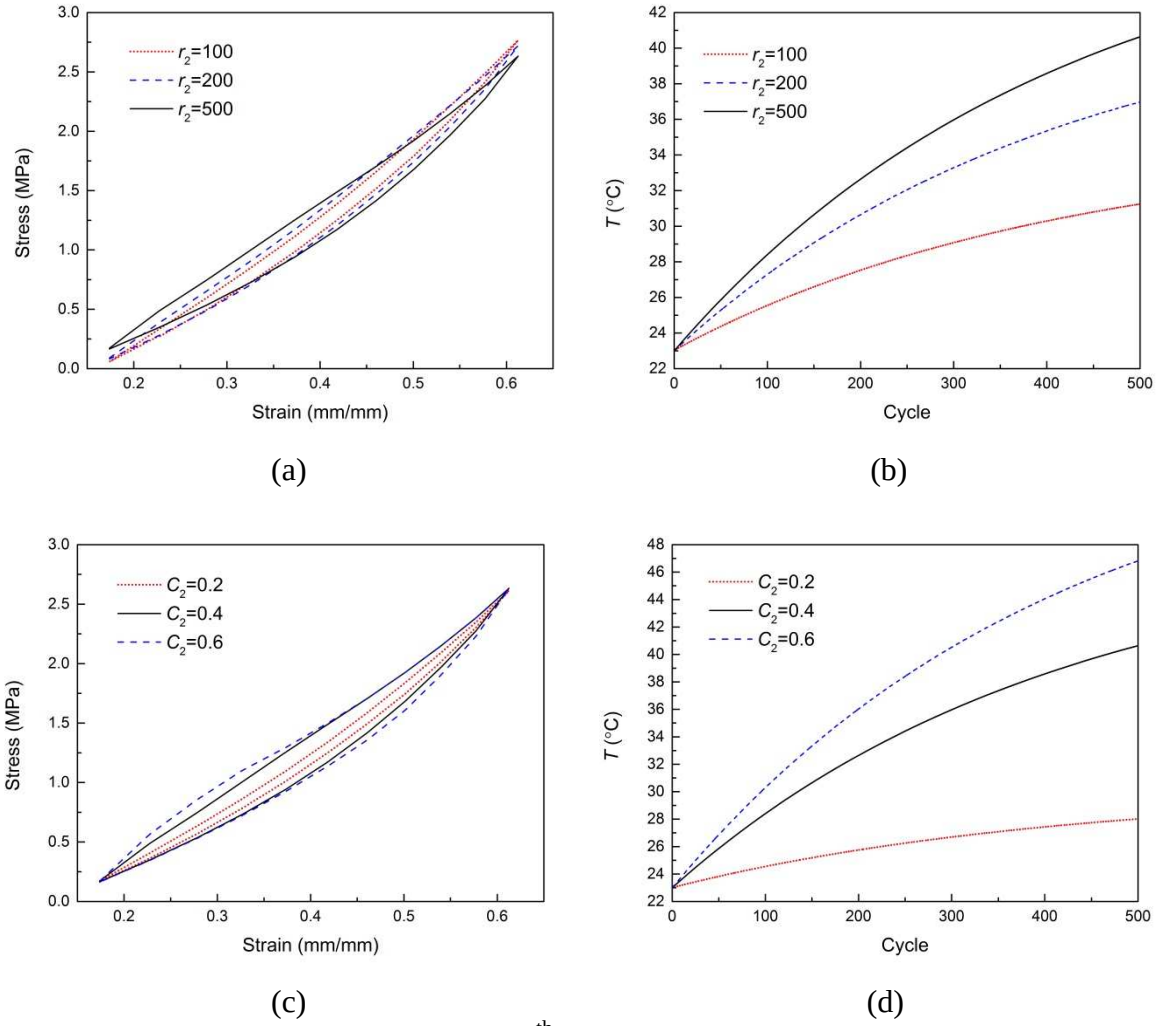

Figure 2.2.5. Hysteretic response at the 5th cycle and temperature evolution during cyclic loading with the effect of (a), (b) r_2 and (c), (d) $C_2 = n_{v\_2}k_B T_0$.

Figure 2.2.5 presents the hysteretic process in the rubber cyclic response, and the associated change in temperature, for various values of the two main parameters affecting the hysteresis loop area, i.e. r_2 and $C_2 = n_{v\_2}k_B T_0$. The higher the values of r_2 and $C_2 = n_{v\_2}k_B T_0$, the higher the loop area. Our predictions show that a small variation of the loop area has a strong impact on the temperature increment in the material.

2.2.3.2. Temperature and damage effects on the rubber fatigue response

The temperature increment and the damage evolution are given in Figure 2.2.6 together with their effects on the network thermal kinetics and the network damage kinetics, respectively.

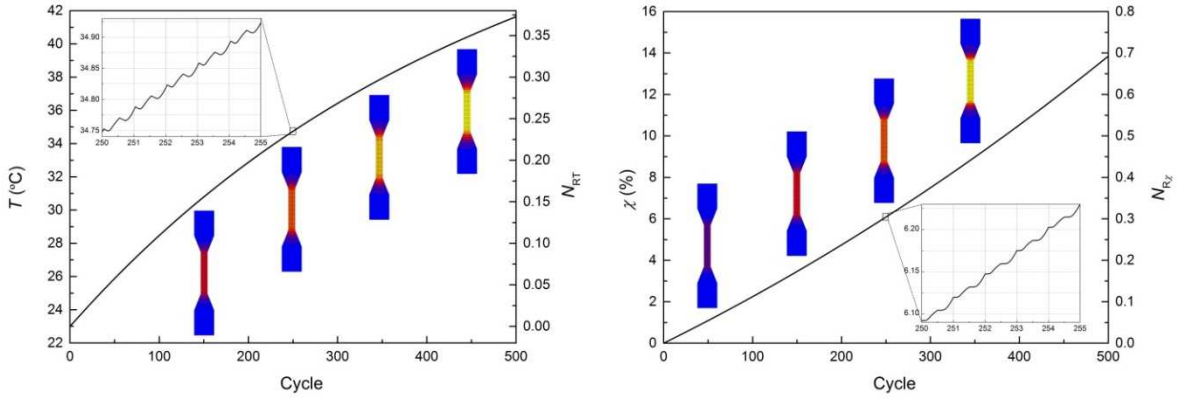

(a) (b)

Figure 2.2.6. Heat build-up and fatigue damage during cyclic loading: (a) temperature evolution and associated network thermal kinetics, (b) damage evolution and associated network damage kinetics.

The contribution of these two effects on the network rearrangements during the cyclic loading is analyzed in Figure 2.2.7a under different couplings for the simulation:

- viscoelasticity: $N_{,T}$ = 0.0 and β = 1.0,
- viscoelasticity-temperature: $N_{,T}$ = 0.02 and β = 1.0,
- viscoelasticity-damage: $N_{,T}$ = 0.0 and β = 1.003,
- viscoelasticity-temperature-damage: $N_{,T}$ = 0.02 and β = 1.003.

The consequences of the internal network rearrangements on the degree to which the rubber is softened are given in Figure 2.2.7b. The addition of the dissipative heating and / or damage effects at the chain-scale may have an important effect at the macroscopic scale, in particular manifested by a deviation from the viscoelasticity-induced stabilized state. The inelastic effects during the cyclic loading in a tensile specimen containing a central hole are further analyzed in order to illustrate the adopted approach. The capability of the approach to simulate the temperature and damage fields in the vicinity of the hole is shown in Figure 2.2.8. The predicted profiles of the temperature and the fatigue damage along the width and the length of the specimen are also plotted in the figure. The temperature distribution along the specimen width shows a maximum value located at a certain distance from the hole.

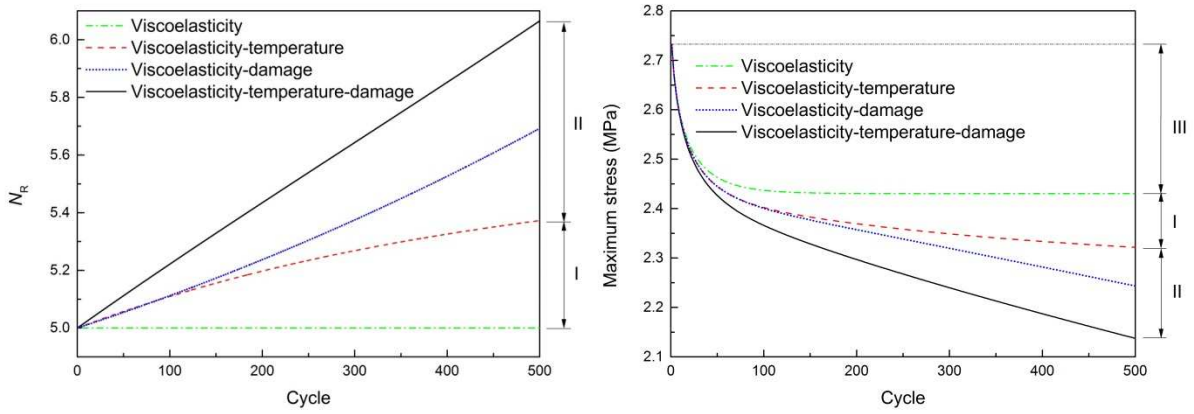

(a) (b)

Figure 2.2.7. Network rearrangement during cyclic loading and resulting stress-softening: (a) network kinetics and (b) maximum stress evolution for different couplings (I: induced by temperature, II: induced by damage, III: induced by viscoelasticity).

Along the specimen length, the temperature distribution slightly increases while moving from the hole and then progressively decreases. The damage distribution exhibits a higher gradient level along the specimen width. After an increase while moving from the hole, the damage distribution along the specimen length becomes progressively uniform.

2.2.4. Partial conclusions

In this part, we have presented a new thermo-viscoelastic-damage approach for the prediction of fatigue thermo-mechanical response in rubbers in connection to the network rearrangements. The constitutive model was incorporated into a finite element code and a numerical analysis was carried out for both a tensile configuration specimen and a specimen containing a central hole. The parametric study highlighted the respective role of key model parameters on the rubber inelastic fatigue response, i.e. stress-softening and hysteresis along with dissipative heating. In particular, the capability of the implemented constitutive model to simulate the effects of the recoverable viscoelastic rearrangements and the unrecoverable damage rearrangements, and their link with the global behavior, was demonstrated. The implemented constitutive model is presented in its most general form with the aim of being applicable to all rubbers and it provides a useful tool for thermal, viscoelastic and damage patterns estimation in cyclically loaded rubber structures.

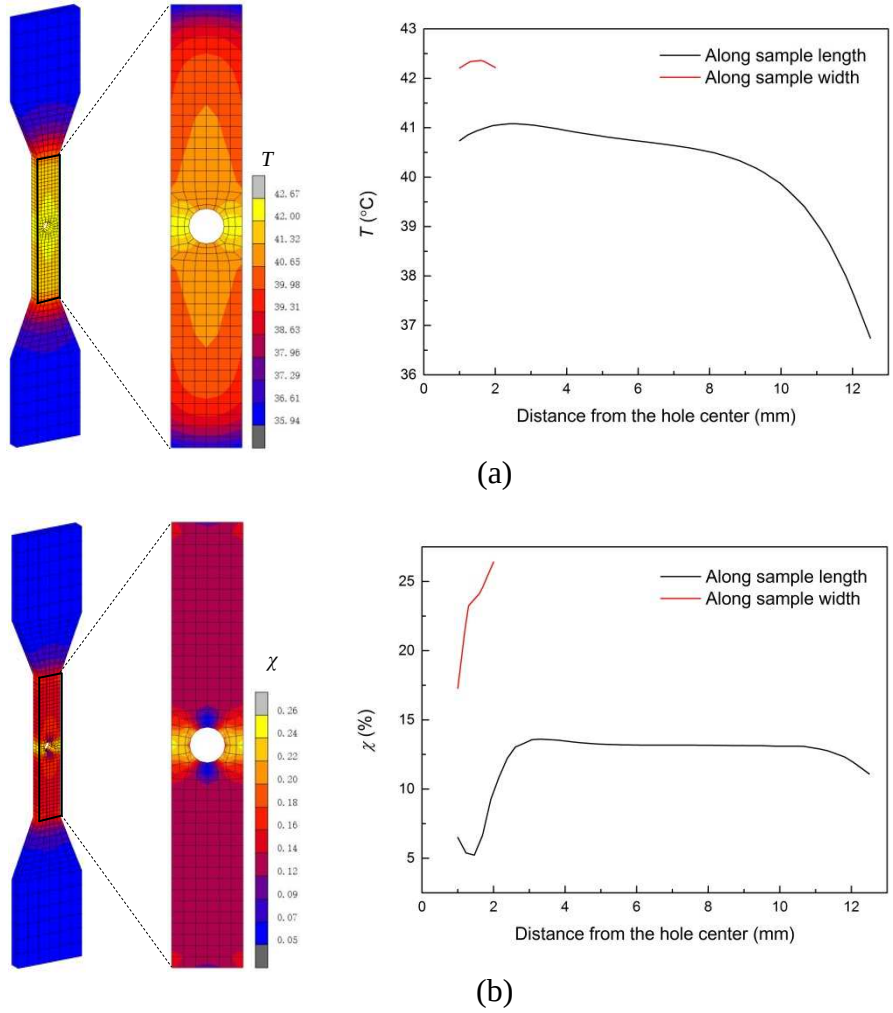

Figure 2.2.8. Heat build-up and fatigue damage distribution in the perforated specimen at the 500th cycle: (a) temperature distribution, (b) damage distribution.

In the following part, the efficiency of the proposed constitutive model to predict the experimental response of filled rubbers will be demonstrated. The application will be performed on a styrene-butadiene rubber containing different amounts of carbon-black and cyclically loaded under different pre-stretch levels. The effective role of carbon-black fillers dispersed in the rubber matrix will be especially emphasized not only on the inelastic fatigue response but also on the underlying physical mechanisms with their pre-stretch dependency.

2.2.5. Appendix

The volumetric, relaxed and viscous Cauchy stresses are obtained from the differentiation of the free energy functions with respect to the corresponding deformations, and are, respectively, given by:

$$\boldsymbol{\sigma}_{\mathrm{vol}} = \frac{\partial \hat{\psi}_{\mathrm{vol}}}{\partial J}\mathbf{I} \tag{2.2.A1}$$

$$\boldsymbol{\sigma}_{\mathrm{R}} = \frac{2}{J}\mathbf{F}_{\mathrm{iso}}\frac{\partial \hat{\psi}_{\mathrm{R}}}{\partial \bar{\mathbf{C}}_{\mathrm{iso}}}\mathbf{F}_{\mathrm{iso}}^{\mathrm{T}} \tag{2.2.A2}$$

$$\boldsymbol{\sigma}_{\mathrm{v}} = \frac{2}{J}\mathbf{F}_{\mathrm{e}}\frac{\partial \hat{\psi}_{\mathrm{v}}}{\partial \bar{\bar{\mathbf{C}}}_{\mathrm{e}}}\mathbf{F}_{\mathrm{e}}^{\mathrm{T}} \tag{2.2.A3}$$

The volumetric Cauchy stress, expressed in Eq. (2.2.87), is obtained by substituting Eq. (2.2.82) into Eq. (2.2.A1). The relaxed and viscous Cauchy stresses, expressed in Eqs. (2.2.88) and (2.2.89), are obtained in a similar manner. Substituting Eq. (2.2.75) into Eq. (2.2.A2) and applying the chain rules of differentiation, the relaxed Cauchy stress is written as follows:

$$\boldsymbol{\sigma}_{\mathrm{R}} = \frac{n_{\mathrm{R}}k_{\mathrm{B}}T}{3J}\frac{\sqrt{N_{\mathrm{R}}}}{\lambda_{\mathrm{iso}}}\zeta_{\mathrm{iso}}\mathbf{F}_{\mathrm{iso}}\frac{\partial I_1}{\partial \bar{\mathbf{C}}_{\mathrm{iso}}}\mathbf{F}_{\mathrm{iso}}^{\mathrm{T}} \tag{2.2.A4}$$

where $I_1 = \mathrm{trace}\left(\bar{\mathbf{C}}_{\mathrm{iso}}\right)$.

Considering the kinematic constraint of the isochoric deformation tensor $\bar{\mathbf{C}}_{\mathrm{iso}}$, i.e. $I_3 = \det\left(\bar{\mathbf{C}}_{\mathrm{iso}}\right) = 1$, Eq. (2.2.A4) can be rewritten as:

$$\boldsymbol{\sigma}_{\mathrm{R}} = \frac{n_{\mathrm{R}}k_{\mathrm{B}}T}{3J}\frac{\sqrt{N_{\mathrm{R}}}}{\lambda_{\mathrm{iso}}}\zeta_{\mathrm{iso}}\mathbf{F}_{\mathrm{iso}}\frac{\partial\left[I_1 - \omega\left(I_3 - 1\right)\right]}{\partial \bar{\mathbf{C}}_{\mathrm{iso}}}\mathbf{F}_{\mathrm{iso}}^{\mathrm{T}} \tag{2.2.A5}$$

where ω serves as a Lagrange multiplier, which may be only found by means of the boundary conditions.

Eq. (2.2.A5) can be also rewritten as follows:

$$\boldsymbol{\sigma}_{\mathrm{R}} = \frac{n_{\mathrm{R}}k_{\mathrm{B}}T}{3J}\frac{\sqrt{N_{\mathrm{R}}}}{\lambda_{\mathrm{iso}}}\zeta_{\mathrm{iso}}\left(\mathbf{B}_{\mathrm{iso}} - \omega\mathbf{I}\right) \tag{2.2.A6}$$

Finally, since the relaxed Cauchy stress tensor $\boldsymbol{\sigma}_{\mathrm{R}}$ is traceless (see Eq. (2.2.33)), ω is identified as λ_{iso}^2 and the expression provided in Eq. (2.2.88) is obtained. The same derivation process is used to obtain the viscous Cauchy stress from Eq. (2.2.A3).

2.2.6. References

Aït Hocine, N., Hamdi, A., Naït-Abdelaziz, M., Heuillet, P., Zaïri, F., 2011. Experimental and finite element investigation of void nucleation in rubber-like materials. International Journal of Solids and Structures 48, 1248-1254.

Anand, L., Ames, N.M., Srivastava, V., Chester, S.A., 2009. A thermo-mechanically coupled theory for large deformations of amorphous polymers. Part I: Formulation. International Journal of Plasticity 25, 1474-1494.

Ames, N.M., Srivastava, V., Chester, S.A., Anand, L., 2009. A thermo-mechanically coupled theory for large deformations of amorphous polymers. Part II: Applications. International Journal of Plasticity 25, 1495-1539.

Arruda, E.M., Boyce, M.C., 1993. A three-dimensional constitutive model for the large stretch behavior of rubber elastic materials. Journal of the Mechanics and Physics of Solids 41, 389-412.

Ayoub, G., Zaïri, F., Naït-Abdelaziz, M., Gloaguen, J.M., 2010. Modelling large deformation behaviour under loading-unloading of semicrystalline polymers: application to a high density polyethylene. International Journal of Plasticity 26, 329-347.

Ayoub, G., Zaïri, F., Naït-Abdelaziz, M., Gloaguen, J.M., 2011a. Modeling the low-cycle fatigue behavior of visco-hyperelastic elastomeric materials using a new network alteration theory: application to styrene-butadiene rubber. Journal of the Mechanics and Physics of Solids 59, 473-795.

Ayoub, G., Zaïri, F., Fréderix, C., Gloaguen, J.M., Naït-Abdelaziz, M., Seguela, R., Lefebvre, J.M., 2011b. Effects of crystal content on the mechanical behaviour of polyethylene under finite strains: experiments and constitutive modelling. International Journal of Plasticity 27, 492-511.

Ayoub, G., Zaïri, F., Naït-Abdelaziz, M., Gloaguen, J.M., Kridli, G., 2014. A visco-hyperelastic damage model for cyclic stress-softening, hysteresis and permanent set in rubber using the network alteration theory. International Journal of Plasticity 54, 19-33.

Behnke, R., Kaliske, M., Kluppel, M., 2016. Thermo-mechanical analysis of cyclically loaded particle-reinforced elastomer components: experiment and finite element simulation. Rubber Chemistry and Technology 89, 154-176.

Bergstrom, J.S., Boyce, M.C., 1998. Constitutive modeling of the large strain time-dependent behavior of elastomers. Journal of the Mechanics and Physics of Solids 46, 931-954.

Bouasse, H., Carrière, Z., 1903. Sur les courbes de traction du caoutchouc vulcanisé. Annales de la Faculté des Sciences de Toulouse 5, 257-283.

Boukamel, A., Méo, S., Débordes, O., Jaeger, M., 2001. A thermo-viscoelastic model for elastomeric behaviour and its numerical application. Archive of Applied Mechanics 71, 785-801.

Bouvard, J.L., Francis, D.K., Tschopp, M.A., Marin, E.B., Bammann, D.J., Horstemeyer, M.F., 2013. An internal state variable material model for predicting the time, thermomechanical, and stress state dependence of amorphous glassy polymers under large deformation. International Journal of Plasticity 42, 168-193.

Bueche, F., 1960. Molecular basis for the Mullins effect. Journal of Applied Polymer Science 4, 107-114.

Chagnon, G., Verron, E., Gornet, L., Marckmann, G., Charrier, P., 2004. On the relevance of continuum damage mechanics as applied to the Mullins effect in elastomers. Journal of the Mechanics and Physics of Solids 52, 1627-1650.

Chagnon, G., Verron, E., Marckmann, G., Gornet, L., 2006. Development of new constitutive equations for the Mullins effect in rubber using the network alteration theory. International Journal of Solids and Structures 43, 6817-6831.

Cohen, A., 1991. A Padé approximant to the inverse Langevin function. Rheological Acta 30, 270-273.

Coleman, B.D., Noll, W., 1963. The thermodynamics of elastic materials with heat conduction and viscosity. Archive for Rational Mechanics and Analysis 13, 167-178.

Dargazany, R., Itskov, M., 2009. A network evolution model for the anisotropic Mullins effect in carbon black filled rubbers. International Journal of Solids and Structures 46, 2967-2977.

Dargazany, R., Khiem, V.N., Itskov, M., 2014. A generalized network decomposition model for the quasi-static inelastic behavior of filled elastomers. International Journal of Plasticity 63, 94-109.

de Gennes, P.G., 1971. Reptation of a polymer chain in the presence of fixed obstacles. Journal of Chemical Physics 55, 572-579.

Derham, C.J., Thomas, A.G., 1977. Creep of rubber under repeated stressing. Rubber Chemistry and Technology 50, 397-402.

Dippel, B., Johlitz, M., Lion, A., 2014. Thermo-mechanical couplings in elastomers - experiments and modelling. Zeitschrift für Angewandte Mathematik und Mechanik 95, 1117-1128.

Doi, M., Edwards, M.F., 1986. The Theory of Polymer Dynamics. Oxford University Press, Oxford.

Drozdov, A.D., Dorfmann, A., 2001. Stress-strain relations in finite viscoelastoplasticity of rigid-rod networks: applications to the Mullins effect. Continuum Mechanics and Thermodynamics 13, 183-205.

Drozdov, A., Christiansen, J., 2009. Thermo-viscoplasticity of carbon black-reinforced thermoplastic elastomers. International Journal of Solids and Structures 46, 2298-2308.

Freund, M., Lorenz, H., Juhre, D., Ihlemann, J., Kluppel, M., 2011. Finite element implementation of a microstructure-based model for filled elastomers. International Journal of Plasticity 27, 902-919.

Garcia-Gonzalez, D., Zaera, R., Arias, A., 2017. A hyperelastic-thermoviscoplastic constitutive model for semi-crystalline polymers: application to PEEK under dynamic loading conditions. International Journal of Plasticity 88, 27-52.

Goktepe, S., Miehe, C., 2005. A micro-macro approach to rubber-like materials. Part III: the micro-sphere model of anisotropic Mullins-type damage. Journal of the Mechanics and Physics of Solids 53, 2259-2283.

Gough, J., 1805. A description of a property of Caoutchouc, or Indian rubber; with some reflections on the cause of the elasticity of this substance. Memoirs of the Literary and Philosophical Society of Manchester 1, 288-295.

Govindjee, S., Simo, J.C., 1991. A micro-mechanically based continuum damage model for carbon black-filled rubbers incorporating Mullins' effect. Journal of the Mechanics and Physics of Solids 39, 87-112.

Gudimetla, M.R., Doghri, I., 2017. A finite strain thermodynamically-based constitutive framework coupling viscoelasticity and viscoplasticity with application to glassy polymers. International Journal of Plasticity 98, 197-216.

Gurtin, M.E., Anand, L., 2005. The decomposition $F= F^e F^p$, material symmetry, and plastic irrotationality for solids that are isotropic-viscoplastic or amorphous. International Journal of Plasticity 21, 1686-1719.

Guth, E., 1945. Theory of filler reinforcement. Journal of Applied Physics 16, 20-25.

Guo, Q., Zaïri, F., Baraket, H., Chaabane, M., Guo, X., 2017. Pre-stretch dependency of the cyclic dissipation in carbon-filled SBR. European Polymer Journal 96, 145-158.

Hachour, K., Zaïri, F., Naït-Abdelaziz, M., Gloaguen, J.M., Aberkane, M., Lefebvre, J.M., 2014. Experiments and modeling of high-crystalline polyethylene yielding under different stress states. International Journal of Plasticity 54, 1-18.

Hanson, D.E., Hawley, M., Houlton, R., Chitanvis, K., Rae, P., Orler, E.B., Wrobleski, D.A., 2005. Stress softening experiments in silica-filled polydimethylsiloxane provide insight into a mechanism for the Mullins effect. Polymer 46, 10989-10995.

Holzapfel, G. A., Simo, J. C., 1996a. A new viscoelastic constitutive model for continuous media at finite thermomechanical changes. International Journal of Solids and Structures 33, 3019-3034.

Holzapfel, G., Simo, J., 1996b. Entropy elasticity of isotropic rubber-like solids at finite strains. Computer Methods in Applied Mechanics and Engineering 132, 17-44.

Horstemeyer, M.F., Bammann, D.J., 2010. Historical review of internal state variable theory for inelasticity. International Journal of Plasticity 26, 1310-1334.

Houwink, R., 1956. Slipping of molecules during the deformation of reinforced rubber. Rubber Chemistry and Technology 29, 888-893.

Johlitz, M., Dippel, B., Lion, A., 2016. Dissipative heating of elastomers: a new modelling approach based on finite and coupled thermomechanics. Continuum Mechanics and Thermodynamics 28, 1111-1125.

Khan, A.S., Lopez-Pamies, O., Kazmi, R., 2006. Thermo-mechanical large deformation response and constitutive modeling of viscoelastic polymers over a wide range of strain rates and temperatures. International Journal of Plasticity 22, 581-601.

Khiem, V.N., Itskov, M., 2017. An averaging based tube model for deformation induced anisotropic stress softening of filled elastomers. International Journal of Plasticity 90, 96-115.

Kim, J.H., Kang, T.J., Yu, W.R., 2010. Thermo-mechanical constitutive modeling of shape memory polyurethanes using a phenomenological approach. International Journal of Plasticity 26, 204-218.

Krairi, A., Doghri, I., 2014. A thermodynamically-based constitutive model for thermoplastic polymers coupling viscoelasticity, viscoplasticity and ductile damage. International Journal of Plasticity 60, 163-181.

Kraus, G., Childers, C.W., Rollmann, K.W., 1966. Stress softening in carbon black-reinforced vulcanizates: strain rate and temperature effects. Journal of Applied Polymer Science 10, 229-244.

Laiarinandrasana, L., Piques, R., Robisson, A., 2003. Visco-hyperelastic model with internal state variable coupled with discontinuous damage concept under total Lagrangian formulation. International Journal of Plasticity 19, 977-1000.

Laiarinandrasana, L., Besson, J., Lafarge, M., Hochstetter, G., 2009. Temperature dependent mechanical behaviour of PVDF: experiments and numerical modelling. International Journal of Plasticity 25, 1301-1324.

Lee, E. H., 1969. Elastic-plastic deformation at finite strains. Journal of Applied Mechanics 36, 1-6.

Li, F., Liu, J., Yang, H., Lu, Y., Zhang, L., 2016. Numerical simulation and experimental verification of heat build-up for rubber compounds. Polymer 101, 199-207.

Li, Y., Tang, S., Kroger, M., Liu, W.K., 2016. Molecular simulation guided constitutive modeling on finite strain viscoelasticity of elastomers. Journal of the Mechanics and Physics of Solids 88, 204-226.

Lion, A., 1997. On the large deformation behaviour of reinforced rubber at different temperatures. Journal of the Mechanics and Physics of Solids 45, 1805-1834.

Lion, A., 2000. Constitutive modelling in finite thermoviscoplasticity: a physical approach based on nonlinear rheological models. International Journal of Plasticity 16, 469-494.

Lion, A., Dippel, B., Liebl, C., 2014. Thermomechanical material modelling based on a hybrid free energy density depending on pressure, isochoric deformation and temperature. International Journal of Solids and Structures 51, 729-739.

Lorenz, H., Kluppel, M., 2012. Microstructure-based modelling of arbitrary deformation histories of filler-reinforced elastomers. Journal of the Mechanics and Physics of Solids 60, 1842-1861.

Lu, S., Pister, K., 1975. Decomposition of deformation and representation of the free energy function for isotropic thermoelastic solids. International Journal of Solids and Structures 11, 927-934.

Makki, M., Ayoub, G., Abdul-Hameed, H., Zaïri, F., Mansoor, B., Naït-Abdelaziz, M., Ouederni, M., Zaïri, F., 2017. Mullins effect in polyethylene and its dependency on crystal content: a network alteration model. Journal of the Mechanical Behavior of Biomedical Materials 75, 442-454.

Marckmann, G., Verron, E., Gornet, L., Chagnon, G., Charrier, P., Fort, P., 2002. A theory of network alteration for the Mullins effect. Journal of the Mechanics and Physics of Solids 50, 2011-2028.

Maurel-Pantel, A., Baquet, E., Bikard, J., Bouvard, J.L., Billon, N., 2015. A thermo-mechanical large deformation constitutive model for polymers based on material network description: application to a semi-crystalline polyamide 66. International Journal of Plasticity 67, 102-126.

McKenna, G.B., Zapas, L.J., 1981. Response of carbon black filled butyl rubber to cyclic loading. Rubber Chemistry and Technology 54, 718-733.

Medalia, A., 1991. Heat generation in elastomer compounds: causes and effects. Rubber Chemistry and Technology 64, 481-492.

Meinecke, E., 1991. Effect of carbon-black loading and crosslink density on the heat build-up in elastomers. Rubber Chemistry and Technology 64, 269-284.

Meo, S., Boukamel, A., Debordes, O., 2002. Analysis of a thermoviscoelastic model in large strain. Computers and Structures 80, 2085-2098.

Miehe, C., 1995a. Discontinuous and continuous damage evolution in Ogden-type large strain elastic materials. European Journal of Mechanics A/Solids 14, 697-720.

Miehe, C., 1995b. Entropic thermoelasticity at finite strains. Aspects of the formulation and numerical implementation. Computer Methods in Applied Mechanics and Engineering 120, 243-269.

MSC.Marc, 2015. MSC. Marc Volume D: User Subroutines and Special Routines. MSC Software Corporation.

Mullins, L., 1948. Effect of stretching on the properties of rubber. Rubber Chemistry and Technology 21, 281-300.

Mullins, L., 1969. Softening of rubber by deformation, Rubber Chemistry Technology 42, 339-362.

Ogden, R.W., Roxburgh, D.G., 1999. A pseudo-elastic model for the Mullins effect in filled rubber. Proceedings of the Royal Society of London A455, 2861-2877.

Osterlof, R., Wentzel, H., Kari, L., 2016. A finite strain viscoplastic constitutive model for rubber with reinforcing fillers. International Journal of Plasticity 87, 1-14.

Ovalle-Rodas, C., Zaïri, F., Naït-Abdelaziz, M., 2013. Thermo-visco-hyperelastic modeling of the rubber self-heating under fatigue. Constitutive Models for Rubber VIII - Proceedings of the 8th European Conference on Constitutive Models for Rubbers, ECCMR 2013, 131-136.

Ovalle-Rodas, C., Zaïri, F., Naït-Abdelaziz, M., 2014. A finite strain thermo-viscoelastic constitutive model to describe the self-heating in elastomeric materials during low-cycle fatigue. Journal of the Mechanics and Physics of Solids 64, 396-410.

Ovalle-Rodas, C., Zaïri, F., Naït-Abdelaziz, M., Charrier, P., 2015a. Temperature and filler effects on the relaxed response of filled rubbers: experimental observations on a carbon-filled SBR and constitutive modeling. International Journal of Solids and Structures 58, 309-321.

Ovalle-Rodas, C., Zaïri, F., Naït-Abdelaziz, M., Charrier, P., 2015b. Filler effects on the heat build-up of filled rubbers during fatigue: experimental observations and constitutive

modelling. Constitutive Models for Rubber IX - Proceedings of the 9th European Conference on Constitutive Models for Rubbers, ECCMR 2015, 173-180.

Ovalle-Rodas, C., Zaïri, F., Naït-Abdelaziz, M., Charrier, P., 2016. A thermo-visco-hyperelastic model for the heat build-up during low-cycle fatigue of filled rubbers: formulation, implementation and experimental verification. International Journal of Plasticity 79, 217-236.

Plagge, J., Kluppel, M., 2017. A physically based model of stress softening and hysteresis of filled rubber including rate-and temperature dependency. International Journal of Plasticity 89, 173-196.

Reese, S., Govindjee, S., 1998. Theoretical and numerical aspects in the thermo-viscoelastic material behaviour of rubber-like polymers. Mechanics of Time-dependent Materials 1, 357-396.

Reese, S., 2003. A micromechanically motivated material model for the thermo-viscoelastic material behaviour of rubber-like polymers. International Journal of Plasticity 19, 909-940.

Raghunath, R., Juhre, D., Kluppel, M., 2016. A physically motivated model for filled elastomers including strain rate and amplitude dependency in finite viscoelasticity. International Journal of Plasticity 78, 223-241.

Sidoroff, F., 1974. Un modèle viscoélastique non linéaire avec configuration intermédiaire. Journal de Mécanique 13, 679-713.

Simo, J.C., 1987. On a fully three-dimensional finite-strain viscoelastic damage model: formulation and computational aspects. Computer Methods in Applied Mechanics and Engineering 60, 153-173.

Srivastava, V., Chester, S.A., Ames, N.M., Anand, L., 2010. A thermo-mechanically-coupled large-deformation theory for amorphous polymers in a temperature range which spans their glass transition. International Journal of Plasticity 26, 1138-1182.

Wineman, A.S., Huntley, H.E., 1994. Numerical simulation of the effect of damaged induced softening on the inflation of a circular rubber membrane. International Journal of Solids and Structures 31, 3295-3313.

Yu, C., Kang, G., Chen, K., 2017a. A hygro-thermo-mechanical coupled cyclic constitutive model for polymers with considering glass transition. International Journal of Plasticity 89, 29-65.

Yu, C., Kang, G., Chen, K., Lu, F., 2017b. A thermo-mechanically coupled nonlinear viscoelastic–viscoplastic cyclic constitutive model for polymeric materials. Mechanics of Materials 105, 1-15.

Zaïri, F., Woznica, K., Naït-Abdelaziz, M., 2005. Phenomenological nonlinear modelling of glassy polymers. Comptes Rendus Mecanique 333, 359-364.

Zaïri, F., Naït-Abdelaziz, M., Woznica, K., Gloaguen, J.M., 2007. Elasto-viscoplastic constitutive equations for the description of glassy polymers behavior at constant strain rate. Journal of Engineering Materials and Technology 129, 29-35.

Zaïri, F., Naït-Abdelaziz, M., Gloaguen, J.M., Lefebvre, J.M., 2008. Modelling of the elasto-viscoplastic damage behaviour of glassy polymers. International Journal of Plasticity 24, 945-965.

Zaïri, F., Naït-Abdelaziz, M., Gloaguen, J.M., Lefebvre, J.M., 2010. Constitutive modelling of the large inelastic deformation behaviour of rubber-toughened poly(methyl methacrylate): effects of strain rate, temperature and rubber-phase volume fraction. Modelling and Simulation in Materials Science and Engineering 18, 1-22.

Zaïri, F., Naït-Abdelaziz, M., Gloaguen, J.M., Lefebvre, J.M., 2011. A physically-based constitutive model for anisotropic damage in rubber-toughened glassy polymers during finite deformation. International Journal of Plasticity 27, 25-51.

CHAPTER 2. FATIGUE RESPONSE OF FILLED RUBBERS

2.3. A THERMO-VISCOELASTIC-DAMAGE CONSTITUTIVE MODEL. EXPERIMENTS AND IDENTIFICATION[18]

Cyclically loaded styrene-butadiene rubber containing different amounts of carbon-black is experimentally examined under different pre-stretch levels at room temperature. The experimental observations, especially related to both the multi-step cyclic response interrupted by relaxation periods and the dissipative heating, provide valuable insights into the pre-stretch and filler effects on the underlying physical mechanisms of this rubber-filler material system. According to the active role of carbon-black fillers dispersed in the rubber matrix on the inelastic phenomena via the local microscopic interactions, the constitutive theory formulated in the previous Part of the *Chapter 2* is modified in order to incorporate explicitly the filler effects. A deterministic identification procedure is proposed to extract the physically interpretable model parameters of the rubber matrix. The properties of the perfect network and the superimposed (entangled and non-entangled) free chains are identified via an amplification-inspired procedure using, respectively, the relaxed-stress data as a function of the filler content and the history-dependent mechanical cyclic response at the highest filler content. The identified rubber matrix properties are introduced into the finite element simulations as input constants and the same thermo-mechanical boundary conditions regarding the experimental tests are simulated. The capabilities of the proposed constitutive model to predict the thermo-mechanical response under two cyclic loading blocks with different pre-stretch levels are verified by comparisons with experiments. The constitutive model is found able to successfully capture the pre-stretch and filler effects on the fatigue-induced stress-softening, the hysteresis and the change in temperature.

Keywords: Fatigue; dissipative heating; rubbers; carbon-black; pre-stretch level.

[18] This Part of this Chapter is based on the following paper: Qiang Guo, Fahmi Zaïri, Xinglin Guo, 2018. A thermo-viscoelastic-damage constitutive model for cyclically loaded rubbers. Part II: Experimental studies and parameter identification. *International Journal of Plasticity* 101, 58-73.

2.3.1. Partial introduction

Rubbers used in engineering applications contain a large proportion of fillers in order to improve the mechanical properties and reduce the cost (Vilgis et al., 2009). The concentration of fillers dispersed in the rubber matrix, and more especially of filler aggregates, has a strong impact on the inelastic fatigue phenomena due to the active role of fillers via the viscous sliding between fillers and filler-rubber matrix, the breakdown-rebound mechanism of inter-aggregates links and, the breakdown and disentanglement of chains between aggregates. Although remaining imprecisely understood to date, these internal recoverable or unrecoverable rearrangements occurring inside the rubber-filler material system during the fatigue loading history induce mechanical response evolution and energy dissipation, whose amounts depend on the filler content. Because it is impossible to directly measure these rearrangements in filled rubbers taking place at any location inside the material and at any time of the fatigue loading process, multiple competing views have been proposed, based upon macroscopic observations, to explain the origin of the stress-softening / hysteresis and the dissipative heating in filled rubbers (see the references in the first Part). Although current theoretical works may contain the rubber network properties and damage effects, they typically ignore the recoverable viscoelastic rearrangements, being significant in filled rubbers.

In the previous Part, a new thermo-viscoelastic-damage approach, in accordance with the thermodynamic principles, is proposed to predict the inelastic effects in cyclically loaded rubbers in connection to the network rearrangements. The proposed formalism enables correlation of the history-dependent cyclic response of rubbers with their microstructure characteristics while taking into account the viscoelasticity effects and the unrecoverable network rearrangements. In the proposed formulation, we assumed the existence of two free chain populations, superimposed to the purely elastic perfect rubber network, to give a physical origin of the inelastic fatigue effects, each being related to one aspect of observations. According to the active role on the inelastic phenomena of the local microscopic interactions in filled rubbers acting between fillers and rubber matrix but also between fillers themselves, the explicit consideration of the presence of fillers may be seen as the second step succeeding the constitutive theory proposed in the previous Part. In this Part, the inelastic fatigue process of styrene-butadiene rubber (SBR) containing different amounts of carbon-black is experimentally described under different pre-stretch levels at room temperature. The experimental observations provide valuable insights into the relationships between the

carbon-black content and the inelastic fatigue effects of this pre-stretched rubber-filler material system. The inherent inelastic fatigue mechanisms with their dependencies on the filler content and the pre-stretch level are studied under the guidance of both the history-dependence multi-step cyclic tests interrupted by relaxation periods and the dissipative heating. After identification of the relative small number of physically interpretable parameters using an original deterministic procedure, the predictive capabilities of the proposed constitutive model formulated in the Part I are also critically discussed by comparisons with the experimental data obtained under two cyclic loading blocks with different pre-stretch levels.

This Part is organized as follows. Section 2.3.2 presents the experimental investigations on a carbon-filled SBR containing different amounts of carbon-black and cyclically loaded under different pre-stretch levels. Section 2.3.3 is dedicated to the comparison between simulation results and experimental data. Finally, some concluding remarks are given in Section 2.3.4.

2.3.2. Experimental

2.3.2.1. Materials and specimen

A sulfur-vulcanized SBR filled with three different amounts of carbon-black (15, 25 and 43 phr, parts per hundred rubber in weight) is selected for a test program. The compound formulation, provided by the manufacturer (Trelleborg Group), is given in Table 2.1.1. The different SBR-filler material systems are referred to as SBRx, where x is the filler content in phr. The phr values are used to calculate the carbon-black volume fraction in the tested specimens, the direct input in the constitutive equations, by using the following densities of the carbon-black fillers and the unfilled SBR material: $\rho_f = 1.8\times10^3$ kg m^{-3} (Abe et al., 2003) and $\rho_m = 1.21\times10^3$ kg m^{-3} (Wood et al., 1943), respectively. The equation allowing the proper conversion of phr to carbon-black volume fraction is given by:

$$v_f = \frac{\text{phr}}{\rho_f}\left(\frac{100}{\rho_m}+\frac{\text{phr}}{\rho_f}\right)^{-1} \tag{2.3.1}$$

Dog-bone shaped specimens with gauge dimensions of 25 mm (length) × 4 mm (width) × 2 mm (thickness) were cut from 2 mm thickness sheets, allowing to obtain both a highest temperature increase in the specimen gauge zone and a nearly homogeneous temperature

across the transverse direction, as evidenced in Section 2.2.3. Although material isotropy is expected, the specimens were cut along the same direction.

2.3.2.2. Experimental method

All the mechanical tests were achieved at room temperature using an electro-pulse testing machine Instron-5500. During the fatigue loading, the axial stretch was ramped, repetitively, to a prescribed maximum value $\lambda_{\max}$ and then ramped down to a prescribed minimum value $\lambda_{\min}$. The same absolute axial strain rate of 1 /s was imposed to the loading and unloading segments. The surface temperature evolution on the specimen gauge zone was measured using an infrared camera Flir SC300 with the following main characteristics: Spectrum response ranged from 7.5 to 13 μm, resolution of 320 × 240 pixel, sensitivity / NETD less than 50 mK and image update rate of 9 Hz.

In order to measure the effects of the carbon-black content and the loading conditions on the SBR inelastic features, different mechanical tests were performed:

- Multi-step stress relaxation tests under a loading-unloading cycle were performed in order to identify the relaxed response. During both the loading and unloading segments, the axial stretch was interrupted at four prescribed levels. At each relaxation period, the stretch was maintained constant during 1 hour. Both the number of prescribed stretch levels and the holding time were found sufficient to reach the stabilized relaxed-response.
- Fatigue tests of 500 cycles under different pre-stretch levels were performed in order to identify the viscous parameters of the proposed constitutive model. Further, in order to provide insights into the fatigue-induced stress-softening, multi-step cyclic tests interrupted by relaxation periods were also performed. Five blocks of 500 cycles were applied between which the minimum axial stretch was interrupted for a holding time of 3 minutes.
- Two-block tests under different pre-stretch levels were performed in order to verify the proposed constitutive model. Low-High and High-Low pre-stretch levels of 250 cycles for each block were considered in which the stretch amplitude $\lambda_{\text{amp}} = \lambda_{\max} - \lambda_{\min}$ is set to be the same:

$$\text{Low} = \{\lambda_{\min} = 1.2, \lambda_{\max} = 1.45\},\ \text{High} = \{\lambda_{\min} = 1.5, \lambda_{\max} = 1.75\} \tag{2.3.2}$$

Previous to all measurements, 15 cycles up to an overstretch of 1.0 at a frequency of 1 Hz were performed to cancel the prime Mullins effect. This pre-conditioning was also applied to eliminate the flake that appears on the specimen surface after the first few cycles and that may alter the temperature-field measurements because of the surface emissivity variation. The infrared camera was located at a distance of 0.5 m in order to reduce the reflected radiation due to surrounding humidity. In order to monitor the environmental changes and further eliminate their effects on the fatigue self-heating measurements, a dummy specimen with the same material but not loaded was positioned close to the tested one. The external radiation sources were reduced by packing the set-up in a relatively closed space using a special thermal insulation material. The stored infrared images were post-processed to extract the surface temperature evolution in the region of interest on the specimen gauge zone. Thermal equilibrium was ensured by a holding time of 10 minutes before measurements.

2.3.2.3. Experimental results

The effects of the carbon-black content on the inelastic phenomena in pre-stretched cyclically loaded SBR are discussed in this subsection. These measurements allow to provide valuable insights into the modifications of the fatigue mechanisms in the rubber-filler material system due to the presence of carbon-black fillers.

2.3.2.3.1. Stress relaxation

The multi-step stress relaxation response under a loading-unloading cycle is presented in Figure 2.3.1 for the three carbon-filled SBR materials. In the unloading segment, the stress evolution during the relaxation periods is much more affected by the stretch level than that in the loading segment. During the relaxation periods, the stress evolves towards an end corresponding to an obvious stabilized relaxed-stress pointed out by a filled point in the figure. The obtained relaxed-stress data are function of the strain level and provide a quantitative judgment of the material nonlinear elastic response. Due to the strain-amplifying effect of the fillers, the large-strain viscoelastic response of carbon-filled SBR is strongly affected by the filler content by acting both on the elasticity and on the viscosity. In particular, the higher the filler content, the higher both the stabilized relaxed-stress and the hysteresis loop area. The viscoelastic mechanisms are strongly dependent on the level of interactions between the chains and the fillers, the chains and the fillers themselves.

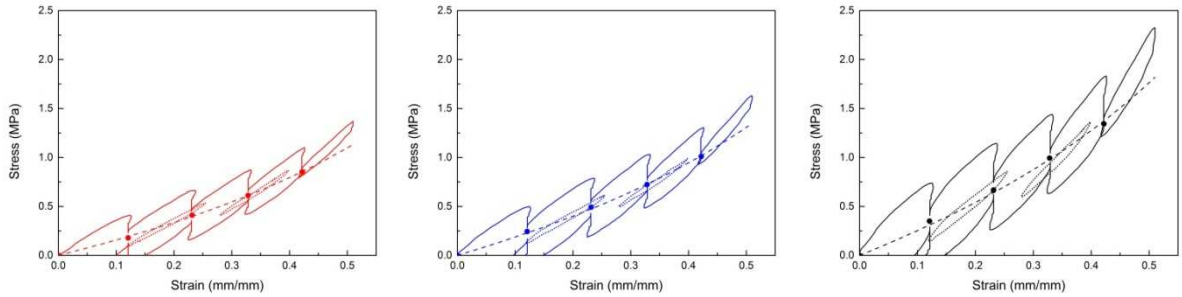

(a) (b) (c)

Figure 2.3.1. Multi-step stress relaxation response under a loading-unloading cycle: (a) SBR15, (b) SBR25, SBR43. Hysteresis loops at 250th cycle for pre-stretch levels of $\lambda_{min}=1.2$ and $\lambda_{min}=1.5$ are also plotted.

The stress evolution during the relaxation periods of the multi-step cyclic tests, normalized by the maximum value, is presented in Figure 2.3.2 for the three carbon-filled SBR materials.

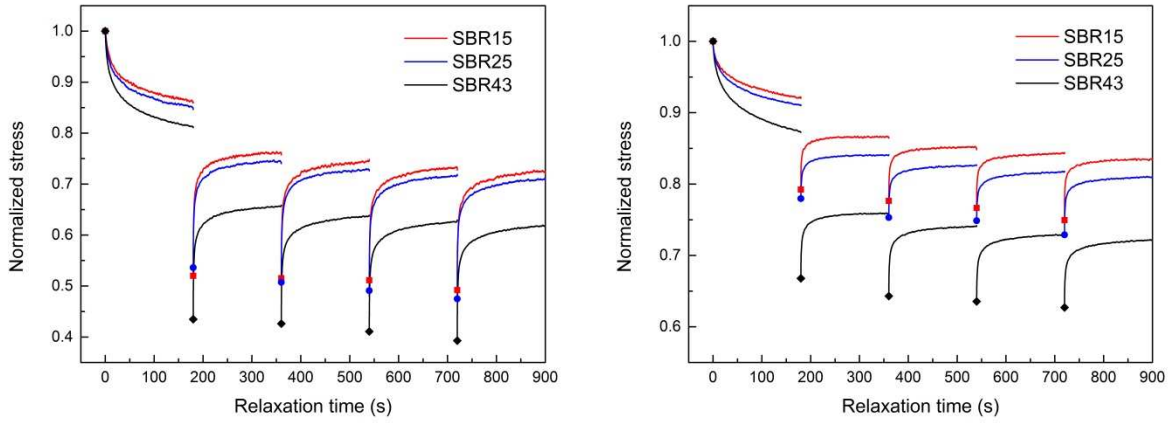

(a) (b)

Figure 2.3.2. Stress evolution during the relaxation periods of the multi-step cyclic tests at different pre-stretch levels: (a) $\lambda_{min}=1.2$, (b) $\lambda_{min}=1.5$.

The stress decreases in the first relaxation period and it increases in the others. At each relaxation period and after the initial transient change in stress, the relaxation response tends towards a stabilized state for which there is no significant change in stress. This tendency of stress stabilization is more pronounced in the test with higher pre-stretch level, and especially for the last four relaxation periods. Since the relaxation response is clearly affected by the pre-stretch level, the nonlinear viscoelasticity of the material is further evaluated. Furthermore, it is observed that the concentration in carbon-black fillers has an important effect on the

normalized stress evolution, which may be explained by the promotion effect of rigid particles on macroscopic viscoelastic strain (Laiarinandrasana et al., 2012).

2.3.2.3.2. Fatigue-induced stress-softening

The fatigue-induced stress-softening response issued from the multi-step cyclic tests, after reaching different assigned pre-stretches, is presented in Figure 2.3.3 for the three carbon-filled SBR materials.

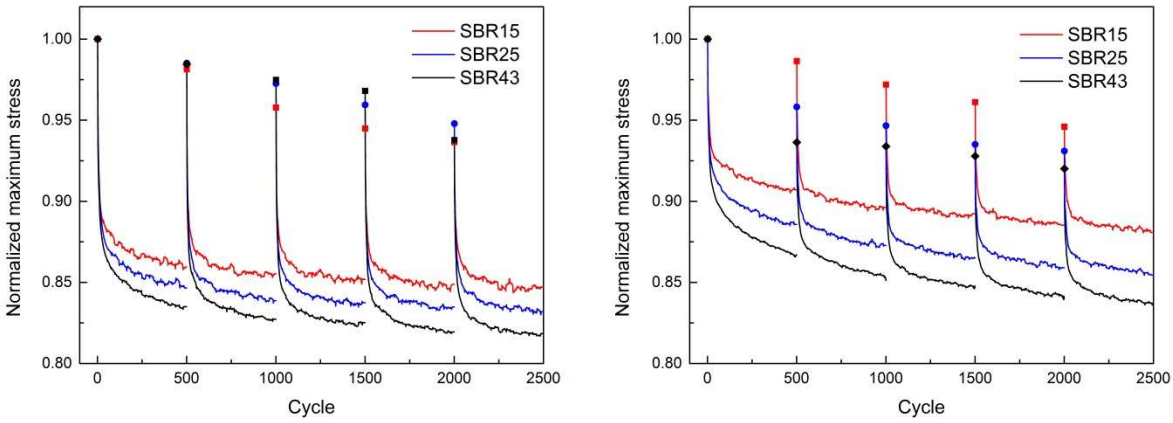

(a) (b)

Figure 2.3.3. Fatigue-induced stress-softening response of the multi-step cyclic tests at different pre-stretch levels: (a) $\lambda_{\min} = 1.2$, (b) $\lambda_{\min} = 1.5$.

At each cyclic loading block, the stress-softening is substantial during the first few cycles and is followed by a more gradual stress-softening which tends towards a stabilized stress dependent on the reinforcement and the applied pre-stretching. The softening magnitude increases with the filler content and decreases with the pre-stretch level. Recall that the stabilized response was associated in our theory to a viscous-related feature. From one block to another and after the initial transient softening, the stress tends further to recapture the path of the interrupted cyclic response. More interestingly, a considerable recovery in fatigue-induced stress-softening is evidenced by means of the multi-step cyclic tests. Indeed, from one block to another, a large part of the initial transient stress-softening is recovered. The underlying physical mechanism is therefore recoverable and associated to material viscoelasticity. The recovery extent of stress-softening is believed to increase with the magnitude of the holding time in the relaxation periods. In the meantime, it can be observed that the recovery in fatigue-induced stress-softening diminishes with the block number. As a consequence, the observable decrease in stress may be associated in part with recoverable

viscoelastic mechanisms and in another part with unrecoverable damage mechanisms. These two types of dissipative network rearrangements occurring inside the rubber-filler material system are two relative mechanisms whose quantification depends on the load time-scale. These observations give significance to the constitutive theory of the previous Part considering these two types of mechanisms in the form of two distinct internal state variables.

The unrecoverable rearrangements inducing damage find several plausible explanations in the literature. The scission mechanism of short chains within the rubber matrix is probably the most trivial (Mullins, 1948; Marckmann et al., 2002; Chagnon et al., 2006; Ayoub et al., 2011, 2014a). This mechanism is activated when the extensibility limit of short chains is reached. More specifically, the decrease in stress observed in the first extension (i.e. Mullins effect) is activated for stretch levels greater than a maximum obtained in the previous deformation history. A similar origin may be associated to the progressive stress degradation in pure rubbers, resulting from the fatigue loading history, but with a lower intensity as it is extended over time. The progressive stress-softening may be associated to the progressive breakdown of short chains being stuck between entangled chains. At each cycle, some entangled chains progressively split open. The chain disentanglement leads to the progressive scission of short chains being stuck between them and reaching their extensibility limit (Ayoub et al., 2011). The process of chain disentanglement / chain scission continues until it is totally consumed leading to the observable stabilized stress. The carbon-black fillers act on the SBR fatigue-induced stress-softening response due to their strain-amplifying effect. As clearly illustrated in Figure 2.3.3, the increase in carbon-black content has a strong effect on the degree to which the material is softened. As a consequence, the previous set of plausible fatigue mechanisms must also consider the filler-matrix interactions. Several competing views were proposed to explain the origin of the stress-softening by involving the fillers in the underlying physical mechanisms: breakdown of short chains between two filler aggregates (Bueche, 1960), chain "slipping" over the filler surface (Houwink, 1956), breakdown of filler aggregates (Kraus et al., 1966) and chain disentanglement between two filler aggregates (Hanson et al., 2005).

2.3.2.3.3. Hysteresis and mechanical dissipation

The cyclic stress-strain response of the rubber-filler material system leads to energy dissipation which results from dissipative network rearrangements modifying the original network to another one at each new cycle. Illustrative examples of the hysteresis loop are provided in Figure 2.3.1 for the three carbon-filled SBR materials, indicating the filler effects

on hysteresis. The breakdown-rebound process of inter-aggregates links may be considered to be the main source of the observable hysteretic response at the macroscopic scale, due to the strong effects of carbon-black fillers on the response. Electrical resistivity measurements showed that the increase in filler content leads to the development of a filler network across the rubber matrix and a higher number of inter-aggregates links (Kraus, 1984; Pramanik et al., 1992; Diaz et al., 2014). The increase in electrical resistivity when the carbon-filled rubber is cyclically loaded is a sign of the breakdown of inter-aggregates links, beginning with the weakest ones and progressing to the strongest ones. The filler aggregates form new inter-aggregate links in new positions inside the rubber-filler material system, which are again broken during the cyclic loading and then reformed in other positions. All these network rearrangements contribute to the hysteretic process leading to energy dissipation at the macroscopic scale. The mechanical energy D dissipated during one complete cycle of cyclically loaded SBR is quantified by the area of the stress-strain hysteresis loop σ - ε :

$$D = \oint \sigma : d\varepsilon \tag{2.3.3}$$

Figure 2.3.4 presents the variations of the mechanical dissipation as a function of the cycle number, issued from the multi-step cyclic tests, after reaching different assigned pre-stretches.

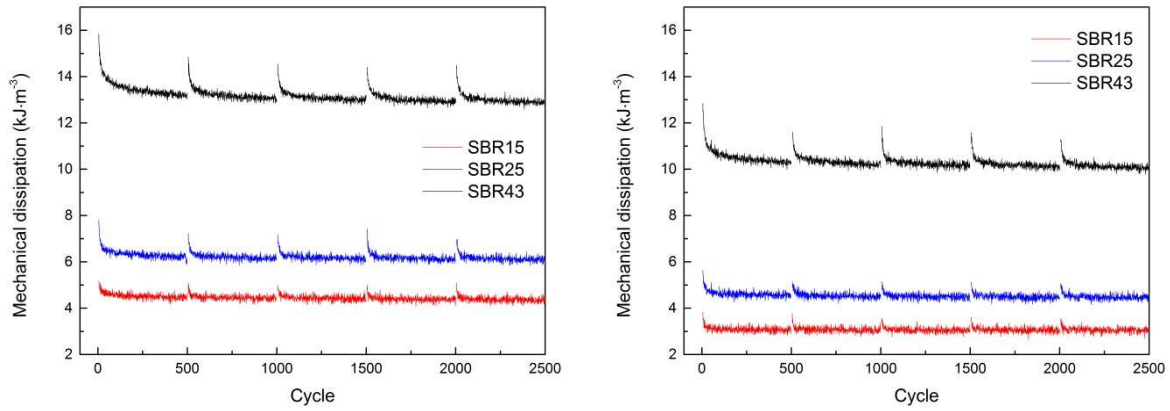

Figure 2.3.4. Mechanical dissipation of the multi-step cyclic tests at different pre-stretch levels: (a) $\lambda_{\min} = 1.2$, (b) $\lambda_{\min} = 1.5$.

By virtue of the fatigue-induced stress-softening, the strongest decrease in mechanical dissipation occurs during the first few cycles of each cyclic loading block and then the mechanical dissipation tends towards a stabilized state. The pre-stretch level dependency of the mechanical dissipation is evidenced in the figure. The higher the pre-stretch level, the smaller the mechanical dissipation. The decrease of the hysteresis loop area with the pre-

stretch level is mainly due to the nonlinear material response (Figure 2.3.1). In addition, the mechanical dissipation and the rate of the decrease with the cycles are observed to increase with the carbon-black content.

2.3.2.3.4. Intrinsic dissipation

When the carbon-filled SBR is cyclically loaded a portion of the mechanical dissipation is converted into heat which leads to an increase in temperature. An abrupt temperature increase occurs during the first few cycles and then tends towards a stabilized state with an equality of the generated heat and the heat lost into the environment (Ovalle-Rodas et al., 2014, 2016). The heat build-up increases with the filler content and the pre-stretch level. Actually, the temperature increase is induced by the intrinsic dissipation (Lion, 1997; Guo et al., 2017), which is closely associated with all irreversible thermodynamic processes involving both damage mechanisms, corresponding to unrecoverable network rearrangements, and viscoelastic mechanisms, corresponding to recoverable network rearrangements. From Eq. (2.2.72), a local zero-dimensional thermal equilibrium equation can be derived for flat and thin specimens with a constant cross-section (Boulanger et al., 2004):

$$C_{\mathrm{T0}}\left(\dot{\theta}+\frac{\theta}{\tau}\right)=\Phi_1+\hbar \tag{2.3.4}$$

where τ is a time constant characterizing the heat exchanges of the specimen gauge zone with the surroundings and $\theta=T-T_0$ is the average temperature variation of the specimen gauge zone, T_0 being the initial temperature. The terms C_{T0}, Φ_1 and $\hbar$ are the specific heat capacity at constant deformation, the intrinsic dissipation and the thermo-visoelastic-damage coupling coefficient, respectively. Considering that the accumulation of the thermo-visoelastic-damage coupling over one complete cycle is imperceptible, the average intrinsic dissipation $\bar{\Phi}_1$ over the cyclic loading process can be evaluated:

$$\bar{\Phi}_1=\frac{C_{\mathrm{T0}}}{n_c}\left(\theta_{n_c}+\frac{1}{\tau}\int_0^{t_{n_c}}\theta(t)\,dt\right) \tag{2.3.5}$$

where n_c and θ_{n_c} are the cycle number and the temperature increment at the end of the cyclic loading history t_{n_c}, respectively.

The average intrinsic dissipation $\bar{\Phi}_1$ is evaluated for the first cyclic block of the multi-step cyclic tests by processing via Eq. (2.3.5) the surface temperature data extracted in the specimen gauge zone. It is plotted in Figure 2.3.5 with the average mechanical dissipation $\bar{D}$:

$$\bar{D} = \frac{1}{n_c} \sum_{1}^{n_c} D \tag{2.3.6}$$

The dependences of the mechanical and intrinsic dissipations on the carbon-black content and on the pre-stretch level are relatively similar. In particular, the increase in dissipations is not linearly dependent on the carbon-black content which suggests modifications in the filler-rubber matrix interactions. It can be clearly observed that the intrinsic dissipation is smaller than the mechanical dissipation. Even it is relatively weak, the difference between the two dissipations gives an indication of the energy quantity stored in the rubber-filler material system, and, by this way, it gives insights into the unrecoverable network rearrangements inducing damage. In the theory formulated in the previous Part - Eqs. (2.2.99) and (2.2.102) - the damage-induced softening implies energy dissipation, i.e. the damage-related internal work $\kappa\dot{\chi}$ is positive and the proportionality coefficient β is superior to unity. The energy quantity stored in the cyclically loaded material highlights the complex role of fillers and the implication of the breakdown of inter-aggregates interactions creating new surfaces, this process increasing with the pre-stretch. A pre-stretch effect on the fatigue-life of carbon-filled SBR was earlier reported (Ayoub et al., 2012, 2014b). Indeed, as shown in Figure 2.3.5, higher pre-stretching leads to smaller dissipations but to higher differences between the two dissipations accelerating the damage accumulation towards degradation and failure.

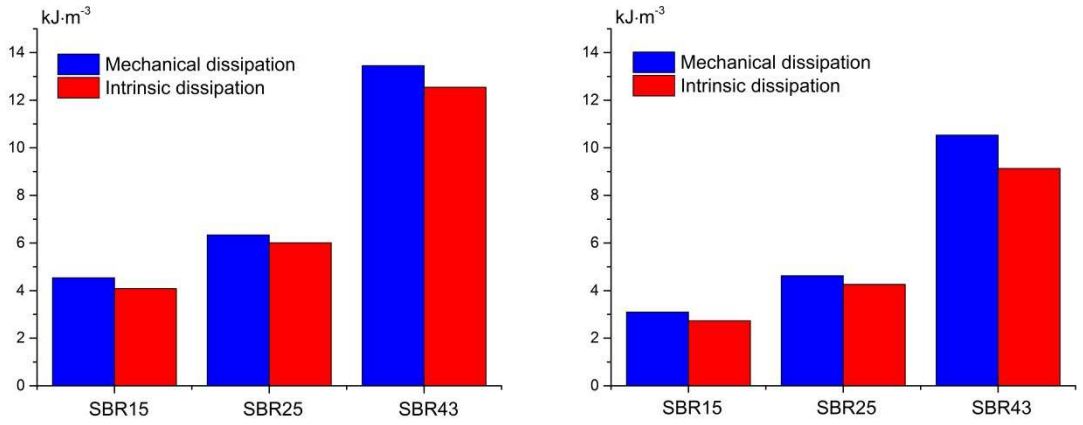

(a) (b)

Figure 2.3.5. Average dissipations at different pre-stretch levels: (a) $\lambda_{\min} = 1.2$, (b) $\lambda_{\min} = 1.5$.

2.3.2.4. Discussions on inelastic fatigue mechanisms

A plausible explanation of the inherent inelastic fatigue mechanisms with the pre-stretch dependency is proposed in this subsection under the guidance of our experimental

observations. An illustration of the physical mechanisms in pre-stretched cyclically loaded carbon-filled SBR is provided in Figure 2.3.6.

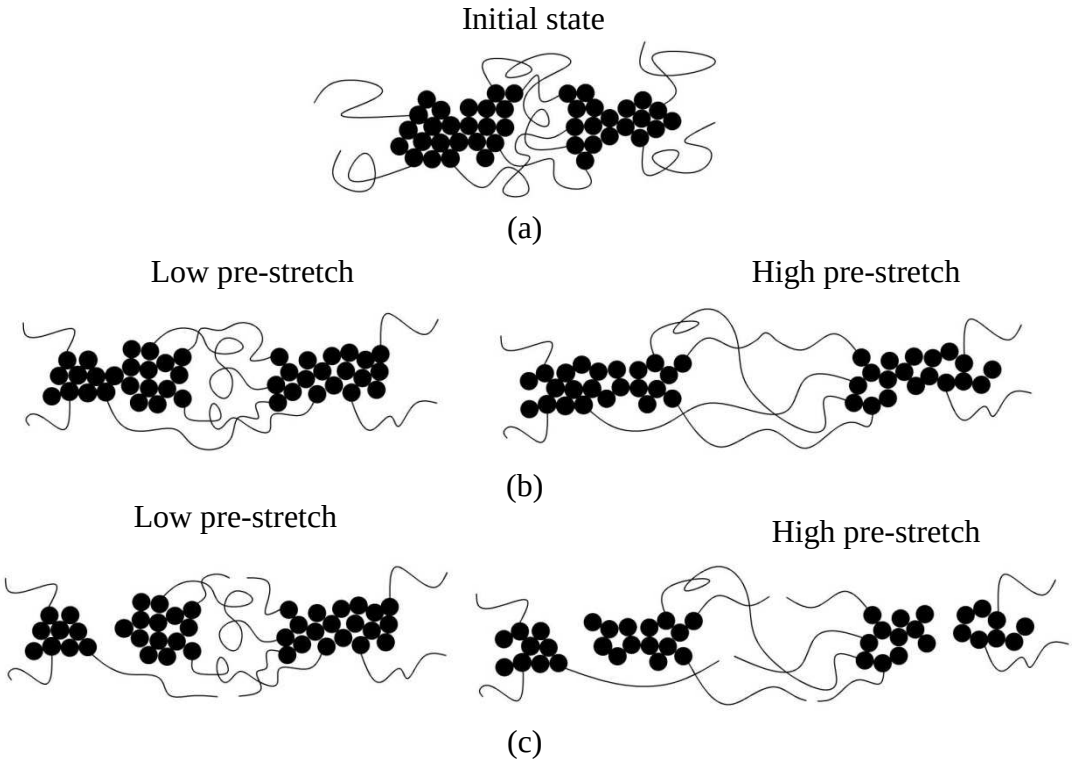

Figure 2.3.6. Physical mechanisms in pre-stretched cyclically loaded filled rubbers: (a) initial network, (b) pre-stretched network and (c) network rearrangement after pre-stretched cyclic loading.

A global view at all presented experimental observations (Figures 2.3.1-2.3.5) indicates that there is a quite significant effect of the two examined factors (i.e. filler content and pre-stretch level) on the reported inelastic phenomena, namely, stress relaxation, fatigue-induced stress-softening, hysteretic response and related mechanical dissipation along with dissipative heating. All these inelastic effects increase with the carbon-black content increase and with the pre-stretch level decrease

From the basic viewpoint of the continuum thermodynamics, the intrinsic dissipation is a consequence of two types of rearrangements in the rubber-filler material system, i.e. recoverable network rearrangements inducing viscoelasticity and unrecoverable network rearrangements inducing damage. The dissipation quantification in Figure 2.3.5 points out that the viscoelastic recoverable rearrangements may be the dominate inelastic fatigue mechanisms in the studied carbon-filled rubber. This is consistent with the stress-softening recovery observed in Figure 2.3.3 from the multi-step cyclic tests. The viscoelastic mechanisms depend on the filler-rubber matrix interactions, the chain-chain interactions and

the filler-filler interactions. The degree of these three types of interactions are highly dependent on, respectively, the filler-rubber matrix interface (chain "slipping" over the filler surface, desorption at the filler surface and bond breakdown at the filler surface), the chain entanglement density (viscous sliding between chains), and the contact surface area between fillers inside the aggregates (viscous sliding between carbon-black fillers). Besides, it has been shown that the addition of fillers impedes the segmental mobility of chains in a rubber compound (Kraus and Gruver, 1970; Thiele and Cohen, 1980). The interfacial interaction between rubber matrix and fillers forms a region where the chain mobility is gradually reduced, through variations in the glass transition temperature as a function of the distance to the filler surface (Berriot et al., 2002, 2003).

The increase in filler content is related to higher interactions between carbon-black fillers inside the aggregates. The internal network rearrangements between aggregates during the cyclic loading leads to the mechanical dissipation manifested by the hysteretic process in the carbon-filled SBR cyclic response. The breakdown-rebound process of inter-aggregates interactions, from which originate the hysteretic response of the rubber-filler material system, is also a recoverable mechanism highly dependent on the load time-scale. As a consequence of the increase in inter-aggregates interactions with the carbon-black content, a higher additional energy is dissipated within the breakdown-rebound process of inter-aggregates links.

The internal network rearrangements during the cyclic loading are schematically illustrated in Figure 2.3.6 at different pre-stretch levels, by involving the plausible recoverable and unrecoverable rearrangements in the rubber-filler material system. The application of a pre-stretch decreases the filler-rubber matrix interactions, the chain entanglement density and the contact surface area between fillers inside the aggregates. As a consequence, the viscous motion degree in the rubber-filler material system decreases with the applied pre-stretch level, leading to the decrease of the inelastic effects at the macroscopic scale. Although the viscoelastic recoverable rearrangements dominate over the inelastic fatigue mechanisms, some damage effects may contribute to the intrinsic dissipation. The possible unrecoverable mechanisms may be induced by the progressive breakdown of short chains between two filler aggregates as well as by the breakdown-rebound process of inter-aggregates links. The latter mechanism may be due to a part of the breakdown of the inter-aggregates links that cannot be reformed on the time-scale of measurements, as evidenced by the fatigue-induced stress-softening response issued from the multi-step cyclic tests (Figure 2.3.3). The pre-stretch level

increases both the number of chain scission between two filler aggregates and the number of permanent filler aggregate ruptures. The two possible damage effects may also potentially modify the material viscosity in two antagonist ways. Indeed, the transformation of some broken chains into dangling chains during the network rearrangements may increase the viscosity, i.e. higher energy dissipated. The rupture of filler aggregates, decreasing the contact surface area between fillers inside the aggregates, may decrease the viscous sliding between fillers, i.e. lower energy dissipated. Among these two possible damage effects, it is believed that the permanent filler aggregate rupture dominates since the dissipation, estimated in Figure 2.3.4 from the multi-step cyclic tests, decreases with the block number. In addition, the degradation of the interphase around the fillers is potentially an additional cause of the weaker filler-rubber matrix interactions (Boutaleb et al., 2009; Zaïri et al., 2011a).

2.3.3. Modeling results and discussion

We propose herein a numerical modeling of the inelastic effects in cyclically loaded SBR and to discuss how the fillers may be included in the constitutive model formulated in the previous Part.

2.3.3.1. Filled network

In addition to a stiffening effect, the concentration in carbon-black fillers enhances the viscosity in the rubber-filler material system due to the viscous sliding between fillers and fillers / free chains. In order to consider the effective contribution of the fillers the Bergstrom and Boyce (1999) amplification procedure may be applied to the average micro-stretch imposed on chains. The right and left Cauchy-Green deformation tensors, given by Eqs. (2.2.24) and (2.2.26), become:

$$\left\langle \bar{\mathbf{C}}_{\mathrm{iso}} \right\rangle = X\left(\bar{\mathbf{C}}_{\mathrm{iso}} - \mathbf{I}\right) + \mathbf{I}\,,\ \left\langle \mathbf{B}_{\mathrm{iso}} \right\rangle = X\left(\mathbf{B}_{\mathrm{iso}} - \mathbf{I}\right) + \mathbf{I} \tag{2.3.7}$$

$$\left\langle \bar{\bar{\mathbf{C}}}_{\mathrm{e\_1}} \right\rangle = X\left(\bar{\bar{\mathbf{C}}}_{\mathrm{e\_1}} - \mathbf{I}\right) + \mathbf{I}\,,\ \left\langle \mathbf{B}_{\mathrm{e\_1}} \right\rangle = X\left(\mathbf{B}_{\mathrm{e\_1}} - \mathbf{I}\right) + \mathbf{I} \tag{2.3.8}$$

$$\left\langle \bar{\bar{\mathbf{C}}}_{\mathrm{e\_2}} \right\rangle = X\left(\bar{\bar{\mathbf{C}}}_{\mathrm{e\_2}} - \mathbf{I}\right) + \mathbf{I}\,,\ \left\langle \mathbf{B}_{\mathrm{e\_2}} \right\rangle = X\left(\mathbf{B}_{\mathrm{e\_2}} - \mathbf{I}\right) + \mathbf{I} \tag{2.3.9}$$

where X is the amplification factor related to the concentration / distribution of fillers in the rubber network. The empirical form of the amplification factor X initially proposed by Guth (1945) is given by the following general formula:

$$X\left(v_f\right) = 1 + 0.67cv_f + 1.62c^2v_f^2 \tag{2.3.10}$$

in which $c \geq 1$ is a shape factor considering the filler agglomeration.

The average free energy function of the carbon-filled SBR material is given by:

$$\psi_{\mathrm{SBR}} = \left(1-v_f\right)\begin{Bmatrix}\hat{\psi}_{\mathrm{R}}\left(T,\left\langle\overline{\mathbf{C}}_{\mathrm{iso}}\right\rangle,\chi\right)+\hat{\psi}_{\mathrm{v\_1}}\left(T,\left\langle\overline{\overline{\mathbf{C}}}_{\mathrm{e\_1}}\right\rangle\right)+\hat{\psi}_{\mathrm{v\_2}}\left(T,\left\langle\overline{\overline{\mathbf{C}}}_{\mathrm{e\_2}}\right\rangle\right)\\+\hat{\psi}_{\mathrm{vol}}\left(T,J\right)\end{Bmatrix} \tag{2.3.11}$$

where $\hat{\psi}_{\mathrm{R}}\left(T,\left\langle\overline{\mathbf{C}}_{\mathrm{iso}}\right\rangle,\chi\right)$ is the amplified relaxed free energy function of Eq. (2.2.75), $\hat{\psi}_{\mathrm{v\_1}}\left(T,\left\langle\overline{\overline{\mathbf{C}}}_{\mathrm{e\_1}}\right\rangle\right)$ and $\hat{\psi}_{\mathrm{v\_2}}\left(T,\left\langle\overline{\overline{\mathbf{C}}}_{\mathrm{e\_2}}\right\rangle\right)$ are the amplified viscous free energy functions of Eq. (2.2.79) (entangled and non-entangled free chains, respectively) and $\hat{\psi}_{\mathrm{vol}}\left(T,J\right)$ is the volumetric free energy function given by Eq. (2.2.82).

The average Cauchy stress of the carbon-filled SBR material is given by:

$$\boldsymbol{\sigma}_{\mathrm{SBR}} = \underline{\boldsymbol{\sigma}}_{\mathrm{R}} + \underline{\boldsymbol{\sigma}}_{\mathrm{v\_1}} + \underline{\boldsymbol{\sigma}}_{\mathrm{v\_2}} + \underline{\boldsymbol{\sigma}}_{\mathrm{vol}} \tag{2.3.12}$$

in which $\underline{\boldsymbol{\sigma}}_{\mathrm{R}}$ is the average relaxed Cauchy stress, $\underline{\boldsymbol{\sigma}}_{\mathrm{v\_1}}$ and $\underline{\boldsymbol{\sigma}}_{\mathrm{v\_2}}$ are the average viscous Cauchy stresses and $\underline{\boldsymbol{\sigma}}_{\mathrm{vol}}$ is the average volumetric Cauchy stress expressed, respectively, as:

$$\underline{\boldsymbol{\sigma}}_{\mathrm{R}} = \left(1-v_f\right) X \frac{n_{\mathrm{R}} k_{\mathrm{B}} T}{3J} \frac{\sqrt{N_{\mathrm{R}}}}{\left\langle\lambda_{\mathrm{iso}}\right\rangle}\left\langle\zeta_{\mathrm{iso}}\right\rangle\left(\mathbf{B}_{\mathrm{iso}} - \left(\lambda_{\mathrm{iso}}\right)^2 \mathbf{I}\right) \tag{2.3.13}$$

$$\underline{\boldsymbol{\sigma}}_{\mathrm{v\_1}} = \left(1-v_f\right) X \frac{n_{\mathrm{v\_1}} k_{\mathrm{B}} T}{3J} \frac{\sqrt{N_{\mathrm{v\_1}}}}{\left\langle\lambda_{\mathrm{e\_1}}\right\rangle}\left\langle\zeta_{\mathrm{v\_1}}\right\rangle\left(\mathbf{B}_{\mathrm{e\_1}} - \left(\lambda_{\mathrm{e\_1}}\right)^2 \mathbf{I}\right) \tag{2.3.14}$$

$$\underline{\boldsymbol{\sigma}}_{\mathrm{v\_2}} = \left(1-v_f\right) X \frac{n_{\mathrm{v\_2}} k_{\mathrm{B}} T}{3J} \frac{\sqrt{N_{\mathrm{v\_2}}}}{\left\langle\lambda_{\mathrm{e\_2}}\right\rangle}\left\langle\zeta_{\mathrm{v\_2}}\right\rangle\left(\mathbf{B}_{\mathrm{e\_2}} - \left(\lambda_{\mathrm{e\_2}}\right)^2 \mathbf{I}\right) \tag{2.3.15}$$

$$\underline{\boldsymbol{\sigma}}_{\mathrm{vol}} = \left(1-v_f\right)\left[\frac{1}{2J} k\left(J^2-1\right) - 3\alpha k\left(T-T_0\right)\right]\mathbf{I} \tag{2.3.16}$$

where $\left\langle\lambda_{\mathrm{iso}}\right\rangle$ is given by Eq. (2.2.76), $\left\langle\zeta_{\mathrm{iso}}\right\rangle$ is given by Eq. (2.2.78), $\left\langle\lambda_{\mathrm{e\_1}}\right\rangle$ and $\left\langle\lambda_{\mathrm{e\_2}}\right\rangle$ are given by Eq. (2.2.80) and $\left\langle\zeta_{\mathrm{v\_1}}\right\rangle$ and $\left\langle\zeta_{\mathrm{v\_2}}\right\rangle$ are given by Eq. (2.2.81).

In what follows, the proposed constitutive model is identified and verified using the carbon-filled SBR experimental data. The results of the finite element simulations are also criticized by comparing the predicted values provided by the proposed model with the experimental data obtained from the two-block tests. A view of the finite element mesh of the tested dog-bone shaped specimen is given in Figure 2.2.3b of the Part I, in which the same thermo-mechanical boundary conditions regarding the experimental tests are simulated for the model identification and verification.

2.3.3.2. Identification

In this subsection, the SBR thermo-mechanical parameters are identified (sometimes specified) in the order of the model parameter list provided in Section 2.2.3. As revealed by our experimental observations, the recoverable and unrecoverable network rearrangements are two relative mechanisms dependent on the loading condition, especially on the load time-scale. In light of the significance of the viscoelastic effects in the carbon-filled SBR inelastic fatigue process, the damage effects on the chain-scale material constants are not considered in the present identification. Furthermore, the temperature-induced network rearrangements are also not considered due to the relative low level in measured dissipative heating.

The numerical parametric study presented in Figures 2.2.4 and 2.2.5 of the previous Part revealed the respective role of selected material constants on the stress-softening, the hysteresis and the heat build-up in the tested dog-bone shaped specimen without alteration of the rubber network by damage-dissipative heating effects. In this part of the work, an original deterministic procedure is proposed to extract using the SBR experimental data the physically interpretable model parameters of the rubber matrix: $n_R k_B T$, N_R, $n_{v\_1} k_B T$, $n_{v\_2} k_B T$, N_{v_1}, N_{v_1}, r_1, r_2, m and d. The properties of the perfect network are identified via an amplification-inspired procedure using the relaxed-stress data whereas the history-dependent mechanical cyclic features of one filler content serve to the identification of the properties of the entangled and non-entangled free chains.

2.3.3.2.1. Network parameters of the cross-linked chains

In the case of incompressible uniaxial deformation, the uniaxial average relaxed Cauchy stress σ_R is given from Eq. (2.3.13), as a function of the uniaxial stretch λ, as follows:

$$\sigma_R = \left(1-v_f\right) X \frac{n_R k_B T}{3} \frac{\sqrt{N_R}}{\langle \lambda_* \rangle} \langle \zeta_* \rangle \left(\lambda^2 - \frac{1}{\lambda} \right) \tag{2.3.17}$$

where:

$$\langle \zeta_* \rangle = \mathcal{L}^{-1}\left(\frac{\langle \lambda_* \rangle}{\sqrt{N_R}} \right) \approx \frac{\langle \lambda_* \rangle}{\sqrt{N_R}} \frac{3N_R - \langle \lambda_* \rangle^2}{N_R - \langle \lambda_* \rangle^2} \tag{2.3.18}$$

$$\langle \lambda_* \rangle = \sqrt{X\left(\lambda_*^2 - 1\right) + 1} \tag{2.3.19}$$

in which:

$$\lambda_* = \sqrt{\frac{1}{3}\left(\lambda^2 + \frac{2}{\lambda} \right)} \tag{2.3.20}$$

In light of the difficulty to regress simultaneously the experimental data of the three carbon-filled SBR materials according to Eq. (2.3.17), a convenient approach is proposed to identify the network parameter $n_R k_B T$ and the filler agglomeration shape factor *c*. By considering the rubber-filler material system as a homogeneous medium, the static stiffness C_R may be extracted from the following formula:

$$C_R = 3\sigma_R \left\{ \frac{\sqrt{N_R}}{\lambda_*} \zeta_* \left(\lambda^2 - \frac{1}{\lambda} \right) \right\}^{-1} \tag{2.3.21}$$

where:

$$\zeta_* = \mathcal{L}^{-1}\left(\frac{\lambda_*}{\sqrt{N_R}} \right) \approx \frac{\lambda_*}{\sqrt{N_R}} \frac{3N_R - \lambda_*^2}{N_R - \lambda_*^2} \tag{2.3.22}$$

Using the relaxed-stress deduced from the multi-step stress relaxation, the value of the static stiffness C_R for each carbon-filled SBR material is obtained. The amplification effect of carbon-black fillers on micro-stretch imposed on chains can be considered as an equivalent amplification effect applied on the static stiffness C_R at the macroscopic scale. Figure 2.3.7a presents the static stiffness C_R as a function of the filler content and the fitting with the following equation:

$$C_R = \hat{C}_R\left(v_f\right) = \left(1 - v_f\right) X n_R k_B T \tag{2.3.23}$$

Considering that the relaxed-stress is deduced from the multi-step stress relaxation, in which the holding time is sufficient for restoring the temperature up to the initial value (i.e. room temperature T_0), the network parameter $n_R k_B T_0$ and the filler agglomeration shape factor *c* can be extracted by means of parametric regression with least square method:

$$n_R k_B T_0 = 0.34 \text{ MPa} \tag{2.3.24}$$

$$c = 3.69 \tag{2.3.25}$$

By combining Eqs. (2.3.21) and (2.3.23), the uniaxial average relaxed Cauchy stress can be alternatively expressed as:

$$\sigma_R = \left(1 - v_f\right) X \frac{n_R k_B T}{3} \frac{\sqrt{N_R}}{\lambda_*} \zeta_* \left(\lambda^2 - \frac{1}{\lambda} \right) \tag{2.3.26}$$

The uniaxial average relaxed Cauchy stress given by Eq. (2.3.17), and issued from the Bergstrom and Boyce (1999) amplified procedure, is compared in Figure 2.3.7b with the proposed formula given by Eq. (2.3.26). The two solutions give very similar results for the three amounts of carbon-black. This micromechanical treatment introducing the nonlinear

dependence on the volume fraction was earlier used for other types of material responses (Ayoub et al., 2010; Zaïri et al., 2010, 2011b).

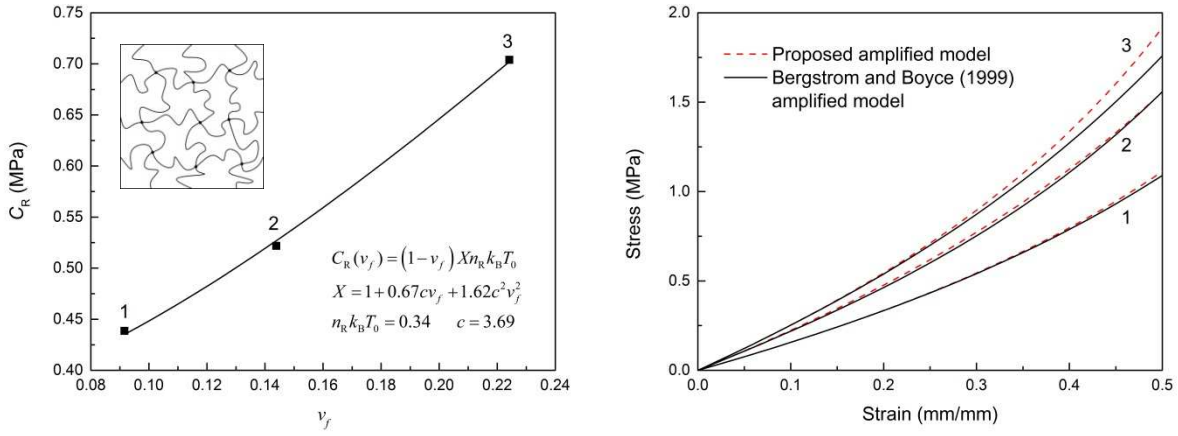

(a) (b)

Figure 2.3.7. Identification of the network parameters of the cross-linked chains: (a) static stiffness as a function of the filler volume fraction, (b) relaxed-stress response considering the two amplified models (1: SBR15, 2: SBR25, 3: SBR43).

The value of N_R can be further determined by considering that the denominator of the Padé approximation given by Eq. (2.3.22) is equal to zero:

$$N_R = \frac{1}{3}\left(\lambda_\infty^2 + \frac{2}{\lambda_\infty}\right) = 6.0 \tag{2.3.27}$$

in which λ_∞ is the uniaxial stretch for which the stress increases in an exponential way.

2.3.3.2.2. Viscous parameters of the free chains

The identification exercise of viscous parameters is not trivial and its difficulty is proportional with the complexity of the constitutive model itself (Pyrz and Zaïri, 2007; Abdul-Hameed et al., 2014a, 2014b).

From a micromechanical viewpoint, we assume that the network properties in the rubber-filler material system are the same as those of the pure rubber network. The remarkable effect of the filler reinforcement on the cyclic dissipation and the stress-softening is seen in Figures 2.3.8 and 2.3.9, in which are plotted the evolutions of the stresses in each sub-network, as a function of time and strain, respectively, for the SBR43 material and the pure rubber network.

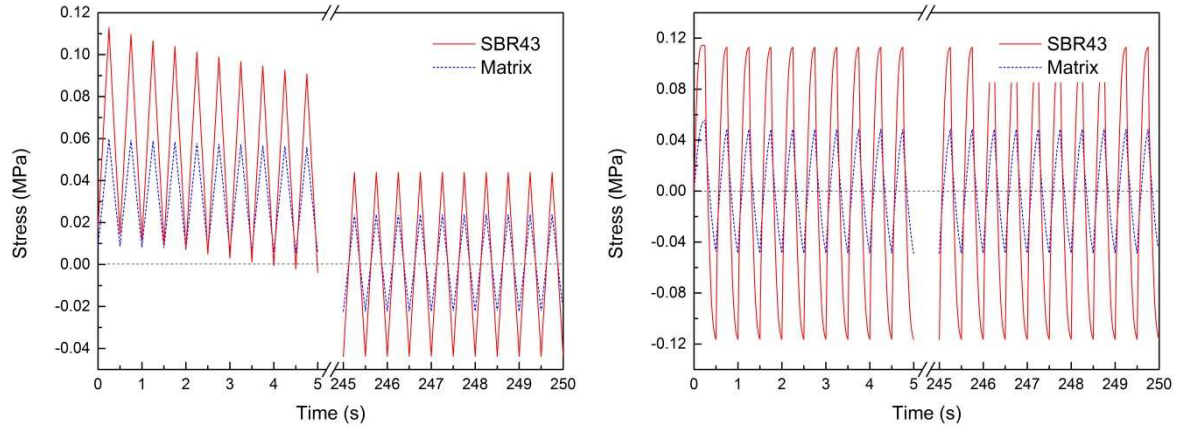

(a) (b)

Figure 2.3.8. Stress as a function of time in: (a) entangled free chains, (b) non-entangled free chains.

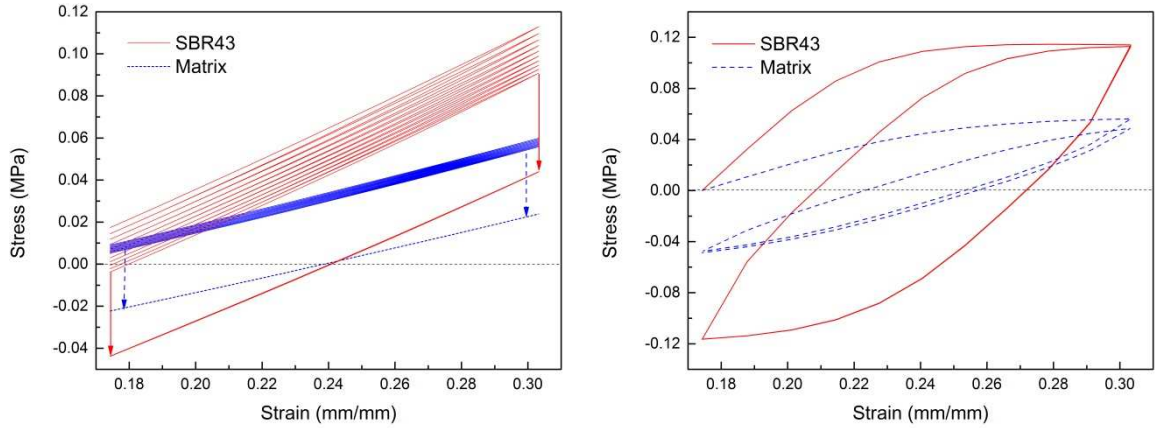

(a) (b)

Figure 2.3.9. Stress as a function of strain in: (a) entangled free chains, (b) non-entangled free chains.

The magnitude of these two phenomena can be also predicted in a given material point of the meshed specimen. As an illustrative example, Figure 2.3.10 gives the local viscous stretch fields. The reduced section in the gauge length allows locating the highest viscous stretch in this region and, as a consequence, the highest stress-softening and hysteresis. The highest magnitude of the intrinsic dissipation related to thermo-hysteretic effects (mainly induced by the non-entangled free chains) occurs in this zone.

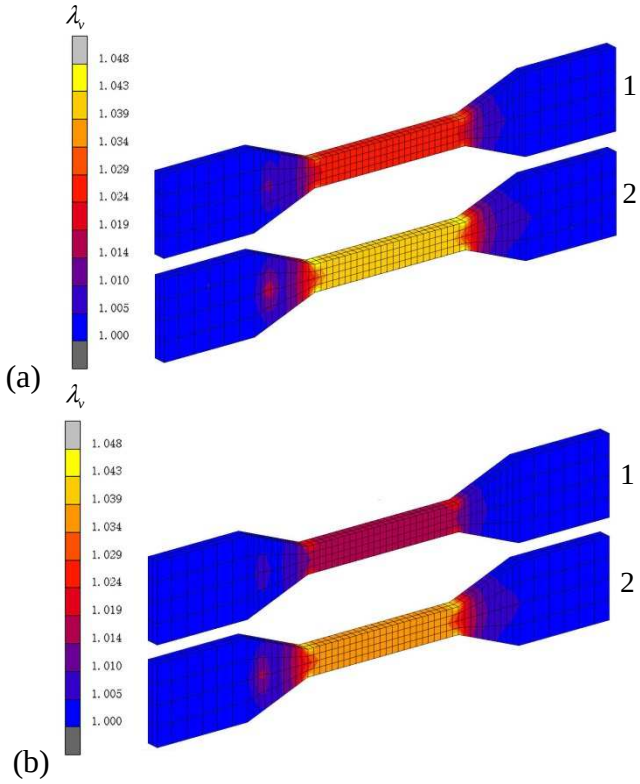

Figure 2.3.10. Contours of the viscous stretches in the flat specimen: (a) SBR43, (b) matrix (1: entangled free chains, 2: non-entangled free chains).

The properties of the entangled and non-entangled free chains are identified via the amplification-inspired procedure. Analogous to the static stiffness C_{R}, the viscous parameters $C_{\mathrm{v\_1}}$ and $C_{\mathrm{v\_2}}$, related, respectively, to the entangled and non-entangled free chains, are defined by considering the rubber-filler material system as a homogeneous medium. In the case of incompressible uniaxial deformation, the viscoelastic response can be analogous to the harmonic response of a simple mechanical model consisting to two parallel Maxwell elements, each constituted by an elastic spring in series with a viscous dashpot. Let us consider the Maxwell element of the entangled free chains cyclically loaded from the minimum strain $\varepsilon_{\min} = \ln \lambda_{\min}$ to the maximum strain $\varepsilon_{\max} = \ln \lambda_{\max}$. Due to the low relaxation rate of the viscous dashpot, the maximum stretch in the elastic spring tends to decrease during the cyclic loading and the middle point of the elastic spring moves monotonously towards the stretch direction until reaching $(\varepsilon_{\max} - \varepsilon_{\min})/2$. The decrease of the maximum stretch in the elastic spring leads to the decrease of the macroscopic stress from the stress $\sigma_{\max\_1}$ of the first cycle to the stress $\sigma_{\max\_n_c}$ of the last cycle. The viscous stiffness $C_{\mathrm{v\_1}}$ is roughly estimated from the stress-softening response by:

$$C_{\mathrm{v\_1}} = \frac{\sigma_{\mathrm{max\_1}} - \sigma_{\mathrm{max\_n_c}}}{\left(\varepsilon_{\max} - \varepsilon_{\min}\right)/2} \tag{2.3.28}$$

The viscous stiffness $C_{\mathrm{v\_2}}$ is determined from a loading-unloading cycle. Using the tangent modulus of the instantaneous unloading $E_{\mathrm{u}} = d\sigma/d\varepsilon$ and the static stiffness $C_{\mathrm{R}}\left(2\lambda_u^2 + 1/\lambda_u\right)/3$ at the uniaxial stretch reversal λ_u, the viscous stiffness $C_{\mathrm{v\_2}}$ is estimated by the following equation:

$$C_{\mathrm{v\_2}} = E_u - \frac{C_{\mathrm{R}}}{3}\left(2\lambda_u^2 + \frac{1}{\lambda_u}\right) - C_{\mathrm{v\_1}} \tag{2.3.29}$$

The viscous stiffness values, identified using the SBR43 experimental data, are:

$$\left(C_{\mathrm{v\_1}}\right)_{\mathrm{SBR43}} = 0.22 \text{ MPa} \tag{2.3.30}$$

$$\left(C_{\mathrm{v\_2}}\right)_{\mathrm{SBR43}} = 0.47 \text{ MPa} \tag{2.3.31}$$

The distribution of the carbon-black fillers is considered identical inside the three parallel networks. In other words, the magnitude of strain-amplifying effect of the fillers is assumed to be the same for the cross-linked chains, the entangled free chains and the non-entangled free chains. Thus, the amplification equation identified for the cross-linked chains may be applied to the two other networks by using similar formulae:

$$C_{\mathrm{v\_1}} = \hat{C}_{\mathrm{v\_1}}\left(v_f\right) = \left(1 - v_f\right) X n_{\mathrm{v\_1}} k_{\mathrm{B}} T \tag{2.3.32}$$

$$C_{\mathrm{v\_2}} = \hat{C}_{\mathrm{v\_2}}\left(v_f\right) = \left(1 - v_f\right) X n_{\mathrm{v\_2}} k_{\mathrm{B}} T \tag{2.3.33}$$

Combining Eqs. (2.3.30), (2.3.31), (2.3.32) and (2.3.33), and ignoring the temperature effect, the material properties of the entangled and non-entangled free chains are easily extracted:

$$n_{\mathrm{v\_1}} k_{\mathrm{B}} T_0 = 0.11 \text{ MPa} \tag{2.3.34}$$

$$n_{\mathrm{v\_2}} k_{\mathrm{B}} T_0 = 0.24 \text{ MPa} \tag{2.3.35}$$

The values of $N_{\mathrm{v\_1}}$ and $N_{\mathrm{v\_2}}$ for the entangled and non-entangled free chains, respectively, are assumed to be equal and to be the same than that identified for N_{R}:

$$N_{\mathrm{v\_1}} = N_{\mathrm{v\_2}} = 6.0 \tag{2.3.36}$$

The values of the other viscous parameters are obtained through the adjustment of the best response for the highest filler content by means of trial and error:

$$r_1 = 3.0 \text{ MPa}^{-2}\text{s}^{-1} \tag{2.3.37}$$

$$r_2 = 265 \text{ MPa}^{-2}\text{s}^{-1} \tag{2.3.38}$$

$$d = -0.01 \tag{2.3.39}$$

$$m = 2.0 \tag{2.3.40}$$

The damage kinetics of the chain-scale material constants given by Eq. (2.2.102) is set to zero and hence the coupling parameter takes the following value:

$$\beta = 1.0 \tag{2.3.41}$$

The identification results of the properties of the entangled and non-entangled free chains are provided in Figures 2.3.11 and 2.3.12, respectively. The ability of the model to capture the SBR43 experimental data can be verified for the two pre-stretch levels.

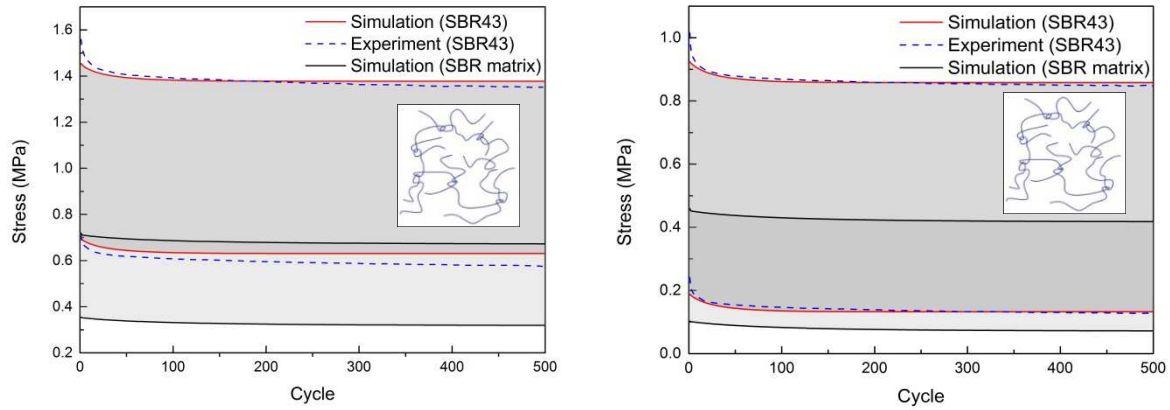

(a) (b)

Figure 2.3.11. Identification of the viscous parameters of the entangled free chains using the SBR43 stress-softening response: (a) $\lambda_{\min} = 1.2$, (b) $\lambda_{\min} = 1.5$.

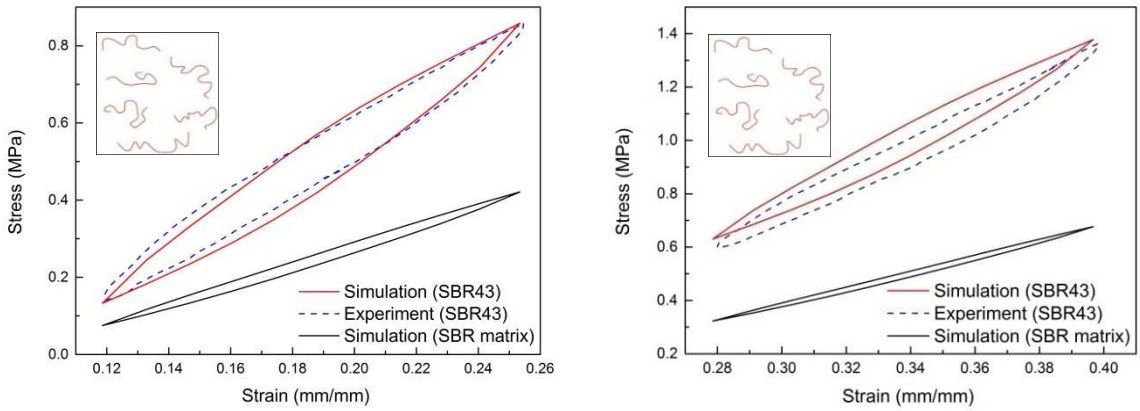

(a) (b)

Figure 2.3.12. Identification of the viscous parameters of the non-entangled free chains using the SBR43 hysteresis loop at the 250th cycle: (a) $\lambda_{\min} = 1.2$, (b) $\lambda_{\min} = 1.5$.

The properties of the rubber network in the rubber compound are supposed to be the same as those of the pure rubber network, for which the responses are also provided in Figures 2.3.11

and 2.3.12. The remarkable effect of the fillers on the increases of fatigue-induced stress-softening and hysteresis is pointed out.

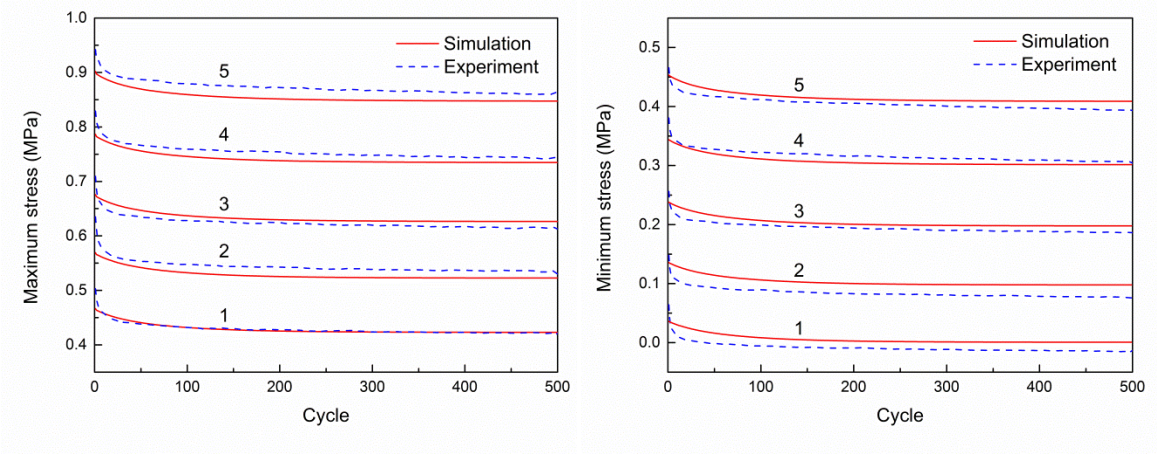

(a)

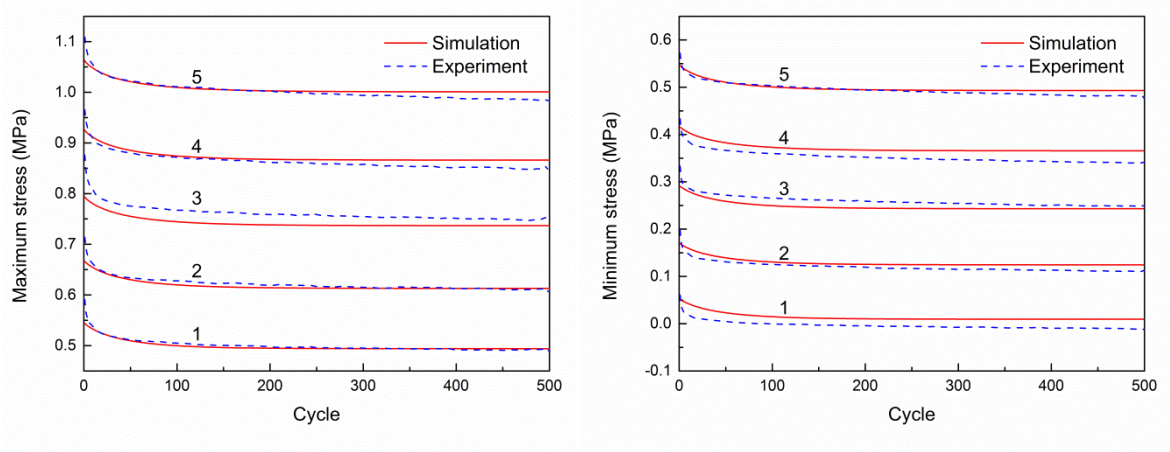

(b)

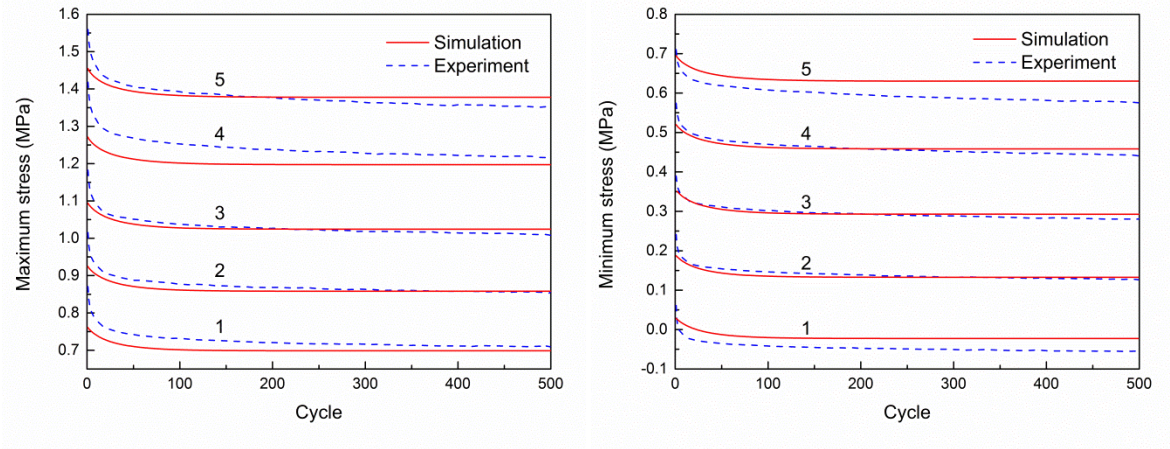

(c)

Figure 2.3.13. Experimental and simulated stress-softening (maximum and minimum stresses) at different minimum stretches (1: λ_{min}=1.1, 2: λ_{min}=1.2, 3: λ_{min}=1.3, 4: λ_{min}=1.4, 5: λ_{min}=1.5): (a) SBR15, (b) SBR25, (c) SBR43.

Remind that the model parameters were fitted to the SBR43 cyclic experimental data, and then the same material parameters were used to predict the SBR15 and SBR25 cyclic responses using the amplified-inspired approach. Therefore, except the relaxed-response parameters, the verification consists in a study of the capability of the model to fit the SBR43 experimental data and, to predict the SBR15 and SBR25 experimental data. The simulations are compared with the experiments in Figures 2.3.13, 2.3.14 and 2.3.15.

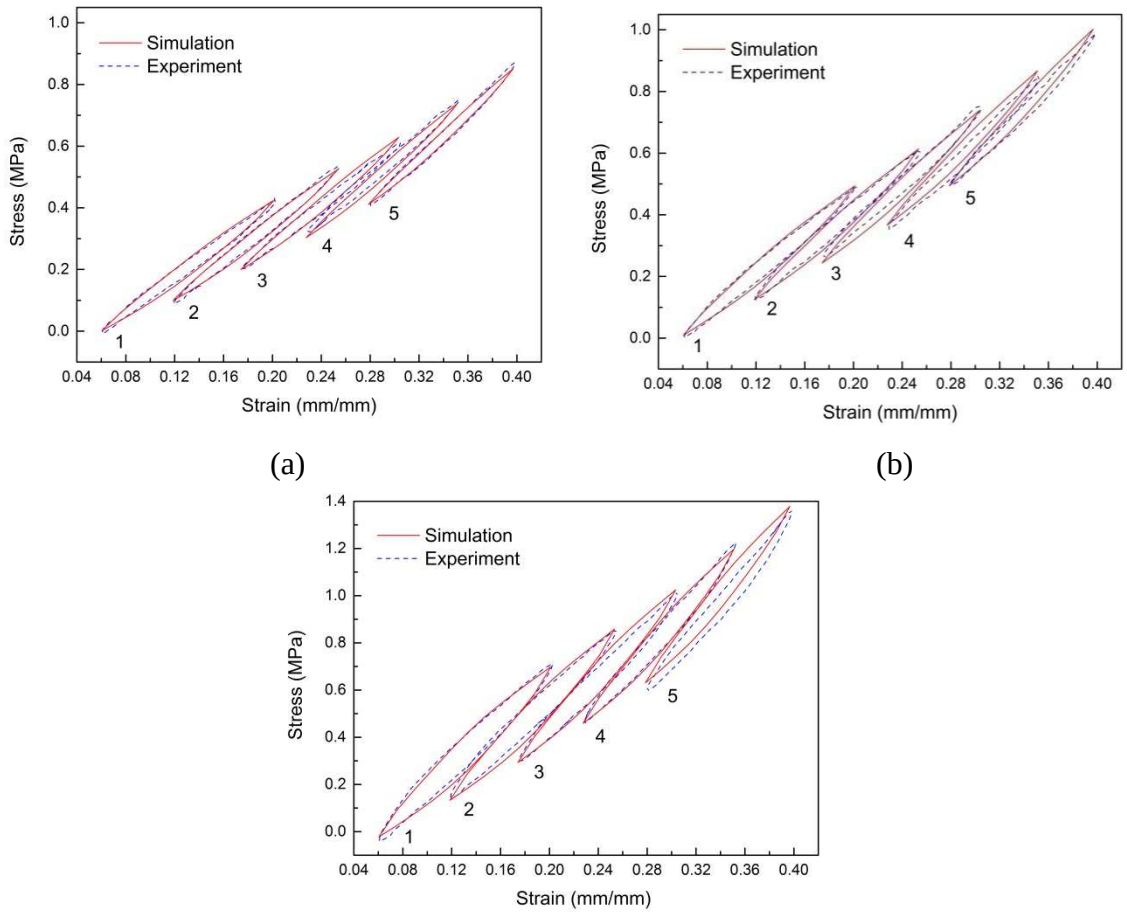

Figure 2.3.14. Experimental and simulated hysteretic response at 250th cycle and at different minimum stretches (1: λ_{min}=1.1, 2: λ_{min}=1.2, 3: λ_{min}=1.3, 4: λ_{min}=1.4, 5: λ_{min}=1.5): (a) SBR15, (b) SBR25, (c) SBR43.

The responses given by the proposed model and the experiments are shown for a material point taken on the gauge length of the dog-bone shaped specimen surface. A global view at these figures shows the ability of the model to capture, over the entire range of minimum stretch levels, the filler content effect on, respectively, the stress-softening, the hysteresis and the surface heat build-up as a function of the cycle number. The model is found able to capture during the fatigue loading history the antagonist effects of minimum stretch and filler

content on stress-softening, hysteresis loop and heat build-up, decreasing with minimum stretch and increasing with filler content. It can be observed in Figure 2.3.13 that the strongest stress-softening occurs at the first cycles in which both the maximum and minimum stresses involve linearly. After a certain number of cycles, the rubber tends towards a stabilized state for which there is no significant change in stress. Although, the general trends provided by the simulations are satisfactory, we must to recognise that the initial rapid transient softening is not well reproduced by the model whose accuracy would be improved by increasing the number of networks.

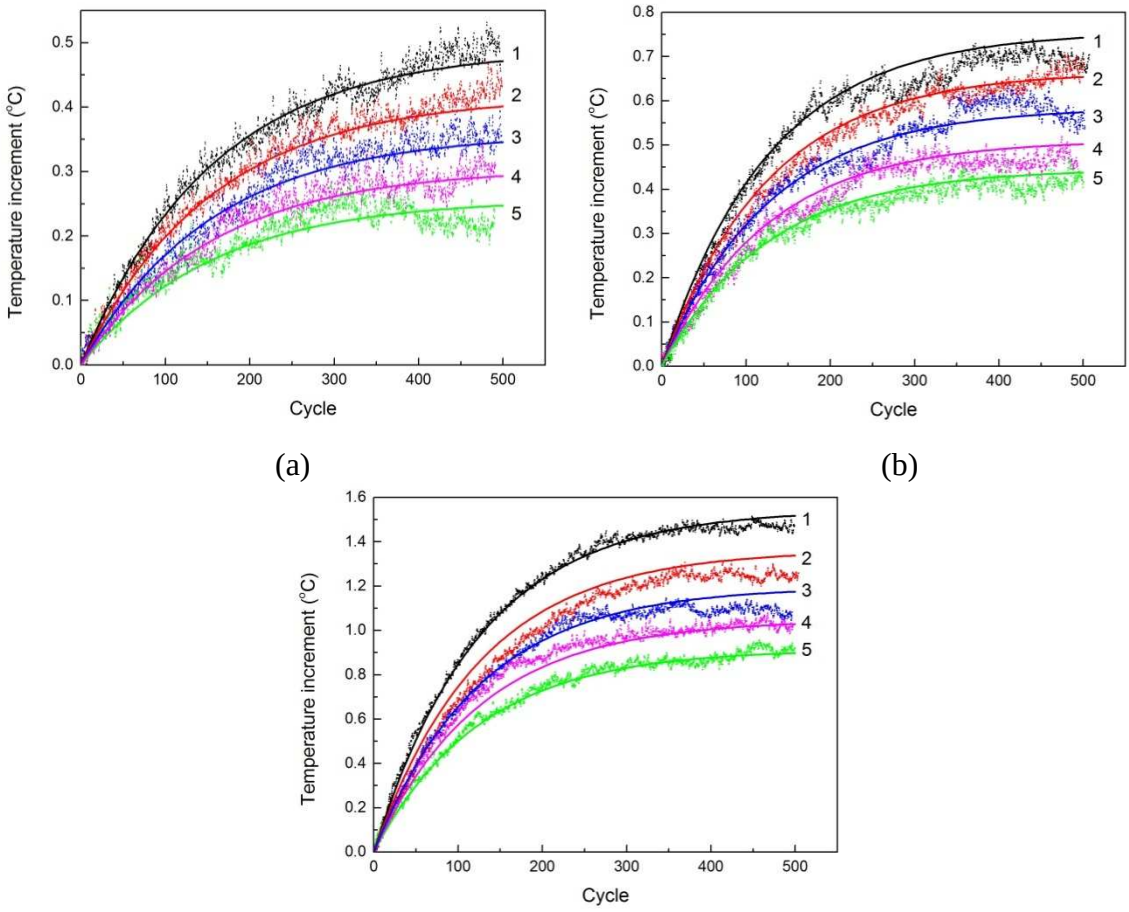

Figure 2.3.15. Experimental and simulated surface temperature at different minimum stretches (1: λ_{min}=1.1, 2: λ_{min}=1.2, 3: λ_{min}=1.3, 4: λ_{min}=1.4, 5: λ_{min}=1.5): (a) SBR15, (b) SBR25, (c) SBR43.

The model is found to describe in a satisfactory manner both the hysteretic response and the temperature evolution due to the heat build-up as highlighted in Figures 2.3.14 and 2.3.15. In particular, the mechanical dissipation, depicted by the hysteresis loop area is well reproduced

by the model, including the dependency vis-à-vis the filler content and the minimum stretch. Almost all the mechanical dissipation is transferred into heat energy inducing the temperature increase reported in Figure 2.3.15. When the amount of generated heat is equal to the amount of heat lost into the environment, the temperature reaches the stabilization observed experimentally as well as numerically. Note that although the model is also able to describe the well-known oscillating temperature, only the average value of the temperature is presented for the sake of simplicity.

2.3.3.2.3. Volumetric and thermal parameters

The volumetric and thermal parameters are assumed to be not dependent on the filler content. The thermal expansion coefficient α of the studied material was obtained in our previous work (Ovalle-Rodas et al., 2015) by means of constant-temperature tests under temperatures ranging from 293 up to 353 K:

$$\alpha = \left(\frac{1}{L_0}\right)\left(\frac{dL}{d\theta}\right) = 3.6\times10^{-4}\,\mathrm{K}^{-1} \tag{2.3.42}$$

where L_0 is the initial specimen length and $dL/d\theta$ is the uniaxial dilatation-absolute temperature slope.

The bulk modulus k, significantly higher than the rubber stiffness, takes the following value:

$$k = 500 n_{\mathrm{R}} k_{\mathrm{B}} T_0 \approx 200\,\mathrm{MPa} \tag{2.3.43}$$

Contrary to the observed trend on pure rubbers (Meyer and Ferri, 1935; Treloar, 2005), a thermal softening of the relaxed stress-strain relation may be observed in filled rubbers (Drozdov and Christiansen, 2009; Li et al., 2011; Ovalle-Rodas et al., 2015). The decrease in stiffness with temperature, acts as an additional softening effect to those induced by viscoelasticity and damage as illustrated in Figure 2.2.7b. The thermal softening may be attributed to the reduction in the effective number of chains per unit volume (Fischer and Henderson, 1967), as described by Eqs. (2.2.84) and (2.2.85). In contrast to pure rubbers, in which the thermo-mechanical response is explained uniquely by the contribution of the entropy-related energy (Meyer and Ferri, 1935; Treloar, 2005), the thermo-mechanical response of filled rubbers can be explained, in addition, by the contribution of the viscosity (Clément et al., 2001). The amount of the viscosity contribution depends on the filler fraction, and can be related to filler-rubber matrix / filler-filler interactions. In the present experimental investigation, the fatigue-induced temperature variations are relatively low and hence should have no significant influence on the chain-scale material constants, such that:

$$N_{,T} = 0.0 \tag{2.3.44}$$

Finally, the following values are, respectively, adopted for the coefficient of thermal conductivity, the specific heat capacity at constant deformation and the coefficient of thermal convection:

$$k_{\mathrm{T}} = 0.19\ \mathrm{W\ m^{-1}K^{-1}} \tag{2.3.45}$$

$$C_{\mathrm{T0}} = 1.78\times10^{6}\ \mathrm{J\ m^{-3}K^{-1}} \tag{2.3.46}$$

$$h = 19\ \mathrm{W\ m^{-2}K^{-1}} \tag{2.3.47}$$

To check the implemented constitutive model, the simulated responses are compared in what follows with the experimental results obtained under two cyclic loading blocks with different pre-stretch levels.

2.3.3.3. Comparison with two-blocks experimental data

The model parameters identified on the SBR matrix are introduced into the finite element simulations as input constants and the quantitative predictions of the constitutive model are compared in Figures 2.3.16-2.3.20 with the experimental data of the three carbon-filled SBR materials cyclically loaded under Low-High (LH) and High-Low (HL) two-block tests. A global view at these results shows that the general trends provided by the model for the prediction of the carbon-filled SBR history-dependent cyclic response are satisfactory for the different pre-stretch levels including the filler-dependency.

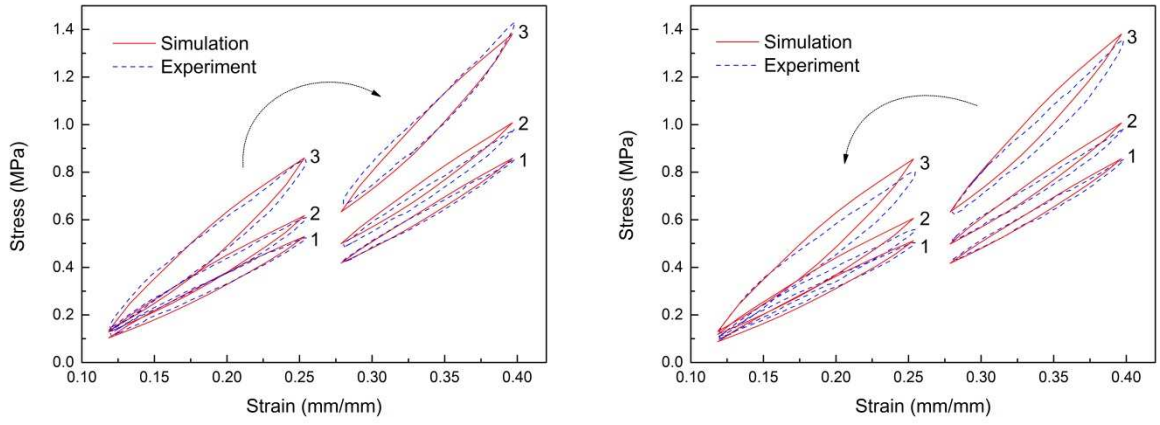

(a) (b)

Figure 2.3.16. Stress-strain curves at the 250th cycle of two blocks with different pre-stretch levels: (a) LH, (b) HL (1: SBR15, 2: SBR25, 3: SBR43).

Figure 2.3.16 presents the comparison regarding the stress-strain hysteresis loop at the 250th cycle. It is satisfactory to observe that the model predictions are in reasonable agreement with the hysteretic responses of the three carbon-filled SBR materials for both LH and HL pre-stretch levels. This observation indicates that the constitutive model can accurately capture the effects of fillers and pre-stretch levels on mechanical dissipative mechanisms. In Figures 2.3.17-2.3.19, the model predictions of the fatigue-induced stress-softening are compared with our experimental data.

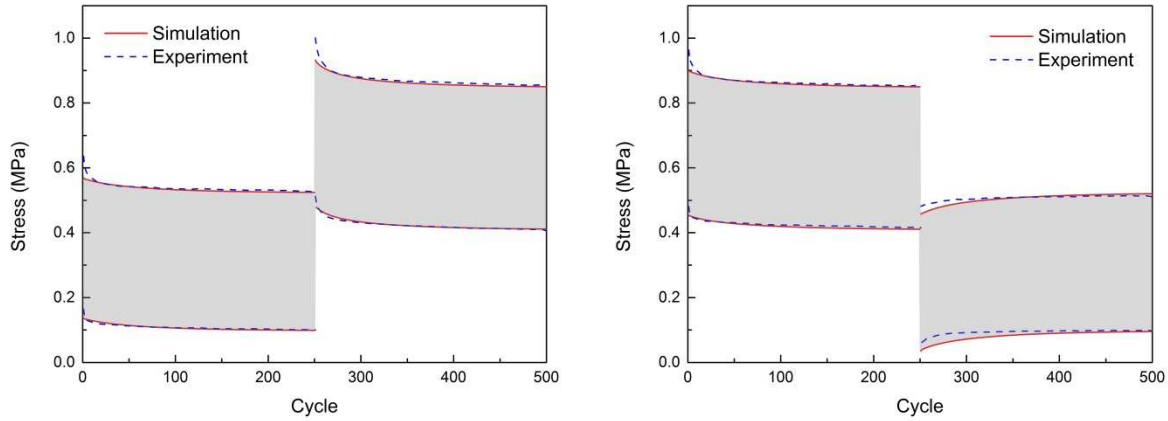

(a) (b)

Figure 2.3.17. Maximum and minimum stress evolution in SBR15 under two blocks with different pre-stretch levels: (a) LH, (b) HL.

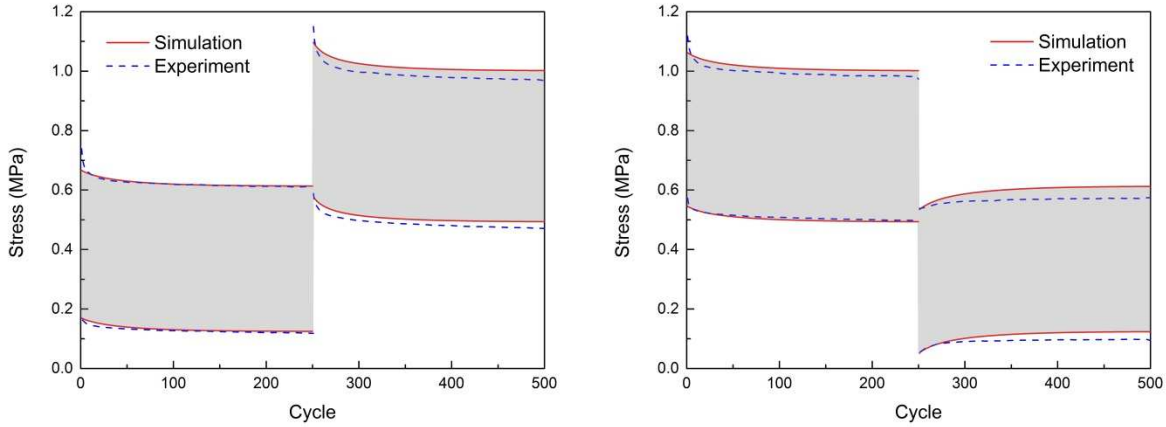

(a) (b)

Figure 2.3.18. Maximum and minimum stress evolution in SBR25 under two blocks with different pre-stretch levels: (a) LH, (b) HL.

A reasonable agreement between simulated and measured stress-softening can be observed. In particular, the general trends in the second block are well reproduced by the simulation, showing a decrease in stress under LH pre-stretch levels and an increase in stress under HL

pre-stretch levels. However, the deviation between the experimental stress-softening responses and the numerical ones, satisfactory in the first block, increases in the second block. It may be induced by the identification of the material viscous properties which should be performed under a wider history-dependent features.

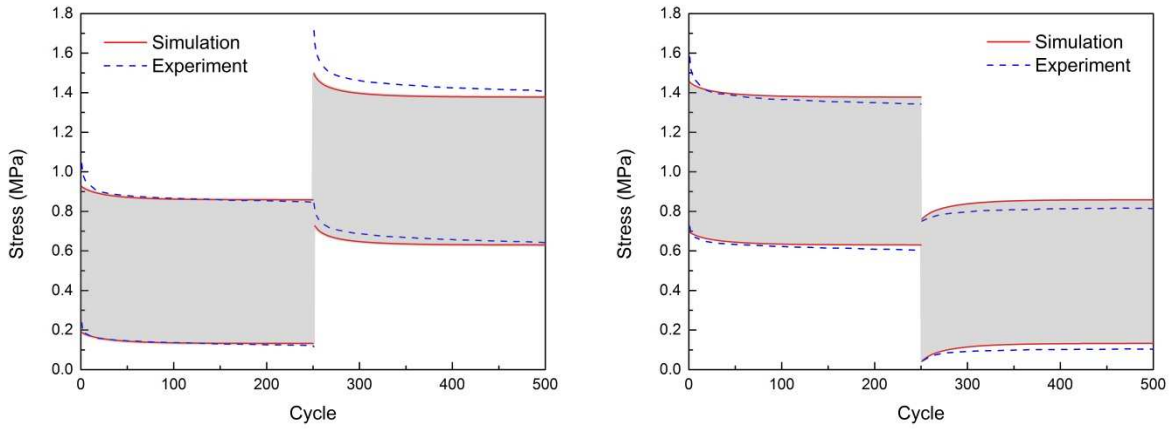

(a) (b)

Figure 2.3.19. Maximum and minimum stress evolution in SBR43 under two blocks with different pre-stretch levels: (a) LH, (b) HL.

The change in temperature, measured in the mid region of the specimen surface, is compared with the numerical results in Figure 2.3.20.

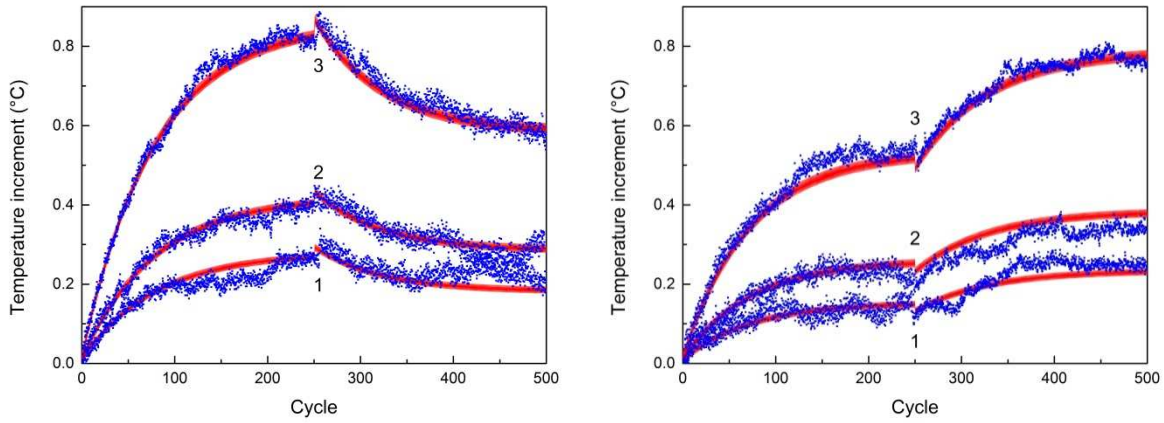

(a) (b)

Figure 2.3.20. Temperature evolution (simulation: red solid line, experiment: blue dots) under two blocks with different pre-stretch levels: (a) LH, (b) HL (1: SBR15, 2: SBR25, 3: SBR43).

It is found that the temperature evolution is successfully predicted by the model, especially for its dependencies on the filler content and the pre-stretch level which are consistent with the observations on the intrinsic dissipation (see Figure 2.3.5). We first focus on the first

block of each test. The temperature rapidly increases during the first few cycles, and then its rate gradually decreases with the cyclic loading. This phenomenon can be explained by the evolutions of the heat production and loss rates. In the beginning, the thermal equilibrium is suddenly broken by the cyclic self-heating, and so that the temperature rises rapidly. With the temperature increase, the heat loss induced by the thermal conduction and convection is accelerated, whereas the heat production rate related with the intrinsic dissipation is almost not affected by the temperature evolution.

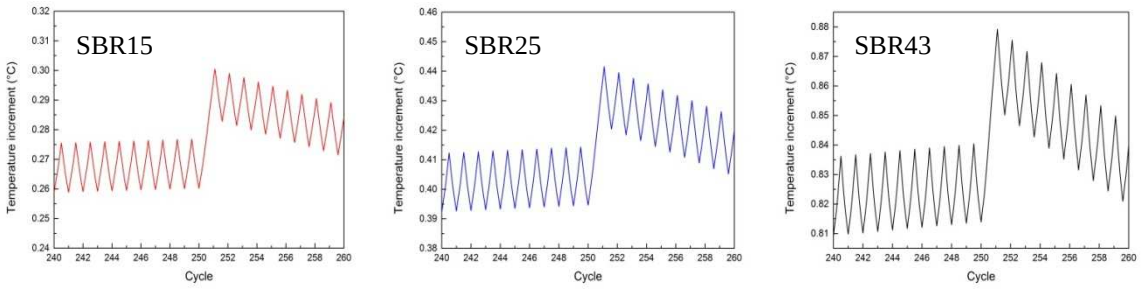

(a)

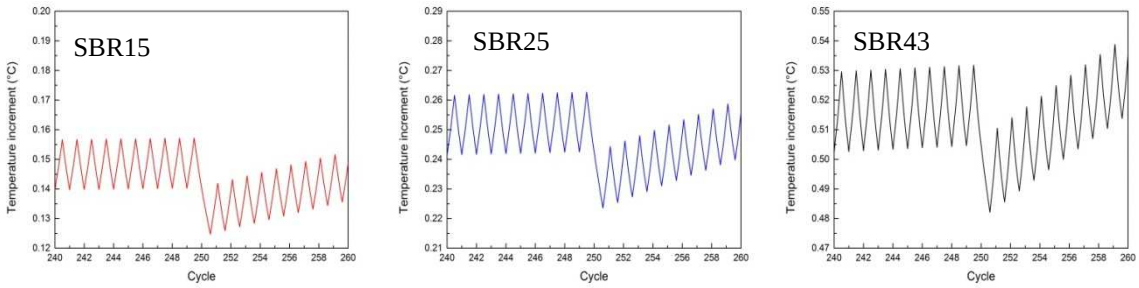

(b)

Figure 2.3.21. Zoom of Figure 2.3.20 showing the simulation in the transition zone between the two blocks: (a) LH, (b) HL.

Hence, the temperature rise gradually becomes slow and slow, and the specimen tends to attain a dynamic thermal equilibrium with a stabilized temperature between the heat production and loss. When the test enters into the second block, the intrinsic dissipation is suddenly changed in a different way between the LH and HL two-block tests. Indeed, for the LH two-block test, a sudden reduction of the heat production rate can be expected when the test passes from the low pre-stretch level to the high one, and the heat loss starts to dominate resulting in the temperature decrease. By contrast, for the HL two-block test, the heat production rate is suddenly increased and hence accelerates the temperature rise, which permits the temperature to reach a higher stabilized level with a new dynamic thermal equilibrium. Moreover, it should be noted that the temperature evolution predicted by the model is actually accompanied with a periodical fluctuation with the same frequency than the

cyclic loading as shown in Figure 2.3.21. It can be observed in the figure that the transition from one block to the other is accompanied by a sudden temperature change. The temperature increases in the HL two-block transition and decreases in the LH two-block transition. These thermal features are actually induced by the thermo-elastic heating and cooling effect dependent on the filler content, and satisfy the characteristics of entropic elasticity. The close agreement between simulated results and test findings validates the capability of the proposed constitutive model to predict the pre-stretched fatigue response of carbon-filled SBR. That indicates that the proposed constitutive theory captures the physical mechanisms occurring inside this rubber-filler material system during the fatigue loading history.

It is worth noting that the model capabilities were only examined for flat and thin specimens with a constant cross-section subjected to a constant-amplitude pre-stretched cyclic loading. The model needs to be further verified under more complex loading conditions and other specimen geometries for which the heat build-up and the damage effects could turn sufficiently important to modify the overall cyclic response of the material.

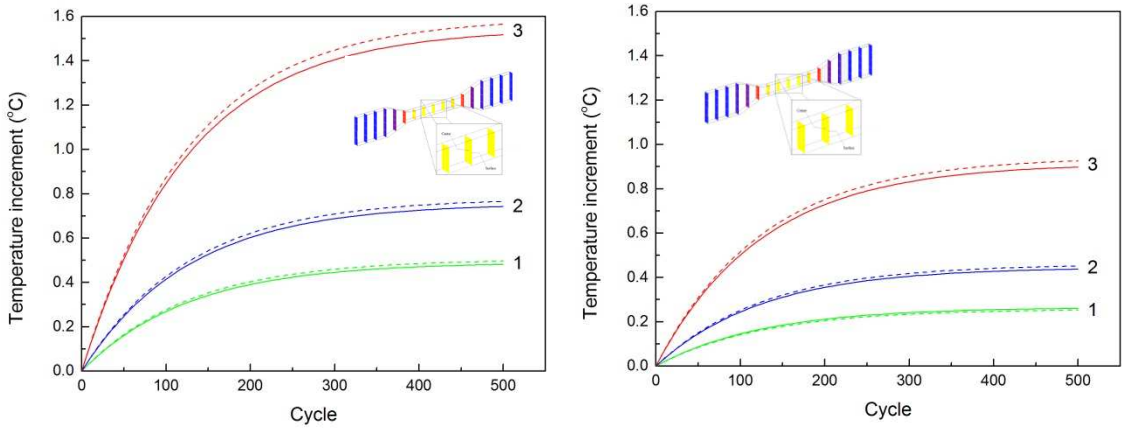

(a) (b)

Figure 2.3.22. Simulated temperature increment in the flat specimen (surface: continuous lines, center: dashed lines) at a minimum stretch of (a) λ_{min}=1.1, (b) λ_{min}=1.5 (1: SBR15, 2: SBR25, 3: SBR43).

2.3.4. Cyclic dissipation in thick rubber specimens[19]

The above results show the ability of the model to capture and predict the significant features of the cyclic response and the heat build-up of carbon-filled SBR. The predictive

[19] This Part of this Chapter is based on the following paper: Qiang Guo, Fahmi Zaïri, Cristian Ovalle-Rodas, Xinglin Guo, 2018. Constitutive modeling of the cyclic dissipation in thin and thick rubber specimens. *ZAMM - Journal of Applied Mathematics and Mechanics* 98, 1878-1899.

capability of the model over a range of filler concentrations is also demonstrated. That indicates that the proposed thermo-mechanical theory captures the intrinsic constitutive response and the basic mechanisms involved during cyclic loading of carbon-filled SBR. The constitutive theory is presented in its most general form with the aim of being applicable to all thermo-viscoelastic filled rubbers, but also to all kinds of rubber structures. The thin specimens involve very weak gradients in the transverse direction, as shown in Figures 2.3.10 and 2.3.22 for viscous stretches and temperature, respectively.

In the case of thick structures significant gradients may be generated. In order to illustrate this aspect, we propose now to analyze how the triaxial stress state may influence the inelastic fatigue effects in relation with the cyclic deformation mechanisms. Triaxial stress states different from the uniaxial state can be induced by the specimen shape: The cylindrical hourglass-shaped specimens, R2 and R42, shown in Figure 2.3.23 present two different curvature radii in order to set different triaxial stress states in the median cross-section. The lower the curvature radius, the higher are the triaxial stresses in the specimen. The three specimens are meshed using 3D 8-node meshing elements, isoparametric and arbitrarily hexahedrics. One specimen end is fixed and the other is subjected to a displacement-controlled cyclic loading. In our simulations, the same equivalent strain in the median cross-section is applied for the two specimens. A constant temperature T_0 = 296 K is applied at both specimen ends and the remaining frontiers are subjected to a convection heat transfer condition, see Eq. (2.2.111).

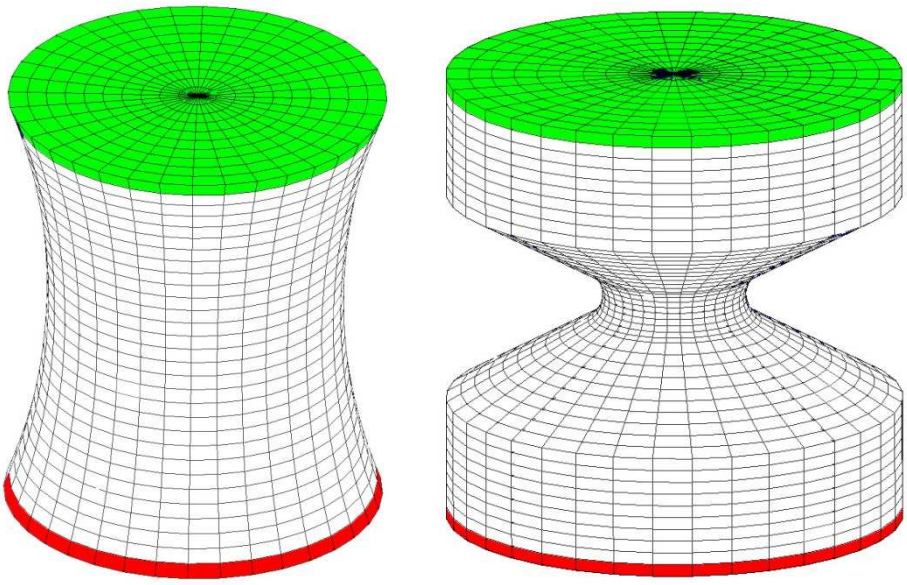

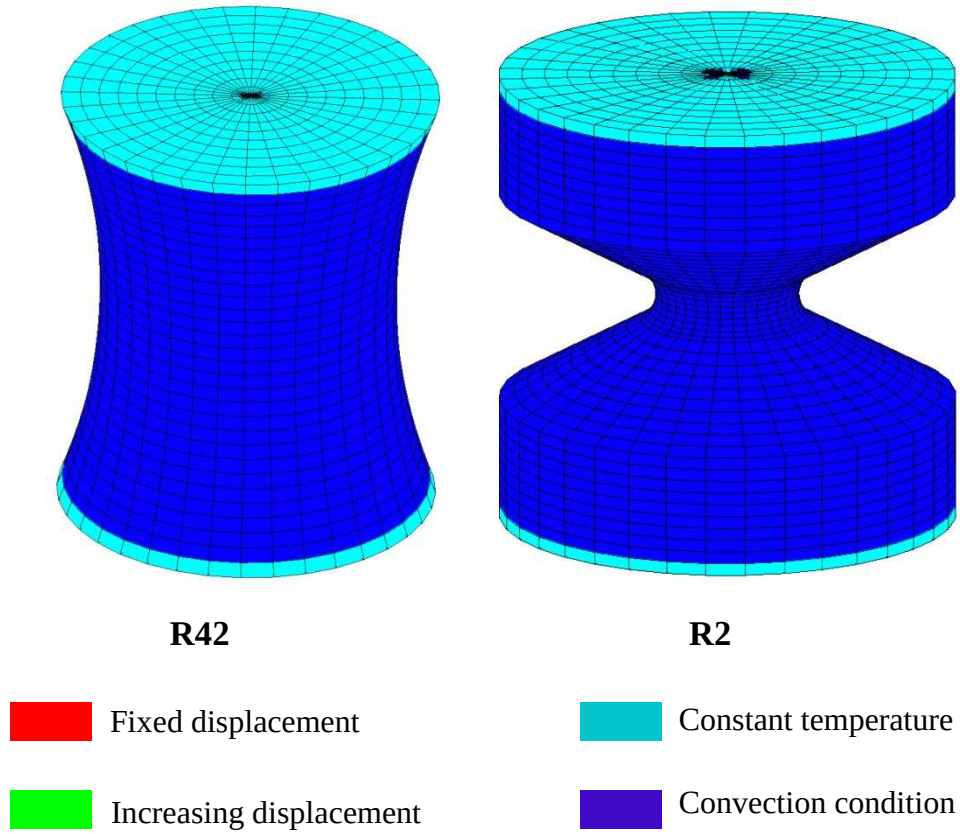

Figure 2.3.23. Boundary conditions for flat and thick specimens.

The fatigue damage and temperature fields inside the simulation model are shown in Figure 2.3.24 for the two thick specimen shapes. Because of symmetry, only one-eighth of the three-dimensional specimen is considered. surface than in the center due to thermal convection.

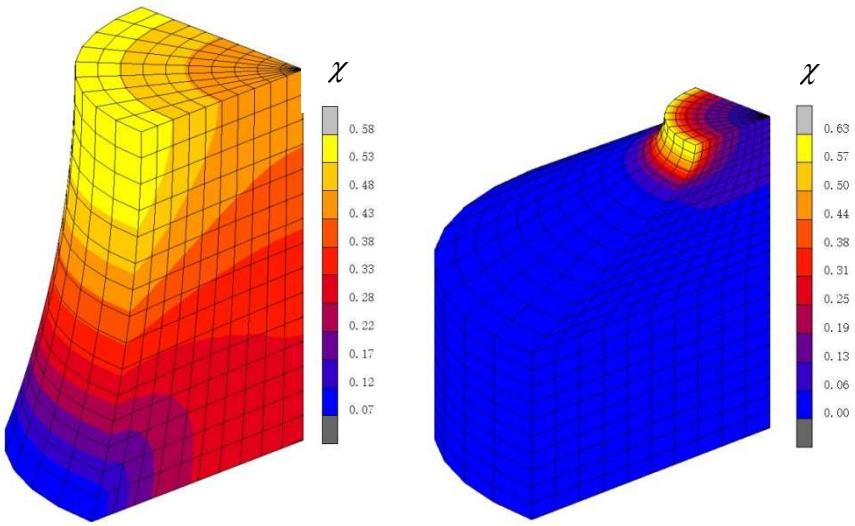

(a)

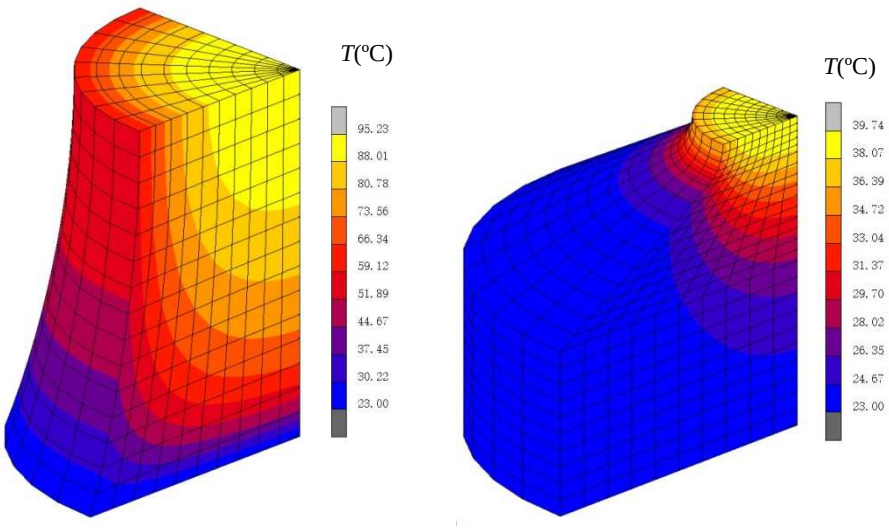

(b)

Figure 2.3.24. Contours of (a) damage and (b) temperature in the AE42 and AE2 specimens.

At the beginning of the cyclic loading, large dissipation gradients induce higher surface temperature on the surface than in the center. Figure 2.3.25 illustrates the damage and temperature evolution predictions at material points in the center and on the surface of the median cross-section. The cyclic dissipation depends on the stress state induced by the specimen shape. A center-to-surface gradient is therefore expected according to the specimen curvature radius, with a dissipation higher on the surface than in the center. Indeed, the damage distribution presented in Figure 2.3.24a exhibits higher damage values on the specimen surface whatever the specimen shape and with a center-to-surface gradient higher for the smallest specimen curvature radius. Figure 2.3.25a shows a nonlinear evolution of the damage under cyclic loading with a continuous increase of the difference between the center and the surface. Although the cyclic dissipation transferred into heat energy is larger on the specimen surface, the thermal convection at the surface with the environment makes the heat energy concentrates in the core and causes the temperature higher on the specimen center, as shown in Figure 2.3.25b. This thermal insulator feature of the rubber makes the bigger specimen with significant thermal gradients. Besides, the high temperatures inside the specimen could be sufficiently important to induce thermal aging effects (Neuhaus et al., 2017). As shown in Figure 2.3.25b, the temperature increases nonlinearly under cyclic loading with a decreasing rate larger on the surface than in the center due to thermal convection. At the beginning of the cyclic loading, large dissipation gradients induce higher surface temperature on the surface than in the center.

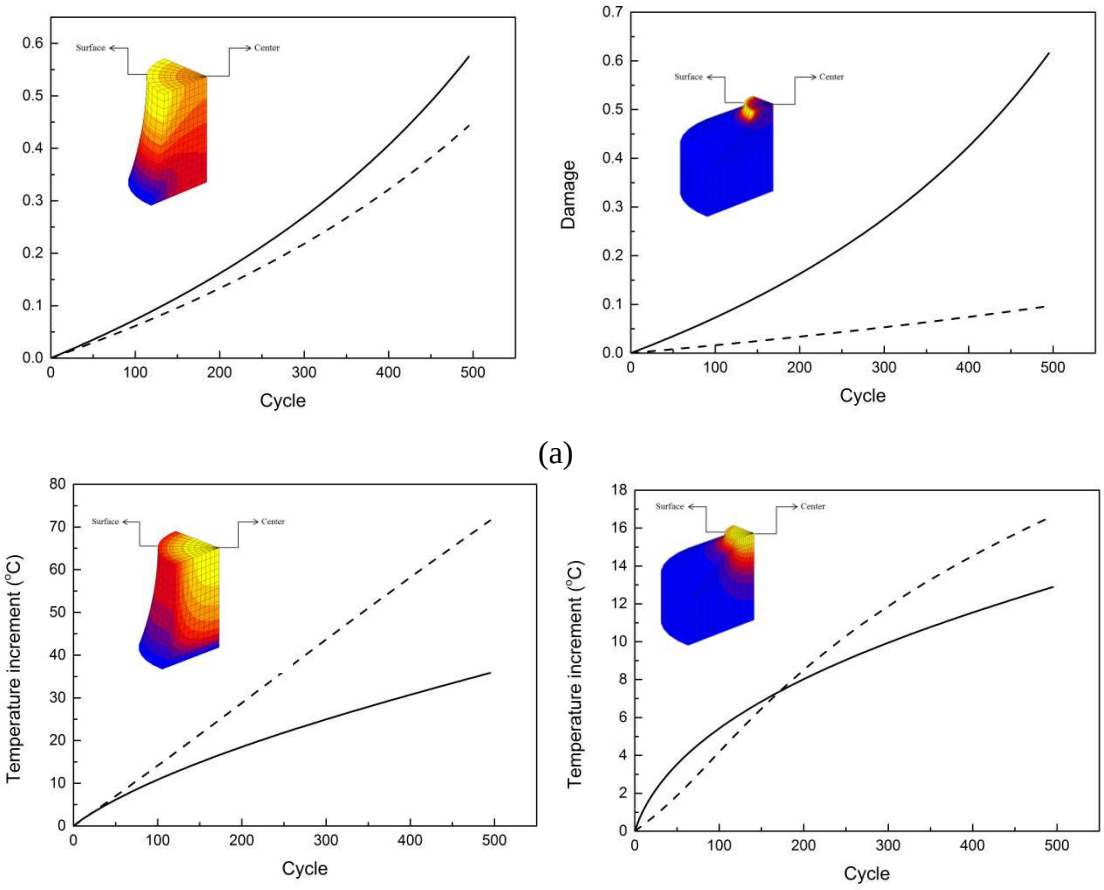

Figure 2.3.25. Simulated (a) damage and (b) temperature increment in the AE42 and AE2 specimens (surface: continuous lines, center: dashed lines).

2.3.5. Partial conclusions

In this Part of this work, the constitutive model was compared to our experimental data obtained on a carbon-filled SBR containing different amounts of carbon-black and cyclically loaded under different pre-stretch levels at room temperature. The respective influence of pre-stretch level and filler content on the inelastic effects (relaxation, stress-softening and dissipations) in carbon-filled SBR was experimentally reported, and the underlying physical mechanisms were deduced. An original amplification-inspired procedure was proposed for the identification of the rubber matrix properties, then used as direct input constants of the constitutive model modified to incorporate explicitly the filler effects. The predictive model capabilities were verified from the comparison between the numerical predictions and the carbon-filled SBR experimental response obtained under two cyclic loading blocks with different pre-stretch levels. The simulated results compared favorably with those obtained from experiments. Numerical applications were carried out on thick specimens with two

different curvature radii in order to set different triaxial stress states in the median cross-section.

The presented model provides a useful tool for damage and thermal patterns estimation in rubber structures. A quantitative evaluation of the model remains however an important issue for future works.

2.3.6. References

Abdul-Hameed, H., Messager, T., Zaïri, F., Naït-Abdelaziz, M., 2014a. Large-strain viscoelastic-viscoplastic constitutive modeling of semi-crystalline polymers and model identification by deterministic/evolutionary approach. Computational Materials Science 90, 241-252.

Abdul-Hameed, H., Messager, T., Ayoub, G., Zaïri, F., Naït-Abdelaziz, M., Qu, Z., Zaïri, F., 2014b. A two-phase hyperelastic-viscoplastic constitutive model for semi-crystalline polymers: application to polyethylene materials with a variable range of crystal fractions. Journal of the Mechanical Behavior of Biomedical Materials 37, 323-332.

Abe, A., Dusek, K., Kobayashi, S., 2003. Filler-Reinforced Elastomer - Scanning Force Microscopy. Springer-Verlag Berlin Heidelber New York.

Ayoub, G., Zaïri, F., Naït-Abdelaziz, M., Gloaguen, J.M., 2010. Modelling large deformation behaviour under loading-unloading of semicrystalline polymers: application to a high density polyethylene. International Journal of Plasticity 26, 329-347.

Ayoub, G., Zaïri, F., Naït-Abdelaziz, M., Gloaguen, J.M., 2011. Modeling the low-cycle fatigue behavior of visco-hyperelastic elastomeric materials using a new network alteration theory: application to styrene-butadiene rubber. Journal of the Mechanics and Physics of Solids 59, 473-795.

Ayoub, G., Naït-Abdelaziz, M., Zaïri, F., Gloaguen, J.M., Charrier, P., 2012. Fatigue life prediction of rubber-like materials under multiaxial loading using a continuum damage mechanics approach: effects of two-blocks loading and R ratio. Mechanics of Materials 52, 87-102.

Ayoub, G., Zaïri, F., Naït-Abdelaziz, M., Gloaguen, J.M., Kridli, G., 2014a. A visco-hyperelastic damage model for cyclic stress-softening, hysteresis and permanent set in rubber using the network alteration theory. International Journal of Plasticity 54, 19-33.

Ayoub, G., Naït-Abdelaziz, M., Zaïri, F., 2014b. Multiaxial fatigue life predictors for rubbers: application of recent developments to a carbon-filled SBR. International Journal of Fatigue 66, 168-176.

Bergstrom, J.S., Boyce, M.C., 1999. Mechanical behavior of particle-filled elastomers. Rubber Chemistry and Technology 72, 633-656.

Berriot, J., Lequeux, F., Monnerie, L., Montes, H., Long, D., Sotta, P., 2002. Filler-elastomer interaction in model filled rubbers, a ^{1}H NMR study. Journal of Non-Crystalline Solids 307-310, 719-724.

Berriot, J., Martin, F., Montes, H., Monnerie, L., Sotta, P., 2003. Reinforcement of model filled elastomers: characterization of the cross-linking density at the filler-elastomer interface by ^{1}H NMR measurements. Polymer 44, 1437-1447.

Boulanger, T., Chrysochoos, A., Mabru, C., Galtier, A., 2004. Calorimetric analysis of dissipative and thermoelastic effects associated with the fatigue behavior of steels. International Journal of Fatigue 26, 221-229.

Boutaleb, S., Zaïri, F., Mesbah, A., Naït-Abdelaziz, M., Gloaguen, J.M., Boukharouba, T., Lefebvre, J.M., 2009. Micromechanics-based modelling of stiffness and yield stress for silica/polymer nanocomposites. International Journal of Solids and Structures 46, 1716-1726.

Bueche, F., 1960. Molecular basis for the Mullins effect. Journal of Applied Polymer Science 4, 107-114.

Chagnon, G., Verron, E., Marckmann, G., Gornet, L., 2006. Development of new constitutive equations for the Mullins effect in rubber using the network alteration theory. International Journal of Solids and Structures 43, 6817-6831.

Clement, F., Bokobza, L., Monnerie, L., 2001. On the Mullins effect in silica-filled polydimethylsiloxane networks. Rubber Chemistry and Technology 74, 847-870.

Diaz, R., Diani, J., Gilormini, P., 2014. Physical interpretation of the Mullins softening in a carbon-black filled SBR. Polymer 55, 4942-4947.

Drozdov, A., Christiansen, J., 2009. Thermo-viscoplasticity of carbon black-reinforced thermoplastic elastomers. International Journal of Solids and Structures 46, 2298-2308.

Fischer, E., Henderson, J., 1967. Effect of temperature on stress-optical properties of styrene butadiene block copolymers. Rubber Chemistry and Technology 40, 1373-1380.

Guo, Q., Zaïri, F., Baraket, H., Chaabane, M., Guo, X., 2017. Pre-stretch dependency of the cyclic dissipation in carbon-filled SBR. European Polymer Journal 96, 145-158.

Guth, E., 1945. Theory of filler reinforcement. Journal of Applied Physics 16, 20-25.

Hanson, D.E., Hawley, M., Houlton, R., Chitanvis, K., Rae, P., Orler, E.B., Wrobleski, D.A., 2005. Stress softening experiments in silica-filled polydimethylsiloxane provide insight into a mechanism for the Mullins effect. Polymer 46, 10989-10995.

Houwink, R., 1956. Slipping of molecules during the deformation of reinforced rubber. Rubber Chemistry and Technology 29, 888-893.

Kraus, G., Childers, C.W., Rollmann, K.W., 1966. Stress softening in carbon black-reinforced vulcanizates: strain rate and temperature effects. Journal of Applied Polymer Science 10, 229-244.

Kraus, G., Gruver, J., 1970. Thermal expansion, free volume, and molecular mobility in a carbon black-filled elastomer. Journal of Polymer Science Part A: Polymer Physics 8, 571-581.

Kraus, G., 1984. Mechanical losses in carbon black filled rubbers. Journal of Applied Polymer Science 39, 75-92.

Laiarinandrasana, L., Jean, A., Jeulin, D., Forest, S., 2012. Modelling the effects of various contents of fillers on the relaxation rate of elastomers. Materials and Design 33, 75-82.

Lion, A., 1997. A physically based method to represent the thermo-mechanical behaviour of elastomers. Acta Mechanica, 123, 1-25.

Li, X., Dong, Y., Li, Z., Xia, Y., 2011. Experimental study on the temperature dependence of hyperelastic behavior of tire rubbers under moderate finite deformation. Rubber Chemistry and Technology 84, 215-228.

Marckmann, G., Verron, E., Gornet, L., Chagnon, G., Charrier, P., Fort, P., 2002. A theory of network alteration for the Mullins effect. Journal of the Mechanics and Physics of Solids 50, 2011-2028.

Medalia, A., 1991. Heat generation in elastomer compounds: causes and effects. Rubber Chemistry and Technology 64, 481-492.

Meinecke, E., 1991. Effect of carbon-black loading and crosslink density on the heat build-up in elastomers. Rubber Chemistry and Technology 64, 269-284.

Meyer, K., Ferri, C., 1935. Sur l'élasticité du caoutchouc. *Helvetica Chimica Acta* 18, 570-589.

Mullins, L., 1948. Effect of stretching on the properties of rubber. Rubber Chemistry and Technology 21, 281-300.

Neuhaus, C., Lion, A., Johlitz, M., Heuler, P., Barkhoff, M., Duisen, F., 2017. Fatigue behaviour of an elastomer under consideration of ageing effects. International Journal of Fatigue 104, 72-80.

Ovalle-Rodas, C., Zaïri, F., Naït-Abdelaziz, M., 2014. A finite strain thermo-viscoelastic constitutive model to describe the self-heating in elastomeric materials during low-cycle fatigue. Journal of the Mechanics and Physics of Solids 64, 396-410.

Ovalle-Rodas, C., Zaïri, F., Naït-Abdelaziz, M., Charrier, P., 2015. Temperature and filler effects on the relaxed response of filled rubbers: experimental observations on a carbon-filled SBR and constitutive modeling. International Journal of Solids and Structures 58, 309-321.

Ovalle-Rodas, C., Zaïri, F., Naït-Abdelaziz, M., Charrier, P., 2016. A thermo-visco-hyperelastic model for the heat build-up during low-cycle fatigue of filled rubbers: formulation, implementation and experimental verification. International Journal of Plasticity 79, 217-236.

Pramanik, P., Khastgir, D., Saha, T., 1992. Conductive nitrile rubber composite containing carbon fillers: studies on mechanical properties and electrical conductivity. Composites Part A: Applied Science and Manufacturing 23, 183-191.

Pyrz, M., Zaïri, F., 2007. Identification of viscoplastic parameters of phenomenological constitutive equations for polymers by deterministic and evolutionary approach. Modelling and Simulation in Materials Science and Engineering 15, 85-103.

Thiele, J., Cohen, R., 1980. Thermal expansion phenomena in filled and unfilled natural rubber vulcanizates. Rubber Chemistry and Technology 53, 313-320.

Treloar, L., 2005. The Physics of Rubber Elasticity. 3rd edition. Great Britain: Clarendon Press - Oxford.

Vilgis, T.A., Heinrich, G., Kluppel, M., 2009. Reinforcement of polymer nano-composites: theory, experiments and applications. Cambridge University Press, USA.

Wood, L.A., Bekkedahl, N., Roth, F.L. 1943. Density measurements on synthetic rubbers. Rubber Chemistry and Technology 16, 244-248.

Zaïri, F., Naït-Abdelaziz, M., Gloaguen, J.M., Lefebvre, J.M., 2010. Constitutive modelling of the large inelastic deformation behaviour of rubber-toughened poly(methyl methacrylate): effects of strain rate, temperature and rubber-phase volume fraction. Modelling and Simulation in Materials Science and Engineering 18, 1-22.

Zaïri, F., Gloaguen, J.M., Naït-Abdelaziz, M., Mesbah, A., Lefebvre, J.M., 2011a. Study of the effect of size and clay structural parameters on the yield and post-yield response of polymer/clay nanocomposites via a multiscale micromechanical modelling. Acta Materialia 59, 3851-3863.

Zaïri, F., Naït-Abdelaziz, M., Gloaguen, J.M., Lefebvre, J.M., 2011b. A physically-based constitutive model for anisotropic damage in rubber-toughened glassy polymers during finite deformation. International Journal of Plasticity 27, 25-51.

CHAPTER 3. STRETCH-INDUCED CRYSTALLIZATION IN RUBBERS

3.1. THERMODYNAMICS AND MECHANICS OF STRETCH-INDUCED CRYSTALLIZATION IN RUBBERS[20]

The aim of this Part of the *Chapter 3* is to provide a quantitative prediction of the stretch-induced crystallization in natural rubber, the exclusive reason of its history-dependent thermo-mechanical features. A new constitutive model based on a micro-mechanism inspired molecular chain approach is formulated within the context of the thermodynamic framework. The molecular configuration of the partially crystallized single chain is analyzed and calculated by means of some statistical mechanical methods. The random thermal oscillation of the crystal orientation, considered as a continuous random variable, is treated by means of a representative angle. The physical expression of the chain free energy is derived according to a two-step strategy by separating crystallization and stretching. This strategy ensures that the stretch-induced part of the thermodynamic crystallization force is null at the initial instant and allows, without any additional constraint, to formulate a simple linear relationship for the crystallinity evolution law. The model contains very few physically interpretable material constants to simulate the complex mechanism: two chain-scale constants, one crystallinity kinetics constant, three thermodynamic constants related to the newly formed crystallites and a function controlling the crystal orientation with respect to the chain. The model is used to discuss some important aspects of the micro-mechanism and the macro-response under the equilibrium state and the non-equilibrium state involved during stretching/recovery and continuous relaxation.

Keywords: Chain configuration; thermodynamics; crystallization; melting; history-dependent effects.

[20] This Part of this chapter is based on the following paper: Guo Qiang, Zaïri Fahmi, Guo Xinglin, 2018. Thermodynamics and mechanics of stretch-induced crystallization in rubbers. *Physical Review E* 97, 052501.

3.1.1. Partial introduction

Firstly observed in 1925 by Katz (1925), the stretch-induced crystallization in natural rubber has a long research history. Although it concerns also synthetic rubbers, it is now well recognized that the ability of this biopolymer to crystallize under stretching is mainly due to the highly regular macromolecular structure. The transformation of the chain from its amorphous to crystalline state can be understood from the thermodynamic viewpoint. When the chain is stretched from its most probable conformation, its alignment results in a decrease in the conformational entropy. Thus, less entropy is needed to be sacrificed in the transformation of the chain from its amorphous to crystalline state. Due to this decrease in total entropy of fusion, the stretch-induced crystallization is allowed to occur at higher temperatures than under quiescent conditions. The process of stretch-induced crystallization has a depth impact on the mechanical properties, and in particular, it contributes to superior fatigue properties and crack growth resistance (Hamed et al., 1996; Mars and Fatemi, 2004; Le Cam and Toussaint, 2008) as well as history-dependent mechanical features such as hysteretic effects (Clark et al., 1940; Murakami et al., 2002; Trabelsi et al., 2003; Albouy et al., 2005, 2014; Rault et al., 2006a, 2006b; Candau et al., 2015a, 2015b) and continuous relaxation (Toki et al., 2005; Tosaka et al., 2012; Bruning et al., 2015; Xie et al., 2017). There are considerable qualitative experimental observations on the stretch-induced crystallization in natural rubber, as reported in recent literature reviews (Huneau, 2011; Toki, 2014; Albouy and Sotta, 2017), but the quantitative predictive modeling of this fascinating phenomenon is far from being fully established and remains a challenging task.

A predictive constitutive theory is, indeed, fundamental to better understand the relationship between the thermo-mechanical response at the macro-scale and the stretch-induced crystallization at the micro-scale, for which numerous phenomena accompanying the material transformation are still misunderstood. A literature survey shows that there exists only five recent contributions dealing with this task in rubbers (Kroon, 2010; Dargazany et al., 2014a, 2014b; Mistry and Govindjee, 2014; Guilie et al., 2015; Rastak and Linder, 2018) and all the proposed constitutive models can be distinguished by the restrictive assumptions, the theoretical approach and the predictive capabilities. The development of a rigorous physically-based predictive model of this mechanism has to take into account, within the context of the thermodynamic framework, the particular chain configuration by means of the statistical mechanics. In this regard, three main aspects have to be taken into account such as

(i) the definition of a pertinent single chain configuration that can be then translated to the chain network, (ii) the derivation of the chain free energy becoming that of the chain network and (iii) the proposition of an appropriate crystallization kinetics and its evolution law. The second point is the key element in the thermodynamic formulation of the constitutive relations between various thermodynamic quantities, and is related to the micro-structural specificities of the rubber gum by means of the first point. The third point introduces into the constitutive relationships the micro-structural evolution using either a purely phenomenological evolution law or a more physically realistic evolution law, its physical consistency allowing especially to limit the number of parameters with no direct physical meaning.

The stretch-induced crystallization in a rubber chain was investigated, using the statistical mechanics and within the thermodynamic framework, for the first time in 1947 by Flory in his early work (Flory, 1947). In his theory, bounded by several simplifying assumptions, Flory (1947, 1949) considered that the final partially crystallized chain is achieved from an initially fully amorphous chain by two separate and distinct steps, namely, stretching and crystallization, and the crystallized part in the chain was assumed to be fully extended and oriented in the stretching direction. The Flory theory (Flory, 1947, 1949) predicts the equilibrium crystallization as a function of stretch and temperature, and was verified with experimental observations (Arlman and Goppel, 1951; Xie et al., 2016). Later, other models based on the Flory theory (Flory, 1947, 1949) were proposed by vanishing some assumptions. Roe et al. (1961), Gaylord (1976) and Gaylord and Lohse (1976) considered the crystallite morphology in crystallized polymer chains whereas Smith (1976) taken into account the orientation of the extended crystallized part with respect to the chain. In the previous models, the crystallization occurs in a thermodynamically most favorable condition, i.e. in a thermodynamic equilibrium condition. Since this equilibrium crystallization is assumed without time evolution and achieved only under infinitesimal change rates, it is necessary to extend the theory to non-equilibrium conditions where the crystallinity evolution should be described in a certain kinetics theory[21]. Different descriptions of the crystallization kinetics were proposed in the five recent contributions (Kroon, 2010; Dargazany et al., 2014a, 2014b; Mistry and Govindjee, 2014; Guilie et al., 2015; Rastak and Linder, 2018). Kroon (2010)

[21] The crystallization kinetics in solids was firstly investigated by Avrami (1939, 1940, 1941) and classical equations have emerged for spherulitic growth in thermally-induced crystallization but are not useful for all kinetics of newly formed crystals due to differences in morphology and in size. As a matter of fact, the micron-sized spherulites in semi-crystalline thermoplastic polymers resulting from quiescent melt crystallization are different than the newly formed nano-sized crystallites in natural rubbers due to stretching.

proposed a model by defining the crystallinity degree as the fraction of the partially crystallized chains with fixed-size nucleated crystallites without crystallite growth. In his model, the contribution of the crystallites to the free energy is neglected and a phenomenological Arrhenius-type kinetics is introduced to govern the crystallinity evolution. Dargazany et al. (2014a, 2014b) also took the crystallite size in a single chain as a material constant whereas the crystallinity evolution law was formulated on the basis of the chain length statistic distribution. Mistry and Govindjee (2014) proposed a model in which the free energy is considered to only consist of a purely thermodynamic part and an elastic part. In their model, the crystallization kinetics is formulated based on the free energy gradient with respect to the crystallinity degree, and a yield-like threshold is introduced to additionally restrict the evolution law. Guilie et al. (2015) also related the crystallization kinetics with the free energy gradient, but they formulated the evolution law using a plastic-like flow rule and made a distinction between the processes of crystallization and melting. Very recently, Rastak and Linder (2018) derived the chain free energy by integrating the chain force with respect to the chain length and adding an integration constant only dependent on the crystallinity degree. In their approach, a linear relationship between the free energy gradient and the crystallization rate was directly adopted to capture the rate-dependent crystallinity evolution.

In this Part of the *Chapter 3*, we present a new micro-mechanism inspired molecular chain model to describe the progressive evolution of the crystallinity degree in rubbers and the history-dependent thermo-mechanical response within the context of the thermodynamic framework. In our model, the orientation of the crystallization domain with respect to the chain is considered as a continuous random variable which is treated by means of a representative angle. In the spirit of the Flory theory (Flory, 1947, 1949), we derive the chain free energy via a two-step strategy by separating crystallization and stretching. Although hypothetical, the method allows to derive a physically realistic model insuring that the free energy gradient, used to formulate the crystallinity evolution law, is null at the initial state under the melting temperature, ignoring the crystallite surface energy. The method avoids the introduction of any additional constraint to describe the progressive evolution of the crystallinity degree which obeys to a linear relationship between the crystallization rate and the corresponding thermodynamic force.

The outline of the present Part is as follows. We give the main elements of the developed model in Section 3.1.2. Section 3.1.3 presents and discusses the model results. Concluding remarks are finally given in Section 3.1.4.

3.1.2. Theory

Let us consider a single chain with a total number of N segments each of length l, for a fully extended chain length of Nl. During the crystallization, a portion of the molecular chain crystallizes while the remaining remains amorphous as illustrated in Figure 3.1.1.

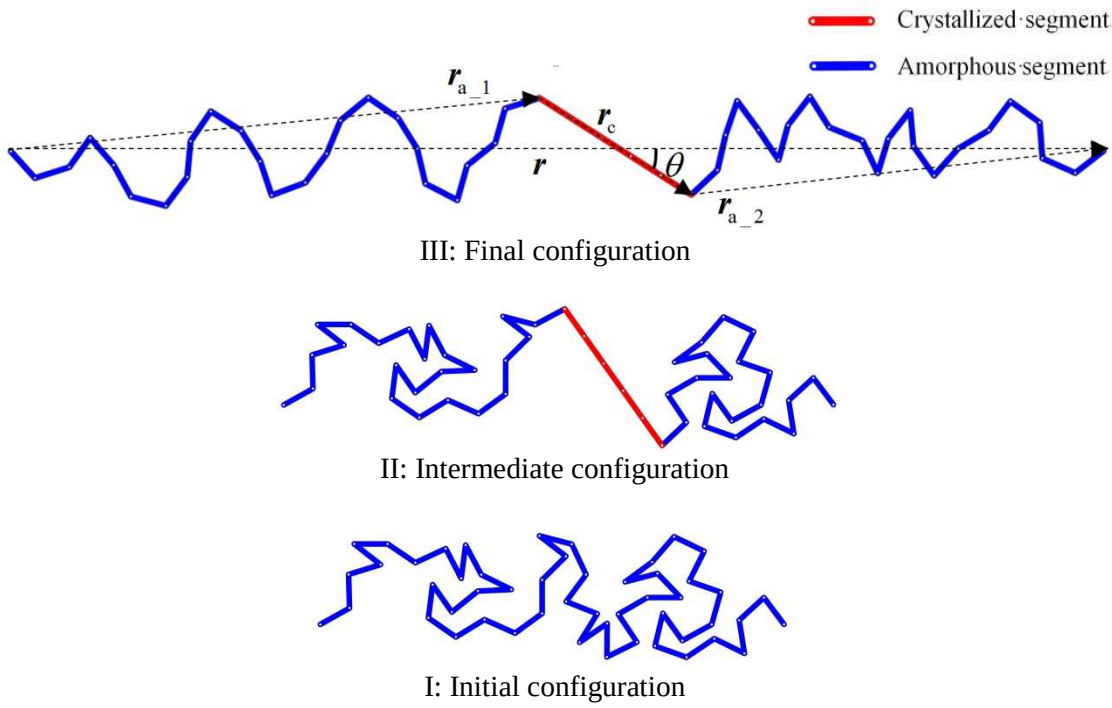

Figure 3.1.1. Configuration changes in the proposed two-step strategy: $\mathrm{I} \rightarrow \mathrm{II}$ thermal-induced crystallization step and $\mathrm{II} \rightarrow \mathrm{III}$ absolutely mechanical stretching step.

The two amorphous subparts are present from either side of the crystallized portion and, are assumed to not interact and to have a random distribution. We confer the subscript 1 to the left amorphous subpart and the subscript 2 to the right amorphous subpart. The conservation of the total number of segments leads to:

$$N = N_c + N_{a\_1} + N_{a\_2} \tag{3.1.1}$$

where N_c is the number of crystallized segments and, $N_a = N_{a\_1} + N_{a\_2}$ is the total number of amorphous segments:

$$N_a = N(1-\chi) \tag{3.1.2}$$

in which $\chi \in [0,1]$ is the crystal fraction in the single chain given by the following ratio[22]:

$$\chi = \frac{N_c}{N} \tag{3.1.3}$$

The chain end-to-end vector $\boldsymbol{r}$ is the sum of three parts:

$$\boldsymbol{r} = \boldsymbol{r}_c + \boldsymbol{r}_{a\_1} + \boldsymbol{r}_{a\_2} \tag{3.1.4}$$

in which $\boldsymbol{r}_c$ is the end-to-end vector of the crystallized part and, $\boldsymbol{r}_a = \boldsymbol{r}_{a\_1} + \boldsymbol{r}_{a\_2}$ is the sum of the end-to-end vectors of the two amorphous subparts. Introducing $\theta \in [0, \pi]$ as the angle between $\boldsymbol{r}$ and $\boldsymbol{r}_c$, a simple relationship between the lengths of these end-to-end vectors is given:

$$r_a = \sqrt{r^2 + r_c^2 - 2rr_c \cos\theta} \tag{3.1.5}$$

where $r = \|\boldsymbol{r}\|$, $r_c = \|\boldsymbol{r}_c\|$ and $r_a = \|\boldsymbol{r}_a\|$.

3.1.2.1. Configuration

As a matter of fact, the partially crystallized chain continuously oscillates due to thermal fluctuations. Owing to the internal rotation of molecular bonds, a huge number of molecular chain configurations are possible which requires statistical mechanical methods to establish the average mechanical properties. In our micro-mechanism inspired molecular chain model, the configurations of the crystallized part and the two amorphous subparts are assumed to be independent from each other, and hence, the configuration of the whole chain can be identified by comprehensively analyzing the individual oscillation of the amorphous and crystallized parts.

The amorphous segments are assumed to be rotationally jointed with complete freedom of orientation and with no interaction (Wang and Guth, 1952), i.e. the rotation is free at each bond junction and all bond angles take the same probability with no preferred bond angle in the absence of external forces. The non-Gaussian statistical method is used to calculate the configurations of the two amorphous subparts. Contrary to a Gaussian treatment, the non-Gaussian probability density function of the molecular chain configuration allows us to

[22] We can notice that the single chain crystallization can be generalized to define the material crystallinity degree by implementing the actual chain structure for all chains in the network. This procedure gives us a spatially averaged measure of the material crystallinity.

introduce the values of $r_{a\_1} = \left\| \boldsymbol{r}_{a\_1} \right\|$ and $r_{a\_2} = \left\| \boldsymbol{r}_{a\_2} \right\|$ over their whole ranges up to the fully extended lengths $N_{a\_1} l$ and $N_{a\_2} l$:

$$\mathrm{P}_{a\_1}\left(\boldsymbol{r}_{a\_1}\right) = \left(\frac{3}{2\pi N_{a\_1} l^2}\right)^{3/2} \exp\left\{-N_{a\_1}\Re\left(\frac{r_{a\_1}}{N_{a\_1} l}\right)\right\} \tag{3.1.6}$$

$$\mathrm{P}_{a\_2}\left(\boldsymbol{r}_{a\_2}\right) = \left(\frac{3}{2\pi N_{a\_2} l^2}\right)^{3/2} \exp\left\{-N_{a\_2}\Re\left(\frac{r_{a\_2}}{N_{a\_2} l}\right)\right\} \tag{3.1.7}$$

in which we define $\Re(x)$ as a function depending on the inverse function $\mathcal{L}^{-1}(x)$ of the Langevin function $\mathcal{L}(x) = \coth(x) - 1/x$:

$$\Re(x) = x\mathcal{L}^{-1}(x) + \ln\frac{\mathcal{L}^{-1}(x)}{\sinh\left(\mathcal{L}^{-1}(x)\right)} \tag{3.1.8}$$

where the Padé approximation $\mathcal{L}^{-1}(x) \approx x\left(3 - x^2\right)/\left(1 - x^2\right)$ is used.

Considering that the two amorphous subparts have independent configurations, the probability density function of the whole amorphous part $\mathrm{P}_a\left(\boldsymbol{r}_a\right)$ can be derived through the convolution integration of the two probability density functions $\mathrm{P}_{a\_1}\left(\boldsymbol{r}_{a\_1}\right)$ and $\mathrm{P}_{a\_2}\left(\boldsymbol{r}_{a\_2}\right)$:

$$\mathrm{P}_a\left(\boldsymbol{r}_a\right) = \mathrm{P}_{a\_1}\left(\boldsymbol{r}_{a\_1}\right) * \mathrm{P}_{a\_2}\left(\boldsymbol{r}_{a\_2}\right) = \int_{R^3} \mathrm{P}_{a\_1}\left(\boldsymbol{r}_{a\_1}\right)\mathrm{P}_{a\_2}\left(\boldsymbol{r}_a - \boldsymbol{r}_{a\_1}\right) d\boldsymbol{r}_{a\_1} \tag{3.1.9}$$

After a series of lengthy but straightforward derivations, we obtain the following expression:

$$\mathrm{P}_a\left(\boldsymbol{r}_a\right) = \left(\frac{3}{2\pi N_a l^2}\right)^{3/2} \exp\left\{-N_a\Re\left(\frac{r_a}{N_a l}\right)\right\} \tag{3.1.10}$$

The formula (3.1.10) points out that the probability density of the amorphous part is invariant with respect to the position of the crystallized domain inside the single chain. In other words, all the possible configurations of the amorphous segments have been taken into account including those induced by the various possible partitions of each amorphous subpart.

In the absence of external forces, the most probable end-to-end distance of the amorphous part r_a, according to Eq. (3.1.10), has the root mean square value $l\sqrt{N_a}$. Thus, a kinematic variable λ_a of the amorphous part can be introduced through the effective stretch definition:

$$\lambda_a = \frac{r_a}{l\sqrt{N_a}} \tag{3.1.11}$$

Similarly, with regard to the partially crystallized chain, the whole stretch λ can be defined as:

$$\lambda = \frac{r}{l\sqrt{N}} \tag{3.1.12}$$

In our micro-mechanism inspired molecular chain model, the crystallized part is considered as a rigid entity with fully extended segments and its length r_c is identically equal to the algebraic sum of the length of N_c crystallized segments:

$$r_c = N_c l \tag{3.1.13}$$

Moreover, the configuration of the crystallized part may be characterized by the angle θ between $\boldsymbol{r}$ and $\boldsymbol{r}_c$. Due to the thermal fluctuations, this angle is in nature a continuous random variable whose probability density function $\mathrm{P}_\theta(\theta)$ is related to the number of the crystallized segments N_c. Thus, for a partially crystallized single chain with a given crystal fraction χ, all the possible configurations of the crystallized segments can be taken into account only by considering the probability distribution of the angle θ. As a consequence, the probability density function $\mathrm{P}_c(\boldsymbol{r}_c)$ of the crystallized domain is identical with that of the angle θ:

$$\mathrm{P}_c(\boldsymbol{r}_c) = \mathrm{P}_\theta(\theta) \tag{3.1.14}$$

Again, considering the configuration-independence between amorphous and crystallized domains, the probability density function of the partially crystallized single chain $\mathrm{P}(\boldsymbol{r})$ is derived through the convolution integration of the amorphous and crystallized probability density functions $\mathrm{P}_a(\boldsymbol{r}_a)$ and $\mathrm{P}_c(\boldsymbol{r}_c)$:

$$\begin{aligned}\mathrm{P}(\boldsymbol{r}) &= \mathrm{P}_a(\boldsymbol{r}_a) * \mathrm{P}_c(\boldsymbol{r}_c) = \int_{R^3} \mathrm{P}_a(\boldsymbol{r}-\boldsymbol{r}_c)\,\mathrm{P}_c(\boldsymbol{r}_c)\,d\boldsymbol{r}_c \\ &= \left(\frac{3}{2(1-\chi)\pi N l^2}\right)^{3/2} \int_0^\pi \exp\left\{-(1-\chi)N\Re\left(\frac{1}{1-\chi}\sqrt{\left(\frac{\lambda}{\sqrt{N}}\right)^2+\chi^2-2\frac{\lambda}{\sqrt{N}}\chi\cos\theta}\right)\right\}\mathrm{P}_\theta(\theta)\,d\theta\end{aligned} \tag{3.1.15}$$

Obviously, due to the complexity of the functional form, it is almost impossible to directly obtain a compact expression of the probability density function $\mathrm{P}(\boldsymbol{r})$ from Eq. (3.1.15), even if an explicit expression of $\mathrm{P}_\theta(\theta)$ is given. In order to overcome this difficulty, we introduce a representative angle $\tilde{\theta}$ by considering the basic property of the probability density function $\mathrm{P}_\theta(\theta)$, i.e. $\int_0^\pi \mathrm{P}_\theta(\theta)\,d\theta = 1$. Then, Eq. (3.1.15) is rewritten as:

$$\mathrm{P}(\boldsymbol{r})=\left(\frac{3}{2(1-\chi)\pi N l^2}\right)^{3/2}\exp\left\{-(1-\chi)N\Re\left(\frac{1}{1-\chi}\sqrt{\left(\frac{\lambda}{\sqrt{N}}\right)^2+\chi^2-2\frac{\lambda}{\sqrt{N}}\chi\cos\tilde{\theta}}\right)\right\}$$
$$=\left(\frac{3}{2\pi N_{\mathrm{a}} l^2}\right)^{3/2}\exp\left\{-N_{\mathrm{a}}\Re\left(\frac{\tilde{\lambda}_{\mathrm{a}}}{\sqrt{N_{\mathrm{a}}}}\right)\right\} \tag{3.1.16}$$

in which $\tilde{\lambda}_{\mathrm{a}}$ can be regarded as the representative effective stretch corresponding to the angle $\tilde{\theta}$:

$$\tilde{\lambda}_{\mathrm{a}}=\sqrt{\frac{\lambda^2+\chi^2 N-2\lambda\sqrt{N}\chi\cos\tilde{\theta}}{1-\chi}} \tag{3.1.17}$$

Above all, the molecular configuration of the partially crystallized single chain has been analyzed and calculated by means of some statistical mechanical methods. Especially for the random thermal oscillation of the crystal orientation, the probability density function $\mathrm{P}_{\theta}(\theta)$ is treated by introducing the representative angle $\tilde{\theta}$, which is a non-random variable depending on both the stretch λ and the crystal fraction χ:

$$\cos\tilde{\theta}=\Omega(\lambda,\chi) \tag{3.1.18}$$

Using the function (3.1.18), the evolution of the random crystal orientation can be captured and analyzed during the stretch-induced crystallization process, for which the exact expression will be specified later.

3.1.2.2. Free energy

A key point in the thermodynamic treatment of the partially crystallized single chain is the identification of the physical expression of its free energy. Taking the stretch-free amorphous state as the reference state, a two-step strategy is adopted to derive the free energy as illustrated in Figure 3.1.1. Within the proposed two-step strategy, the description of the first step is very similar to a thermal-induced crystallization and that of the second step is similar to an absolutely mechanical stretching.

3.1.2.2.1. First-step: thermal-induced crystallization

In the first step, the transformation of N_{c} amorphous segments into crystallized segments is performed on the condition that the ends of the remaining amorphous subparts keep free to

occupy most probable locations. This step can be achieved by applying, in a certain manner, a thermodynamic force driving crystallization, and the free energy change can be given by:

$$\Delta\psi_{\mathrm{I}\to\mathrm{II}} = -N_{\mathrm{c}}\left(\Delta H_{\mathrm{m}} - T\Delta S_{\mathrm{m}}\right) + U_{\mathrm{s}} \tag{3.1.19}$$

where ΔH_{m} and ΔS_{m} are the enthalpy and entropy changes associated with the fusion of equivalent segments from a perfect crystal. These two material constants are obtained from the thermodynamic equilibrium state between crystallized and melted segments in the stretch-free state, and their ratio $T_{\mathrm{m}}^{0} = \Delta H_{\mathrm{m}}/\Delta S_{\mathrm{m}}$ corresponds to a characteristic temperature, namely, the equilibrium melting temperature. This temperature is associated to a critical state in which all crystallites can melt theoretically when heated very slowly. In reality, however, the rubber chains without stretching can maintain the fully amorphous state even in a large temperature range quite lower than T_{m}^{0}. This phenomenon is usually attributed to the additional requirements of the free energy for the formation of the interface between the crystallite and the surrounding amorphous phase, and for the formation of the crystallite surface. These interfacial free energies are totally considered in our theory by introducing U_{s} in Eq. (3.1.19) as a general form. Due to the fact that all the interfacial free energies depend heavily on the crystallite morphology, different crystallization theories can give different expressions for U_{s} (Candau et al., 2014; Dolynchuk et al., 2015) . In this work, considering the form of the fully extended crystallization, a linear relationship between the surface free energy U_{s} and the crystallized segment number N_{c} is adopted as a specific example to simplify the simulation, i.e. $U_{\mathrm{s}} = u_{\mathrm{s}}N_{\mathrm{c}}$, u_{s} being the proportionality coefficient. Accordingly, Eq. (3.1.19) can be rewritten as:

$$\Delta\psi_{\mathrm{I}\to\mathrm{II}} = -N_{\mathrm{c}}\Delta H_{\mathrm{m}}\left(1-\frac{T}{T_{\mathrm{m}}^{0}}\right) + u_{\mathrm{s}}N_{\mathrm{c}} \tag{3.1.20}$$

Besides, recall that after this step, the amorphous subparts occupy the most probable locations. It means that, the end-to-end distance of the amorphous part r_{a} is identically equal to the root mean square value $l\sqrt{N_{\mathrm{a}}}$. Under this constraint condition, the chain configuration after the first step is identified and the corresponding probability density P_{II} can be calculated by degenerating the convolution integration in Eq. (3.1.15):

$$\mathrm{P}_{\mathrm{II}} = \left(\frac{3}{2\pi N_{\mathrm{a}}l^{2}}\right)^{3/2}\exp\left\{-N_{\mathrm{a}}\mathfrak{R}\left(\frac{1}{\sqrt{N_{\mathrm{a}}}}\right)\right\} \tag{3.1.21}$$

3.1.2.2.2. Second-step: absolutely mechanical stretching

In the second step, the ends of the partially crystallized chain are dragged to the expected position, the crystal fraction remaining unchanged. Since the crystal is considered as a rigid entity and substantially stiffer than the amorphous part, we assume no stored strain energy during the stretching. The free energy change is fully attributed to the change of the conformational entropy:

$$\Delta\psi_{\mathrm{II}\to\mathrm{III}} = -T\left(s_{\mathrm{III}} - s_{\mathrm{II}}\right) \tag{3.1.22}$$

where $s_{\mathrm{III}} = k_B \ln\left(\mathrm{P}_{\mathrm{III}}\right)$ and $s_{\mathrm{II}} = k_B \ln\left(\mathrm{P}_{\mathrm{II}}\right)$ are the conformational entropies related to the probability densities $\mathrm{P}_{\mathrm{III}} = \mathrm{P}\left(\boldsymbol{r}\right)$ and P_{II}. The term k_B is the Boltzmann's constant.

Substituting Eqs. (3.1.16) and (3.1.21) into Eq. (3.1.22), we can obtain:

$$\Delta\psi_{\mathrm{II}\to\mathrm{III}} = k_{\mathrm{B}} T N_{\mathrm{a}} \left\{ \mathfrak{R}\left(\frac{\tilde{\lambda}_{\mathrm{a}}}{\sqrt{N_{\mathrm{a}}}} \right) - \mathfrak{R}\left(\frac{1}{\sqrt{N_{\mathrm{a}}}} \right) \right\} \tag{3.1.23}$$

which represents the stored free energy resulting from the change of the representative effective stretch (3.1.17) without any chemical energy change.

3.1.2.2.3. Final expression

The free energy of the partially crystallized chain ψ is identified as the sum of the two previous free energy changes, i.e. $\psi = \Delta\psi_{\mathrm{I}\to\mathrm{II}} + \Delta\psi_{\mathrm{II}\to\mathrm{III}}$. Consequently, it takes the following final expression:

$$\psi = -N_{\mathrm{c}}\Delta H_{\mathrm{m}}\left(1 - \frac{T}{T_{\mathrm{m}}^{0}}\right) + u_{\mathrm{s}} N_{\mathrm{c}} + k_{\mathrm{B}} T N_{\mathrm{a}} \left\{ \mathfrak{R}\left(\frac{\tilde{\lambda}_{\mathrm{a}}}{\sqrt{N_{\mathrm{a}}}} \right) - \mathfrak{R}\left(\frac{1}{\sqrt{N_{\mathrm{a}}}} \right) \right\} \tag{3.1.24}$$

It is worth noting that, although the two-step strategy applied for the free energy derivation is hypothetical, it results in a real and accurate physical expression of the free energy. As a thermodynamic potential, the value of the free energy is only dependent on the initial and final states and independent on the thermo-mechanical history during processing. The original intention of conceiving this two-step strategy is to employ the thermodynamic material parameters coming from the stretch-free equilibrium state and, to satisfy the physical consistency.

3.1.2.3. Kinetics

In general, the stretch-induced crystallization is a recoverable micro-mechanism associated with a dissipative hysteretic response, which can be viewed as an irreversible thermodynamic

process accompanied with energy dissipation (Guo et al., 2017). In order to exactly describe this process in a single chain, the set of the selected independent state variables[23] includes not only the temperature T and the stretch λ, but also the crystal fraction χ. As an internal state variable, the crystal fraction χ can effectively capture the crystallization-induced micro-structural evolution of the single chain, which leads to the history-dependent thermo-mechanical response at the macro-scale. According to the internal state variable theory, the non-negative intrinsic dissipation D during the stretch-induced crystallization process can be expressed as:

$$D = \kappa\dot{\chi} \geq 0 \tag{3.1.25}$$

where $\dot{\chi}$ is the crystallization rate and can be regard as a generalized thermodynamic flux, and $\kappa = -\partial\psi/\partial\chi$ is a thermodynamic entity conjugated to the crystal fraction χ and can be correspondingly regard as a generalized thermodynamic force. In line with Eq. (3.1.24), the specific expression of the thermodynamic force κ can be deduced as:

$$\kappa = \underbrace{N\Delta H_{\mathrm{m}}\left(1-\frac{T}{T_{\mathrm{m}}^{0}}\right)}_{\kappa_T} \underbrace{-u_{\mathrm{s}}N}_{\kappa_{\mathrm{S}}} + \underbrace{k_{\mathrm{B}}TN\left\{Z\left(\alpha,\frac{\tilde{\lambda}_{\mathrm{a}}}{\sqrt{N_{\mathrm{a}}}}\right)-Z\left(\frac{1}{2\sqrt{N_{\mathrm{a}}}},\frac{1}{\sqrt{N_{\mathrm{a}}}}\right)\right\}}_{\kappa_{\lambda}} \tag{3.1.26}$$

in which we define $Z(x,y)$ as a function written as:

$$Z(x,y) = x\mathcal{L}^{-1}(y) + \ln\frac{\mathcal{L}^{-1}(y)}{\sinh\mathcal{L}^{-1}(y)} \tag{3.1.27}$$

and the term α is expressed as:

$$\alpha = \frac{\Omega\dfrac{\lambda}{\sqrt{N}} + \chi\dfrac{\lambda}{\sqrt{N}}\dfrac{\partial\Omega}{\partial\chi} - \chi}{\sqrt{\left(\dfrac{\lambda}{\sqrt{N}}\right)^{2} + \chi^{2} - 2\chi\Omega\dfrac{\lambda}{\sqrt{N}}}} \tag{3.1.28}$$

From the (non-equilibrium) thermodynamic viewpoint the partially crystallized single chain tends towards a thermodynamic equilibrium state, which may be considered as a limiting case where all the thermodynamic quantities do not depend upon time. This implies that the internal state variable χ has a tendency to reach a stable value under the prescribed stretch λ i.e. $\dot{\chi} = 0$. This tendency, characterized by the thermodynamic flux $\dot{\chi}$, can be considered to

[23] All the other thermodynamic quantities are regarded as functions of these selected independent state variables, and especially, the free energy function $\psi(T,\lambda,\chi)$ contains all thermodynamic information about the partially crystallized single chain.

be driven by the thermodynamic force κ. On the condition that the deviation from the thermodynamic equilibrium state is small and considering that the intrinsic dissipation D must be non-negative, a linear relationship is assumed between the thermodynamic flux $\dot{\chi}$ and the force κ:

$$\dot{\chi} = A\kappa \tag{3.1.29}$$

where A is a positive coefficient.

Moreover, from Eq. (3.1.26), we can find that the thermodynamic force κ consists of three parts. The first part κ_T is the thermally-activated crystallization force correlated to the process activation at temperatures lower than T_{m}^0 and to the process impedance at temperatures higher than T_{m}^0. The second part κ_{S} is the crystallization resistance which is produced by the interface and surface formation and, accounts for the delay of crystallization in temperature and stretch. The last and third part κ_λ is the stretch-induced crystallization force, which should vanish to zero at the initially fully amorphous state without stretching, $\lambda = 1$ and $\chi = 0$. This initial condition related to the material thermodynamic stability is crucial for the model formulation. It can be satisfied by letting $\cos\tilde{\theta} = \Omega(1,0) = 1/2\sqrt{N}$ in Eq. (3.1.18), which may reveal that, for a single chain with sufficiently large length, the crystallite forms initially in a direction nearly perpendicular to the chain axis. However, considering the fact that the newly formed crystal after stretching tends to orient itself towards the chain direction, we formulate the specific dependence of $\tilde{\theta}$ on both λ and χ as follows:

$$\cos\tilde{\theta} = \Omega(\lambda,\chi) = \frac{2\sqrt{N}-1}{2\sqrt{N}\left(1-e^{-\gamma}\right)}\left(1-e^{-\gamma\omega}\right) + \frac{1}{2\sqrt{N}} \tag{3.1.30}$$

where the parameter γ is a coefficient controlling the orientation rate of the newly formed crystal with the chain axis, and the variable ω is given by:

$$\omega = a\frac{\lambda-1}{\sqrt{N}-1} + b\chi \tag{3.1.31}$$

in which $a \in [0,1]$ and $b \in [0,1]$ are the weight coefficients for the stretch and crystallization effects on the angle $\tilde{\theta}$, respectively, and the sum of them is unit, i.e. $a+b=1$. Figure 3.1.2 presents the $\cos\tilde{\theta}$ evolution with the variable ω in which we can appreciate the γ-dependence of the rate in crystal orientation with the chain axis. Although exponential

functions are introduced in Eq. (3.1.30) to describe the evolution of the crystal orientation, other functional expressions satisfying the requirements could be employed. In the remaining of the paper, the following values are retained: $a = 0.2$, $b = 0.8$ and $\gamma = 10$.

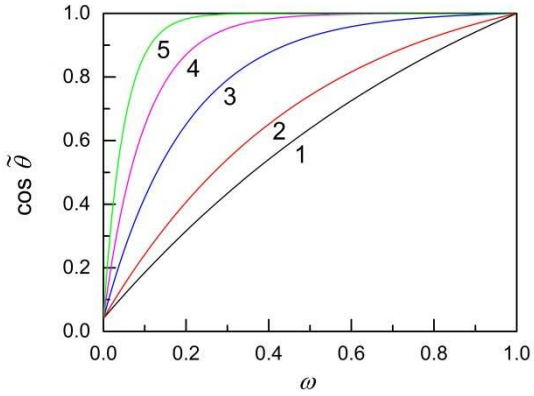

Figure 3.1.2. Crystal orientation with the ω parameter, 1: γ=1, 2: γ=2, 3: γ=5, 4: γ=10, 5: γ=20.

The normalized force f in the single chain is obtained from the differentiation of the free energy function (3.1.24) with respect to the chain stretch:

$$f = \frac{\partial \psi}{\partial \lambda} = k_B T N \beta \mathcal{L}^{-1}\left(\frac{\tilde{\lambda}_a}{\sqrt{N_a}}\right) \tag{3.1.32}$$

in which the term β is expressed as:

$$\beta = \frac{\frac{\lambda}{N} - \Omega\frac{\chi}{\sqrt{N}} - \chi\frac{\lambda}{\sqrt{N}}\frac{\partial \Omega}{\partial \lambda}}{\sqrt{\left(\frac{\lambda}{\sqrt{N}}\right)^2 + \chi^2 - 2\chi\Omega\frac{\lambda}{\sqrt{N}}}} \tag{3.1.33}$$

The macro-kinematic variables are obtained through an averaging over all possible orientations of the micro-stretch λ. In this procedure, the average number of chains per unit reference volume n is introduced and N becomes the average number of segments in the chain network.

3.1.3. Model results and discussion

In this section, the main factors governing the crystallinity and the macro-response are examined using the proposed model under the equilibrium state and the non-equilibrium state involved during stretching/recovery and continuous relaxation. In the bellow discussion, the

term λ corresponds to the uniaxial stretch applied at the macro-level. Several inputs related to micro-structural and thermodynamic properties[24] are required by the modeling: nk_BT_0 = 0.06 MPa (T_0 = 20°C), N = 150, A = 5.0×10^{16} MPa^{-1} s^{-1}, ΔH_m = 4400 J mol^{-1}, T_m^0 = 25°C, u_s = 1500 J mol^{-1}.

3.1.3.1. Equilibrium state

Prior to examine the crystallinity evolution, numerical simulations are carried out to address the influence of temperature as well as stretch on the equilibrium crystallization. A key point of our theory is the thermodynamic force κ in Eq. (3.1.26) which is a decreasing function of the crystallinity and an increasing function of the stretching. These two opposite evolutions are shown in Figure 3.1.3. Since the thermodynamic force drives the crystallinity evolution by the kinetics law (3.1.29), the equilibrium state corresponds to a free thermodynamic force, i.e. κ=0. From the experimental viewpoint, the true thermodynamic equilibrium state at a certain temperature T and a certain stretch λ may require a quasi-infinite duration in an isothermal monotonic stretching.

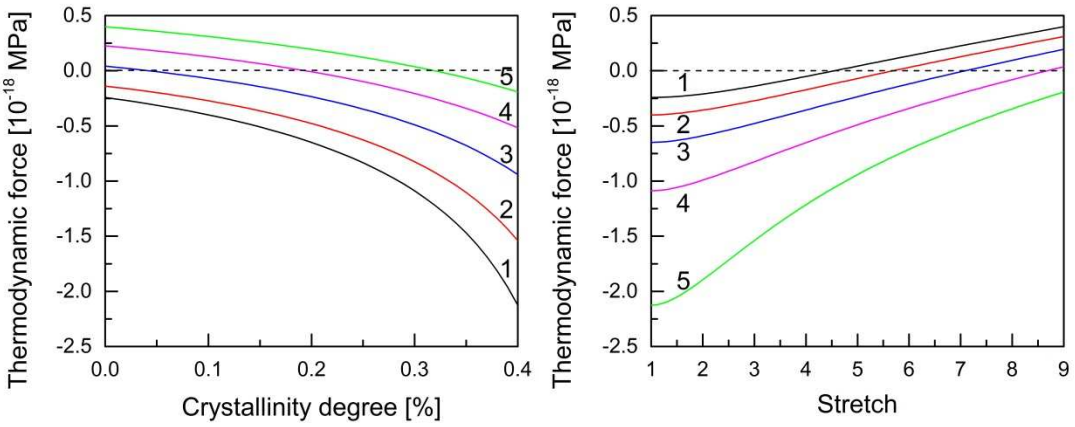

Figure 3.1.3. Thermodynamic force at T=20°C (a) as a function of crystallinity degree for different stretches, 1: λ=1, 2: λ=3, 3: λ=5, 4: λ=7, 5: λ=9, (b) and as a function of stretch for different crystallinity degrees, 1: χ=0%, 2: χ=10%, 3: χ=20%, 4: χ=30%, 5: χ=40%.

[24] It is important to note that non-realistic values for the melting enthalpy ΔH_m and the melting temperature T_m^0 must be used as inputs of existing constitutive theories in order to obtain correct quantitative comparisons with experiments (Flory, 1947, 1949; Arlman and Goppel, 1951; Mistry and Govindjee, 2014; Xie et al., 2016). More realistic values are used in this work by introducing in our theory the crystallite surface free energy. A quantitative evaluation of our theory remains however an important issue for further studies.

In order to overcome this difficulty, two experimental protocols in two steps have been used in the literature (Huneau, 2011; Toki, 2014; Albouy and Sotta, 2017). The first method consists of a cooling of a sample loaded at constant stretch λ well below a certain temperature T and the quasi-equilibrium state can be then reached after progressively warming back up to T. The second method consists of a stretching of a sample at constant temperature T well above a certain stretch λ and the quasi-equilibrium state can be then reached after relaxation to λ. However, the equilibrium state obtained by means of the two experimental protocols is usually different, which indicates the great complexity of the history-dependent thermo-mechanical response during the stretch-induced crystallization process.

The evolution of the simulated equilibrium state is presented in Figure 3.1.4 as a function of stretch and in Figure 3.1.5 as a function of temperature.

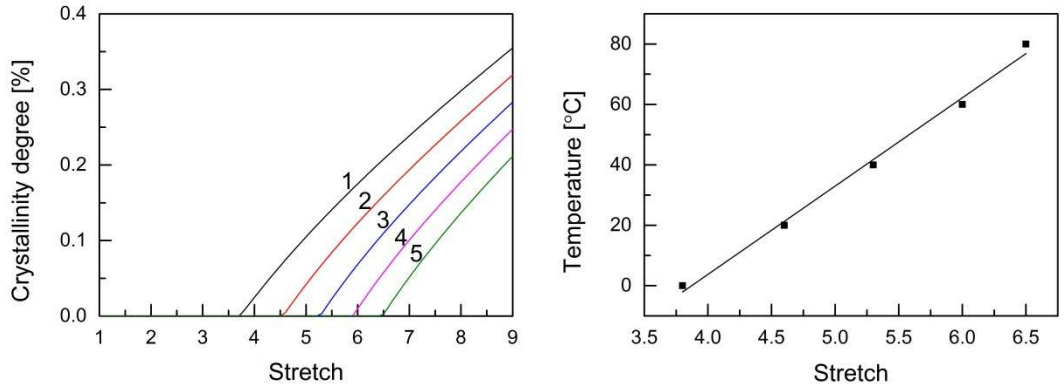

(a) (b)

Figure 3.1.4. Equilibrium crystallization: (a) crystallinity vs. stretch, (b) temperature vs. critical stretch, 1: T=0°C, 2: T=20°C, 3: T=40°C; 4: T=60°C, 5: T=80°C.

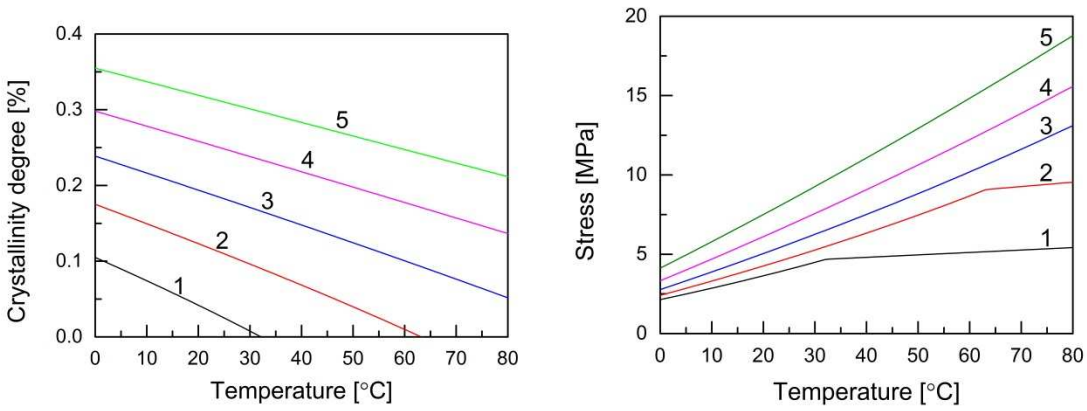

(a) (b)

Figure 3.1.5. Equilibrium crystallization: (a) crystallinity vs. temperature, (b) stress vs. temperature, 1: λ_{max}=5, 2: λ_{max}=6, 3: λ_{max}=7, 4: λ_{max}=8, 5: λ_{max}=9.

The plots in Figure 3.1.4a show a quasi-linear relationship between the crystallinity degree and the stretch. It can be observed that the higher the temperature, the lower the crystallinity degree and the higher the critical stretch at which the crystallization is non-zero. The critical stretch deduced from Figure 3.1.4a is plotted with the corresponding temperature in Figure 3.1.4b such that a straight-line fit adequately describes the results. This is a well-known experimental observation (Trabelsi et al., 2003). Figure 3.1.5 demonstrates that both the crystallinity degree and the stress evolve linearly with temperature but in an opposite manner. This opposite evolution was experimentally highlighted by several authors (Trabelsi et al., 2003; Albouy and Sotta, 2017). The stress increase with temperature is due to two concomitant factors, the decrease in crystallinity degree and the increase in entropy stiffness $nk_{\mathrm{B}}T$ of the amorphous domain. That explains why the slope decreases for the two lower stretch levels after a temperature where the crystallization does not take place. Indeed, in the absence of crystallization, the slope only depends on the entropy effect. Interestingly, this difference in slope was experimentally highlighted by Toki et al. (2005).

3.1.3.2. Non-equilibrium state

The question which arises now is how the above factors could affect the kinetics of crystallization during the course of a stretching followed by a recovery. During these simulations, the stretch λ is ramped to a maximum level $\lambda_{\max}$ and then ramped down to one. Figures 3.1.6, 3.1.7 and 3.1.8 provide the stretching/recovery response for different key factors (namely stretch-level $\lambda_{\max}$, stretch-rate $\dot{\lambda}$ and temperature T) governing the micro-mechanism and the macro-response. It is satisfactory to point out that the model is able to reproduce the delay in the onset of crystallization by using a simple kinetics law given by Eq. (3.1.29) with no additional threshold or restriction. A global view at these plots shows that the stretch-induced crystallization during stretching and the stretch-induced melting during recovery differ which is the exclusive reason of the observed stress hysteresis. This result reveals that the mechanical hysteresis loop is entirely controlled by the crystallization/melting process and not due to viscous effects of the amorphous rubber network since no viscous component is introduced in our theory, which is in accordance with experimental evidences (Clark et al., 1940; Murakami et al., 2002; Trabelsi et al., 2003). Actually, all history-dependent thermo-mechanical features at macro-scale or micro-scale originate from the rate-dependent crystallinity evolution governed by Eq. (3.1.29).

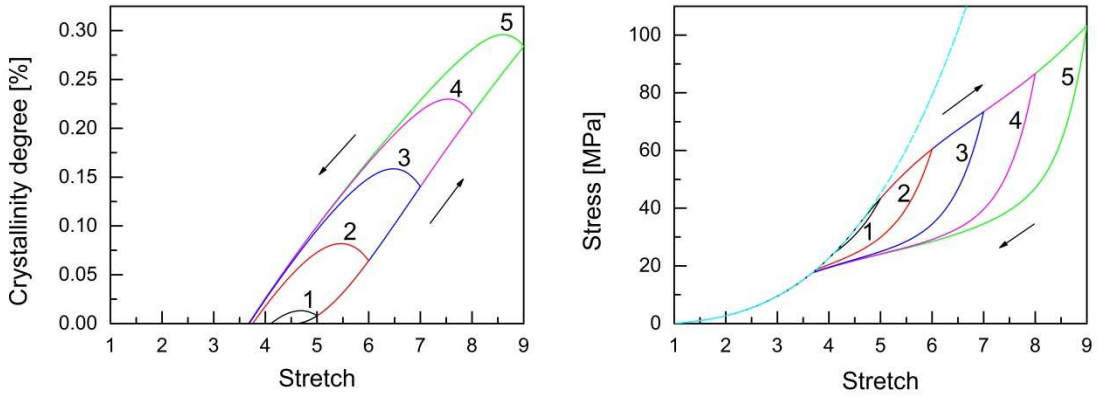

(a) (b)

Figure 3.1.6. Stretch-level influence on stretching/recovery: (a) crystallization kinetics, (b) macro-response, T=20°C, $\dot{\lambda}$=0.05/s, 1: λ_{max}=5, 2: λ_{max}=6, 3: λ_{max}=7, 4: λ_{max}=8, 5: λ_{max}=9.

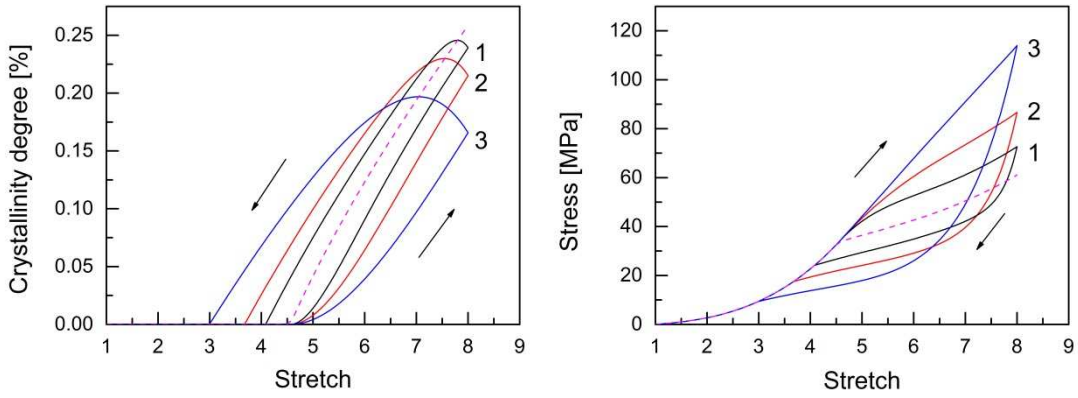

(a) (b)

Figure 3.1.7. Stretch-rate influence on stretching/recovery: (a) crystallization kinetics, (b) macro-response, T=20°C, 1: $\dot{\lambda}$=0.025/s, 2: $\dot{\lambda}$=0.05/s, 3: $\dot{\lambda}$=0.1/s, λ_{max}=8.

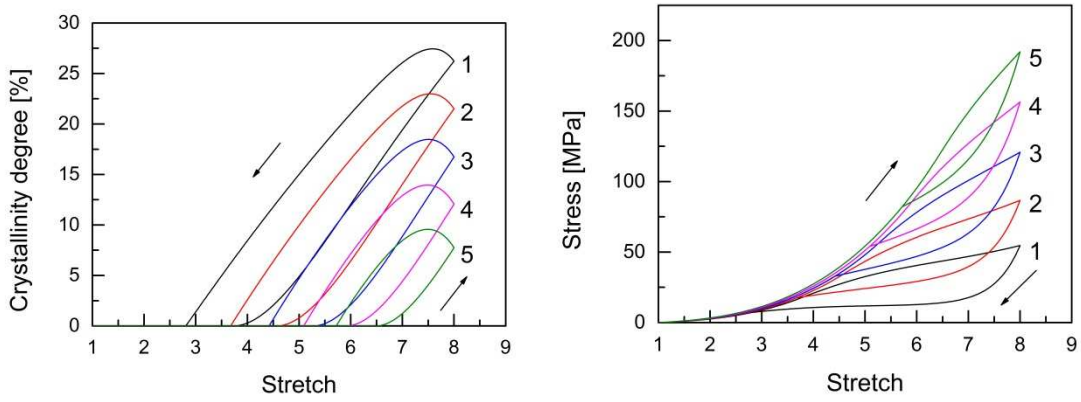

(a) (b)

Figure 3.1.8. Temperature influence on stretching/recovery: (a) crystallization kinetics, (b) macro-response, 1: T=0°C, 2: T=20°C, 3: T=40°C; 4: T=60°C, 5: T=80°C, $\dot{\lambda}$=0.05/s, λ_{max}=8.

More specifically, the crystallization rate depends on the thermodynamic crystallization force expressed by Eq. (3.1.26). The latter, obtained from the differentiation of the proposed free

energy in Eq. (3.1.24) with respect to the crystallization, is a function of stretch level and temperature. Furthermore, the fact that the crystallinity degree at a given stretch is higher during unloading than during loading is a feature well described by our theory. By decreasing the effective stretch in Eq. (3.1.17) the crystallinity thus induces a stress-softening, resulting in the stress difference between the loading path and the unloading path. The stress hysteresis and the crystallization hysteresis can be related from an energetic viewpoint by considering the two scales. At the scale of the micro-mechanism, the crystallization evolution driven by the thermodynamic force induces a local energy dissipation formulated in Eq. (3.1.25). This local thermodynamic dissipation is the exclusive reason of the energy dissipation at the macro-scale manifested by the stress hysteresis.

Figure 3.1.6 presents the crystallinity evolution and the macro-response for various maximum stretch levels. If the maximum stretch level is lower than a certain critical stretch (equal to 4.7 at 20°C as shown in Figure 3.1.4b) for the onset of crystallization the response during stretching/recovery coincide with that of the amorphous rubber network, provided in a dashed line in Figure 3.1.6b. At levels of stretch greater than the crystallization-onset stretch, a hysteretic response is observed whose area increases with the maximum stretch. The crystallinity affects the form of the macro-response by the apparition of a stress inflexion from which the strain-hardening decreases. The stress upturn experimentally observed at very large stretches requires to account for a crystallization-induced stiffening effect since it is not due to the contribution of the remaining amorphous fraction (Albouy et al., 2014). The same mechanism is responsible of two antagonist phenomena, which render it unique, a softening inducing a stress inflexion at moderate stretches and a stiffening inducing a stress upturn at very large stretches. Solely the crystallization-induced softening is accounted for in our theory. As illustrated in Figure 3.1.3b, the thermodynamic force given by Eq. (3.1.26) increases monotonically with the stretch level. During the course of a stretching, the stretch level increases the crystallinity which consequently decreases the strain hardening. The macro-response is strongly related to the crystallinity but also to the crystal form. The stiffening could be accounted for by introducing explicitly the crystal form into the molecular configuration of the partially crystallized chain. Consequently, in addition to the crystallinity and the crystal orientation, the effective stretch in Eq. (3.1.17) could be reformulated to take into account the crystal form.

Let us now focus on the stretch-rate effects. Remind that no viscous component is introduced in our theory to reproduce any time-dependent feature. Figure 3.1.7a shows a

strong influence of the stretch-rate on the crystallinity evolution. The crystallization hysteresis loop area gets smaller and the crystallinity degree increases with decreasing stretch-rate. This feature was already experimentally highlighted in (Rault et al., 2006a; Candau et al., 2015a, 2015b). The rate-dependency of the stretch-induced crystallization is a consequence of the time-dependency of the crystallization kinetics driven by the thermodynamic force given in Eq. (3.1.26). Large stretch-rate leads to less time for crystallization and melting, and vice-et-versa. The stretch at complete melting is also found sensitive to the stretch-rate whereas the onset of crystallization is found independent on that. A stretch-rate dependence of the nucleation may be predicted by inserting that in the energy barrier to the surface formation of newly formed crystallites. In addition, the stretch-rate dependency of the stretch-induced material transformation leads to the rate-dependent stress response observed in Figure 3.1.7b. Indeed, it can be seen that both the amount of stress hysteresis loop area and the magnitude of strain-hardening decrease with decreasing stretch-rate. If the stretch-rate tends to an infinitesimal value the stretch-induced crystallization appears in the form of equilibrium state and no difference between crystallization and melting happens, that is to say that no mechanical hysteresis is observed. This response is provided in dashed lines in Figure 3.1.7. This is again a confirmation that the crystallization/melting process is the source of the stress hysteresis and more generally of all history-dependent thermo-mechanical features. It is now interesting to focus on the temperature effects during stretching/recovery. Figure 3.1.8 presents the crystallinity evolution and the macro-response for various temperatures. It can be observed a regular decrease of the crystal content with temperature which is consistent with experimental observations (Albouy et al., 2005; Rault et al., 2006a, 2006b). The temperature effect on the macro-stress implies numerous phenomena yet misunderstood in the literature, resulting in a high difference in strain-hardening ability due to chain stretching. Basically, the temperature affects the macro-response by entropy effect of the amorphous domain. This phenomenon is concomitant with an increase in crystallinity degree by decreasing the temperature, as a consequence of the temperature dependency of the thermodynamic force given in Eq. (3.1.26). Recall that solely the crystallization-induced softening is introduced in our theory via to the effective stretch expressed in Eq. (3.1.17). Therefore, both phenomena contribute to an increase in stress with temperature. Furthermore, both the onset of crystallization and the completion of melting are strongly affected by the temperature, and increase regularly. The delay $\Delta T = T_{\mathrm{m}} - T_{\mathrm{c}}$ in crystallization is typically termed supercooling under temperature-induced crystallization. The melting temperature T_{m} is usually considered

as a thermodynamic property whereas the crystallization temperature T_c is not since it depends on the experimental conditions, in particular on the cooling rate. The origin of the supercooling comes from the energy barrier to the surface formation of crystallites, which depends on the crystallite form and dimension, both being sensitive to the loading conditions. Under isothermal stretch-induced crystallization, the crystallites completely melt at a lower stretch than at which crystallization starts. This delay $\Delta\lambda = \lambda_m - \lambda_c$ in crystallization can be seen as a superstretching phenomenon as named by Candau et al. (2014). The stretch data for the onset of crystallization λ_c and the completion of melting λ_m extracted from Figure 3.1.8a are plotted in Figure 3.1.9 such that two nearly parallel straight-line fits appear and illustrate these two phenomena. This temperature dependence of crystallization and melting is consistent with the experimental observations of Albouy et al. (2005).

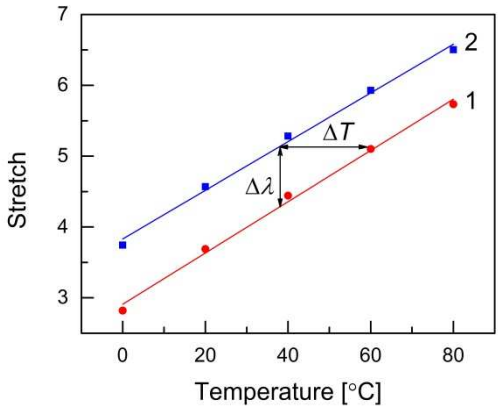

Figure 3.1.9. Supercooling ΔT and superstretching $\Delta\lambda$ phenomena deduced from Figure 3.1.8, 1: onset of crystallization, 2: completion of melting.

As a final point of discussion, we propose to examine the crystallization response under continuous relaxation. These simulations consist firstly to apply a stretching up to a pre-determined level under constant stretch-rate and secondly to keep constant this stretch for a prescribed delay during which the evolutions in crystallinity and in stress are computed. The stretching is performed at a sufficiently high rate to limit the crystallization before relaxation. As shown in Figures 3.1.10a and 3.1.11a, the crystallization during relaxation starts to increase linearly with the time but it rapidly exhibits a curved profile and tends towards a stabilized state for which there is no change in crystallinity. The reached maximum crystallinity degree corresponds to the equilibrium state plotted in Figures 3.1.4a and 3.1.5a. This crystallization evolution process, corresponding to the course of the thermodynamic state from non-equilibrium to equilibrium, is driven in our theory by the thermodynamic force given by Eq. (3.1.26). The latter decreases monotonically with crystallinity degree as shown

in Figure 3.1.5a. Recently, Bruning et al. (2015) measured the crystallinity evolution under continuous relaxation for different stretch-levels and temperatures, but without providing the stress evolution. Our simulations in Figures 3.1.10a and 3.1.11a give similar tendencies.

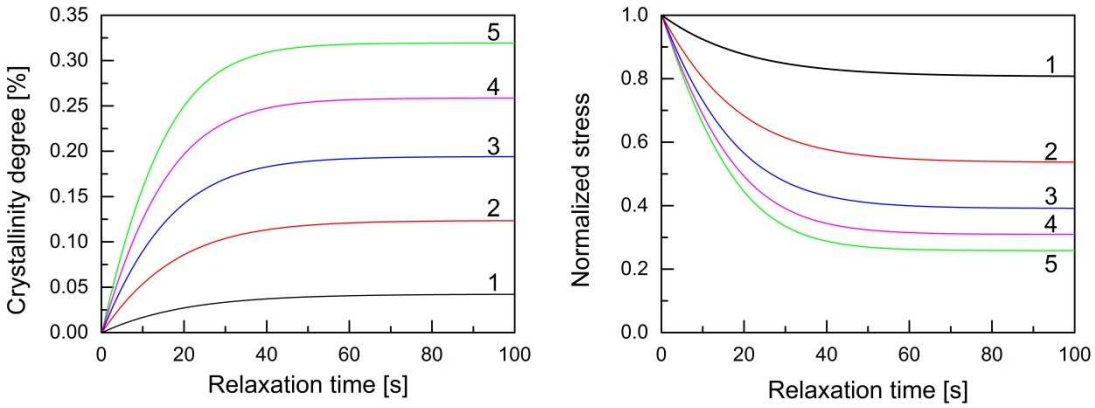

(a) (b)

Figure 3.1.10. Stretch-level influence on continuous relaxation: (a) crystallization kinetics, (b) macro-response, T=20°C, 1: λ_{max}=5, 2: λ_{max}=6, 3: λ_{max}=7, 4: λ_{max}=8, 5: λ_{max}=9.

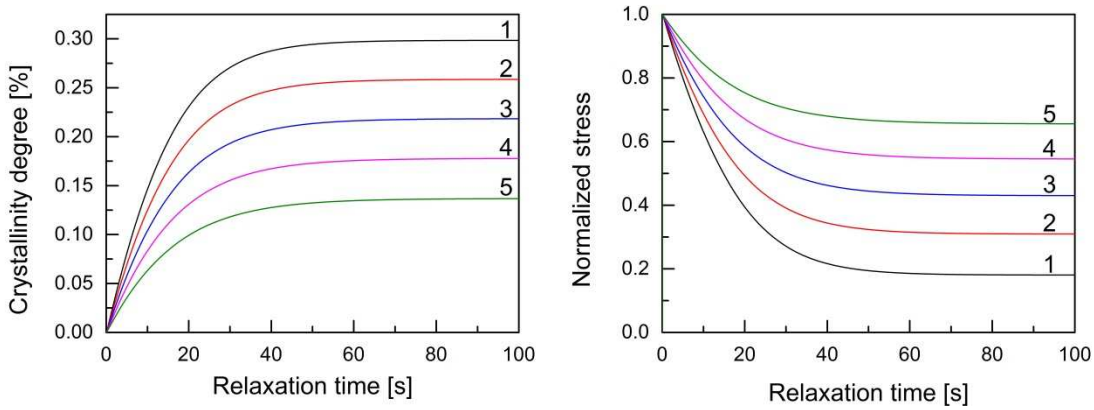

(a) (b)

Figure 3.1.11. Temperature influence on continuous relaxation: (a) crystallization kinetics, (b) macro-response, 1: T=0°C, 2: T=20°C, 3: T=40°C; 3: T=60°C, 4: T=80°C, λ_{max}=8.

More recently, Xie et al. (2017) measured the stretch-level and temperature dependencies of the continuous stress relaxation as a signature of the crystallinity evolution in a crystallizing rubber, but without definitely providing the crystallinity degree. The authors reported the same trends as those observed in Figures 3.1.10b and 3.1.11b. As for the stress hysteresis for which the viscous effects of the amorphous rubber network must be not invoked, according to our simulations the stress relaxation is believed to be solely controlled by the crystallization process under relaxation. Quite interestingly, the normalization of the stress with its maximum value points out a nonlinearity of the stretch-level and temperature effects.

3.1.3.3. Discussion

Our theory provides significant physical insights about a fascinating phenomenon still misunderstood and involves very few physically interpretable material constants: two chain-scale constants, one crystallinity kinetics constant, three thermodynamic constants related to the newly formed crystallites and a function controlling the crystal orientation with respect to the chain. The complex history-dependent thermo-mechanical response of natural rubbers necessitates to provide a set of formulae, not to increase the flexibility of the resulting model but in the aim to describe the entire set of phenomena in connection to the real system. Our theory, based on a micro-mechanism inspired molecular chain approach, formulated within the context of the thermodynamic framework, requires a few assumptions, e.g. rotationally joints of amorphous segments, fully extension of crystallized segments and proportionality of surface free energy. In spite of these assumptions, our model provides significant insights about the relationship between the micro-mechanism of crystallization in stretched rubbers and the history-dependent thermo-mechanical response at the macro-scale. The satisfactory simulation results provided by our theory can be attributed to its solid physical foundation. More specifically, the molecular configuration of the partially crystallized chain is objectively analyzed and reasonably described by means of some statistical mechanical methods, especially considering the random thermal oscillation of the crystal orientation. The present theory treats the stretch-induced crystallization as an irreversible thermodynamic process driven by a thermodynamic crystallization force induced by the non-equilibrium thermodynamic state. A realistic physical expression of the chain free energy is derived according to a two-step strategy by separating crystallization and stretching. This strategy can ensure that the theory satisfies a crucial physical condition related to the material thermodynamic stability, that is, the thermodynamic crystallization force is null at the initial state under the melting temperature. This is a key point that earlier Flory (1947) pointed out as a weakness of his theory, and to date only Mistry and Govindjee (2014) try to solve this issue by introducing a “phenomenological” yield-like function in their theory. As far as we know, this key point is treated from a physical viewpoint for the first time in our theory.

More work is however needed to introduce into our theory the micro-structure of crystallites and its evolution. In particular, in addition to the crystal fraction and orientation, it

is believed that the crystallite morphology, in terms of form[25] and size, could also control the thermo-mechanical macro-response. It is a way to account for in our theory the crystallization-induced stiffening. Moreover, a morphology-dependence of the surface free energy would be interesting to establish in order to propose a more realistic onset of crystallization, in particular in terms of rate-dependency which can be also viewed as a rate-dependency of the necessary supercooling or superstretching. This effect has been experimentally highlighted recently by Candau et al. (2015b). Also, we must recognize that the crystallization kinetics, inherently dominated by the formula (3.1.29) that we have proposed to relate the thermodynamic force and the crystallization rate, is too simple to represent the complex phenomenon. The kinetics law would consider at least: (i) a nonlinear relationship that introduces an increase in crystallization resistance during the stretch-induced crystallization, (ii) a difference between the crystallization path during stretching and the melting path during recovery and, (iii) an explicit temperature-dependency. Further work is needed to incorporate these important ideas in a comprehensive constitutive theory.

3.1.4. Partial conclusions

In this work, we present a new micro-mechanism inspired molecular chain model to describe the thermodynamics and mechanics of stretch-induced crystallization in rubbers. Key factors governing the phenomenon were investigated to better understand the relation between micro-mechanism and macro-response under the equilibrium state and the non-equilibrium state involved during stretching/recovery and continuous relaxation. The proposed approach contains very few physically interpretable material constants and seems to be sufficiently rich to provide important indications concerning this fascinating phenomenon.

A quantitative evaluation of our approach remains however an important issue for further studies. Furthermore, the capability of our approach needs to be further verified under more complex loading conditions. Especially, the coupling between stored/dissipated energy and material transformation during cycling loading could be investigated using the constitutive theory that we have proposed in a recent work (Guo et al., 2018a, 2018b). Moreover, as introduced in the discussion section, our approach, although quite sophisticated, needs

[25] In Anoukou et al. (2014) the incidence of the crystal form on the stiffening has been studied by means of the concepts of micromechanical homogenization without molecular configuration. It would be interesting to consider this aspect into the present theory in our future works.

improvement for a fully realistic description of the micro-structure, such as size and form of crystallites, and its evolution.

3.1.5. References

Albouy, P.A., Marchal, J., Rault, J., 2005. Chain orientation in natural rubber. I. The inverse yielding effect. The European Physical Journal E: Soft Matter and Biological Physics 17, 247-259.

Albouy, P.A., Vieyres, A., Perez-Aparicio, R., Sanseau, O., Sotta, P., 2014. The impact of strain-induced crystallization on strain during mechanical cycling of cross-linked natural rubber. Polymer 55, 4022-4031.

Albouy, P.A., Sotta, P., 2017. Strain-induced crystallization in natural rubber. Advances in Polymer Science 277, 167-205.

Anoukou, K., Zaïri, F., Naït-Abdelaziz, M., Zaoui, A., Z. Qu, Gloaguen, J.M., Lefebvre J.M., 2014. A micromechanical model taking into account the contribution of α- and γ-crystalline phases in the stiffening of polyamide 6-clay nanocomposites: a closed-formulation including the crystal symmetry. Composites Part B 64, 84-96.

Arlman, J.J., Goppel, J.M., 1951. On the degree of crystallinity in natural rubber. Applied Scientific Research 2, 1-8.

Avrami, M., 1939. Kinetics of phase change. I. General theory. The Journal of Chemical Physics 7, 1103-1112.

Avrami, M., 1940. Kinetics of phase change. II. Transformation-time relations for random distribution of nuclei. The Journal of Chemical Physics 8, 212-224.

Avrami, M., 1941. Granulation, phase change, and microstructure. III. Kinetics of phase change. The Journal of Chemical Physics 9, 177-184.

Bruning, K., Schneider, K., Roth, S.V., Heinrich, G., 2015. Kinetics of strain-induced crystallization in natural rubber: a diffusion-controlled rate law. Polymer 72, 52-58.

Candau, N, Laghmach R, Chazeau L, Chenal, J., Gauthier, C., Biben, T., Munch, E., 2014. Strain-induced crystallization of natural rubber and cross-link densities heterogeneities. Macromolecules 47, 5815-5824.

Candau, N., Chazeau, L., Chenal, J.M., Gauthier, C., Ferreira, J., Munch, E., Thiaudière, D., 2015a. Strain induced crystallization and melting of natural rubber during dynamic cycles. Physical Chemistry Chemical Physics 17, 15331-15338.

Candau, N., Laghmach, R., Chazeau, L., Chenal, J.M., Gauthier, C., Biben, T., Munch, E., 2015b. Influence of strain rate and temperature on the onset of strain induced crystallization in natural rubber. European Polymer Journal 64, 244-252.

Clark, G.L., Kabler, M., Blanker, E., Ball, J.M., 1940. Hysteresis in crystallization of stretched vulcanized rubber from X-ray data: correlation with stress-strain behavior and resilience. Industrial and Engineering Chemistry 32, 1474-1477.

Dargazany, R,. Khiem, V.N., Itskov, M., 2014a. A generalized network decomposition model for the quasi-static inelastic behavior of filled elastomers. International Journal of Plasticity 63, 94-109.

Dargazany, R., Khiem, V.N., Poshtan, E.A., Itskov, M., 2014b. Constitutive modeling of strain-induced crystallization in filled rubbers. Physical Review E 89, 022604.

Dolynchuk, O., Kolesov, I., Androsch, R., Radusch, H.J., 2015. Kinetics and dynamics of two-way shape-memory behavior of crosslinked linear high-density and short-chain branched polyethylenes with regard to crystal orientation. Polymer 79, 146-158.

Flory, P.J., 1947. Thermodynamics of crystallization in high polymers. I. Crystallization induced by stretching. The Journal of Chemical Physics 15, 397-408.

Flory, P.J., 1949. Thermodynamics of crystallization in high polymers. IV. A theory of crystalline states and fusion in polymers, copolymers, and their mixtures with diluents. The Journal of Chemical Physics 17, 223-240.

Gaylord, R.J., 1976. A theory of the stress-induced crystallization of crosslinked polymeric networks. Journal of Polymer Science Part B: Polymer Physics 14, 1827-1837.

Gaylord, R.J., Lohse, D.J., 1976. Morphological changes during oriented polymer crystallization. Polymer Engineering and Science 16, 163-167.

Guilie, J., Thien-Nga, L., Le Tallec, P., 2015. Micro-sphere model for strain-induced crystallisation and three-dimensional applications. Journal of the Mechanics and Physics of Solids 81, 58-74.

Guo, Q., Zaïri, F., Baraket, H., Chaabane, M., Guo, X., 2017. Pre-stretch dependency of the cyclic dissipation in carbon-filled SBR. European Polymer Journal 96, 145-158.

Guo, Q., Zaïri, F., Guo, X., 2018a. A thermo-viscoelastic-damage constitutive model for cyclically loaded rubbers. Part I: Model formulation and numerical examples. International Journal of Plasticity 101, 106-124.

Guo, Q., Zaïri, F., Guo, X., 2018b. A thermo-viscoelastic-damage constitutive model for cyclically loaded rubbers. Part II: Experimental studies and parameter identification. International Journal of Plasticity 101, 58-73.

Hamed, G.R., Kim, H.J., Gent, A.N., 1996. Cut growth in vulcanizates of natural rubber, cis-polybutadiene, and a 50/50 blend during single and repeated extension. Rubber Chemistry and Technology 69, 807-818.

Huneau, B., 2011. Strain-induced crystallization of natural rubber: a review of X-ray diffraction investigations. Rubber Chemistry and Technology 84, 425-452.

Katz, J.R., 1925. Rontgenspektrographische untersuchungen am gedehnten kautschuk und ihre mogliche bedeutung fur das problem der dehnungseigenschaften dieser substanz. Naturwissenschaften 13, 410-416.

Kroon, M., 2010. A constitutive model for strain-crystallising rubber-like materials. Mechanics of Materials 42, 873-885.

Le Cam, J.B., Toussaint, E., 2008. Volume variation in stretched natural rubber: competition between cavitation and stress-induced crystallization. Macromolecules 41, 7579-7583.

Mars, W.V., Fatemi, A., 2004. Observations of the constitutive response and characterization of filled natural rubber under monotonic and cyclic multiaxial stress states. Journal of Engineering Materials and Technology 126, 19-28.

Murakami, S., Senoo, K., Toki, S., Kohjiya, S., 2002. Structural development of natural rubber during uniaxial stretching by in situ wide angle X-ray diffraction using a synchrotron radiation. Polymer 43, 2117-2120.

Mistry, S.J., Govindjee, S., 2014. A micro-mechanically based continuum model for strain-induced crystallization in natural rubber. International Journal of Solids and Structures 51, 530-539.

Rastak, R., Linder, C., 2018. A non-affine micro-macro approach to strain-crystallizing rubber-like materials. Journal of the Mechanics and Physics of Solids 111, 67-99.

Rault, J., Marchal, J., Judeinstein, P., Albouy, P.A., 2006a. Chain orientation in natural rubber. II. ^{2}H-NMR study. The European Physical Journal E: Soft Matter and Biological Physics 21, 243-261.

Rault. J., Marchal, J., Judeinstein, P., Albouy, A., 2006b. Stress-induced crystallization and reinforcement in filled natural rubbers: ^{2}H NMR study. Macromolecules 39, 8356-8368.

Roe, R.J., Smith Jr, K.J., Krigbaum, W.R., 1961. Equilibrium degrees of crystallization predicted for “single pass” and folded chain crystallite models. The Journal of Chemical Physics 35, 1306-1311.

Smith, K.J., 1976. Crystallization of networks under stress. Polymer Engineering and Science 16, 168-175.

Toki, S., Sics, I., Hsiao, B.S., Tosaka, M., Poompradub, S., Ikeda, Y., Kohjiya, S., 2005. Probing the nature of strain-induced crystallization in polyisoprene rubber by combined thermomechanical and in situ X-ray diffraction techniques. Macromolecules 38, 7064-7073.

Toki, S., 2014. The effect of strain-induced crystallization (SIC) on the physical properties of natural rubber (NR). In: Kohjiya, S., Ikeda, Y. (Eds.) Chemistry, Manufacture and Applications of Natural Rubber. WoodHead/Elsevier, Cambridge.

Tosaka, M., Senoo, K., Sato, K., Noda, M., Ohta, N., 2012. Detection of fast and slow crystallization processes in instantaneously-strained samples of cis-1,4-polyisoprene. Polymer 53, 864-872.

Trabelsi, S., Albouy, P.A., Rault, J., 2003. Crystallization and melting processes in vulcanized stretched natural rubber. Macromolecules 36, 7624-7639.

Wang, M.C., Guth, E., 1952. Statistical theory of networks of non-Gaussian flexible chains. The Journal of Chemical Physics 20, 1144-1157.

Xie, Z., Wei, C., Guyomar, D., Sebald, G., 2016. Validity of Flory's model for describing equilibrium strain-induced crystallization (SIC) and thermal behavior in natural rubber. Polymer 103, 41-45.

Xie, Z., Sebald, G., Guyomar, D., 2017. Temperature dependence of the elastocaloric effect in natural rubber. Physics Letters A 381, 2112-2116.

CHAPTER 3. STRETCH-INDUCED CRYSTALLIZATION IN RUBBERS

3.2. A MICRO-MACRO CONSTITUTIVE MODEL FOR STRETCH-INDUCED CRYSTALLIZABLE RUBBERS[26]

In this Part of the *Chapter 3*, a physically-based constitutive model, considering the crystallization micro-mechanism at the chain-scale, is formulated within the framework of the continuum thermodynamics. The stretch-induced formation of crystallized segments in the molecular chain is regarded as an irreversible thermodynamic process accompanied with energy dissipation. The microsphere-based strategy is employed to realize the transition from chain-scale to macro-scale, and to account for the crystallization anisotropy induced by the preferred network orientation. The two antagonist phenomena, i.e. the crystallization-induced softening and stiffening, are well reproduced by controlling the spatial orientation and form of the crystallized segments at the chain-scale. The micro-macro constitutive model fully tridimensional is implemented into a finite element program and a quantitative evaluation of the model is performed by comparisons with a few illustrative experiments. A fairly well agreement of the model is shown with tensile experiments under stretching/recovery, in terms of stress-stretch curves and crystallization kinetics, at different stretch levels and temperatures. To illustrate further the capability of the model, numerical simulations are compared to experimental non-homogeneous tensile response in terms of local crystallization/orientation fields of a specimen containing cracks.

Keywords: Stretch-induced crystallization; rubbers; thermodynamics; micro-macro transition; crystallization anisotropy.

[26] This Part of this chapter is based on the following paper: Guo Qiang, Zaïri Fahmi, Guo Xinglin, 2019. A micro-macro constitutive model for stretch-induced crystallizable rubbers.

3.2.1. Partial introduction

The stretch-induced crystallization in rubbers is a fascinating phenomenon, observed firstly by Katz in the first quarter of the last century (Kartz, 1925). Nonetheless, still to date, several features accompanying the relationship between the stretch-induced phase transformation in the material and the overall thermo-mechanical response are still misunderstood (Huneau, 2011; Toki, 2014; Albouy and Sotta, 2017; Le Cam, 2017). The formulation of physically-based constitutive models, including a detailed knowledge of the separate and synergistic effects of key parameters that govern the response of the stretch-induced crystallizable rubber, is of prime importance.

In the mid of the last century, Flory (1947, 1949) proposed the first theory using the statistical mechanics to describe the crystallization micro-mechanism in rubbers. The Flory theory was verified experimentally in several papers (e.g. Arlman and Goppel, 1951; Xie et al., 2016). Then, some refinements of the Flory theory were proposed (Roe et al., 1961; Gaylord, 1976; Gaylord and Lohse, 1976; Smith, 1976) but restricted to the context of the most thermodynamically favorable condition by focusing only on the equilibrium stretch-induced crystallization (i.e. infinitesimal change rate). However, the crystallization micro-mechanism is the solely origin of the inelastic effects (e.g. stress hysteresis and relaxation) in stretch-induced crystallizable rubbers (Clark et al., 1940; Murakami et al., 2002; Trabelsi et al., 2003; Albouy et al., 2005, 2014; Toki et al., 2005; Rault et al., 2006a, 2006b; Tosaka et al., 2012; Samaca Martinez et al., 2013a, 2013b; Rublon et al., 2014; Bruning et al., 2015; Candau et al., 2014, 2015a, 2015b; Laghmach et al., 2015; Le Cam, 2017; Xie et al., 2017). The stretch-induced crystallization is a history-dependent phenomenon. Therefore, the crystallization kinetics is a key physical feature to introduce into any modeling to reproduce the non-equilibrium process. It is only in very recent years that constitutive models were proposed to reproduce the stretch-induced crystallization in rubbers with an intensification the last two years (Kroon, 2010; Dargazany et al., 2014a, 2014b; Mistry and Govindjee, 2014; Guilie et al., 2015; Behnke et al., 2018; Guo et al., 2018; Khiem and Itskov, 2018; Nateghi et al., 2018; Rastak and Linder, 2018; Gros et al., 2019a, 2019b). The foundation of any constitutive model is the formulation of the free energy, from which the constitutive law is obtained. All proposed constitutive models in the literature are distinguished by the final expression of the free energy and the way it is derived. The phenomenon of transformation of the chain from its amorphous state to the partially crystalline state is a multi-scale problem

which may be investigated from the thermodynamic viewpoint. As a common point of all proposed constitutive models, the primary observation of the newly formed nano-sized crystallite is made at the chain-scale. In that sense, the previous models are physically-based. The only difference between the models is the representation of the partially crystallized molecular chain. The transition from the chain-scale to the continuum body scale is realized by translating the partially crystallized single chain to the chain network through an averaging over all possible orientations. The evolution law for the crystallization kinetics is also a key point treated differently in the previous models. For two main reasons, a physically realistic evolution law cannot employ the classical Avrami (1939) formulation for micron-sized spherulite formation in semi-crystalline thermoplastic polymers. The first reason is a difference in morphology and in size of crystals. The second reason is a difference in crystallization condition. The phenomenon in rubbers is allowed to occur at higher temperatures than under quiescent conditions due to a stretch-induced decrease of the conformational entropy.

In this Part of the *Chapter 3*, a physically-based thermo-mechanical constitutive model, considering the crystallization micro-mechanism at the chain-scale, is formulated within the framework of the continuum thermodynamics. A two-step strategy, separating crystallization and stretching, is implemented to derive the free energy of the partially crystallized single chain. Although this two-step strategy is hypothetical, the derived free energy is only dependent on the initial and final states while containing as input the thermodynamic features coming from the stretch-free equilibrium state. The stretch-induced formation of crystallized segments in the molecular chain is regarded as an irreversible thermodynamic process accompanied with energy dissipation and the crystal fraction is introduced as an internal state variable in our theory. The microsphere-based strategy is employed to realize the transition from the crystallization-induced micro-structural evolution of the single chain to the history-dependent thermo-mechanical macro-response. The constitutive model, fully tridimensional, is implemented into a finite element program. A quantitative evaluation of the model is performed by comparisons with tensile experiments, in terms of stress-stretch curves and crystallization kinetics, at different stretch levels and temperatures. The example of a specimen containing cracks is presented to illustrate further the model capability.

The outline of the present Part is as follows. The different aspects of the theory at the macro-scale, at the chain-scale and the transition from chain-scale to macro-scale are provided

in Section 2. The model results are given in Section 3. Section 4 closes the paper with some concluding remarks.

3.2.2. Theory

3.2.2.1. Macro-scale: thermodynamics and mechanics of a continuum body

In this subsection, a constitutive model for stretch-induced crystallizable rubbers is formulated within the framework of the continuum thermodynamics considering the stretch-induced crystallization as an exclusive irreversible thermodynamic mechanism.

The following notation is used throughout the text. Tensors and vectors are denoted by normal boldfaced letters and italicized boldfaced letters, respectively, while scalars and individual components of vectors and tensors are denoted by normal italicized letters. The superposed dot designates the time derivative. Simple contraction of two vectors is denoted by a dot ‘‘$\cdot$’’, double contraction of two tensors by a colon‘‘:’’, and a direct (outer) product by the symbol $\otimes$. Superscript $(\bullet)^{\mathrm{T}}$ denotes transposition, and $\|\bullet\|$ is the norm of a vector defined as $\|\bullet\|=\sqrt{\bullet\cdot\bullet}$.

3.2.2.1.1. Kinematics

Consider a rubber material at the scale of the continuum body. If $\boldsymbol{x}$ is the actual position of a material point located at $\boldsymbol{X}_0$ in the reference configuration, the deformation gradient is: $\mathbf{F}=\partial\boldsymbol{x}/\partial\boldsymbol{X}_0$. Considering the intermediate position $\boldsymbol{X}_{\mathrm{T}}$ at a thermal stress-free configuration, but at a homogeneous absolute temperature T different from the initial temperature T_0, the deformation gradient can be further multiplicatively split into the isothermal mechanical response of the continuum body and the stress-free thermal dilatation of the continuum body:

$$\mathbf{F}=\mathbf{F}_{\mathrm{M}}\mathbf{F}_{\mathrm{T}} \tag{3.2.1}$$

in which $\mathbf{F}_{\mathrm{M}}=\partial\boldsymbol{x}/\partial\boldsymbol{X}_{\mathrm{T}}$ is the mechanical deformation gradient and $\mathbf{F}_{\mathrm{T}}=\partial\boldsymbol{X}_{\mathrm{T}}/\partial\boldsymbol{X}_0$ is the thermal deformation gradient given in the case of thermally isotropic conditions by (Holzapfel and Simo, 1996):

$$\mathbf{F}_{\mathrm{T}}=F_{\mathrm{T}}\mathbf{I},\ F_{\mathrm{T}}=\exp\left(\int_{T_0}^{T}\alpha_{\mathrm{T}}(u)\,du\right) \tag{3.2.2}$$

where $\alpha_{\mathrm{T}}(T)$ is the thermal expansion coefficient and $\mathbf{I}$ is the unit tensor.

The volume change $J=\det\mathbf{F}$ is defined as:

$$J = J_{\mathrm{M}} J_{\mathrm{T}} \tag{3.2.3}$$

where the mechanical volume change is $J_{\mathrm{M}} = \det \mathbf{F}_{\mathrm{M}} = 1$ due to the mechanical incompressibility of the continuum body, and the thermal volume change is:

$$J_{\mathrm{T}} = \det \mathbf{F}_{\mathrm{T}} = \exp\left(\int_{T_0}^{T} 3\alpha_{\mathrm{T}}(u)\, du \right) \tag{3.2.4}$$

3.2.2.1.2. Thermodynamics

As an irreversible thermodynamic process, the stretch-induced crystallization can cause energy dissipation (Guo et al., 2017), and hence the process has to conform to the first and second laws of thermodynamics involving the following fields defined in the continuum body: the stress and strain fields, the internal energy E, the entropy S, the absolute temperature T and the heat flux $\boldsymbol{Q}$.

The first law of thermodynamics requires the following energy balance equation to be satisfied:

$$\dot{E} = \mathbf{P} : \dot{\mathbf{F}} - \nabla_X \cdot \boldsymbol{Q} \tag{3.2.5}$$

where $\mathbf{P}$ is the first Piola-Kirchhoff stress tensor and $\nabla_X \cdot \boldsymbol{Q}$ is the divergence of the Piola-Kirchhoff heat flux $\boldsymbol{Q}$.

The second law requires that the Clausius-Duhem inequality is satisfied:

$$S_{\mathrm{g}} = \dot{S} - \nabla_X \cdot \left(-\boldsymbol{Q}/T \right) \geq 0 \tag{3.2.6}$$

where S_{g} represents the entropy generation rate being equal to the difference between the change rate of the entropy $\dot{S}$ and the divergence of the entropy flow $\nabla_X \cdot \left(-\boldsymbol{Q}/T \right)$.

Combining Eqs. (3.2.5) and (3.2.6), we obtain the following hybrid inequality for the total energy dissipation D which may be correspondingly split into two parts:

$$D = \underbrace{\mathbf{P} : \dot{\mathbf{F}} - \dot{E} + T\dot{S}}_{D_1} + \underbrace{\nabla_X T \cdot \left(-\boldsymbol{Q}/T \right)}_{D_2} \geq 0 \tag{3.2.7}$$

in which the first part D_1 represents the intrinsic dissipation induced by the irreversible energy conversion, such as from the mechanical energy to the thermal energy, and the second part D_2 represents the thermal dissipation induced by the irreversible energy flow, such as heat flowing in non-uniform temperature fields.

The intrinsic dissipation D_1 is given in a stronger form via the so-called Clausius-Planck inequality, in which the existence of a free energy for a unit reference volume (a special form of the Helmholtz free energy potential $\psi = E - TS$) is postulated:

$$D_1 = \mathbf{P} : \dot{\mathbf{F}} - \dot{\psi} - S\dot{T} \geq 0 \tag{3.2.8}$$

All thermodynamic quantities are considered to be dependent on three independent state variables, two external variables: T and $\mathbf{F}_\mathrm{M}$, and one internal variable related to the crystallization micro-mechanism $\boldsymbol{X}$. The latter vector characterizes the crystallization anisotropy, i.e. the crystallinity in any direction of a material point. In this regard, the free energy function ψ, as a thermodynamics function, is: $\psi = \psi\left(T, \mathbf{F}_\mathrm{M}, \boldsymbol{X}\right)$. By introducing the time derivative of the free energy function $\dot{\psi} = \left(\partial\psi/\partial T\right)\dot{T} + \left(\partial\psi/\partial\mathbf{F}_\mathrm{M}\right) : \dot{\mathbf{F}}_\mathrm{M} + \left(\partial\psi/\partial\boldsymbol{X}\right)\cdot\dot{\boldsymbol{X}}$ and the time derivative of the deformation gradient $\dot{\mathbf{F}} = F_\mathrm{T}\dot{\mathbf{F}}_\mathrm{M} + \alpha_\mathrm{T}\mathbf{F}$ into the inequality (3.2.8), the intrinsic dissipation D_1 can be re-written as:

$$D_1 = \left(F_\mathrm{T}\mathbf{P} - \frac{\partial\psi}{\partial\mathbf{F}_\mathrm{M}}\right) : \dot{\mathbf{F}}_\mathrm{M} - \left(S + \frac{\partial\psi}{\partial T} - \alpha_\mathrm{T}\varphi\right)\dot{T} - \frac{\partial\psi}{\partial\boldsymbol{X}}\cdot\dot{\boldsymbol{X}} \geq 0 \tag{3.2.9}$$

in which $\varphi = \mathbf{P} : \mathbf{F}$.

Applying the Coleman-Noll procedure (Coleman and Noll, 1963) to the inequality (3.2.9), we can obtain the constitutive relationships:

$$\mathbf{P} = \frac{1}{F_\mathrm{T}}\frac{\partial\psi}{\partial\mathbf{F}_\mathrm{M}} - p\mathbf{F}_\mathrm{M}^{-\mathrm{T}},\ S = \alpha_\mathrm{T}\varphi - \frac{\partial\psi}{\partial T} \tag{3.2.10}$$

where p is a Lagrange multiplier, which may be only found by means of the boundary conditions.

A residual inequality indicating that the intrinsic dissipation D_1 originates entirely from the crystallization mechanism is obtained:

$$D_1 = \boldsymbol{K}\cdot\dot{\boldsymbol{X}} \geq 0 \tag{3.2.11}$$

in which $\boldsymbol{K}$ is the thermodynamic conjugate vector for $\boldsymbol{X}$:

$$\boldsymbol{K} = -\frac{\partial\psi}{\partial\boldsymbol{X}} \tag{3.2.12}$$

Based on Eq. (3.2.10), and applying the chain rule of differentiation, Eq. (3.2.5) may be written in an alternative form:

$$C\dot{T} = D_1 - \nabla_X\cdot\mathbf{Q} + T\left(F_\mathrm{T}\frac{\partial\mathbf{P}}{\partial T} - \alpha_\mathrm{T}\frac{\partial\phi}{\partial\mathbf{F}_\mathrm{M}}\right) : \dot{\mathbf{F}}_\mathrm{M} - T\left(\frac{\partial\boldsymbol{K}}{\partial T} + \alpha_\mathrm{T}\frac{\partial\varphi}{\partial\boldsymbol{X}}\right)\dot{\boldsymbol{X}} \tag{3.2.13}$$

where $C = T\,\partial S/\partial T$ is a heat capacity-related coefficient and $\phi = \varphi - \psi$ is the complementary energy function.

The free energy function can be written using an additive form:

$$\psi\left(T,\mathbf{F}_{\mathrm{M}},\boldsymbol{X}\right)=\psi_{\mathrm{T}}\left(T\right)+\psi_{\mathrm{M}}\left(T,\mathbf{F}_{\mathrm{M}},\boldsymbol{X}\right) \tag{3.2.14}$$

in which the thermal contribution ψ_{T} is given by:

$$\psi_{\mathrm{T}}\left(T\right)=-\int_{T_0}^{T}C_{\mathrm{T}}\left(u\right)\left(T-u\right)\frac{du}{u} \tag{3.2.15}$$

where C_{T} is the specific heat capacity.

The mechanical contribution $\psi_{\mathrm{M}}\left(T,\mathbf{F}_{\mathrm{M}},\boldsymbol{X}\right)$ is specified in the next subsection.

3.2.2.2. Micro-scale: thermodynamics and mechanics of a single chain

In this subsection, a new micro-mechanism inspired molecular chain approach is developed within the thermodynamic framework in the aim to describe the thermo-mechanical response of a partially crystallized single chain.

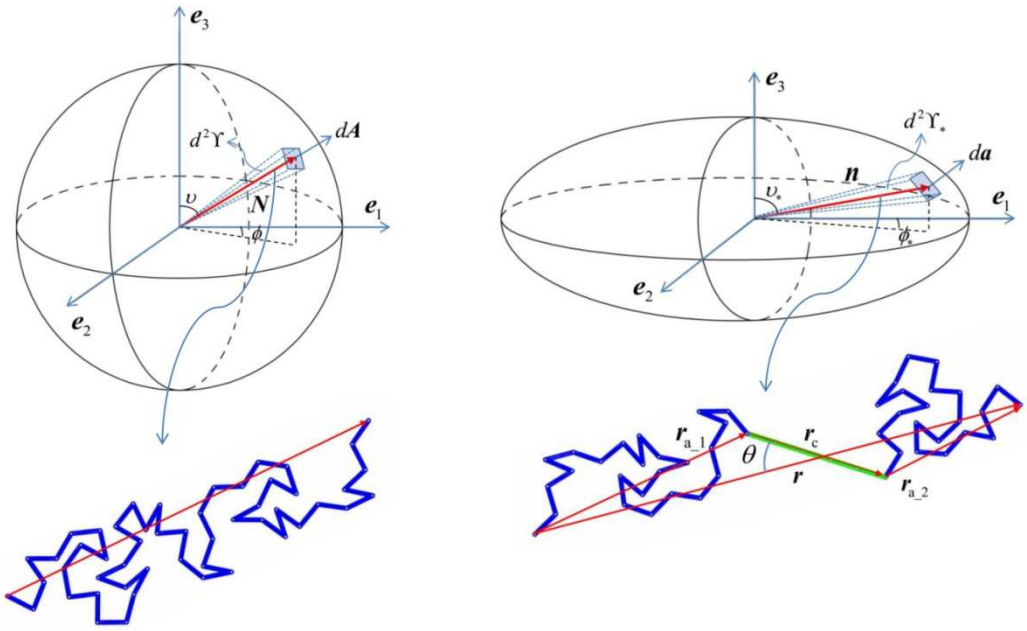

(a) (b)

Figure 3.2.1. Configuration changes due to stretching along the $\boldsymbol{e}_1$-axis of the microsphere: (a) initial and amorphous state, (b) stretched and partially-crystallized state.

3.2.2.2.1. Description of a single chain

The partially crystallized molecular chain consists of N_a amorphous segments, each of length l, and N_c crystallized segments as illustrated in Figure 3.2.1. The crystallization degree χ in the chain is defined as the ratio between the numbers of crystallized segments N_c and the total number of segments $N = N_c + N_a$:

$$\chi = \frac{N_c}{N} \tag{3.2.16}$$

in which χ varies between 0 (totally amorphous state, i.e. $N_a = N$) and 1 (fully crystallized state, i.e. $N_a = 0$) with $N_a = N(1-\chi)$.

The chain end-to-end vector $\boldsymbol{r}$ is the sum of the chain end-to-end vectors of the crystallized part $\boldsymbol{r}_c$ and of the amorphous part $\boldsymbol{r}_a$ such that $\boldsymbol{r} = \boldsymbol{r}_c + \boldsymbol{r}_a$. The angle θ between the chain end-to-end vectors $\boldsymbol{r}$ and $\boldsymbol{r}_c$ is given by the following expression:

$$\|\boldsymbol{r}_a\| = \sqrt{\|\boldsymbol{r}\|^2 + \|\boldsymbol{r}_c\|^2 - 2\|\boldsymbol{r}\|\|\boldsymbol{r}_c\|\cos\theta} \tag{3.2.17}$$

As a representative molecular description, two amorphous subparts from either side of the crystallized part are considered. With continuous oscillations due to thermal fluctuations, a huge number of configurations are possible due to rotation of molecular bonds. The statistical mechanical approach is required to establish the relationship between the configurations of the partially crystallized chain and the average chain response. Following Wang and Guth (1952), the amorphous segments have a random distribution with no interaction and they are rotationally jointed with complete freedom of orientation. By this way, there is no preferred bond angle when no external force is applied. That is to say, all bond angles take the same probability in the un-stretched condition. To calculate the respective molecular chain conformations of the two amorphous subparts the following probability density functions are proposed:

$$\mathrm{P}_{a\_i}\left(\boldsymbol{r}_{a\_i}\right) = \left(\frac{3}{2\pi N_{a\_i} l^2}\right)^{3/2} \exp\left\{-N_{a\_i}\Re\left(\frac{\|\boldsymbol{r}_{a\_i}\|}{N_{a\_i} l}\right)\right\} \tag{3.2.18}$$

in which the subscript i denotes the respective amorphous subparts, 1 and 2.

In Eq. (3.2.18), the function $\Re(x)$ is defined as follows:

$$\Re(x) = x\mathcal{L}^{-1}(x) + \ln\frac{\mathcal{L}^{-1}(x)}{\sinh\left(\mathcal{L}^{-1}(x)\right)} \tag{3.2.19}$$

where $\mathcal{L}^{-1}(x)$ is the inverse Langevin function given by a Padé approximant $\mathcal{L}^{-1}(x) \approx x(3-x^2)/(1-x^2)$.

The probability density function of the whole amorphous part $\mathrm{P}_\mathrm{a}(\boldsymbol{r}_\mathrm{a})$ is derived through the convolution integration of the probability density functions of the two amorphous subparts, $\mathrm{P}_{\mathrm{a\_1}}(\boldsymbol{r}_{\mathrm{a\_1}})$ and $\mathrm{P}_{\mathrm{a\_2}}(\boldsymbol{r}_{\mathrm{a\_2}})$:

$$\mathrm{P}_\mathrm{a}(\boldsymbol{r}_\mathrm{a}) = \int_{R^3} \mathrm{P}_{\mathrm{a\_1}}(\boldsymbol{r}_{\mathrm{a\_1}}) \mathrm{P}_{\mathrm{a\_2}}(\boldsymbol{r}_\mathrm{a} - \boldsymbol{r}_{\mathrm{a\_1}}) d\boldsymbol{r}_{\mathrm{a\_1}} = \left(\frac{3}{2\pi N_\mathrm{a} l^2}\right)^{3/2} \exp\left\{-N_\mathrm{a} \Re\left(\frac{\|\boldsymbol{r}_\mathrm{a}\|}{N_\mathrm{a} l}\right)\right\} \tag{3.2.20}$$

Because the partition of the two amorphous subparts is arbitrary, the probability density function (3.2.20) actually considers all the possible configurations of the amorphous segments, and its expression is not affected by the position of the crystallized part inside the single chain. Analogously, the probability density function of the partially crystallized single chain $\mathrm{P}(\boldsymbol{r})$ is also derived through the convolution integration of the probability density functions of the amorphous part $\mathrm{P}_\mathrm{a}(\boldsymbol{r}_\mathrm{a})$ and the crystallized part $\mathrm{P}_\mathrm{c}(\boldsymbol{r}_\mathrm{c})$:

$$\mathrm{P}(\boldsymbol{r}) = \int_{R^3} \mathrm{P}_\mathrm{a}(\boldsymbol{r} - \boldsymbol{r}_\mathrm{c}) \mathrm{P}_\mathrm{c}(\boldsymbol{r}_\mathrm{c}) d\boldsymbol{r}_\mathrm{c} \tag{3.2.21}$$

The crystal can be considered as a rigid entity of length $\|\boldsymbol{r}_\mathrm{c}\| = \xi N_\mathrm{c} l$ in which ξ is a factor controlling the extension degree of the segments and determined by the stretch level and the crystallization degree; for $\xi = 1$ the crystallized segments are fully extended. By this way, the crystallized potion is assimilated as an equivalent segment, replacing the transformed amorphous segments. For the partially crystallized single chain, there is no external effect to restrict the thermal fluctuations of the crystallized segments, even though the rotation of internal bonds is fixed due to the crystallization effect. Nevertheless, the new links between the remaining amorphous subparts and the crystallized portion are different from the rotationally jointed links between amorphous segments. The continuous random thermal fluctuations of the crystal orientation related to the probability distribution of the angle θ gives therefore all the possible conformations of the crystallized part. That is to say that $\mathrm{P}_\mathrm{c}(\boldsymbol{r}_\mathrm{c}) = \mathrm{P}_\theta(\theta)$. Eq. (3.2.21) is thus re-written as follows:

$$\mathrm{P}(\boldsymbol{r}) = \left(\frac{3}{2\pi N_\mathrm{a} l^2}\right)^{3/2} \int_0^\pi \exp\left\{-N_\mathrm{a} \Re\left(\frac{\lambda_\mathrm{a}}{\sqrt{N_\mathrm{a}}}\right)\right\} \mathrm{P}_\theta(\theta) d\theta \tag{3.2.22}$$

in which λ_a is the effective stretch corresponding to the angle θ:

$$\lambda_{\mathrm{a}} = \frac{\|\boldsymbol{r}_{\mathrm{a}}\|}{l\sqrt{N_{\mathrm{a}}}} = \sqrt{\frac{\lambda^2 + \chi^2\xi^2 N - 2\lambda\sqrt{N}\chi\xi\cos\theta}{1-\chi}} \tag{3.2.23}$$

where $\lambda = \|\boldsymbol{r}\| \big/ l\sqrt{N}$ is the total stretch of the single chain.

The basic property of the probability density function $\mathrm{P}_\theta(\theta)$, i.e. $\int_0^\pi \mathrm{P}_\theta(\theta)\,d\theta = 1$, is considered to reformulate Eq. (3.2.22) in the following form:

$$\mathrm{P}(\boldsymbol{r}) = \left(\frac{3}{2\pi N_{\mathrm{a}} l^2}\right)^{3/2} \exp\left\{-N_{\mathrm{a}}\Re\left(\frac{\tilde{\lambda}_{\mathrm{a}}}{\sqrt{N_{\mathrm{a}}}}\right)\right\} \tag{3.2.24}$$

To ensure the material thermodynamic stability as well as the trend of the newly formed crystal to orient itself towards the chain direction, the term $\tilde{\lambda}_{\mathrm{a}}$ in Eq. (3.2.24) is regarded as a representative effective stretch whose expression is given in Eq. (3.2.23) by replacing the angle θ by a representative angle $\tilde{\theta}$:

$$\cos\tilde{\theta} = \Theta(\lambda,\chi) = \frac{2\sqrt{N}-1}{2\sqrt{N}\left(1-e^{-\gamma}\right)}\left(1-e^{-\gamma\omega}\right) + \frac{1}{2\sqrt{N}} \tag{3.2.25}$$

where γ is a coefficient controlling the orientation rate of the newly formed crystal with the chain axis, and the variable ω is given by:

$$\omega = a\frac{\lambda-1}{\sqrt{N}-1} + b\chi \tag{3.2.26}$$

in which $a \in [0,1]$ and $b \in [0,1]$ are the weight coefficients for the stretch and crystallization effects, respectively, and the sum of them is unit, i.e. $a+b=1$. By this way, we translate the characterization related to the random thermal oscillation of the crystal orientation into that of the non-random variable $\tilde{\theta}$, i.e. Eq. (3.2.25). Besides, in order to consider the stiffening observed at large strains, we can control the extension degree of the crystallized part, for which the following expression of the factor ξ is proposed:

$$\xi = \Omega(\lambda,\chi) = 1 - \delta\omega^{\eta} \tag{3.2.27}$$

where δ and η are coefficients. In order to simplify, the weight coefficients for the stretch and crystallization effects are considered equal, i.e. $a = b = 0.5$.

Remark 1: In the models of Kroon (2010), Mistry and Govindjee (2014) and, Rastak and Linder (2018), the chain end-to-end vectors of the crystallized part is constrained to be parallel to the chain end-to-end vector. In the Flory model (Flory, 1947), the chain traverses the crystallite in the same direction as the displacement between the ends of the chain located

at cross-linkages. These models actually neglect the random thermal fluctuations of the crystal orientation, and thus underestimate the possible configurations of the partially crystallized single chain. The probability of the crystal orientation was also introduced into the probability density function by Smith (1976) but in the context of equilibrium crystallization as a function of stretch and temperature.

3.2.2.2.2. Free energy of a single chain

The derivation of the free energy of a partially crystallized single chain is inspired from the Flory two-step strategy (Flory, 1947). In his theory, Flory considered the fully crystallized single chain as the reference state. The partially crystallized chain is achieved by two separate and distinct steps, namely, (i) melting to form the amorphous part and (ii) stretching to assign the expected position of the chain ends. In this subsection, we reformulate the Flory derivation by considering the stretch-free fully amorphous state as the reference state. The latter represents a notable difference with the Flory theory. Also a hypothetical two-step strategy is formulated. The first step is very similar to a thermal-induced crystallization and the second step is similar to a purely mechanical stretching. As a potential function, the free energy ψ_c is determined only by the current thermodynamic state, independent on the loading history, and hence it is the sum of the contributions of the two steps:

$$\psi_c = \underbrace{\Delta\psi_{I\to II}}_{\text{thermal-induced}} + \underbrace{\Delta\psi_{II\to III}}_{\text{mechanical-induced}} \tag{3.2.28}$$

In the first step, a thermodynamic force driving crystallization is applied, in a certain manner, to transform N_c amorphous segments into crystallized segments, the remaining amorphous subparts keeping free to occupy most probable locations. The free energy change in this step has the following expression:

$$\Delta\psi_{I\to II} = -N_c\Delta H_m\left(1-\frac{T}{T_m^0}\right)+u_s N_c \tag{3.2.29}$$

in which $T_m^0 = \Delta H_m/\Delta S_m$ is the equilibrium melting temperature corresponding to the ratio between enthalpy change ΔH_m and entropy change ΔS_m both associated with the fusion of segments from a perfect crystal, and obtained from the thermodynamic equilibrium process between crystallized and melted states under the stretch-free condition. The term u_s is a proportionality coefficient between the surface free energy U_s and the crystallized segment number N_c. Although different crystallization theories give different expressions for U_s

(Candau et al., 2014; Dolynchuk et al., 2015), the linear relationship is adopted as a specific example to simplify the simulation.

In the second step, the expected position of the chain ends is achieved by stretching without modification of the crystal fraction. Considering the crystallites as infinitely stiff compared to the amorphous part, the free energy change is fully attributed to the change of the conformational entropy: $\Delta\psi_{\mathrm{II}\to\mathrm{III}} = -T\left(s_{\mathrm{III}} - s_{\mathrm{II}}\right)$ in which s_{III} and s_{II} are the conformational entropies related to the final state and the intermediate state, respectively:

$$s_{\mathrm{III}} = k_B \ln\left(\mathrm{P}\left(\boldsymbol{r}\right)\right) = k_B \ln\left(\left(\frac{3}{2\pi N_{\mathrm{a}} l^2}\right)^{3/2} \exp\left\{-N_{\mathrm{a}}\Re\left(\frac{\tilde{\lambda}_{\mathrm{a}}}{\sqrt{N_{\mathrm{a}}}}\right)\right\}\right) \tag{3.2.30}$$

$$s_{\mathrm{II}} = k_B \ln\left(\mathrm{P}_{\mathrm{II}}\right) = k_B \ln\left(\left(\frac{3}{2\pi N_{\mathrm{a}} l^2}\right)^{3/2} \exp\left\{-N_{\mathrm{a}}\Re\left(\frac{1}{\sqrt{N_{\mathrm{a}}}}\right)\right\}\right) \tag{3.2.31}$$

where k_B is the Boltzmann's constant. In the intermediate state, the amorphous subparts occupy the most probable locations and the probability density P_{II} may be considered as a special case of Eq. (3.2.30) in which the representative effective stretch $\tilde{\lambda}_{\mathrm{a}}$ = 1. As a consequence, the free energy change in the second step can be expressed as:

$$\Delta\psi_{\mathrm{II}\to\mathrm{III}} = k_{\mathrm{B}} T N_{\mathrm{a}} \left\{\Re\left(\frac{\tilde{\lambda}_{\mathrm{a}}}{\sqrt{N_{\mathrm{a}}}}\right) - \Re\left(\frac{1}{\sqrt{N_{\mathrm{a}}}}\right)\right\} \tag{3.2.32}$$

Remark 2: The free energy function of the partially crystallized single chain is formulated in the literature by using two methods. In the first method, the free energy function is considered as the sum of two parts (Kroon, 2010; Mistry and Govindjee, 2014). The first part is related to the melting enthalpy in the crystallized portion of the single chain, and the second part is related to the configurational entropy in the remaining amorphous portion. By considering only nucleated crystallites, the Kroon (2010) model is formulated by neglecting the contribution of the crystallization-induced enthalpy and entropy changes in the free energy of the single chain. Mistry and Govindjee (2014) considered the enthalpy and entropy contributions by directly introducing the melting temperature in the free energy expression. This method considers only the current molecular structure and neglects the description of the crystallization process. That results in an ambiguous, and even inconsistent, reference state for the calculation of the free energy change. In fact, the method attempts to calculate the free energy of each part separately. However, the configuration of the whole partially crystallized single chain depends simultaneously on the two parts. Calculating separately the

configurational entropy change of each part is meaningless, and the resulting free energy is not accurate. In the line of the Flory (1947, 1949) theory, the second method calculates the free energy based on the studying of the crystallization process and integrally treat with the configuration change of the whole partially crystallized single chain (Guo et al., 2018; Nateghi et al., 2018; Rastak and Linder, 2018). In order to deduce its expression, some hypothetical steps are used to separate the respective changes related with different mechanisms. The key point of the two-step method is to reasonably describe the configuration change of the whole partially crystallized single chain and accurately calculate the free energy change in each step. Although imaginary, the steps are reasonable while considering infinitesimal evolution. Nateghi et al. (2018) considered the fully crystallized single chain as the reference state. Nevertheless, the calculation of the free energy change in the second step does not introduce the configuration after the first step, and hence results in the overestimation of the corresponding configurational entropy change. Rastak and Linder (2018) derived the free energy of the partially crystallized single chain by integrating the force in the chain with respect to its length. But, the method requires an integration constant dependent on the stretch-free state of the single chain, e.g. the crystal degree and the initial chain force. In fact, the most important point of the two-step method is to describe the configuration after the first step whatever it is crystallization or melting. This is because that the nature of the second step is dragging the two ends of the single chain to the expected position, and the configuration after the first step is indentified as the starting condition of the dragging process. The second heuristic term (i.e. the penalty term) of the integration constant in the Rastak and Linder (2018) model is actually related to this intermediate state although it was interpreted as the effect of the surrounding chains.

3.2.2.2.3. Thermodynamics

The stretch-induced crystallization is regarded as an irreversible thermodynamic process accompanied with energy dissipation (Guo et al., 2017). The Clausius-Planck inequality (3.2.8) can be expressed for a single chain as follows:

$$d_1 = f\dot{\lambda} - \dot{\psi}_c - s\dot{T} \geq 0 \tag{3.2.33}$$

in which d_1 is the corresponding intrinsic dissipation and f is the chain force conjugated to the chain stretch λ.

All thermodynamic quantities at the chain-scale are considered to be dependent on three independent state variables, temperature T, stretch λ and crystallinity degree χ. In this

regard, the free energy function ψ_c, as a thermodynamics function, is: $\psi_c = \psi_c(T, \lambda, \chi)$. By introducing the time derivative of the free energy function $\dot{\psi}_c = \dot{T}\,\partial\psi_c/\partial T + \dot{\lambda}\,\partial\psi_c/\partial\lambda + \dot{\chi}\,\partial\psi_c/\partial\chi$, the intrinsic dissipation d_1 can be re-written as:

$$d_1 = \left(f - \frac{\partial \psi_c}{\partial \lambda} \right)\dot{\lambda} - \left(\frac{\partial \psi_c}{\partial T} + s \right)\dot{T} - \frac{\partial \psi_c}{\partial \chi}\dot{\chi} \geq 0 \tag{3.2.34}$$

Again applying the Coleman-Noll procedure (Coleman and Noll, 1963) to the inequality (3.2.34), we can obtain the constitutive relationships:

$$f = \frac{\partial \psi_c}{\partial \lambda},\ s = -\frac{\partial \psi_c}{\partial T} \tag{3.2.35}$$

and a residual inequality:

$$d_1 = \kappa\dot{\chi} \geq 0 \tag{3.2.36}$$

in which κ is the thermodynamic entity conjugated to the crystallinity degree χ, referenced as crystallization force:

$$\kappa = -\frac{\partial \psi_c}{\partial \chi} \tag{3.2.37}$$

Considering the expression of the chain free energy defined in the previous subsection, the chain force f, the entropy s and the crystallization force κ are given, respectively, by:

$$f = k_B T N \beta \mathcal{L}^{-1}\left(\frac{\tilde{\lambda}_a}{\sqrt{N_a}} \right) \tag{3.2.38}$$

$$s = \frac{N_c \Delta H_m}{T_m^0} - k_B N_a \left\{ \Re\left(\frac{\tilde{\lambda}_a}{\sqrt{N_a}} \right) - \Re\left(\frac{1}{\sqrt{N_a}} \right) \right\} \tag{3.2.39}$$

$$\kappa = \underbrace{N \Delta H_m \left(1 - \frac{T}{T_m^0} \right)}_{\kappa_T} - \underbrace{u_s N}_{\kappa_S} + \underbrace{k_B T N \left\{ \Im\left(\alpha, \frac{\tilde{\lambda}_a}{\sqrt{N_a}} \right) - \Im\left(\frac{1}{2\sqrt{N_a}}, \frac{1}{\sqrt{N_a}} \right) \right\}}_{\kappa_\lambda} \tag{3.2.40}$$

The crystallization force is composed of a thermally-activated part κ_T, a surface energy-induced part κ_S and a stretch-induced part κ_λ. The terms α and β in Eqs. (3.2.38) and (3.2.40) are expressed as:

$$\alpha = \frac{\Omega\Theta\dfrac{\lambda}{\sqrt{N}} + \chi\Omega\dfrac{\lambda}{\sqrt{N}}\dfrac{\partial\Theta}{\partial\chi} - \chi\Omega^2 - \chi^2\Omega\dfrac{\partial\Omega}{\partial\Omega} + \chi\Theta\dfrac{\lambda}{\sqrt{N}}\dfrac{\partial\Omega}{\partial\chi}}{\sqrt{\left(\dfrac{\lambda}{\sqrt{N}}\right)^2 + \chi^2\Omega^2 - 2\chi\Omega\Theta\dfrac{\lambda}{\sqrt{N}}}} \tag{3.2.41}$$

$$\beta=\frac{\frac{\lambda}{N}+\chi^2\Omega\frac{\partial\Omega}{\partial\lambda}-\chi\Theta\frac{\lambda}{\sqrt{N}}\frac{\partial\Omega}{\partial\lambda}-\Omega\Theta\frac{\chi}{\sqrt{N}}-\chi\Omega\frac{\lambda}{\sqrt{N}}\frac{\partial\Theta}{\partial\lambda}}{\sqrt{\left(\frac{\lambda}{\sqrt{N}}\right)^2+\chi^2\Omega^2-2\chi\Omega\Theta\frac{\lambda}{\sqrt{N}}}} \tag{3.2.42}$$

In Eq. (3.2.40), the function $\Im(x,y)$ is defined as follows:

$$\Im(x,y)=x\mathcal{L}^{-1}(y)+\ln\frac{\mathcal{L}^{-1}(y)}{\sinh\mathcal{L}^{-1}(y)} \tag{3.2.43}$$

From the irreversible thermodynamic viewpoint, the crystallization evolution, regarded as a generalized thermodynamic flux, is driven by the thermodynamic crystallization force and should obey the second thermodynamic law. To this end, we formulate a linear relationship between the crystallization rate $\dot{\chi}$ and the corresponding force κ:

$$\dot{\chi}=A_c\kappa \text{ and } \dot{\chi}=A_m\kappa \tag{3.2.44}$$

where A_c and A_m are coefficients related to crystallization path and melting path, respectively, with $A_c\geq 0$ and $A_m\geq 0$ to satisfy condition (3.2.36). The crystallization kinetics defined in Eq. (3.2.44) reflects the intrinsic trend of irreversible thermodynamic process, that is, the trend from a non equilibrium thermodynamic state to an equilibrium state where all the thermodynamic quantities do not depend upon time.

In order to reveal the thermodynamic essence of the partially crystallized molecular chain model, the free energy and the corresponding thermodynamic force are plotted in the stretch-crystallinity space, as shown in Figure 3.2.2. A global view at these plots shows that the formulated free energy function is a concave function and the thermodynamic force has opposition trend for the increase of stretch and crystallinity. These characteristics of the thermodynamic potential and force ensure the existing of a stable equilibrium state for any stretch condition. More precisely, the free energy in the stretched condition first decreases with the crystallinity and then increases. The minimum free energy value corresponds to the equilibrium state in which the thermodynamic force is null. Nevertheless, in the un-stretched condition, the free energy immediately increases with the crystallinity and the minimum value occurs in the fully amorphous state. For the rubbers under stretch-free condition with melting temperature, all the internal molecular chains are in a critical state where the un-stretched fully amorphous chain can immediately crystallize once it is subjected to stretching or cooling. This critical state is achieved by formulating the evolution function of the

representative angle $\tilde{\theta}$ to satisfy the initial condition $\cos\tilde{\theta}=\Theta(1,0)=1/2\sqrt{N}$, see Eq. (3.2.25). In conclusion, our model ensures that the stretch-induced crystallizable rubbers have thermodynamic stability without the introduction of any additional heuristic constraint.

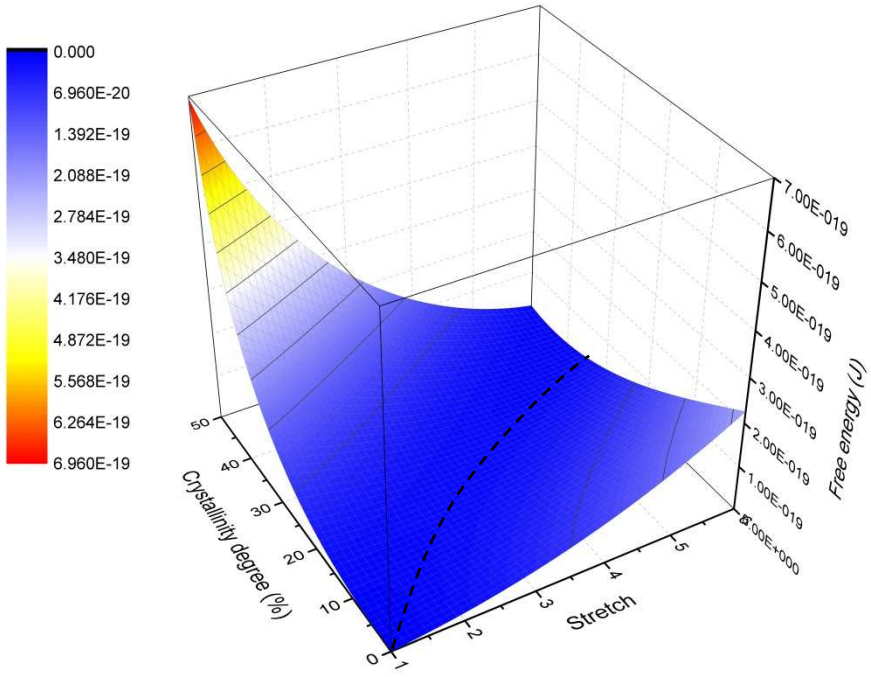

(a)

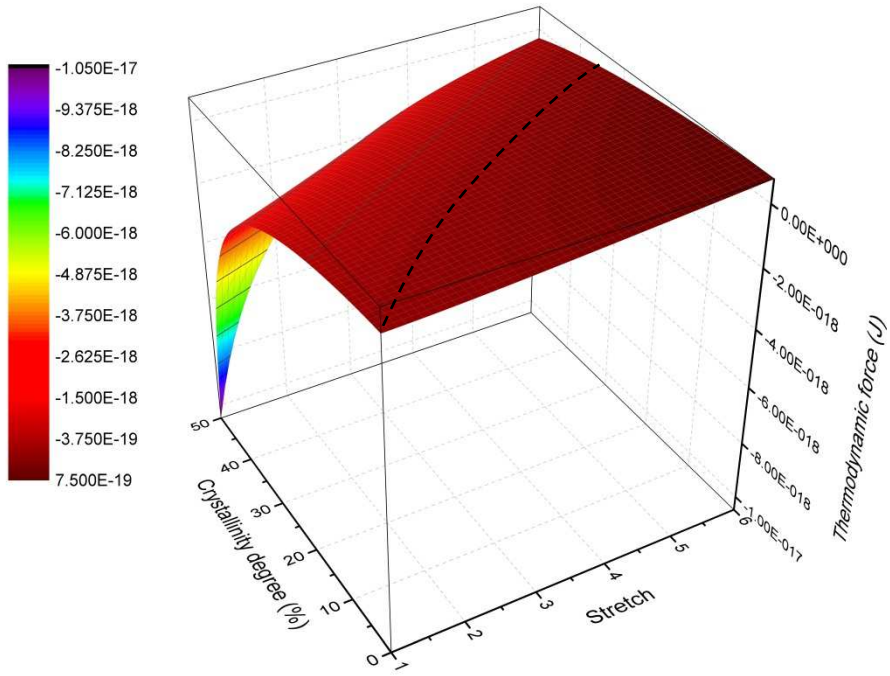

(b)

Figure 3.2.2. Surface of (a) free energy and (b) thermodynamic force in the stretch-crystallinity space.

Remark 3: In their models, Kroon (2010) and Dargazany et al. (2014a, 2014b) introduced the crystallinity evolution as an evolution of the number of fixed-size nucleated crystallites. In the Kroon (2010) model the crystallinity evolution is governed by a phenomenological Arrhenius-type kinetics, coming from the classical mathematical formulation of thermally-induced crystallization processes. In the Dargazany et al. (2014a, 2014b) model the crystallinity evolution is governed by the chain length statistic distribution. Mistry and Govindjee (2014), Guilie et al. (2015) and, Rastak and Linder (2018) use the same crystallization kinetics than Eq. (3.2.44) in their models. Nevertheless, in order to ensure the crystallization does not develop spontaneously on the stretch-free condition, some additional conditions have to be made to offset the positive thermodynamic force in the initial state. Those constructed additional conditions are often interpreted as the crystallization resistance induced by the interface or surface formation, which actually do not being considered at all in their model formulation. Mistry and Govindjee (2014) and, Guilie et al. (2015) introduced a yield-like threshold to additionally restrict the evolution law whereas Rastak and Linder (2018) introduced the surrounding chain effect by formulating a differentiable logarithmic penalty function. Furthermore, Guilie et al. (2015) introduced different evolution laws to capture crystallization and melting processes. In the same manner, the model proposed by Gros et al. (2019a, 2019b) introduced nucleation, crystallization and melting thresholds using the theory proposed by Candau et al. (2014) in which the form and surface energy of nucleated crystallites is considered (Laghmach et al., 2015).

3.2.2.3. Transition from micro to macro-scale

Our description of the partially crystallized single chain can be implemented into all molecular chains of the network to get the spatially averaged rubber response. All macro-quantities at every material point are derived from micro-quantities by means of the transition scale microsphere-based method (Bazant and Oh, 1986; Miehe et al., 2004). A schematic representation of the microsphere is provided in Figure 3.2.1. The method consists in the symbolization of a material point by a unit sphere O_0 considering a perfect random-in-space distribution of molecular chains. As a result of a preferred network orientation, a non-uniform distribution of the crystallization micro-mechanism at the chain-scale is expected. The initially isotropic network becomes thus anisotropic.

Let us introduce the material unit vector $\boldsymbol{N}$ which is considered to be embedded with a un-stretched molecular chain and oriented from the centre to the surface of the microsphere. The material unit vector $\boldsymbol{N}$ in the referential orientation space O_0 may be expressed as:

$$\boldsymbol{N}=\cos\phi\sin\upsilon\boldsymbol{e}_1+\sin\phi\sin\upsilon\boldsymbol{e}_2+\cos\upsilon\boldsymbol{e}_3 \tag{3.2.45}$$

where $\upsilon\in[0,\pi]$ and $\phi\in[0,2\pi]$ are the classical spherical angles, and $\{\boldsymbol{e}_1,\boldsymbol{e}_2,\boldsymbol{e}_3\}$ denote the axes of a Cartesian coordinate system. Furthermore, the differential area element of the unit sphere Π takes in terms of these angles the following expression: $d^2\Upsilon=\sin\upsilon d\phi d\upsilon$ which is referenced as the solid angle and whose integral provides the unit sphere total area $S_{\mathrm{u}}=\int_0^{\pi}\int_0^{2\pi}\sin\upsilon d\phi d\upsilon=4\pi$.

Subsequently, the internal state variable $\boldsymbol{X}$ related to the crystallization micro-mechanism can be considered as a vector whose components are the crystallinity degrees at the chain-sale in all directions in the referential orientation space $\chi(\boldsymbol{N})$:

$$\boldsymbol{X}=\{\chi(\boldsymbol{N})\} \tag{3.2.46}$$

and hence the macroscopic crystallinity degree X at the material point can be defined as the average value of the crystallinity degree in all directions $\chi(\boldsymbol{N})$, which is obtained by integrating $\chi(\boldsymbol{N})$ over the unit sphere surface:

$$X=\frac{1}{4\pi}\int_{\Pi}\chi(\boldsymbol{N})\,d\Upsilon \tag{3.2.47}$$

Upon application of the macro-deformation $\mathbf{F}_{\mathrm{M}}$, the referential orientation space O_0 transforms to the spatial orientation space O_* with the corresponding referential unit vectors mapping to spatial stretch vectors as:

$$\lambda\boldsymbol{n}=\mathbf{F}_{\mathrm{M}}\boldsymbol{N},\ \lambda=\sqrt{\boldsymbol{N}\cdot\mathbf{C}_{\mathrm{M}}\boldsymbol{N}} \tag{3.2.48}$$

where $\mathbf{C}_{\mathrm{M}}=\mathbf{F}_{\mathrm{M}}^{\mathrm{T}}\mathbf{F}_{\mathrm{M}}$ is the right Cauchy-Green deformation tensor and $\boldsymbol{n}$ is a unit vector characterizing the orientation of the material vector $\boldsymbol{N}$ in the current conformation:

$$\boldsymbol{n}=\cos\phi_*\sin\upsilon_*\boldsymbol{e}_1+\sin\phi_*\sin\upsilon_*\boldsymbol{e}_2+\cos\upsilon_*\boldsymbol{e}_3 \tag{3.2.49}$$

Consequently, the referential unit sphere transforms to a ellipsoid and the corresponding solid angle in the spatial orientation space O_* is $d^2\Upsilon_*=\sin\upsilon_* d\phi_* d\upsilon_*$. The change in the oriented surface, from that on the referential unit sphere $d\boldsymbol{A}=dA\boldsymbol{N}$ to that on the current ellipsoid $d\boldsymbol{a}=da\tilde{\boldsymbol{n}}$, is given by:

$$d\boldsymbol{a}=\mathbf{F}_{\mathrm{M}}^{-\mathrm{T}}d\boldsymbol{A},\ da=\frac{dA}{\lambda} \tag{3.2.50}$$

where $\tilde{\boldsymbol{n}}$ is a unit vector characterizing the orientation of the material surface $\boldsymbol{N}$ in the current conformation. The vectors $\boldsymbol{N}$ fill the solid angle $d^2\Upsilon$ and the vectors $\boldsymbol{n}$ fill the solid angle $d^2\Upsilon_*$. Their relationship can be obtained by the infinitesimal surface obtained by the projection of $da\tilde{\boldsymbol{n}}$ over $\boldsymbol{n}$ divided by the square of the sphere radius intersecting the ellipsoid at the given point, i.e., λ^2:

$$d^2\Upsilon_*=\frac{\left(da\tilde{\boldsymbol{n}}\right)\cdot\boldsymbol{n}}{\lambda^2}=\frac{dA}{\lambda^3}=\frac{d^2\Upsilon}{\lambda^3} \tag{3.2.51}$$

Since in the experiments the stretch-induced crystallization is measured in the current configuration, the crystallization degree in different orientations must be present in spatial orientation space, which $\chi_*\left(\boldsymbol{n}\right)$ satisfies this relation $\chi_*\left(\boldsymbol{n}\right)d\Upsilon_*=\chi\left(\boldsymbol{N}\right)d\Upsilon$. So that:

$$\chi_*\left(\boldsymbol{n}\right)=\lambda^3\chi\left(\boldsymbol{N}\right) \tag{3.2.52}$$

Similarly to the definition of the macroscopic crystallinity degree, the free energy function ψ_{M} can be obtained by integrating the chain free energy function ψ_{c} over the unit sphere surface:

$$\psi_{\mathrm{M}}\left(T,\mathbf{F}_{\mathrm{M}},\boldsymbol{X}\right)=\frac{n}{4\pi}\int_{\Pi}\psi_{\mathrm{c}}\left(T,\lambda\left(\mathbf{F}_{\mathrm{M}},\boldsymbol{N}\right),\chi\left(\boldsymbol{N}\right)\right)d\Upsilon \tag{3.2.53}$$

in which n is the chain density.

The average stress, the average entropy and the average thermodynamic force at the material point are, respectively, given by:

$$\mathbf{P}=\frac{n}{4\pi F_{\mathrm{T}}}\int_{\Pi}\frac{\partial\psi_{\mathrm{c}}\left(T,\lambda\left(\mathbf{F}_{\mathrm{M}},\boldsymbol{N}\right),\chi\left(\boldsymbol{N}\right)\right)}{\partial\mathbf{F}_{\mathrm{M}}}d\Upsilon-p\mathbf{F}_{\mathrm{M}}^{-\mathrm{T}} \tag{3.2.54}$$

$$S=\alpha_{\mathrm{T}}\varphi-\frac{n}{4\pi}\int_{\Pi}\frac{\partial\psi_{\mathrm{c}}\left(T,\lambda\left(\mathbf{F}_{\mathrm{M}},\boldsymbol{N}\right),\chi\left(\boldsymbol{N}\right)\right)}{\partial T}d\Upsilon \tag{3.2.55}$$

$$\boldsymbol{K}=-\frac{n}{4\pi}\int_{\Pi}\frac{\partial\psi_{\mathrm{c}}\left(T,\lambda\left(\mathbf{F}_{\mathrm{M}},\boldsymbol{N}\right),\chi\left(\boldsymbol{N}\right)\right)}{\partial\boldsymbol{X}}d\Upsilon \tag{3.2.56}$$

After a series of straightforward derivations, these macroscopic quantities take the form:

$$\mathbf{P}=\frac{n}{4\pi F_{\mathrm{T}}}\mathbf{F}_{\mathrm{M}}\int_{\Pi}\frac{f\left(T,\lambda\left(\mathbf{F}_{\mathrm{M}},\boldsymbol{N}\right),\chi\left(\boldsymbol{N}\right)\right)}{\lambda\left(\mathbf{F}_{\mathrm{M}},\boldsymbol{N}\right)}\left(\boldsymbol{N}\otimes\boldsymbol{N}\right)d\Upsilon-p\mathbf{F}_{\mathrm{M}}^{-\mathrm{T}} \tag{3.2.57}$$

$$S=\alpha_{\mathrm{T}}\varphi-\frac{n}{4\pi}\int_{\Pi}s\left(T,\lambda\left(\mathbf{F}_{\mathrm{M}},\boldsymbol{N}\right),\chi\left(\boldsymbol{N}\right)\right)d\Upsilon \tag{3.2.58}$$

$$\boldsymbol{K}=\left\{\kappa\left(T,\lambda\left(\mathbf{F}_{\mathrm{M}},\boldsymbol{N}\right),\chi\left(\boldsymbol{N}\right)\right)\right\} \tag{3.2.59}$$

The intrinsic dissipation at the two scales $D_1=\boldsymbol{K}\cdot\dot{\boldsymbol{X}}$ and $d_1=\kappa\dot{\chi}$ can be also related:

$$D_1=\frac{n}{4\pi}\int_{\Pi}d_1\left(T,\lambda\left(\mathbf{F}_{\mathrm{M}},\boldsymbol{N}\right),\chi\left(\boldsymbol{N}\right)\right)d\Upsilon \tag{3.2.60}$$

3.2.3. Results and discussion

Experimental studies on the stretch-induced crystallization are usually performed by means of the in-situ wide-angle X-ray scattering (WAXD) technique (Huneau, 2011; Toki, 2014; Albouy and Sotta, 2017). The high intensity of synchrotron X-rays allowed the collection of two-dimensional WAXD patterns during the deformation of stretch-induced crystallizable rubbers. After a series of process and analysis on the scattering intensity of the WAXD patterns, the crystallinity degree can be quantitatively obtained, as well as the crystallization anisotropy. On basis of experiment data in the literature, we perform some simulations and make some discussions.

The micro-macro constitutive model has ten parameters, each of which has a clear micro-structural or thermodynamic interpretation: the chain-scale constants: n and N, the crystal kinetics constants: A_{c} and A_{m}, the crystal thermodynamic constants: ΔH_{m}, T_{m}^{0} and u_{s}, the crystal orientation constant: γ, and the crystal form constants: δ and η.

3.2.3.1. Key features of stretch-induced crystallization

The capability of the model to account for key features governing the phenomenon of stretch-induced crystallization can be highlighted by a stretching to a maximum stretch level at a certain stretch-rate followed by a recovery at the same absolute stretch-rate. Figure 3.2.3 presents the crystallization kinetics and the stress-stretch curve during stretching/recovery using the following set of model parameters: $nk_{\mathrm{B}}T_0$ = 0.6 MPa (T_0 = 20°C), N = 75.0, A_{c} = 50.0×10^{16} MPa^{-1} s^{-1}, A_{m} = 15.0×10^{16} MPa^{-1} s^{-1}, ΔH_{m} = 7.0×10^{-21} J, T_{m}^{0} = 25°C, u_{s} = 3.5×10^{-21} J, γ=10.0, δ =1.5, η =5.0. The model shows that the stress response during stretching exhibits a relatively stable stress when the crystallization occurs (point B) and a gradual hardening when the crystallization continues from point C to point D. During recovery, the crystallinity degree at a given stretch is higher than during stretching that leads to a hysteretic response in the crystallization kinetics. The stress response exhibits a relatively stable value

from point E to point F and the hysteresis loop is closed at the melting point F. Due to this difference between crystallization path and melting path, a stress hysteresis loop occurs. The latter is not induced by viscosity effects since no viscous component is introduced in the model.

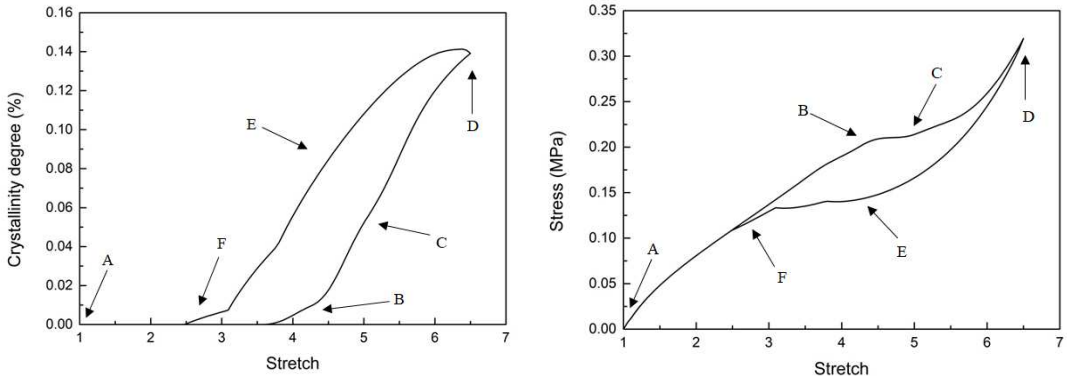

(a) (b)

Figure 3.2.3. Typical stages in (a) crystallization kinetics and (b) stress-stretch curve.

Obviously, the crystallization evolution law (see Eq. (3.2.44)) is formulated by means of a rate-dependent theory, which allows the crystallization to evolve consistently with time until reaching the equilibrium thermodynamic state with the crystallization force being null. Longer time duration hence indicates lager crystallization evolution under the same condition. In the extreme case, the crystallization can evolve along a single path keeping in the state of thermodynamic equilibrium. Consequently, we can expect that an infinitesimal loading rate would drive to no difference between crystallization path and melting path, and to the stress hysteresis vanishing.

The relationship between the crystallization micro-mechanism and the macro-response seems well described by the proposed physically-based model. Especially, the appearance of the stress inflexion (from point B to point C) and the hardening (from point C to point D) during the course of the stretching are entirely due to crystallization-induced softening at large stretches and crystallization-induced stiffening at larger stretches. The two antagonist phenomena, i.e. the crystallization-induced softening and stiffening, are well reproduced by formulating skill fully the governing equations to control the spatial orientation and form of the crystallized segments at the chain-scale (see Eqs. (3.2.25) and (3.2.27)). More precisely, the decrease of the representative angle $\tilde{\theta}$ is response for the crystallization-induced softening whose rate is controlled by the crystal orientation constants γ, whereas the decrease of the

extension degree ξ is response for the crystallization-induced hardening whose rate is controlled by the crystal form constants δ and η.

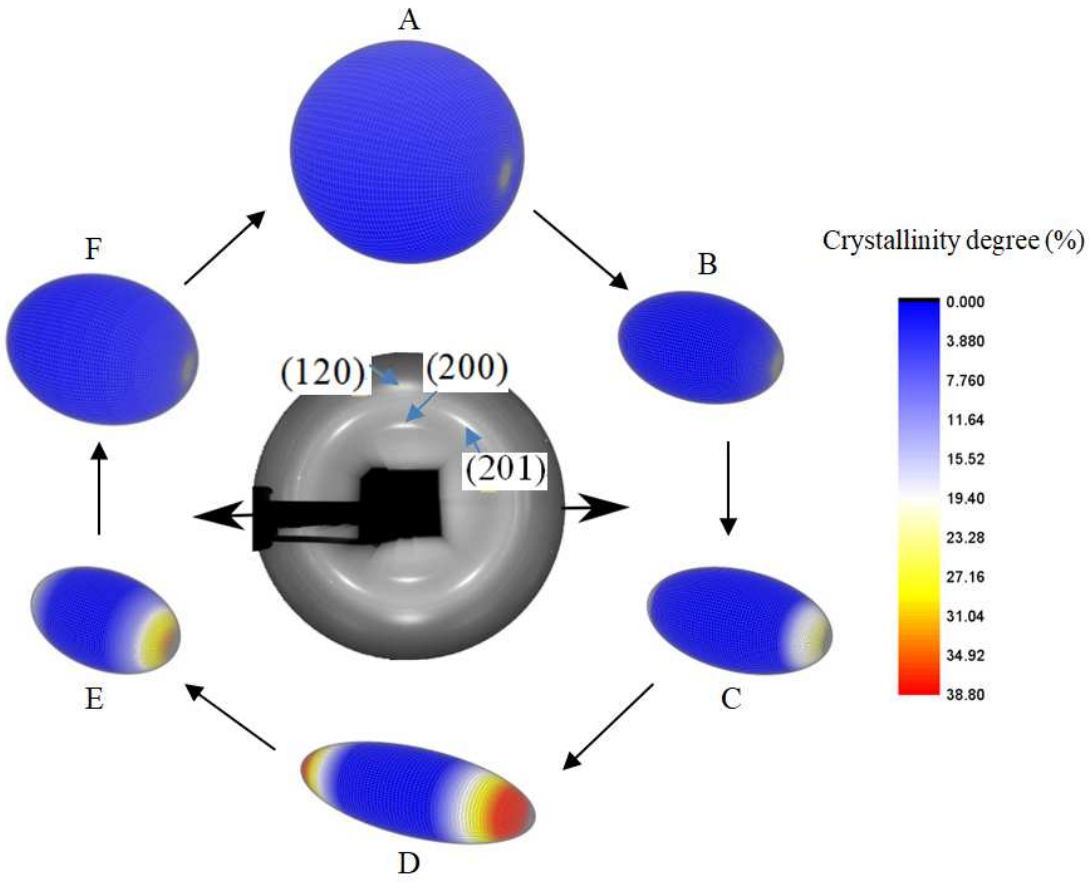

Figure 3.2.4. Typical microsphere evolution and crystallinity distribution at different stages of stretching-recovery indicated by letters in Figure 3.2.3; The WAXD pattern is taken from (Rublon et al., 2014).

The realistic description of the microstructure at the chain-scale comes with a deformation-induced anisotropy. In the experiments, the crystallization anisotropy is evidenced by the scattering intensity distribution with the azimuthal angle that is read out from the WAXD pattern. With regard to the uniaxial stretch, the orientation with the maximum scattering intensity is along the tensile direction and the dispersion of the scattering intensity reflects thecrystallinity distribution around the tensile direction, which is the nature of crystallization anisotropy (Trabelsi et al., 2003; Tosaka et al., 2004). The stretch-induced crystallization process simulated by the model is recorded in Figure 3.2.4 in the form of contour plots at different stages of stretching/recovery. Once the crystallization begins at the macro-scale, it is initiated at the microsphere pole (Figure 3.2.4B) where the molecular chains are oriented in

the stretching direction. Due to the progressive crystallization of other molecular chains induced by their progressive ordering, the local crystallization increases (Figures 3.2.4C and 3.2.4D) in intensity and in extent as the stretching increases. As expected, but quite interestingly, in the microsphere equator, where the molecular chains are in the perpendicular plan of the stretching direction, the molecular chains remain amorphous. During the melting process (Figures 3.2.4E and 3.2.4F), the crystallization degree decreases to reach the initial amorphous state (Figure 3.2.4A) and the ellipsoid microsphere re-becomes spherical.

3.2.3.2. Comparison with experiments

The question which arises now is the capability of the model to reproduce experimental data. In what follows, a quantitative evaluation of the model is presented.

3.2.3.2.1. Homogeneous tests

The stretching/recovery response constitutes the most common homogeneous experiment, for which a large variety of material behaviors and of crystallization kinetics exist as reported in some literature reviews (Huneau, 2011; Toki, 2014; Albouy and Sotta, 2017). That is mainly due to a strong, and complex, relationship between the material microstructure, the molecular ordering and the loading conditions such as the maximum stretch level and the stretching temperature. The capability of the model to account for the respective influence of these two important factors governing the stretching/recovery response is quantitatively evaluated in Figures 3.2.5 and 3.2.6. The model is compared to experimental data of Rault et al. (2006a) and Marchal (2006) who measured, respectively, the maximum stretch level effect and the stretching temperature effect on the in-situ material response of crystallizable rubbers and the inherent crystallization. From the adjustment of the best response with the database of Rault et al. (2006a), the following set of model parameters are deduced: nk_BT_0 = 0.6 MPa (T_0 = 20°C), N = 75.0, A_c = 50.0×10^{16} MPa^{-1} s^{-1}, A_m = 15.0×10^{16} MPa^{-1} s^{-1}, ΔH_m = 7.0×10^{-21} J, T_m^0 = 25°C, u_s = 3.5×10^{-21} J, γ=10.0, δ =1.5, η =5.0. From the database of Marchal (2006), the model parameters are: nk_BT_0 = 0.52 MPa (T_0 = 20°C), N = 70.0, A_c = 100.0×10^{16} MPa^{-1} s^{-1}, A_m = 10.0×10^{16} MPa^{-1} s^{-1}, ΔH_m = 15.0×10^{-21} J, T_m^0 = 25°C, u_s = 1.33×10^{-23} J, γ=10.0, δ =0.8, η =5.0. A global view at Figures 3.2.5 and 3.2.6 shows that the hysteresis in crystallization and in stress is greatly affected by the effects of the maximum stretch level and the stretching temperature. It is satisfactory to observe that the model is able to adequately reproduce both effects. In particular, the hysteretic response is remarkably well described

while accounting for the stretch-induced anisotropy accompanied with molecular ordering. In the light of this result, the model is verified. Nonetheless, the verification of model capabilities under more complex loading conditions is an important issue.

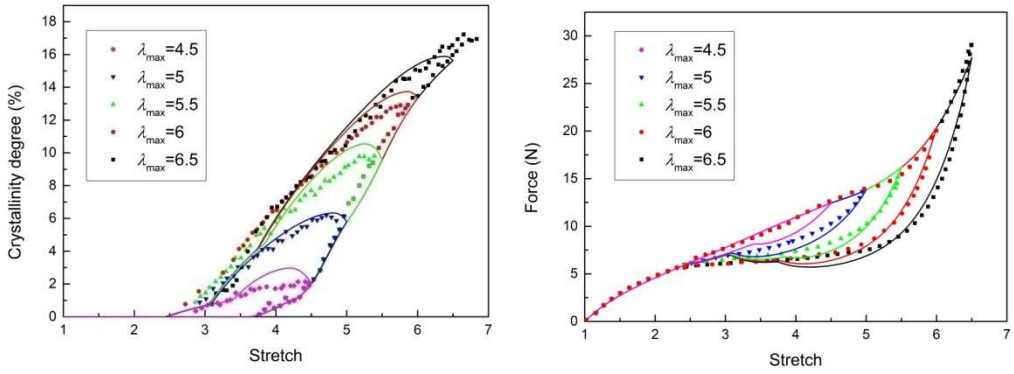

(a) (b)

Figure 3.2.5. Experiments (symbols) and simulations (lines) of the (a) crystallization kinetics and (b) stress-stretch curve at different maximum stretch levels; The experimental points are taken from (Rault et al., 2006a).

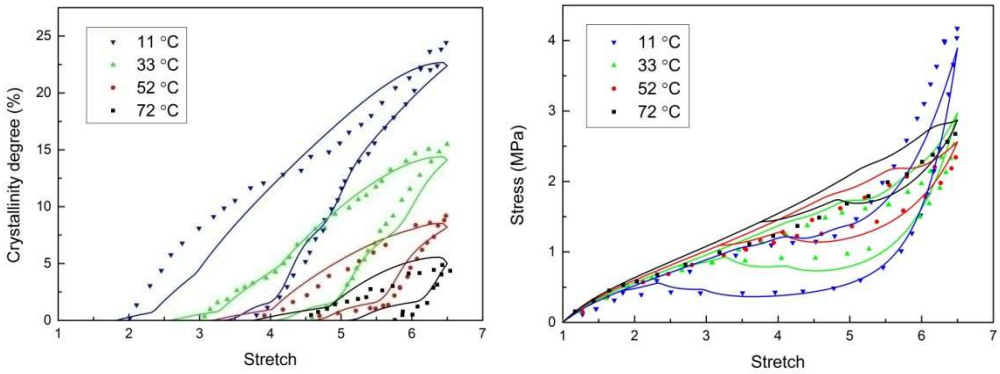

(a) (b)

Figure 3.2.6. Experiments (symbols) and simulations (lines) of the (a) crystallization kinetics and (b) stress-stretch curve at different stretching temperatures; The experimental points are taken from (Marchal, 2006).

Moreover, our simulation results indicate that the intrinsic dissipation is always non-negative whether during stretching or recovery. This appearance accords with the second thermodynamic law which requires non-negativity of intrinsic dissipation for any thermodynamic process. Evidently the accumulation of intrinsic dissipation after the process of stretching/recovery is equivalent to the mechanical dissipation identified by the area of the stress-stretch hysteresis loop. Since only stretch-induced crystallization is introduced as an irreversible thermodynamic mechanism into our proposed model, the energy dissipated by crystallization or melting cannot be stored in other physical mechanisms, but transform into

thermal energy inducing temperature variation. Based on temperature measurement and quantitative calorimetry, Le Cam and Toussaint (2008), Samaca Martinez et al. (2013a, 2013b) and Le Cam (2017) experimentally studied the evolution of intrinsic dissipation during mechanical tests and proposed a method to determine rubber crystallinity. In those experiments the accumulation of intrinsic dissipation was found to be null after any one load cycle. The physical interpretation for this phenomenon was given, that is, the mechanical dissipation is entirely used by the material to change its microstructure and stored as the internal energy accompanying with crystallization evolution. However it is incredible that those experiments exhibited negative intrinsic dissipation during recovery, which obviously goes against the second thermodynamic law.

3.2.3.2.2. Non-homogeneous tests

As a final illustrative example, the non-homogeneous tensile response of a cracking specimen made of a crystallizable rubber is examined. Rublon et al. (2014) studied experimentally the crystallization and orientation in a specimen containing cracks. The specimen dimensions are 157 mm (length) × 13 mm (width) × 2 mm (thickness). They introduced three cracks, two 20 mm-long cracks at the edge and one 30 mm-long at the middle. A numerical analysis of this "classical" problem is performed using the developed constitutive model.

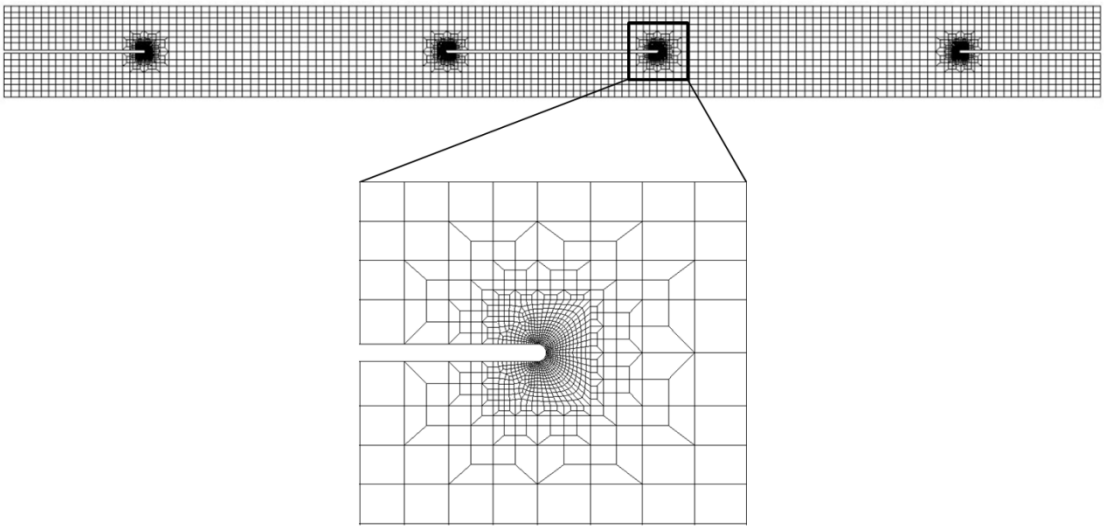

Figure 3.2.7. Mesh of the specimen containing cracks.

Figure 3.2.7 presents the three-dimensional finite element mesh of the specimen with a view of one of the four crack-tips. We consider the crack-tip as a 0.2 mm-radius mid-cylinder. Three-dimensional, eight node, brick solid elements were used with a gradient in mesh size and a refined mesh near the crack-tip. The set of model parameters in Section 3.1 is used, except for the crystal kinetics constants, $A_c = 5000.0\times10^{16}$ MPa^{-1} s^{-1} and $A_m = 5000.0\times10^{16}$ MPa^{-1} s^{-1}. They are set quite large to simulate a quasi-static loading condition.

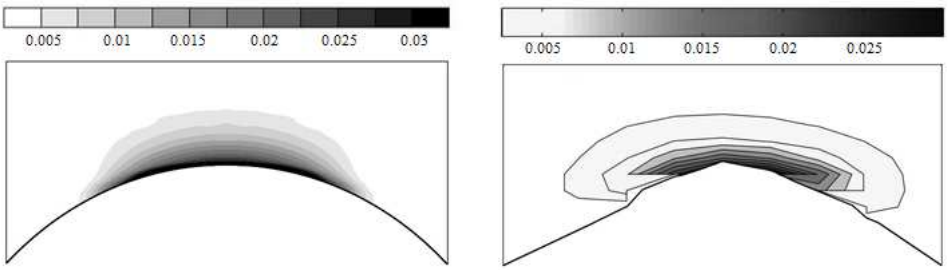

(a)

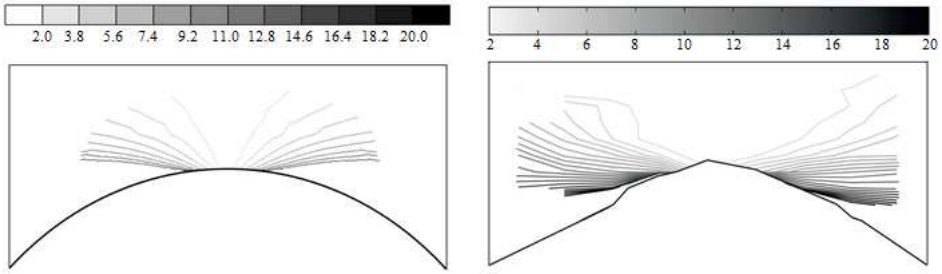

(b)

Figure 3.2.8. Distribution of (a) crystallization and (b) orientation around the crack-tip; right: experimental findings from (Rublon et al., 2014), left: our simulation.

The left plot of Figure 3.2.8a presents the predicted distribution of crystallization by our model near the crack-tip at an applied stretch of 1.92. As expected, the crystallinity distribution exhibits the highest value at the crack-tip with a high gradient level and becomes progressively null while moving from this zone. The crystallization zone is confined around the crack-tip and expands upon increasing the applied stretch. This simulation result is quite acceptable, comparing with the experimental data presented in the right plot of Figure 3.2.8a.

The left plot of Figure 3.2.8b presents the model-predicted angle between the crystallization orientation and the loading direction illustrated by thin bands. The crystallization orientation identified by the microsphere model is defined as the orientation with the maximum crystallization degree in the spatial orientation space. This orientation is actually equivalent to

the principal strain direction corresponding to the maximum stretch ratio, due to the quasi-static loading condition. We can find that the angle is null at the pole of the crack-tip and progressively evolves while moving around it. By this way, the stretch-induced crystallization anisotropy is further demonstrated. The right plot of Figure 8b is the experimental results, in which the orientation with the maximum scattering intensity extracted from the WAXD pattern is considered as the crystallinity orientation. The agreement between simulation and experiment is obviously acceptable.

3.2.4. Partial conclusions

The stretch-induced phase transformation in rubbers is a fascinating phenomenon implying multi-scale features which cannot be treated by purely phenomenological approaches for a rigorous modeling. A micro-macro constitutive model with physically interpretable material constants was proposed in the current paper to describe the crystallization anisotropy and the hysteretic response induced by the molecular ordering in stretch-induced crystallizable rubbers. Our approach is based upon the thermodynamic framework. Key micro-structural and thermodynamic parameters, governing the crystallization micro-mechanism, were introduced in the proposed physically-based model. It was found that the model correctly simulates tensile experiments, in terms of stress-stretch curves and crystallization kinetics, at different stretch levels and temperatures. The example of a specimen containing cracks was presented in order to show the capability of the model to simulate the local crystallization/orientation fields in the vicinity of cracks.

The proposed model seems to be a powerful tool to predict the macro-response along with the micro-structural evolution in rubbers induced by the molecular ordering and the phase transformation. The verification of model capabilities under more complex loading conditions is in progress, but restricted by the scarcity of the literature experimental data. Adding fillers (e.g. carbon-black particles) to reinforce the rubber compound is a common industrial practice, and taking into account the effects of the filler-rubber gum and filler-filler interactions on the material response modeling of stretch-induced crystallizable rubbers is a valuable challenge for future works.

3.2.5. References

Albouy, P.A., Marchal, J., Rault, J., 2005. Chain orientation in natural rubber. I. The inverse yielding effect. The European Physical Journal E: Soft Matter and Biological Physics 17, 247-259.

Albouy, P.A., Vieyres, A., Perez-Aparicio, R., Sanseau, O., Sotta, P., 2014. The impact of strain-induced crystallization on strain during mechanical cycling of cross-linked natural rubber. Polymer 55, 4022-4031.

Albouy, P.A., Sotta, P., 2017. Strain-induced crystallization in natural rubber. Advances in Polymer Science 277, 167-205.

Arlman, J.J., Goppel, J.M., 1951. On the degree of crystallinity in natural rubber. Applied Scientific Research 2, 1-8.

Avrami, M., 1939. Kinetics of phase change. I. General theory. The Journal of Chemical Physics 7, 1103-1112.

Bazant, Z., Oh, B., 1986. Efficient numerical-integration on the surface of a sphere. Zeitschrift fur Angewandte Mathematik und Mechanik 66, 37-49.

Behnke, R., Berger, T., Kaliske, M., 2018. Numerical modeling of time- and temperature-dependent strain-induced crystallization in rubber. International Journal of Solids and Structures 141, 15-34.

Bruning, K., Schneider, K., Roth, S.V., Heinrich, G., 2015. Kinetics of strain-induced crystallization in natural rubber: a diffusion-controlled rate law. Polymer 72, 52-58.

Candau, N, Laghmach R, Chazeau L, Chenal, J., Gauthier, C., Biben, T., Munch, E., 2014. Strain-induced crystallization of natural rubber and cross-link densities heterogeneities. Macromolecules 47, 5815-5824.

Candau, N., Chazeau, L., Chenal, J.M., Gauthier, C., Ferreira, J., Munch, E., Thiaudière, D., 2015a. Strain induced crystallization and melting of natural rubber during dynamic cycles. Physical Chemistry Chemical Physics 17, 15331-15338.

Candau, N., Laghmach, R., Chazeau, L., Chenal, J.M., Gauthier, C., Biben, T., Munch, E., 2015b. Influence of strain rate and temperature on the onset of strain induced crystallization in natural rubber. European Polymer Journal 64, 244-252.

Clark, G.L., Kabler, M., Blanker, E., Ball, J.M., 1940. Hysteresis in crystallization of stretched vulcanized rubber from X-ray data: correlation with stress-strain behavior and resilience. Industrial and Engineering Chemistry 32, 1474-1477.

Coleman, B.D., Noll, W., 1963. The thermodynamics of elastic materials with heat conduction and viscosity. Archive for Rational Mechanics and Analysis 13, 167-178.

Dargazany, R,. Khiem, V.N., Itskov, M., 2014a. A generalized network decomposition model for the quasi-static inelastic behavior of filled elastomers. International Journal of Plasticity 63, 94-109.

Dargazany, R., Khiem, V.N., Poshtan, E.A., Itskov, M., 2014b. Constitutive modeling of strain-induced crystallization in filled rubbers. Physical Review E 89, 022604.

Dolynchuk, O., Kolesov, I., Androsch, R., Radusch, H.J., 2015. Kinetics and dynamics of two-way shape-memory behavior of crosslinked linear high-density and short-chain branched polyethylenes with regard to crystal orientation. Polymer 79, 146-158.

Flory, P.J., 1947. Thermodynamics of crystallization in high polymers. I. Crystallization induced by stretching. The Journal of Chemical Physics 15, 397-408.

Flory, P.J., 1949. Thermodynamics of crystallization in high polymers. IV. A theory of crystalline states and fusion in polymers, copolymers, and their mixtures with diluents. The Journal of Chemical Physics 17, 223-240.

Gaylord, R.J., 1976. A theory of the stress-induced crystallization of crosslinked polymeric networks. Journal of Polymer Science Part B: Polymer Physics 14, 1827-1837.

Gaylord, R.J., Lohse, D.J., 1976. Morphological changes during oriented polymer crystallization. Polymer Engineering and Science 16, 163-167.

Gros, A., Huneau, B., Verron, E., Tosaka, M., 2019a. A physically-based model for strain-induced crystallization in natural rubber. Part I: life cycle of a crystallite. Journal of the Mechanics and Physics of Solids 125, 164-177.

Gros, A., Verron, E., Huneau, B., 2019b. A physically-based model for strain-induced crystallization in natural rubber. Part II: derivation of the mechanical model. Journal of the Mechanics and Physics of Solids 125, 255-275.

Guilie, J., Thien-Nga, L., Le Tallec, P., 2015. Micro-sphere model for strain-induced crystallisation and three-dimensional applications. Journal of the Mechanics and Physics of Solids 81, 58-74.

Guo, Q., Zaïri, F., Baraket, H., Chaabane, M., Guo, X., 2017. Pre-stretch dependency of the cyclic dissipation in carbon-filled SBR. European Polymer Journal 96, 145-158.

Guo, Q., Zaïri, F., Guo, X., 2018. Thermodynamics and mechanics of stretch-induced crystallization in rubbers. Physical Review E 97, 052501.

Holzapfel, G., Simo, J., 1996. Entropy elasticity of isotropic rubber-like solids at finite strains. Computer Methods in Applied Mechanics and Engineering 132, 17-44.

Huneau, B., 2011. Strain-induced crystallization of natural rubber: a review of X-ray diffraction investigations. Rubber Chemistry and Technology 84, 425-452.

Katz, J.R., 1925. Rontgenspektrographische untersuchungen am gedehnten kautschuk und ihre mogliche bedeutung fur das problem der dehnungseigenschaften dieser substanz. Naturwissenschaften 13, 410-416.

Khiem, V.N., Itskov, M., 2018. Analytical network-averaging of the tube model: strain-induced crystallization in natural rubber. Journal of the Mechanics and Physics of Solids 116, 350-369.

Kroon, M., 2010. A constitutive model for strain-crystallising rubber-like materials. Mechanics of Materials 42, 873-885.

Laghmach, R., Candau, N., Chazeau, L., Munch, E., Biben, T., 2015. Phase field modelling of strain induced crystal growth in an elastic matrix. The Journal of chemical physics 142, 244905.

Le Cam, J.B., Toussaint, E., 2008. Volume variation in stretched natural rubber: competition between cavitation and stress-induced crystallization. Macromolecules 41, 7579-7583.

Le Cam, J.B., 2017. Energy storage due to strain-induced crystallization in natural rubber: the physical origin of the mechanical hysteresis. Polymer 127, 166-173.

Marchal, J., 2006. Cristallisation des caoutchoucs chargés et non chargés sous contrainte: effet sur les chaînes amorphes. PhD. Thesis, Université Paris XI.

Miehe, C., Goktepe, S., Lulei, F., 2004. A micro-macro approach to rubber-like materials. Part I: the non-affine micro-sphere model of rubber elasticity. Journal of the Mechanics and Physics of Solids 52, 2617-2660.

Mistry, S.J., Govindjee, S., 2014. A micro-mechanically based continuum model for strain-induced crystallization in natural rubber. International Journal of Solids and Structures 51, 530-539.

Murakami, S., Senoo, K., Toki, S., Kohjiya, S., 2002. Structural development of natural rubber during uniaxial stretching by in situ wide angle X-ray diffraction using a synchrotron radiation. Polymer 43, 2117-2120.

Nateghi A, Dal H, Keip M A, Miehe, C., 2018. An affine microsphere approach to modeling strain-induced crystallization in rubbery polymers. Continuum Mechanics and Thermodynamics 30, 485-507.

Rastak, R., Linder, C., 2018. A non-affine micro-macro approach to strain-crystallizing rubber-like materials. Journal of the Mechanics and Physics of Solids 111, 67-99.

Rault, J., Marchal, J., Judeinstein, P., Albouy, P.A., 2006a. Chain orientation in natural rubber. II. ^{2}H-NMR study. The European Physical Journal E: Soft Matter and Biological Physics 21, 243-261.

Rault. J., Marchal, J., Judeinstein, P., Albouy, A., 2006b. Stress-induced crystallization and reinforcement in filled natural rubbers: ^{2}H NMR study. Macromolecules 39, 8356-8368.

Roe, R.J., Smith, K.J., Krigbaum, W.R., 1961. Equilibrium degrees of crystallization predicted for "single pass" and folded chain crystallite models. The Journal of Chemical Physics 35, 1306-1311.

Rublon, P., Huneau, B., Verron, E., Saintier, N., Beurrot, S., Leygue, A., Mocuta, C., Thiaudière, D., Berghezan, D., 2014. Multiaxial deformation and strain-induced crystallization around a fatigue crack in natural rubber. Engineering Fracture Mechanics 123, 59-69.

Samaca Martinez, J.R., Le Cam, J.B., Balandraud, X., Toussaint, E., Caillard, J., 2013a. Mechanisms of deformation in crystallizable natural rubber. Part 1. Thermal characterization. Polymer 54, 2717-2726.

Samaca Martinez, J.R., Le Cam, J.B., Balandraud, X., Toussaint, E., Caillard, J., 2013b. Mechanisms of deformation in crystallizable natural rubber. Part 2. Quantitative calorimetric analysis. Polymer 54, 2727-2736.

Smith, K.J., 1976. Crystallization of networks under stress. Polymer Engineering and Science 16, 168-175.

Toki, S., Sics, I., Hsiao, B.S., Tosaka, M., Poompradub, S., Ikeda, Y., Kohjiya, S., 2005. Probing the nature of strain-induced crystallization in polyisoprene rubber by combined thermomechanical and in situ X-ray diffraction techniques. Macromolecules 38, 7064-7073.

Toki, S., 2014. The effect of strain-induced crystallization (SIC) on the physical properties of natural rubber (NR). In: Kohjiya, S., Ikeda, Y. (Eds.) Chemistry, Manufacture and Applications of Natural Rubber. WoodHead/Elsevier, Cambridge.

Tosaka, M., Murakami, S., Poompradub, S., Kohjiya, S., Ikeda, Y., Toki, S., Sics, I., Hsiao, B.S., 2004. Orientation and crystallization of natural rubber network as revealed by WAXD using synchrotron radiation. Macromolecules 37, 3299-3309.

Tosaka, M., Senoo, K., Sato, K., Noda, M., Ohta, N., 2012. Detection of fast and slow crystallization processes in instantaneously-strained samples of cis-1,4-polyisoprene. Polymer 53, 864-872.

Trabelsi, S., Albouy, P.A., Rault, J., 2003. Crystallization and melting processes in vulcanized stretched natural rubber. Macromolecules 36, 7624-7639.

Wang, M.C., Guth, E., 1952. Statistical theory of networks of non-Gaussian flexible chains. The Journal of Chemical Physics 20, 1144-1157.

Xie, Z., Wei, C., Guyomar, D., Sebald, G., 2016. Validity of Flory's model for describing equilibrium strain-induced crystallization (SIC) and thermal behavior in natural rubber. Polymer 103, 41-45.

Xie, Z., Sebald, G., Guyomar, D., 2017. Temperature dependence of the elastocaloric effect in natural rubber. Physics Letters A 381, 2112-2116.

GENERAL CONCLUSIONS

This PhD dissertation is a contribution to the thermo-mechanical coupling of rubbers. Both the inelastic cyclic response of carbon-filled rubbers and the stretch-induced crystallization of natural rubbers were investigated.

In *Chapter 2*, a combined approach including experimental investigation and constitutive theory was developed to study the heat build-up due to thermo-mechanical coupling in carbon-filled rubbers. The internal state variable theory was adopted and the intrinsic dissipation was quantified to investigate the carbon-filled SBR history-dependent cyclic response. The intrinsic dissipation was regarded as a consequence of two types of rearrangements, i.e. recoverable rearrangement inducing viscoelasticity and unrecoverable rearrangement inducing damage. The effects of pre-stretch and filler content on the macro-response and the underlying inelastic fatigue mechanisms were highlighted. A new constitutive model was proposed for thermal, viscoelastic and damage patterns estimation in cyclically loaded rubber structures. The thermo-viscoelastic-damage model, fully three-dimensional and implemented into a finite element code by means of a strain energy function subroutine, was presented in its most general form with the aim of being applicable to all carbon-filled rubbers. The model was based upon the assumption that the two types of dissipative network rearrangements exist in the rubber: unrecoverable damage rearrangement and recoverable viscoelastic rearrangement. The latter was assumed to be induced by the move of entangled and non-entangled free chains superimposed on a purely elastic perfect rubber network. Each population of free chains was considered to be the main source of one aspect of the history-dependent mechanical cyclic features, i.e. stress-softening and hysteresis, respectively. It was shown that the proposed model provides a useful tool to simulate the effects of the network rearrangements on the inelastic fatigue response, i.e. stress-softening and hysteresis along with dissipative heating. The effect of the

filler content over the thermo-mechanical response was explicitly taken into account. The efficiency of the model to predict the inelastic fatigue response of carbon-filled SBR with different filler amounts was demonstrated. A first step towards the study of cyclically loaded thick specimens was provided via numerical simulations.

In *Chapter 3*, a new micro-mechanism inspired molecular chain model was proposed within the context of the thermodynamic framework to describe the thermo-mechanical response of stretch-induced crystallizable rubbers. The stretch-induced crystallization was considered as an irreversible thermodynamic process driven by a thermodynamic crystallization force induced by the non-equilibrium thermodynamic state. In the spirit of the Flory theory, a realistic physical expression of the chain free energy was derived via a two-step strategy by separating crystallization and stretching. The major weakness of the Flory theory was eliminated since the thermodynamic crystallization force in our approach is well null at the initial state under the melting temperature. The microsphere-based strategy was used by implementing the proposed chain free energy to make the micro-macro transition. It was shown that the proposed model provides a useful tool to simulate the macro-response under the equilibrium state and the non-equilibrium state involved during stretching/recovery and continuous relaxation. A quantitative evaluation of the model was performed by comparisons with experiments. The proposed approach contains very few physically interpretable material constants and seems to be sufficiently rich to provide important indications concerning this fascinating phenomenon in terms of crystallization-induced anisotropy and dissipation. The satisfactory simulation results provided by our theory can be attributed to its solid physical foundation. More specifically, the molecular configuration of the partially crystallized chain is objectively analyzed and reasonably described by means of some statistical mechanical methods, especially considering the random thermal oscillation of the crystal orientation.

RESEARCH PERSPECTIVES

The results of the present work open the way to several perspectives:

- The first concerns the filled rubbers. The coupled effect of the temperature and the filler content on the time-dependent response of the material could enhance the model capability. Besides, notice that, a higher temperature is related with a smaller hysteresis loop. Likewise, the hysteresis loop characteristics depend upon the analysis material point, as a consequence of the inner temperature gradient. Thereafter, the experimental study of an inner temperature field will bring light about the heterogeneous thermo-mechanical behavior of the material. The model capability to describe and predict the dissipative heating of filled rubbers during different fatigue conditions is a subject to be investigated. In order to understand the thermo-mechanical origins of the stress-softening due to cyclic loading, the study of the time-effect of the dissipative heating on the stress will bring some light about. Besides, the thermo-mechanical model scope could be improved by considering the dissipative heating path from the reference configuration until failure. Then, the proposed model could be enhanced by adding the well-known sudden heat build-up before failure. Since the thermal degradation could play an important role, the dissipative heating effects on the material lifetime is an additional interesting subject to be investigated. Finally, the potential of the model to predict the dissipative heating due to crack initiation or crack growth is a subject to be studied.
- The second concerns the stretch-induced crystallizable rubbers. Our theory provided significant physical insights about a fascinating phenomenon still misunderstood and involved very few physically interpretable material constants. More work is however needed to introduce into our theory the micro-structure of crystallites and its evolution. In particular, in addition to the crystal fraction and orientation, it is believed that the crystallite morphology, in terms of form and size, could also control the thermo-mechanical macro-response. A morphology-

dependence of the surface free energy would be interesting to establish in order to propose a more realistic onset of crystallization, in particular in terms of rate-dependency which can be also viewed as a rate-dependency of the necessary supercooling or superstretching. Bu using our model, we can predict the stress hysteresis evolution and the temperature evolution during cyclic loading. These predictions could bring a better understanding of the relationship between the two evolutions in the aim to better understand the origin of the stress hysteresis (Le Cam, 2017) in relation with possible microstructure changes. In this regard, the coupling between stored/dissipated energy and microstructure changes during cycling loading could be investigated using the constitutive theory that we have proposed in *Chapter 2*. Finally, the potential of the model to predict the crack initiation or crack growth in crystallizable rubbers is also a subject to be studied.

Abstract

This PhD thesis is focused on the fatigue and the stretch-induced crystallization in rubbers. For these two aspects, new thermo-mechanical constitutive models are mathematically formulated, and incorporated into a computer code in the aim to perform numerical simulations on rubber structures. The models are physically-based in the sense that some key elements of the actual microstructure and the mechanisms (viscoelasticity, damage, heat build-up, crystallization) are incorporated. The input data needed by the models are identified on experimental observations performed on different loading conditions and the predictive capabilities are verified on other experiments. The cyclic dissipation, the fatigue damage and the anisotropy are key points of the PhD thesis.

Keywords: Rubbers; Cyclic dissipation; Constitutive theory; Crystallization; Anisotropy.

Résumé

Cette thèse porte sur la fatigue et la cristallisation induite par étirement dans les caoutchoucs. Pour ces deux aspects, de nouveaux modèles de comportement thermo-mécaniques sont formulés mathématiquement et incorporés dans un code informatique dans le but de réaliser des simulations numériques sur des structures en caoutchouc. Les modèles sont physiquement fondés en ce sens que certains éléments clés de la microstructure réelle et des mécanismes (viscoélasticité, endommagement, auto-échauffement, cristallisation) sont incorporés. Les données d'entrée nécessaires aux modèles sont identifiées à partir d'observations expérimentales effectuées dans différentes conditions de chargement et les capacités prédictives sont vérifiées sur d'autres expériences. La dissipation cyclique, l'endommagement par fatigue et l'anisotropie sont des points clés de la thèse.

Mots-clés: Caoutchoucs; Dissipation cyclique; Théorie constitutive; Cristallisation; Anisotropie.